Transient scattering effects in Sentinel 1 ground deformation analyses of the rural UK

A thesis submitted to Imperial College London in partial fulfilment of the requirements for the degree of Doctor of Philosophy

Stewart Agar

March 2023

Department of Civil and Environmental Engineering

Imperial College London

London SW7 2AZ

Abstract

Interferometric analysis of Synthetic Aperture Radar (SAR) data is widely performed to measure deformation of the ground and infrastructure. Through analysis of SAR interferograms calculated for diverse windows in time, 'Multi-Temporal InSAR' (MTI) analysis techniques using current imaging satellites can regularly measure certain features to millimetric precision, over regions spanning hundreds of kilometres.

The accuracy of MTI measurements is drastically reduced when measuring surface features in rural areas, as the impermanent geometry and radiometric properties of vegetation and soil (which are semi-transparent at typical SAR frequencies) scatterers cause decorrelation of the interferometric phase over relatively short periods of time.

While this decorrelation has historically been modelled as a zero-mean noise, more recent literature has demonstrated mechanisms whereby this model does not hold. Phenomena affecting the dielectric properties of soil and vegetation lead to gradual changes in scattering and subsequent interferometric phase variation, and the spatial and temporal correlation of these phenomena can significantly deformation measurements.

This work presents a set of approaches for systematically identifying and evidencing these transient scattering processes. Distinct patterns in non-zero mean phase are identified and highlighted using *a priori* maps of vegetation type. These distinct patterns are associated with transient scattering behaviour of the soil and vegetation under study, and this work demonstrates that these patterns are pervasive in time and occur across a range of rural land covers and types of vegetation.

This work has significant implications for MTI deformation measurements in vegetated environments. Where present, significant transient scattering phases necessitate modifications to existing approaches and the interpretations of their results.

A novel method has been presented to isolate distinct patterns in transient scattering behaviour using K-means clustering of correlations found in the frequency domain. Valuable improvements to deformation measurements are subsequently demonstrated.

Statement of Originality

This thesis is my own work except where due referencing and acknowledgement has been made.

Stewart Agar

London, April 2023

Copyright Declaration

The copyright of this thesis rests with the author. Unless otherwise indicated, its contents are licensed under a Creative Commons Attribution-Non Commercial 4.0 International Licence (CC BY-NC). Under this licence, you may copy and redistribute the material in any medium or format. You may also create and distribute modified versions of the work. This is on the condition that: you credit the author and do not use it, or any derivative works, for a commercial purpose. When reusing or sharing this work, ensure you make the licence terms clear to others by naming the licence and linking to the licence text. Where a work has been adapted, you should indicate that the work has been changed and describe those changes. Please seek permission from the copyright holder for uses of this work that are not included in this licence or permitted under UK Copyright Law.

Acknowledgements

There is a long list of individuals and interactions without which this piece of research would never have begun or ended.

Firstly, I would like to thank my supervisors: Dr. James Jawrence, Dr. Philippa Mason, and Prof. Richard Ghail. Their passion and enthusiasm have been infectious throughout. From here I hope we can work together for a very long time on a range of exciting and evolving topics. I would particularly like to thank James for his efforts and support far beyond the call of duty, for which I will always be extremely grateful. Thank you all so much for these opportunities. There's no way I can fit sufficient thanks into this page.

The technical aspects of this work were invigorated by Alessio Rucci and Alessandro Ferretti of Tre Altamira. They introduced me to 'Crazy Fields' in InSAR, statistical testing of scatterers, and ideas regarding clustering. Together, these concepts led to the most valuable findings of this work.

This project was generously supported by Nuclear Waste Services (formerly Radioactive Waste Management Ltd.). From there I would like to particularly thank Sally Thompson and Matt Bailey who have been helpful, insightful and a joy to work with.

The project was aided in moments of crisis by the administration of Sarah Willis and Jonathan Tate at Imperial College, and I would like to sincerely thank them for their help.

My PhD colleagues provided me with a free and ongoing education in Geology and Geotechnics, along with many great memories. Tom Morgan's insights into UK Geology and inspirational experiments in marine biology deserve particular acknowledgement.

I am extremely privileged by the support of my parents and their commitment to my education throughout the years. None of my opportunities would have been available without their hard work and I cannot thank them enough.

Finally, I would like to thank my wife Danielle for her patience and the joy she brings. Throughout an endless chain of rental properties, vanishing finances, and a pandemic you have been my continual happiness.

Contents

Abstract 1

Statement of Originality 2

Copyright Declaration 2

Acknowledgements 3

List of Figures 9

List of Equations 16

List of Publications 18

List of Abbreviations and Terminology 19

1. Introduction 24

1.1. Research motivation 26

1.2. Aims and objectives 27

1.3. Structure of this document 29

2. Literature Review 31

2.1. Fundamentals of Radar 32

2.1.1. Electromagnetic wave propagation 34

2.1.2. Interference and radar resolution 36

2.1.3. Resolution of scatterers parallel to a simple, stationary radar 37

2.1.4. Resolution of scatterers down-range of a simple, stationary radar 39

2.1.5. Scattering 40

2.2. Synthetic Aperture Radar 42

2.2.1. Imaging Geometry 42

2.2.2. Azimuth Resolution 43

2.2.3. Focusing and Geocoding 45

2.2.4. SAR measurements 46
2.3. SAR Satellites 49
2.3.1. Sentinel 1 50
2.4. Interferometric phase 52
2.4.1. Deformation 53
2.4.2. Orbital determination error 54
2.4.3. Topography 54
2.4.4. Atmospheric Phase Screen (APS) 56
2.4.5. Scatterer behaviour 57
2.4.6. Noise 57
2.4.7. Coherence 58
2.5. InSAR stacks 61
2.5.1. Coregistration 62
2.5.2. Time series decorrelation 63
2.5.3. Processing InSAR stacks 64
2.6. Summary of gaps in literature 65
2.7. Conclusion 65
3. Methodology 67
3.1. Introduction 67
3.1.1. Motivation 67
3.1.2. OpenInSAR 69
3.2. High-level Design 70
3.2.1. Stakeholders 70
3.2.2. Requirements 70
3.2.3. Specification 73

3.2.4. Architecture 74
3.2.5. Delivery 77
3.3. PSI Reference Processor 80
3.3.1. Orbital positioning 82
3.3.2. Geocoding 82
3.3.3. Coregistration 84
3.3.4. Persistent Scatterer Identification 85
3.3.5. Atmospheric Phase Screen (APS) 88
3.3.6. Modelling Height and Linear Deformation 89
3.4. Qualification of the software system 90
3.5. Current limitations and ongoing development 92
3.6. Hardware and operating systems 92
3.7. Conclusion 93
4. Transient Scattering 94
4.1. Introduction 94
4.2. Background 97
4.2.1. Reflection and transmission at dielectric interfaces 98
4.2.2. Scattering models 102
4.3. Soil moisture 106
4.3.1. SAR measurement of soil moisture 107
4.3.2. Soil moisture in interferometry 108
4.4. Transient scattering in vegetation 112
4.5. Isolating transient scattering phase 115
4.6. Investigation 123
4.6.1. Land cover data 127

4.6.2. Methodology 127
4.7. Results 128
4.8. Analysis 135
4.8.1. Soil moisture 137
4.9. Conclusions 142
5. Quantitative analysis of transient scatterers 143
5.1. Introduction 143
5.2. Useful observables 146
5.2.1. Stability and stationarity 146
5.2.2. Amplitude analysis 149
5.2.3. Coherence analysis 150
5.2.4. Polarimetry 157
5.3. Identifying TS 160
5.4. Time series analysis via Fourier components 161
5.5. Time series clustering 164
5.5.1. K-means clustering 164
5.5.2. Training Data 165
5.5.3. Automation 166
5.5.4. Basic classification 169
5.5.5. Analysis 175
5.6. Conclusions 177
6. Transient scatterer deformation analysis in South Wales 179
6.1. Introduction 179
6.2. Methodology 182
6.3. Results 183

6.4. Analysis 187
6.4.1. East Pentwyn and Bourneville Landslides 192
6.4.2. Margam mine 198
6.4.3. Ffos-y-fran project 200
6.4.4. K-means and land cover 204
6.5. Conclusion 206
7. Conclusions 208
7.1. Summary of research 209
7.2. Novel contributions 211
7.3. Recommendations for further work 213
References 215

List of Figures

Figure 2-1: Terminology in a basic radar measurement 32
Figure 2-2: Orthogonality of the magnetic and electric fields in an electromagnetic wave as it travels along the dimension z with wavenumber k 35
Figure 2-3: Radiation patterns for a linear antenna, using an approach where the antenna is modelled as a series of interfering point sources (Bamler, 2000). 38
Figure 2-4: Demonstration of electronic steering via altering the phase of antenna elements according to their position along its profile. 39
Figure 2-5: The scattering cross section, $\boldsymbol{\sigma}$, as a function of a spherical scatterers circumference $\boldsymbol{2\pi a}$, with respect to the EM wavelength, $\boldsymbol{\lambda}$ (Skolnik, 2001). 41
Figure 2-6: SAR imaging geometry and terminology, via (Engdahl, 2013). 43
Figure 2-7: Overview of recent InSAR capable satellite constellations and their approximate operational timelines (Moreira *et al.*, 2013; Mason *et al.*, 2022). 49
Figure 2-8: Typical phase errors produced by inaccuracy in a DEM. 55
Figure 2-9: Spatial correlation of the atmospheric phase screen (Grebenitcharsky and Hanssen, 2005). 56
Figure 3-1: Statistically dissimilar behaviour of targets on Chalk and clay in the Salisbury Plain area. A modified PSI processing chain was required to further investigate this observed phenomenon. Key: OC/KF Oxford Clay and Kellaways; KCF: Kimmeridge Clay; UGS; Upper Greensand; WC: White Chalk. (Agar *et al.*, 2018) 68
Figure 3-2: Typical use cases for *OpenInSAR* for various stakeholders. 75
Figure 3-3: High-level conceptual diagram of the *OpenInSAR* Architecture 76
Figure 3-4: Flow diagram depicting how *OpenInSAR* produces results. Plugins specify their requirements and the data they produce, as such processing chains are constructed upon specific data being requested. 79
Figure 3-5: Block diagram for the reference PSI processing chain, showing the main InSAR signal processing operations implemented within the software. 81
Figure 3-6: SAR imaging geometry. The motion of the satellite along its track produces a Doppler effect that can be used to geolocate samples. This is combined with the timing

of the echo which varies with the range between the satellite and scatterers on the ground. (Ford, 1993) 83
Figure 3-7: Demonstration of the relationship between SAR amplitude dispersion and InSAR phase noise, recreated from (Ferretti, Prati and Rocca, 2001). Both dispersion index (unitless) and phase standard deviation (rad) are plotted on the y-axis. 87
Figure 3-8: Distribution of PS points generated from ascending (a) and descending (b) Sentinel 1 orbits for the Ventnor Scheme 2020.....91
Figure 4-1: Unfiltered deformation rate measurements from Sentinel 1 Orbit 81 between Jan 2015 and August 2019 (Grant, 2020). A clear correlation between apparent uplift (Blue) and Gault Clay areas can be seen, whilst other rural areas show more locally clustered patterns of apparent subsidence behaviour (red) especially south of Maidstone. Urban areas can be seen as areas of relative stability (green). Despite the limitations of the data a land cover correlation can be appreciated. 95
Figure 4-2: Diagram representation of backscatter from a persistent scatterer (a), and a distributed scatterer (b), including phase simulated with small movements of the elementary scatterers between samples. From (Hooper, 2006) via (Grant, 2020). 97
Figure 4-3: Sketch showing reflection and refraction at a dielectric boundary. 101
Figure 4-4: Orientation of polarised waves. The satellite's instantaneous velocity is in the axis given in yellow, while signals are emitted in the green line's axis, the Vertical polarisation (V) is measured along the red axis, while Horizontal (H) is measured in the blue axis. Sentinel image credit ESA. 101
Figure 4-5: Volumetric, double-bounce, and single-bounce scattering 104
Figure 4-6: The Freeman Durden Three Component Model (3C) (Lopez-Sanchez *et al.*, 2021).....105
Figure 4-7: The empirically measured relationship between a loamy soil's volumetric moisture content, $\boldsymbol{mv}$. and its relative permittivity, $\boldsymbol{\varepsilon}$ (Hallikainen *et al.*, 1985). Physical parameters of a soil control both its in-situ moisture retention characteristics and its dielectric relationship. 106
Figure 4-8: The propagation of a microwave in a soil media, in terms of the wavenumber and wave equation, from (De Zan *et al.*, 2014). The phase advances more quickly per unit distance in the soil, owing to its greater permittivity. 110

Figure 4-9: Example interferometric phase shift predicted as a result of a difference in soil moisture content, assuming C-band radar and a sandy soil with a uniform distribution of inhomogeneities with depth, following (De Zan *et al.*, 2014). 111
Figure 4-10: [Top] Sentinel 2 optical satellite image showing the extensive agricultural area around Winnipeg, Canada [Bottom] Sentinel 1 C-band interferogram the area. The scene dates are 23 January 2020 and 4 February 2020. A rectangular multi-look of 4 in azimuth and 20 in Investigation has been applied. The colour axis shows phase in the range $[-\boldsymbol{\pi}, \boldsymbol{\pi}]$, while the brightness corresponds to the spatial coherence. 113
Figure 4-11: Potential mechanism for stratified scattering from the canopy and ground in vegetated areas, developed from (Zwieback and Hajnsek, 2016) to suggest how scattering mechanisms may shift as vegetation grows. The diffuse volumetric scattering from the fully developed crops can be appreciated as highly sensitive to geometry and moisture content of the canopy.....114
Figure 4-12: Optical imagery for the area of interest in the Vale of Glamorgan, shown encapsulated by the red polygon. The area can be seen here and in 124
Figure 4-13: Topographic elevation for the area of interest in the Vale of Glamorgan, given by the black dotted polygon. 125
Figure 4-14: Crop polygons used, via the UKCEH Land Cover® plus: Crops dataset (UK Centre for Ecology and Hydrology, 2018) 126
Figure 4-15: Phase of the mean coherence matrix measured from crop subsets after calibration for non-scattering errors, the argument of γSk.....129
Figure 4-16: Mean absolute coherence of the coherence matrices for DS corresponding to each field in the Land Cover+ Crops data. 130
Figure 4-17: Difference in absolute coherence as compare to the whole population of fields, for each subset of crops. 131
Figure 4-18: Coherence of normalised phase values for the coherence matrices under analysis, the magnitude of γS.....132
Figure 4-19: Average phase residual after removing the phase of the principal eigenvector for the types of crop under study. 133
Figure 4-20: Average residual phase after removing the phase from the first super-diagonal of each field DS, for each crop under study. 134

Figure 4-21: COSMOS-UK soil moisture data and a simple sinusoidal model. 139
Figure 4-22: Simulated moisture driven phase shift using the model of (De Zan *et al.*, 2014) and approximate figure and timings for soil moisture contents using UK cosmic ray sensors (Stanley, 2021). 140
Figure 4-23: Results for a speculative reflection phase shift occurring in only winter months. 141
Figure 5-1; Real and imaginary components of a stable but noisy scatterer. The distribution of amplitude values is described by the Rice distribution. 146
Figure 5-2: A stable scatterer with additive noise, identical to that of Figure 1, albeit with an additional contribution from a Brownian noise component and hence a drift in in-phase and quadrature amplitudes. 147
Figure 5-3: [Top] Amplitude stability measurements for the Vale of Glamorgan, 2018. The colour axis has been scaled such that black pixels are represent the 1st percentile of expected measurements from a Rayleigh distributed time series of equivalent size (1.8644), as produced by pure noise in the in-phase and quadrature channels. White values are an arbitrary value below this (1.5) chosen for display purposes. 149
Figure 5-4: Coherence matrices resulting from two similar models of temporal coherence. Exponential decay (a) occurs where there are Brownian noise processes while sudden jumps in coherence between dates can be described with a Markov model (b), from (Rocca, 2007). 153
Figure 5-5: 60 scenes were available from Sentinel 1's orbital track 30 for the year 2018. These were split into interferometric stacks of 20 each. [Top] optical image showing the area of interest, the Vale of Glamorgan [Middle] false-colour image showing KS test probability of amplitudes from each stack as being drawn from the same distribution as values for the entire year [Bottom] Shannon entropy false-colour image whereby each smaller stack is used to form a band. 156
Figure 5-6: [Top] Temporal coherence between VV and VH measurements (0-1), with white indicating maximum coherence and black indicating no coherence. An additional metric for PS. [Bottom] False colour polarisation image, with channels scaled for visualisation purposes (R) log VV amplitude (G) log mean product of VV and VH amplitude (B) log mean VH amplitude. 159

Figure 5-7: False colour image showing the correlation coefficient between time-series DFTs of the pixel indicated by the black wheel and the rest of the image. Correlations take values between 0 and 1 corresponding directly to the brightness of the channels: (R) VV amplitude, (G) VH amplitude, (B) the product of VV and VH.....163
Figure 5-8: Improvement in score under a variety of subset correction approaches (Y axis) as a ratio of the score calculated when no correction is applied. The X axis shows the number of clusters (in the case of K-means, red curve, or randomly selected subsets, blue curve). For the crop data, green wheel, the X axis represents the number of labels. Multiple iterations of the sub-setting were performed, with the dotted lines representing +/-1 standard deviation. 168
Figure 5-9: By finding the maximum of $\beta K_K-means-2*\beta K_Random$ the improvement of βK should be maximised while ensuring each increment outweighs the error introduced due to selection bias. 169
Figure 5-10: Agreement between land cover data and the K-means clustering solution. 171
Figure 5-11: Extract from the a priori Land Cover map and the K-means clustering solution, showing an area of relatively good agreement in groupings. For crop label colour legend see Figure 5-10.....173
Figure 5-12: Area of relatively poor agreement between the a priori Land Cover map and the K-means clustering solution. For crop label colour legend see Figure 5-10.....173
Figure 5-13: Agreement between clustering solution and *a priori* crop map. As the number of clusters *k* increases, as does the agreement with the available ground truth regarding land cover. Due to limitations of either the clustering or the ground truth this will converge at reach a point where further improvements are minimal. This point can be seen around 15 clusters for the data above. 174
Figure 5-14: [Top] Argument of the Subset of Scatterers coherence $\angle\gamma S_k$, corresponding to average phase for clusters automatically fitted to the *a priori* crop data. [Bottom] Magnitude of this coherence γS_k, reflecting the degree of agreement between normalised phase values over the subset. 176
Figure 6-1: Results from a prior study of the area of interest (Bateson *et al.*, 2015). Bateson et al. used European Remote-Sensing Satellite 1 and 2. (a) SBAS methodology (Berardino

et al., 2002) and Intermittent SBAS (Sowter *et al.*, 2013) which uses any interferogram for which sufficient spatial coherence exists, rather than the traditional approach which requires sufficient spatial coherence for all small-baseline interferograms.....180
Figure 6-2: UKCEH Land Cover Map 2018 for comparison with Figure 6-4. 181
Figure 6-3: Phase of the scattering subset coherence, γS, for two cluster labels corresponding to areas classified as [A] arable and horticulture (presumed by author to be mainly winter wheat) and [B] improved grassland (presumed by author to be livestock-grazed). 182
Figure 6-4: Geocoded K-means cluster labels automatically assigned to SAR pixels. A random colour has been assigned to each. Black pixels indicate those marked as PS or DS which exhibit limited transient scattering behaviour, including woodlands.....184
Figure 6-5: Results from PSI study of South Wales. The pink rectangles demarcate areas discussed in further detail in Section 6.4, the corresponding labels are as follows - A: Margam Open Pit (Figure 6 10); B: Ffos-y-Fran project (Figure 6 11); C: Blaina landslides (Figure 6 7).....185
Figure 6-6: Results from MTI study of South Wales including compensation of apparent Transient Scattering behaviour. The pink rectangles demarcate areas discussed in further detail in Section 6.4, the corresponding labels are as follows - A: Margam Open Pit (Figure 6-17); B: Ffos-y-Fran project (Figure 6-18); C: Blaina landslides (Figure 6-12).....186
Figure 6-7: PSI results for Port Talbot showing subsidence of residential areas built upon sites of historical landfill and deformation of a harbour wall. 189
Figure 6-8: Historical imagery for the areas of settlement and subsidence shown in Figure 6-7. The pink square shows the construction of a large school, where the pink triangle shows construction of a number of houses on an existing landfill site. Other landfill sites are visible in the area, in line with the areas extensive industrial usage.....190
Figure 6-9: PSI Deformation Rate results showing settlement of a marina and spoil heap slope movements associated with areas of historically recorded and ongoing landfill activity (Natural Resources Wales, 2017) shown via pink polygons. 191
Figure 6-10: Deformation results for Bourneville Landslide, Abertillery, South Wales. The white overlay demarcates the extent of landslide zones identified by Blaenau Gwent council as shown in Figure 6-14. 193

Figure 6-11: Displacement time series for Bourneville landslide. The blue curve corresponds to TS-corrected data, the red to DS data without correction, and the black dashed line follows a 2nd order polynomial fit of the TS-corrected data. 193
Figure 6-12: Overview and 3D projection of the East Pentwyn and Bourneville landslides, near Abertillery. 194
Figure 6-13: Deformation rates for East Pentwyn and Bourneville landslides, as measured by PSI (left) and DS data without correction for TS behaviour (right).....195
Figure 6-14: Map of the Bourneville Slip landslide near Blaina, kindly provided by Blaenau Gwent council. 196
Figure 6-15: Photographs of the Bourneville Slip kindly provided by Blaenau Gwent council. 197
Figure 6-16: Slope movement and settlement at the Margam open cast mine. 198
Figure 6-17: Deformation rates for Margan open cast mine, as measured by PSI (left) and DS data without correction for TS behaviour (right). 199
Figure 6-18: Downslope ground movement at Ffos-y-fran open cast coal mine (Scoular *et al.*, 2021).....200
Figure 6-19: Deformation rates for Ffos-y-Fran, as measured by PSI (left) and DS data without correction for TS behaviour (right). 201
Figure 6-20: Plans for the Ffos-y-Fran land reclamation and coal excavation scheme, showing the stage immediately prior to this investigation (Miller Argent & RPS, 2015).202
Figure 6-21: Plans for the Ffos-y-Fran land reclamation and coal excavation scheme, showing the planned status of the groundworks at the time of this investigation (Miller Argent & RPS, 2015). 203
Figure 6-22: Comparison of land cover labels for the main sites analysed: 1) Blaina; 2) Ffos-y-fran; 3) Margam. A) Google Earth optical imagery; B) CEH Land Cover Crop Classification (legend); C) K-mean radar cluster labels (see text regarding omission of legend). 205

List of Equations

Equation 2-1: The two-way travel equation. 33
Equation 2-2: The Radar Equation 33
Equation 2-3: Propagation of a planar EM wave. 35
Equation 2-4: Radiation from an EM point source. 36
Equation 2-5: Planar illumination pattern from a linear antenna 37
Equation 2-6: Pulsed radar range resolution 39
Equation 2-7: Azimuth resolution of a SAR 44
Equation 2-8: Minimum pulse-repetition frequency to avoid aliasing in azimuth. 44
Equation 2-9: Exponential form representation of a complex SAR measurement. 48
Equation 2-10: Interferometric phase sample measurement 52
Equation 2-11: Interferometric phase components 53
Equation 2-12: Interferometric phase due to deformation. 53
Equation 2-13: Interferometric phase due to topography 54
Equation 2-14: Interferometric coherence 58
Equation 2-15: The sample estimator for interferometric coherence 59
Equation 2-16: Temporal coherence 60
Equation 2-17: Decorrelation factors for an InSAR time series 64
Equation 3-1: The InSAR phase model. 80
Equation 3-2: Range-Doppler equations for geocoding and image coregistration. 83
Equation 3-3: Coherent Cross Correlation optimisation. 84
Equation 3-4: Modelling the relationship between SAR amplitude noise and interferometric phase noise. 86
Equation 3-5: The Amplitude Dispersion (D_A) metric for PS identification. 86
Equation 3-6: The Ordinary Kriging system. 88
Equation 3-7: The coherence optimisation approach for measurement of height error and linear deformation rate. 89
Equation 4-1: Refractive index in non-magnetic media 99
Equation 4-2: Fresnel Coefficients (Born and Wolf, 1999) 100
Equation 4-3: Snell's Law 100

Equation 4-4: Model for estimating the transient scattering phase.....115
Equation 4-5: The coherence of interferometric phases in a subset of scatterers.....116
Equation 4-6: Estimate of the probability for a give phase offset under a zero-mean phase model hypothesis.....118
Equation 4-7: Significance of a set of interferograms.....118
Equation 4-8: Total significance of offsets over a set of interferograms, for a subset of DS selected based on their distinct scattering behaviour 119
Equation 4-9: Combined error variance of the calibrated phase.....121
Equation 4-10: Weighted estimation of the coherence in phase over a subset of scatterers 121
Equation 4-11: Sinusoidal model for a seasonal soil moisture trend typical of the UK..138
Equation 5-1: Temporal Decorrelation.....151
Equation 5-2: Shannon Entropy, H, as a function of eigenvalues λi.....155
Equation 5-3: Number of significant eigenpairs, given by the Kaiser criterion.....155
Equation 5-4: Cross-correlation between pixels measured via discrete Fourier transform. 161
Equation 5-5: Significance of an individual DFT component 162
Equation 5-6: Subset of Scatterers coherence as sampled for a cluster 167
Equation 5-7: Score for a given clustering solution.....167

List of Publications

Agar, S. A., J. A. Lawrence, R. C. Ghail, P. J. Mason, and S. Thompson. 'PSInSAR Remote Sensing Observations of Deformation Behaviour at Salisbury Plain, UK.' In *Engineering in Chalk*, 269–74. Imperial College, London, UK: ICE Publishing, 2018. https://doi.org/10.1680/eiccf.64072.269.

Shire, Tom, James Lawrence, Stewart Agar, Richard Ghail, and Tony Judge. 'Satellite Remote Sensing of UK Embankment Dams: Influence of Dam Features on Monitoring Quality'. *Dams and Reservoirs*, 2023, 1–11.

Wang, Zixiao, James Lawrence, Richard Ghail, Philippa Mason, Anthony Carpenter, Stewart Agar, and Tom Morgan. 'Characterizing Micro-Displacements on Active Faults in the Gobi Desert with Time-Series InSAR'. *Applied Sciences* 12, no. 9 (January 2022): 4222. https://doi.org/10.3390/app12094222.

Scoular, Jennifer, Stewart Agar, Anthony Carpenter, Tom Morgan, James Lawrence, Richard Ghail, and Philippa Mason. 'Expanding Horizons'. *GEOSCIENTIST*, 31 May 2021. https://geoscientist.online/sections/features/expanding-horizons/.

O'Connor, William, Gosia Mider, James A. Lawrence, Stewart Agar, Philippa J. Mason, Richard Ghail, and Jennifer Scoular. 'An Investigation into Ground Movement on the Ventnor Landslide Complex, UK Using Persistent Scatterer Interferometry'. *Remote Sensing* 13, no. 18 (January 2021): 3711. https://doi.org/10.3390/rs13183711.

List of Abbreviations and Terminology

AOI – Area of Interest:

A specific area under analysis in remote sensing applications.

Antenna Gain:

A parameter describing the power of a signal radiated by an antenna in a specified direction as a multiple of the input signal power.

Azimuth:

(Radar context) - the angular direction or dimension that lies in the horizontal plane, often measured clockwise from a reference direction, such as north, toward a particular point or target.

(SAR imaging context) – the direction along the flight path of a Synthetic Aperture Radar (*SAR*) system, and a corresponding dimension of 2-dimensional SAR Images (the other dimension being *Range*).

APS – Atmospheric Phase Screen:

A phenomenon affecting the phase in interferograms due to changes in atmospheric conditions (such as changes in water vapour in the troposphere or free electron concentrations in the ionosphere). See Section 2.4.4.

Baseline:

The distance between two sensors, of interest when comparing their measurements. See also *Perpendicular Baseline*, *Temporal Baseline.*

BGS – British Geological Survey:

An institution in the United Kingdom which provides national geological data.

CEH – Centre for Environment and Hydrology:

See *UKCEH*

Coherence:

A measure of correlation between two *SAR* signals in terms of their phase and amplitude.

DEM – Digital Elevation Model:

A dataset conveying the elevation of an area. See *DTM*, *DSM*.

DTM – Digital Terrain Model:

A dataset measuring the topographical height of the ground's surface.

DSM – Digital Surface Mode:

A dataset measuring surface height, including any land cover such as infrastructure and vegetation canopies.

DFT – Discrete Fourier Transform:

An algorithm transforming a time series signal into an equivalent spectrum of component signals with discrete frequencies.

Doppler frequency:

A shift in signal frequency caused by relative motion between the source and the point of measurement along the signal's direction of travel.

DS – Distributed Scatterers:

A spatially localised collection of individual scatterers which behave somewhat independent of one another, and therefore exhibit InSAR decorrelation, but can be processed jointly as a statistical population to extract useful information. The exact definition of a DS and the analytical techniques used varies among authors (Hooper *et al.*, 2004; Guarnieri and Tebaldini, 2008; Hooper, 2008; Ferretti *et al.*, 2014).

ESA – European Space Agency:

A space agency responsible for commissioning and managing, among other missions, SAR satellites such as Sentinel 1.

Gain:

See *Antenna Gain*

IDW – Inverse Distance Weighting:

A technique for spatially filtering and/or interpolating a dataset.

InSAR – Interferometric Synthetic-Aperture Radar:

A technique calculating and analysing changes in phase between SAR images to provide additional insight.

LOS – Line of Sight:

The axial direction between a radar transceiver and the surface it is illuminating, or a specific scatter being illuminated.

Main Lobe:

An angular region around an antenna in which it radiates the highest relative power.

MTI – Multi-temporal InSAR:

InSAR as specifically applied to time series of *SAR* images.

Multi-looking:

A process applied to reduce noise in a *SAR* image or interferogram by averaging or otherwise filtering values from a localised window of adjacent pixels.

OS – Ordnance Survey:

An institution in the United Kingdom responsible for general mapping of the nation.

Perpendicular Baseline:

The distance between the *SAR* transceiver, between successive measurements, along the axis that produces geometrical decorrelation of interferograms (Zebker and Villasenor, 1992). This axis corresponds to a direction that is perpendicular to both the SAR direction of travel (*Azimuth* axis) and the *Line of Sight* (*Range* axis).

PS – Persistent Scatterers:

Scatterers which consistently exhibit high coherence in *InSAR* analysis. The exact techniques used to identify *PS* varies between authors (Crosetto *et al.*, 2016).

PSI – Persistent Scatter Interferometry:

A multi-temporal *InSAR* measurement technique which focuses specifically on *Persistent Scatterers*, generally used to measure ground deformation.

Radiation Pattern:

See *Antenna Gain*.

Resolution:

The level of detail discernible within an image, for a given dimension.

RCS – Radar Cross Section:

A parameter used to characterise a radar *Scatterer*, measuring the proportion of incident energy redirected backscatter to the radar *Transceiver*.

SAR – Synthetic-Aperture Radar:

A technique used to significantly increase radar imaging *Resolution* via combining multiple measurements from an antenna moving along a known track to form a 'synthetic' antenna.

Sentinel 1:

A *SAR* satellite constellation providing regular near-global coverage of the Earth's landmass.

SBAS – Small Baseline Subsets:

A multi-temporal *InSAR* measurement technique whereby the interferograms used for combined analysis are selected based on favourable properties such as having a low *Perpendicular Baseline* between images (Berardino *et al.*, 2002; Hooper, 2008).

SHP – Statistically Homogenous Pixels:

A selection of pixels with similar time-series *SAR* amplitude behaviour, identified via a statistical test and subsequently treated as a DS (Ferretti *et al.*, 2014).

SLC – Single Look Complex:

A data format for *SAR* images whereby measurements are provided as complex numbers at full resolution (i.e. without *Multi-looking*)

SNR – Signal to Noise Ratio:

The ratio comparing the power of a useful signal to the power of noise signals.

Spatial Baseline:

See *Baseline*

Swath:

The area on the ground imaged by a remote sensing satellite.

(SAR imaging context) – An area of a surface which a *SAR* image measures.

Temporal Baseline:

The difference in time between two or more measurements under comparison.

TOPS – Terrain Observation through Progressive Scans:

A method for increasing the spatial coverage of a *SAR* image by electronically varying the radiation pattern of an antenna system in both azimuth and range dimensions.

Transceiver:

An antenna capable of both transmitting and receiving signals remotely.

TS – Transient Scatterers:

A subset of *DS* which exhibit *Transient Scattering*.

Transient Scattering:

Temporary periods of consistent scattering behaviour, with subsequent interferometric decorrelation caused by some deterministic factor (as opposed to purely random noise or Brownian motion).

TSP – Transient Scattering Phase:

Phase shifts measured and associated with Transient Scattering behaviours.

UKCEH – UK Centre for Environment and Hydrology:

Research organisation focused on environmental science and data provision for the UK.

1. Introduction

Time series analysis of synthetic aperture radar (SAR) data can provide valuable measurements of deformation phenomena affecting ground and infrastructure (Moreira *et al.*, 2013; Crosetto *et al.*, 2016; Osmanoğlu *et al.*, 2016). SAR is a system which emits radar signals toward a target volume and measures the signal returned. The measurements are generally focused into a 2D image according to the spatial position of the scatterers (a scatterer being any object responsible for a measurable return). Satellite-mounted SAR systems are a unique tool for these measurements due to their high spatial coverage and fine spatial resolution (Moreira *et al.*, 2013).

Precise measurements of surface deformation are achieved by analysis of interferometric SAR (InSAR) data (Rosen *et al.*, 2000). InSAR analysis of deformation exploits the relationship between the phase of a radar signal and the two-way distance it travels between the radar antenna and a scatterer. The InSAR phase is, however, additionally sensitive to temporal variations in scatterer properties, atmospheric properties, and topography. Multiple SAR images, analysed as a time series by Multi-temporal InSAR (MTI) techniques (Ferretti, Prati and Rocca, 2001; Hooper, 2008; Crosetto *et al.*, 2016), allow for separating these various components. These techniques can achieve impressive accuracies, in certain cases identifying scatterer movement of less than a millimetre (Ferretti *et al.*, 2007). MTI has been applied in studies of landslides (Herrera *et al.*, 2011; Osmanoğlu *et al.*, 2016), active faulting (Colesanti *et al.*, 2003; Mason *et al.*, 2015), and anthropogenic subsidence (Scoular *et al.*, 2020; Bischoff, 2019b).

The European Space Agency (ESA) has recently launched two Sentinel 1 (S1) satellites (April 2014, April 2016) (*Sentinel-1 Product Specification*, 2016). S1 data is made available to end users free of charge, a step which has removed cost barriers in the research, development, and ongoing application of SAR data analysis (Desnos *et al.*, 2017). S1 was specifically designed to facilitate ground deformation measurement through PSI and related methods (Torres *et al.*, 2012; Yague-Martinez *et al.*, 2016), offering a significant reduction in time between repeat measurements (6 days compared to 35 days with the

ESA's Envisat mission launched in 2002) which greatly increases the accuracy of deformation estimates (Ferretti, Prati and Rocca, 2001; Rocca, 2007).

This project set out to investigate MTI applications in the context of delivering a Geological Disposal Facility (GDF) for radioactive waste in the United Kingdom (UK). For practical purposes, the GDF will be sited away from major population centres (*IAEA Safety Standards: Geological Disposal Facilities for Radioactive Waste*, 2011). Crucially, MTI performance is significantly worse in vegetated, rural, areas as compared to urban areas (Rocca, 2007; Plank, Singer and Thuro, 2013; Ferretti *et al.*, 2014; Osmanoğlu *et al.*, 2016). Activities prior to this project therefore explored these limitations in rural areas of the UK (Agar *et al.*, 2018). These limitations were then targeted for research and development of potential data processing improvements.

MTI, in combination with extensive S1 data sets, may offer significant value for the UK GDF programme. Accurate, regional scale, measurements of ground deformation phenomena may be of value in specific activities undertaken during GDF delivery (White *et al.*, 2004; NDA / RWMD, 2011; *Implementing Geological Disposal*, 2014), such as identifying and characterising faults during ground investigation (Colesanti *et al.*, 2003; Mason *et al.*, 2015); monitoring excavation-related subsidence (Kemeling, 2006); monitoring uplifts driven by thermal expansion from the heat of the waste (*Project Ankhiale: Estimating the uplift due to high-heat-generating waste in a Geological Disposal Facility*, 2015).

It should be noted that none of the geographical areas of the UK explored during this work were chosen based on being of interest to the UK GDF program, but rather due to interesting technical qualities or simply being representative of rural UK land cover. This work is entirely independent of any efforts or considerations in selecting a GDF site. The process for selecting a GDF site incorporates political, social, and geological considerations far beyond the concern of this work.

1.1. Research motivation

The significant value of MTI is limited by its performance in rural areas. Interferometric signals from the majority of natural scatterers decorrelate significantly over time (Zebker and Villasenor, 1992), while measurement of surface deformation requires temporal correlation in the phase. This 'temporal decorrelation' has been traditionally attributed to diffuse motion of vegetation (Hooper, 2006; Sansosti *et al.*, 2006; Rocca, 2007), and occurring in addition to a 'geometric decorrelation' phenomena associated with scattering occurring at different heights within a resolution cell (Gatelli *et al.*, 1994).

Rural decorrelation inhibits MTI applications in the delivery and monitoring of a GDF in the UK, which would likely be situated in a rural area. Prior literature has focused on remediating decorrelation from a statistical or signal processing perspective, such as spatiotemporal filtering to reduce the signal power of noise (Rocca, 2007; Guarnieri and Tebaldini, 2008; Ferretti *et al.*, 2014), statistical approaches for improved identification of stable areas (and false positives) (Hooper *et al.*, 2004; Ferretti *et al.*, 2014), and selective criteria for rejecting particularly noisy interferometric measurements (Berardino *et al.*, 2002; Sowter *et al.*, 2013).

These filtering approaches are effectively built upon the assumption that changes in vegetative scattering produce a zero-mean noise term in the phase time series. Consistent non-zero phase shifts associated with vegetation and soil moisture have been relatively underexplored (Zwieback and Hajnsek, 2016; Zwieback, Hensley and Hajnsek, 2017). Experimental evidence and theoretical models however show that non-zero mean phase shifts can manifest from gradual changes in the scattering properties of vegetation and bare soils (Hensley *et al.*, 2011; De Zan *et al.*, 2014; De Zan, Zonno and Lopez Dekker, 2015; Zwieback and Hajnsek, 2016; Zwieback, Hensley and Hajnsek, 2017). These shifts may be spatially correlated, with similar behaviour occurring in spatially extensive land cover, and temporally correlated due to relatively slow changes in e.g. vegetative biomass and moisture contents. Rather than simply filtering out affected areas and being selective with data, this suggests there is a potential to identify and correct for these transient scattering effects directly according to the scattering properties observed at a location.

1.2. Aims and objectives

The main aims and objectives of the research are as follows:

1) Produce software to perform MTI analysis of Sentinel 1 data reliably and efficiently.

To facilitate the analysis of Sentinel 1 data in the rural UK, a software has been produced to directly implement MTI analysis and subsequent tests and experiments.

2) Investigate the behaviour of scatterers in rural areas.

Given the evidence that traditional models of temporal decorrelation do not fully account for the range of behaviours observed in SAR time series, explore techniques and tests to identify variations in the data which are inconsistent with zero-mean noise processes and thus indicate more complex or land-cover specific mechanisms.

3) Test if the time-series variations in scattering behaviour observed from rural scatterers significantly affect the phase of Sentinel 1 interferometric data.

Apply the tests developed to identify transient scattering processes in data.

Determine to what degree these processes are correlated with land cover and time.

Determine if these phenomena are associated with phase shifts that are statistically significant as compared to just being random noise.

Evaluate the subsequent implications for MTI deformation studies.

4) Assess and develop new methods to compensate for transient scattering processes in MTI deformation analyses.

Where transient scattering phenomena are found to affect and MTI deformation studies, assess if the phase can be estimated and modelled so as to minimise the impact upon accuracy of MTI results.

5) Demonstrate the findings in rural areas of the UK, demonstrating application of MTI in similar land cover conditions to those that may be investigated for a UK GDF.

Exhibit how insights into rural scattering may lead to value in better measurement or confidence in the measurements of rural deformation phenomena.

1.3. Structure of this document

Chapter 1: Introduction

This chapter briefly introduces the value of accurate rural deformation monitoring, highlights the challenges with rural analysis and the research need.

Chapter 2: Literature review

This chapter explores the principles of SAR and the development of InSAR and MTI methods for remote monitoring of deformation. This chapter focuses on the various reported error sources in InSAR deformation estimates and the processing techniques, and the gaps in knowledge in how to ideally isolate and correct for these.

Chapter 3: Methodology

The development of software for performing the numerous steps required to process SAR images into accurate information regarding ground deformation. This provides the methodological basis for the further research.

Chapter 4: Transient scattering processes

Chapter 4 provides an exploration of how various mechanisms proposed in literature can cause time-series variations in the observed scattering which do not align with existing models for decorrelation. An agricultural area of South Wales, UK, is investigated and statistically significant phase shifts are found.

Chapter 5: Quantifying transient scattering

Chapter 5 develops statistical tests for transient scattering behaviour, and the direct identification of affected areas from a range of different SAR observables and derived measurements. A clustering technique is presented whereby distinct populations of transient scatterers can be isolated and analysed.

Chapter 6: Case study: South Wales coal field

The clustering approach is applied to the wider South Wales area, and a wide range of deformation phenomena are highlighted as distinct from those apparent in existing MTI processes.

Chapter 7: Conclusions

This chapter reviews the work undertaken. It summarises the approaches and techniques which were developed, and experimental data. The chapter presents concluding remarks and recommendations for future research.

2. Literature Review

This chapter aims to present and review the available literature regarding remote measurement of ground deformation using time series InSAR. There are numerous other phenomena which affect the InSAR phase measurement, and as such it is useful to review how InSAR signals are produced and processed to assess the state of knowledge regarding more specific phenomena.

Section 2.1 gives a brief introduction to radar systems, while the use of a synthetic aperture to increase resolution is examined in Section 2.2. A range of physical phenomena affecting radar interferometric phase are introduced in Section 2.4. Sections 2.5 and 2.5.3 examine practical techniques for investigating these phenomena.

2.1. Fundamentals of Radar

A generic radar system uses a *transmitter* antenna to radiate a beam of electromagnetic (EM) waves. These waves propagate through a medium; interact with some object or volume of interest via *scattering* processes which modify the waves; and have their energy redirected via the scattering processes to a *receiver* antenna which measures the induced voltage. A radar system hence measures the modification of EM waves in time and intensity due to propagation and scattering effects. An object or volume giving rise to a measured voltage is termed a *scatterer*. This terminology is shown visually in Figure 2-1.

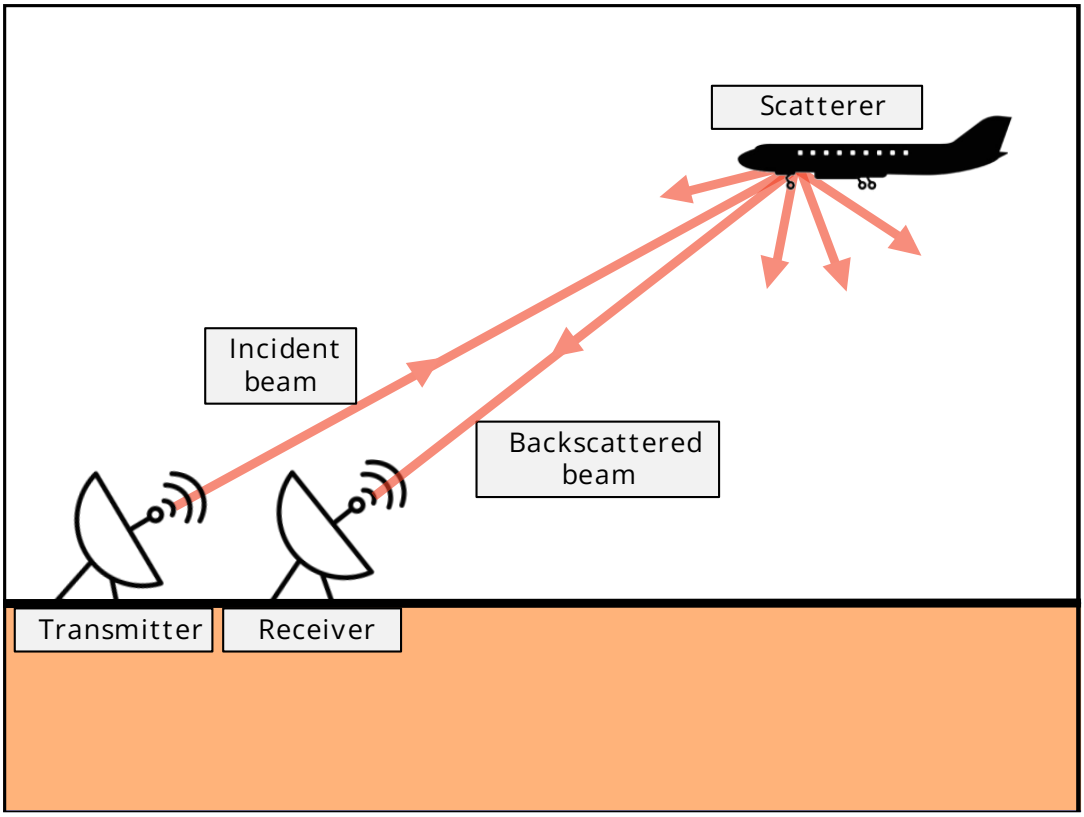


Figure 2-1: Terminology in a basic radar measurement

The radar systems of interest to this study use the same antenna to transmit and receive, a configuration which is hence termed a *transceiver*. A common application of such a radar is towards measuring the distance between the transceiver and a target scatterer. This distance is termed the radar *range*, as discussed further in Section 2.2.1 and shown there in Figure 2-6. Range is proportional to the delay in transmitting a wave and subsequently measuring a signal backscattered from a target, as shown in Equation 2-1:

Equation 2-1: The two-way travel equation.

$$R = \frac{c\,\Delta t}{2}$$

where the range R, is a function of the speed of light, c, and the time delay measured between transmission of a signal and reception of the echo from a target, Δt. The term *range* is also used to describe the direction in which this measurement takes place; the direction in which the radar waves propagate.

The power of a received signal is valuable along with its timing. The power of the received signal is affected by many factors but can be approximated with the Radar Equation. A form of this is given in Equation 2-2, the radar received power equation, which gives the received power P_r as a product of multiple factors (Skolnik, 2001, chap. 2):

Equation 2-2: The Radar Equation

$$P_r = \frac{P_t \cdot G^2 \cdot \sigma \cdot \lambda^2}{(4\pi)^3 \cdot R^4}$$

The received power, P_r, depends upon:

- P_t, the power of the transmitted signal.
- G, the gain of the antenna. A multiplicative factor describing how effectively the antenna coverts input power into the power of the radiated signal.

- σ, the *Radar Cross Section* of the target. This is a property of the scatterer itself and will vary with material properties and geometry.
- λ, the wavelength of the signal.

If the radar system and scatter location does not vary between repeated measurements, changes in received power will indicated a change in σ. Analysis of this scatterer-specific property allows for remote analysis of scatterers, as discussed in Section 2.1.5.

Received signal power measurements can therefore remotely measure changes in the (radiometric) properties of a target, although factors such as propagation media and noise complicate this in practice (Skolnik, 2001, chap. 2).

2.1.1. Electromagnetic wave propagation

The theory describing how electromagnetic waves form and behave was set out in the work of Maxwell in the 19th century ('II. A dynamical theory of the electromagnetic field', 1864). Maxwell's equations describe the relationships between electrical charge, electrical fields, and magnetic fields. These notably predicted that an oscillating electrical current can induce a propagating wave of electric and magnetic fields in nearby media: i.e. an electromagnetic (EM) wave such as a radio or microwave (Sevgi, 2014).

The electric and magnetic fields of an EM wave propagating in free space are geometrically orthogonal to one another, as shown in Figure 2-2. When the wave interacts with various media it can be polarised, affecting the orientation of its fields. Controlling the orientation of the fields can allow information to be measured regarding the polarising behaviour of a scatterer. This is the basic principle allowing the radar remote sensing field of Polarimetry to discriminate between scatterers based on how they polarise a backscattered signal.

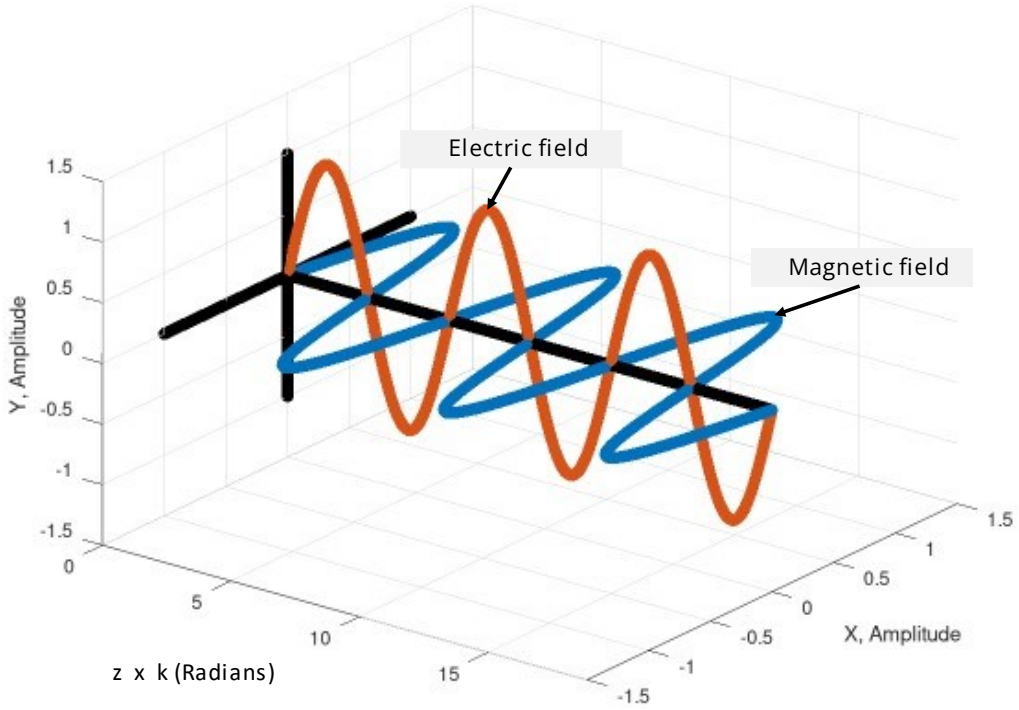


Figure 2-2: Orthogonality of the magnetic and electric fields in an electromagnetic wave as it travels along the dimension z with wavenumber k

An EM wave in free space can be described in terms of a single field with strength oscillating sinusoidally with time, t, and position along an axis of propagation, z. This is described in Equation 2-3:

Equation 2-3: Propagation of a planar EM wave.

$$E(z,t) = E_0 e^{j(\omega t - kz)}$$

where the instantaneous electric field strength $E(z,t)$ depends on:

- E_0, the signal amplitude at source
- ω, the angular frequency of the signal
- k, is the wavenumber
- j, the imaginary unit $j := \sqrt{-1}$

This equation represents a sinusoidal wave propagating in the z direction. The phase of the wave at any point in space and time is given by the term $\omega t - kz$. Interferometric methods which compare this phase can hence measure changes in scatterer position with precisions finer than the signal wavelength.

2.1.2. Interference and radar resolution

Photons that constitute EM waves do not directly interact with each other, and hence the fields from multiple waves will superimpose additively at a given point in space and time. The instantaneous measurement of a combination of fields is the complex sum of constituents such as can be modelled by $E(z,t)$ in Equation 2-3. The modification of one wave by another is termed interference.

It is interference which allows an antenna to radiate energy in a particular direction. To illustrate it is useful to derive the resolution of a simple radar measurement system (Bamler, 2000; Van Zyl and Kim, 2011).

An antenna can be modelled as a continuous series of points which each radiate EM waves spherically. To estimate the induced field from such a point, the coordinate along a plane of propagation, z, in Equation 2-3 can be replaced by the spherical distance from each point source, r. A source electric field strength E_0 will reduce as a function of distance according to the inverse square law.

Equation 2-4: Radiation from an EM point source.

$$E = \frac{E_0 e^{j\omega t - jkr}}{4\pi r^2}$$

Reducing this model to a 2-dimensional plane and a 1-dimensional antenna simplifies the analysis. The electric field strength, E, at a point in space and time can be found by integrating the complex contributions from all sources, in this case from the line of point sources representing the antenna (Bamler, 2000). If we assume the phase of the source

electric field is the same at all points along the antenna, the illumination pattern produced far away from the antenna is found to be a sinc function as shown in Equation 2-5:

Equation 2-5: Planar illumination pattern from a linear antenna.

$$E(\theta) = L\,\mathrm{sinc}\left(\frac{\pi\, L\ \sin(\theta)}{\lambda}\right)$$

L is the antenna length. The electric field strength of an antenna's radiation varies with angle θ, the angle between the antenna observation axis and a point in the measured field. An example of this illumination pattern is shown diagrammatically in Figure 2 3. The width of the beam depends on the ratio L/λ, as seen via Equation 2-5

2.1.3. Resolution of scatterers parallel to a simple, stationary radar

In real scenarios there will be multiple scatterers at different ranges and angular offsets, and these may all contribute to the measured radar signal. A radar systems ability to resolve these contributions as being from distinct sources is valuable to identify and characterise the scene and its contents.

It is useful to explore this imaging resolution of radar systems, using Equation 2-5 as a starting point. As the angle θ increases the signal field strength is reduced. The first minima are found where $\sin(\theta) = \lambda/L$. In radar terminology this angular region of relatively high field strength around the maxima at $\theta = 0$ is termed the 'main lobe' as opposed to the 'side lobes' found corresponding to other maxima.

The angular offset between a point in space and the centre of the main lobe is termed the *azimuth*.

Ignoring the side lobes for simplicity, an approximate introduction to angular resolution can be provided: A scatterer positioned in the main lobe region of the antennas field will be illuminated and therefore detectable. If scatterers are spaced at an angular distance

greater than $\sin^{-1}(\lambda / L)$ then the system will be able to detect the presence or absence of individual scatterers within the main lobe. If the scatterers are more finely spaced then the system will be unable to resolve whether the main lobe contains an individual scatterer or multiple scatterers.

The ratio λ / L hence determines the angular limit of resolution for a number of optical systems, although the exact formulation will depend on the imaging system (Born and Wolf, 1999, chap. 8). A smaller wavelength or larger antenna can improve resolution. It is worth noting that altering the phase of the signal can somewhat concentrate the illumination of a point, but this is only relevant at distances close to the antenna relative to the antenna diameter with respect to wavelength (Fraunhofer distance (Bamler, 2000)). Perhaps of greater interest to remote sensing applications is that applying a progress phase delay to the elements of an antenna can *steer* the illumination pattern to illuminate at different angles relative to the normal of the antenna plane as shown diagrammatically in Figure 2-4. This technique is used significantly in SAR satellites such as Sentinel 1 (Hees *et al.*, 2013).

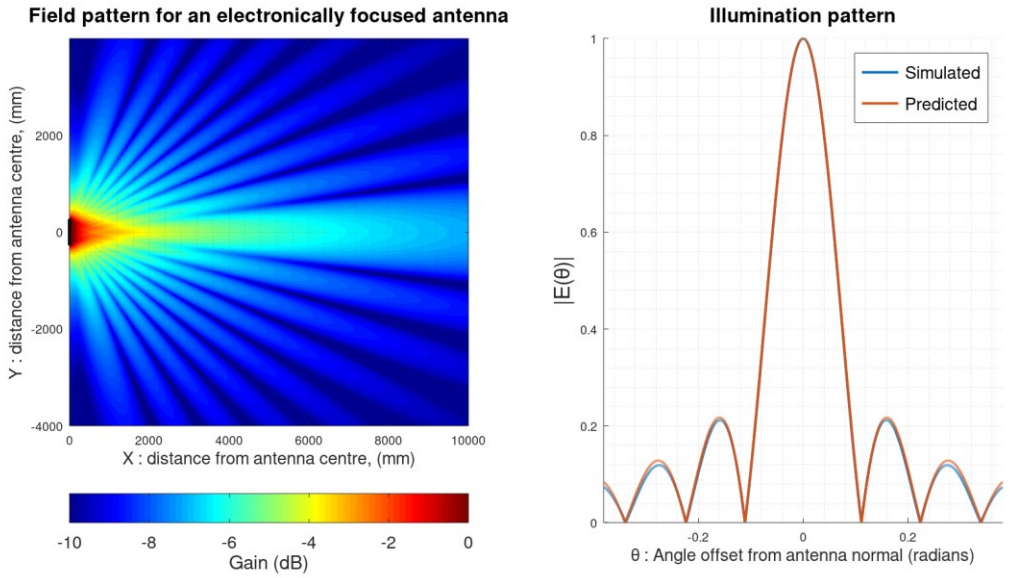


Figure 2-3: Radiation patterns for a linear antenna, using an approach where the antenna is modelled as a series of interfering point sources (Bamler, 2000).

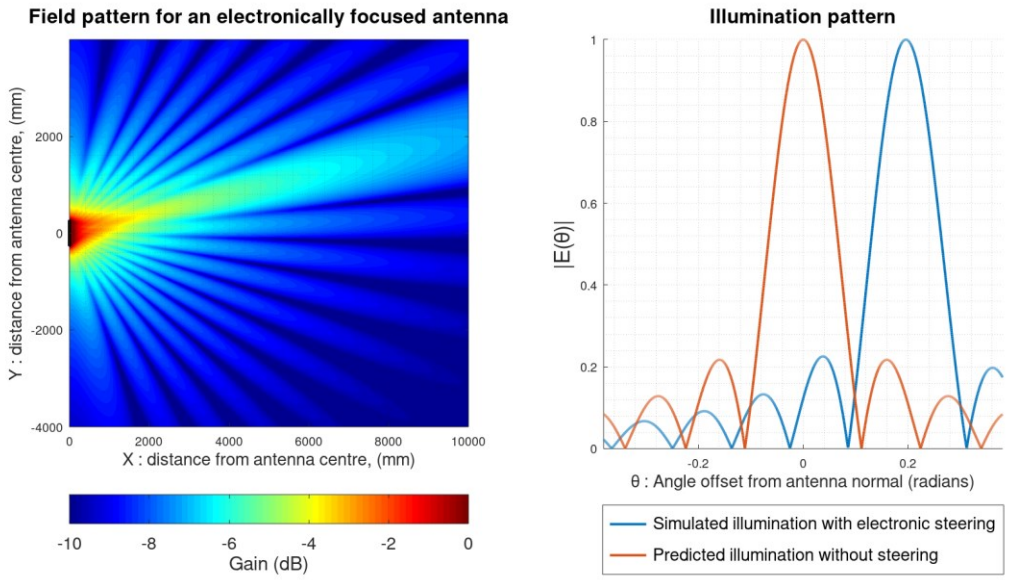


Figure 2-4: Demonstration of electronic steering via altering the phase of antenna elements according to their position along its profile.

2.1.4. Resolution of scatterers down-range of a simple, stationary radar

In the direction of radiation (known as down-range or range) this resolution depends on separating two signal pulses as shown in Equation 2-6 (Van Zyl and Kim, 2011):

Equation 2-6: Pulsed radar range resolution

$$\Delta R_{slant} = \frac{c\tau}{2}$$

$$\Delta R_{ground} = \frac{c\tau}{2\sin(\theta)}$$

where a pulse with length τ is radiated by a system. To maximise range a system would ideally illuminate each object separately and for a minimum amount of time in order that the backscatter contains very narrow peaks at times corresponding to the range of each object. An infinitely narrow pulse is termed a Dirac Delta function.

Unfortunately, minimizing the amount of time a scatterer is illuminated also minimises the energy that is backscattered and measured by the receiver. At large ranges, the

backscatter is already very small as seen by the r^4 term in Equation 2-2. Detecting and measuring scatterers necessitates a finite pulse-length in order to transfer energy back-and-forth from the scatter to the receiver and hence distinguish each scatterers response from noise.

Another consideration is that an infinite bandwidth of frequencies is required to form an infinitely narrow pulse. Real-world hardware has limits in terms of bandwidth. We hence must increase the pulse length in order to accommodate practical limitations in bandwidth and distinguishing the backscatter from noise.

By using a 'chirp' whereby the frequency of the pulse is varied in time, the instantaneous frequency of the backscattered signal can be used to resolve scatterers instead of the signal power alone. This allows for a longer pulse duration and practical signal energies. The matched filter is the optimal method of resolving chirps (European Space Agency, 2007; Cheney and Borden, 2009). This technique is termed pulse compression. In the case of pulse compression τ in Equation 2-6 is replaced by the *effective* pulse length which is shorter by approximately the bandwidth of the chirp (Bamler, 2000; Van Zyl and Kim, 2011).

2.1.5. Scattering

EM waves will interact with charged particles they intersect, causing these to oscillate at an identical frequency and reradiate some portion of the EM field in a new direction. The general term *scattering* is used to describe these microscopic wave-particle interactions, but in radar engineering it is more commonly used in the context of more macroscopic wave-volume interactions, considering factors such as the overall material composition, geometry, and distribution. Where the waves have been directed such that they intersect the radar receiver, a measurable voltage will be induced by the EM fields.

The radar cross section (RCS) of a scatter quantifies the strength of the signal that is directed back to the receiver, after accounting for any losses due to other phenomena. It is defined as the ratio of the power of the backscattered signal to the power of the

incident signal. The RCS can be thought of as the "size" of an object as seen by the radar system.

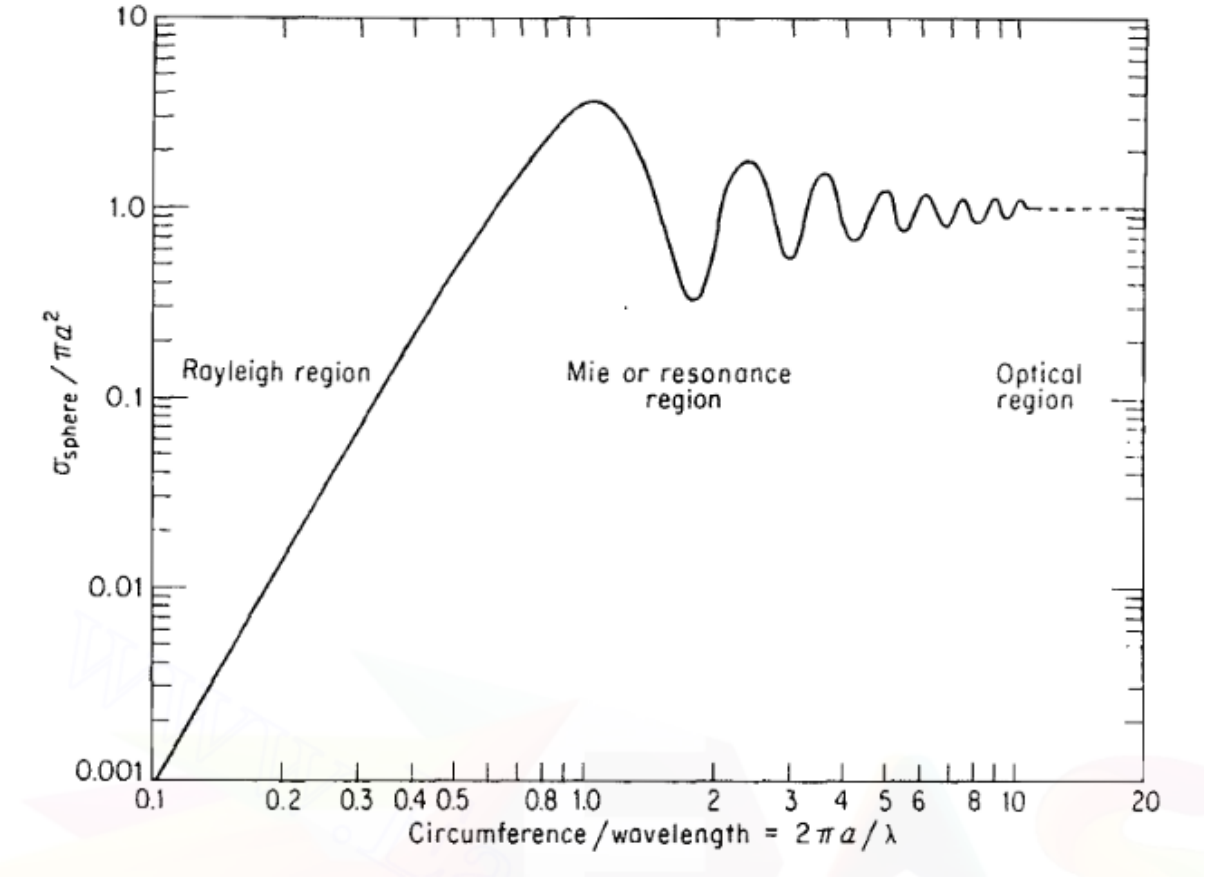


Figure 2-5: The scattering cross section, σ, as a function of a spherical scatterers circumference $2\pi a$, with respect to the EM wavelength, λ (Skolnik, 2001).

The relationship between RCS and object size is complex and can be influenced by a number of factors, including the shape and surface characteristics of the object and the wavelength of the radar signal. As shown in Figure 2-5, different ranges of scatterer size are associated with three distinct phenomenological treatments: Rayleigh scattering, Mie scattering, and Geometric Optics.

In a Synthetic Aperture Radar (SAR) system, the scattering volumes that form a resolution cell are typically large enough that the Geometric Optics are of primary concern. While the scattering volume maybe broken down into smaller objects, as these are smaller than a SAR can resolve they must generally be treated as an ensemble volume.

2.2. Synthetic Aperture Radar

The azimuth resolution of a 'real' aperture radar as presented in Section 2.1.2 is of limited practical benefit for remote sensing applications at ground engineering scales. Synthetic-Aperture Radar (SAR) is a technique which can significantly improve this.

SAR data uses a moving sensor to record multiple echo time-series from regular intervals along a track or 'azimuth'. Knowledge of the sensor geometry and velocity are then used to focus these time-series into images of amplitude and phase with axes corresponding to the 'slow' time between successive transmissions along the satellites track and the 'fast' time between signal transmission and the sample being measured. This timing information can be used to estimate the location of scatterers on the ground in a process known as geocoding. (Bamler, 2000).

2.2.1. Imaging Geometry

If a radar is pointing directly normal to the imaged surface, there will be an ambiguity as to which side of the imaged surface the scattering has been measured from. To solve this range ambiguity, it is necessary to angle the beam relative to the surface. In this configuration the range is often termed the *slant range* to differentiate it from the range projected along the imaged surface, which is typically termed the *ground range*.

In the context of SAR images, the distance of a SAR along its track is conventionally used to form one dimension of the image, and this image dimension is termed the azimuth. These terms are depicted schematically in Figure 2 6.

The overall area illuminated within a SAR image is termed a *swath*.

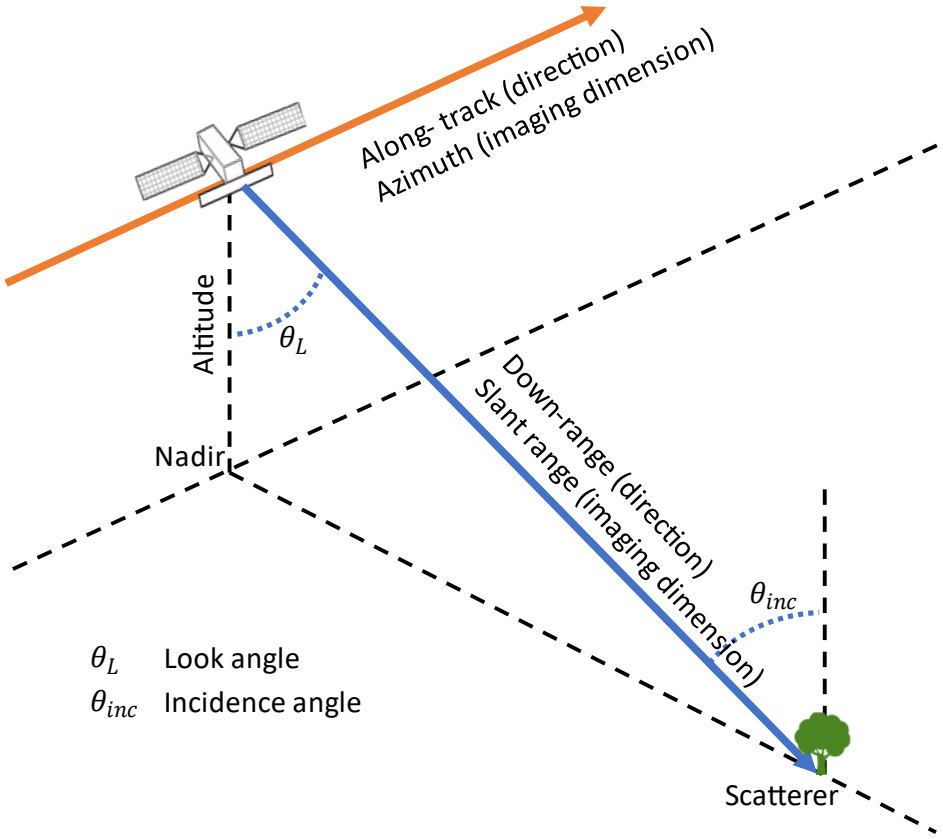


Figure 2-6: SAR imaging geometry and terminology, via (Engdahl, 2013).

2.2.2. Azimuth Resolution

The smallest difference in a measurement that can be detected by a system is termed the resolution. The spatial resolution of a SAR system is hence an important parameter defining the minimum distance required for two spatially separated scatterers to be discerned as distinct from one another (Ozdemir, 2012). This places limits on the spatial density of information recovered from the ground and the confidence in which different results can be attributed to specific features.

As seen in Equation 2-5, the illumination pattern of a real-aperture radar is approximated as λ/L_{real} where $L_{real}$is the length of the antenna. Due to the velocity of a SAR, v the effective length of its antenna is instead $v \cdot L_{real}$ granting an illumination time shown in Equation 2-7 (a). The velocity also produces a Doppler shift with bandwidth B shown in Equation 2-7 (b), combining these factors produces azimuth resolutions as described by Equation 2-7 (c) (Van Zyl and Kim, 2011).

Equation 2-7: Azimuth resolution of a SAR

$$a) \quad \tau_{azimuth} = \frac{R\,\lambda}{\upsilon L_{real}}$$

$$b) \quad B = \frac{2\upsilon}{L_{real}}$$

$$c) \quad \Delta R_{azimuth} = \frac{L_{real}}{2}$$

To achieve this resolution, the number of independent samples must match the number of imaged resolution cells. To avoid aliasing the pulse repetition frequency of the radar along the azimuth must be greater than the value given in Equation 2-8.

Equation 2-8: Minimum pulse-repetition frequency to avoid aliasing in azimuth.

$$\mathrm{PRF} > \frac{2\upsilon}{L_{real}}$$

In practise the Pulse Repetition Frequency (PRF) is limited by the data handling hardware (such as the available data rate for communication back to earth) and that time is required between pulses in which to measure the echoes.

2.2.3. Focusing and Geocoding

Measured, 'raw', SAR echoes can be focused into an image through exploitation of their timing and frequency. The exact details are not immediately relevant to this review but a few details are worth introducing now, with further detail available in literature (European Space Agency, 2019).

A backscattered signal will be delayed according to the distance between the sensor and scatterer (range) due to the finite speed of light. It will further be Doppler shifted according to the relative velocity of the sensor and scatterer. The SAR images can be focused by extracting contributions with similar ranges (time offset) and Doppler shifts from the raw echoes. In practice, this can performed using a 'matched filter' to compare the expected signal from each point in the range-azimuth grid with the raw data (European Space Agency, 2007, 2019)

A satellite SAR sensor generally faces the ground to one side of its orbital track, as seen in Figure 2-6, and thus at any point in time the satellite may be moving toward or away from a scatter in terms of the azimuth dimension. At the point of crossing between moving toward and away from the scatterer, the observed Doppler shift will be zero. The SAR image is hence arranged with each row corresponding to the signal contributions with zero-Doppler shift with respect to the satellite position at a given pulse and each column corresponding to a constant range offset.

There exists a plane in geographic space whereby any scatterers in that plane will return a signal with zero Doppler shift relative to the azimuth position of the satellite. There further exists a sphere around the sensor whereby there will be a constant range offset. By finding the intersection of this sphere and plane with the imaged surface, the mapping between the SAR coordinates and geographic location can be made. Mapping known geolocations into SAR coordinates is known as back-geocoding, while determining the geolocation corresponding to a given SAR coordinate is known as forward geocoding (Small and Schubert, 2019).

2.2.4. SAR measurements

This section examines the useful quantities measured by a SAR.

Amplitude

The raw SAR data is a 'digital number' proportional to the voltage measured in the receiver. To convert this to a number representative of the scattering behaviour requires calibration of the factors in the Radar Equation (El-Darymli *et al.*, 2014; Miranda and Meadows, 2015).

Factors such as the antenna gain are generally modelled and calibrated prior and during operation (Hees *et al.*, 2013), with these factors given in look-up-tables along with the data (*Sentinel-1 Product Specification*, 2016). Terms such as range, antenna gain, and wavelength can be treated approximately as identical when comparing image-to-image in repeat-pass satellite imagery. Within the image there will be significant variations in amplitude due to surface topography. Where the slope of the surface varies from resolution cell to resolution cell there will be an associated variation in the area of the imaged surface being measured. Different calibrated amplitude values can be determined based on different choices of reference area used to compensate for this effect (El-Darymli *et al.*, 2014).

Polarisation

The Fresnel equations describe how an electromagnetic wave's polarisation (the orientation of its electrical and magnetic fields relative to its propagation direction) will affect how it interacts with scattering media. Observed quantities of backscatter intensity and phase in a SAR system may varying depending on the polarisation of both the emitted and measured signal, and these observed variations will further depend on the inherent geometrical and material properties of the scatter. This field of study – known as SAR polarimetry – is hence used to identify different types of scatterers, land covers, or objects in SAR images(Pottier and Lee, 2017).

Sentinel 1 (S1) satellites (see section 2.3.4.1) is equipped with two antennae sets, orientated to emit or measure waves either vertically or horizontally (with respect to the ground plane). S1 data can hence be used to determine the presence of land cover such as forest, grassland, agricultural, urban standing water (Banque *et al.*, 2015). The PhD project is investigating the analysis of time-series variations in this polarimetric behaviour as a method for better differentiation of vegetation types and measurement of their growth patterns. The goal is to determine if different seasonal behaviours of vegetation affect the InSAR phase in different ways. If so, correcting for this vegetative phase behaviour in the PSI approach should yield improvements in the accuracy of rural deformation measurements.

Speckle

The signals backscattered from elementary scatterers in a resolution cell will superimpose, with signals in-phase with one another combining constructively whilst those that are opposite in phase will combine destructively. Surfaces that are optically rough as compared to the wavelength of the imaging system will backscatter a signal that is the combined sum of backscatters from many small facets who may be distributed randomly over the range of possible phase values. This leads to a phenomena known as speckle whereby the overall amplitude of the response is stochastic (Goodman, 1976).

Often the speckle is referred to as a 'noise' process. This is misleading. The speckle is in fact a deterministic process determined by the geometry of the scatterers within a resolution cell (Goodman, 1976).

Spatial patterns in speckle within an image will persist between images unless there has been some physical change in the scatterer, and hence speckle is ultimately predictable and useful for quantifying changes in scattering behaviour between images (Guarnieri and Prati, 1997). Describing speckle as noise may be considered useful shorthand, as it causes spatial variations in amplitude that are stochastic, like noise. 'Noise-like' is perhaps a more accurate term (Touzi, 2002).

Phase

The phase of the raw backscattered signal provides a precise measurement of its delay. The phase has been used since at least 1974 to provide interferometric measurement of properties such as surface topography (Graham, 1974). A more comprehensive exploration of the interferometric phase is found in Section 2.4.

The voltage measured at the antenna is demodulated it by two separate copies of the carrier frequency delayed by $\pi/2$, The two demodulated signals are traditionally named 'in-phase' (I) and 'quadrature' (Q), with I being the real part of the signal and Q being an accurate estimate of the imaginary component (Cohen, 1995; Cheney and Borden, 2009). The phase of a SAR signal or sample is the argument of these two orthogonal components:

Due to the focus on interferometric phase in interferometric studies, it is convenient to represent a SAR measurement sample in exponential form as in Equation 2-9:

Equation 2-9: Exponential form representation of a complex SAR measurement.

$$s = I + jQ = Ae^{j\varphi}$$

where j represents the imaginary unit, $j := \sqrt{-1} \equiv e^{j\pi/2}$. A is the signal amplitude and φ is the signal phase.

2.3. SAR Satellites

Satellites provide an effective platform for SAR given their ability to illuminate large areas. Through electronic steering of an antenna, as introduced in Section 2.1.2, the incidence angle of the beam and thus the illuminated area of the earth's surface can be controlled without altering the orbit or the sensor orientation. While satellites are generally constrained by size and weight considerations, the improvements in resolution offered by the SAR technique allow the use of a far smaller physical antenna and thus dramatically improve the practicality of satellite radar.

The potential for global coverage has attracted significant investment from space programs internationally. There are now many past, present, and future satellite SAR missions, as shown in Figure 2-7. The number of satellites currently operational has approximately doubled over the last decade. New units added to constellations such as ALOS, Cosmo SkyMed, and Sentinel 1. More countries are developing SAR programmes such as the Argentinian space agency's SAOCOM and Chinese space agency's GP3. Microsatellite constellations such as ICEYE highlight the potential market for smaller commercial ventures (Mason *et al.*, 2022).

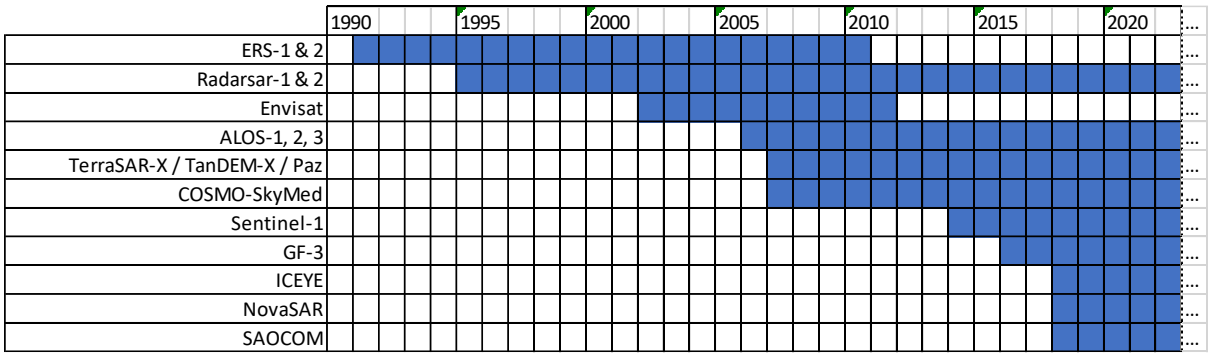


Figure 2-7: Overview of recent InSAR capable satellite constellations and their approximate operational timelines (Moreira *et al.*, 2013; Mason *et al.*, 2022).

A satellite SAR system architecture generally includes a "radio-frequency (RF) frontend" which includes the antenna, "digital backend", and several supporting subsystems which support but do not directly alter the measurement. The front end is responsible for

amplifying the emitted signal, radiating this, then amplifying the received signal. The backend is responsible for generating the reference signal, instructing the front end when to amplify and emit this, instructing the frontend when to receive, filtering and digitising the received signal.

2.3.1. Sentinel 1

Sentinel 1 is a two-satellite constellation, with Sentinel 1A launched in October 2014 and Sentinel 1B launched in October 2016 (Panetti *et al.*, 2014; *Sentinel-1 Product Specification*, 2016). Through use of a large, electronically steerable phased array a variety of imaging modes can be employed. Of particular interest is the Interferometric Wide (IW) swath mode which implements the Terrain-Observation by Progressive Scans (TOPSAR) imaging approach (De Zan and Guarnieri, 2006), IW was developed specifically for repeat-pass regional InSAR surveys (Desnos *et al.*, 2017). TOPSAR progressively steers the beam to observe 'sub-swaths' at opportune times. There is a necessary compromise required in terms of pulse-repetition frequency and hence azimuthal resolution, which is thus lower than in the traditional strip-map imaging mode (De Zan and Guarnieri, 2006).

This large swath coverage allows for unprecedented data coverage, with 99% of global landmass imaged during the S1 orbit sequency. Individual orbits cycles repeat roughly every 90 minutes in the 600km low earth orbit, allowing for most areas of the globe to be repeat-imaged from the same geometry every 12 days. Areas of Europe are revisited every 6 days. In certain areas where swaths overlap up to 8 images from 4 geometries can be regularly captured every 12 days.

The high frequency of revisits is a key performance improvement from previous satellites, offering greater volumes of data from which to estimate distinguish temporally correlated behaviour associated with the physical scatterers from error sources such as instrument noise (Rucci *et al.*, 2012).

Sentinel 1 has been described as a 'workhorse' with respect to satellites capable of large-area interferometric monitoring (Yague-Martinez *et al.*, 2016).

The experiments in this work focus exclusively on Sentinel 1 data. While given unlimited scope and resources it would be beneficial to assess a wider range of sensors, the C-band data of Sentinel 1 is at the midpoint of frequencies used by extant SAR satellites (See Figure 2-7) and is thus broadly representative. The convenience of global coverage, regular updates, and a complete lack of monetary cost to the end user ensure that results for Sentinel 1 are of significant interest to industry and research.

2.4. Interferometric phase

The phase of the signal is retained in each measurement sample (pixel) in a SAR image. A change in the phase measured from a scatterer between two images can be used to infer a change in phenomena which affect signal propagation (e.g. displacement of the scatterer due to ground deformation) or scattering (e.g. a change in the material properties of the scatterer). This is termed interferometry (Rosen *et al.*, 2000). The interferometric phase 'shift' between two SAR images can be calculated by element-wise multiplication of one image and the other's complex conjugate, as shown in Equation 2-10:

Equation 2-10: Interferometric phase sample measurement

$$\Delta\varphi_{AB}(x,y) = \angle(s_A(x,y) \cdot s_B(x,y)^*)$$

where:

- Subscript labels A and B each refer to a SAR image.
- s_A and s_B are SAR measurement samples in these images.
- (x,y) subscripts denote a row and column of the images.
- $\Delta\varphi$ is the interferometric phase measurement.
- The * operator indicates taking the complex conjugate.
- The $\angle$ operator indicates taking the argument (phase angle) of a complex number.

$\Delta\varphi$ is found via multiplication of one image's sample by the complex conjugate of the other image sample. It is assumed that images A and B are coregistered, i.e. projected so that a given (x,y) subscript corresponds to the same geographic location in both images (see Section 2.5.1). Analysis of SAR phase shifts is generally described as 'Interferometric SAR' (*InSAR*). There are in fact multiple physical and procedural contributions to the phase shifts observed in satellite interferograms, with models generally identifying the 6 additive factors shown in Equation 2-11 or some combination thereof (Ferretti, Prati and Rocca, 2001; Moreira *et al.*, 2013; Crosetto *et al.*, 2016):

Equation 2-11: Interferometric phase components

$$\Delta\varphi = \varphi_{defo} + \varphi_{orbit} + \varphi_{topo} + \varphi_{atm} + \varphi_{scat} + \varphi_{noise}$$

where the measured phase shift $\Delta\varphi$, is the sum of shifts induced by:

- Displacement of the scatterers relative to one another, such as due to ground deformation, φ_{defo}
- Orbital differences, φ_{orbit}
- Scatterer topographic height, φ_{topo}
- Atmospheric refraction, φ_{atm}
- Scatterer position and compositional changes, φ_{scat}
- Instrument noise, φ_{noise}

The characteristics of these individual contributions are worth exploration, as the accuracy of measuring a contribution is dependent on the combined accuracy of estimating the rest.

2.4.1. Deformation

Phase shifts between SAR measurements hence offer a fine measure of sensor-to-scatterer distance, such as may be caused by small movements of the ground.

Equation 2-12: Interferometric phase due to deformation.

$$\varphi_{defo} = \frac{4\pi}{\lambda} \Delta r$$

where the phase shift φ_{defo} is produced by the difference in range Δr as a fraction of signal wavelength λ.

2.4.2. Orbital determination error

The exact position of the satellites is generally only known to a few centimetres of accuracy. Error in estimating satellite position leads to errors in compensating for this factor in phase, errors propagate into the phase as long-wavelength spatial variations, which may be estimated through low-pass filtering the interferograms (Moreira *et al.*, 2013; Yague-Martinez *et al.*, 2016).

2.4.3. Topography

As the satellite position often changes by a few hundred meters (*Sentinel-1 Product Specification*, 2016) between passes, the relative range between scatterers of different topographical height will vary. The resulting phase component is described in Equation 2-13 (Bamler, 2000):

Equation 2-13: Interferometric phase due to topography

$$\varphi_{topo} = \frac{4\pi}{\lambda}\frac{B}{r\sin(\theta)}\Delta h$$

where B is the distance between satellite positions in the passes, perpendicular to the sensing direction. The sensor-to-scatter range is *r*, the error in estimating the topographical height of a scatterer is Δh, while θ is the off-vertical angle of the sensing direction. With knowledge of $B, r, and\ \theta$ for multiple images via the orbital positions, the corresponding interferometric phase measurements can be regressed to estimate Δh.

The error due to topography can be reduced through use of an accurate Digital Elevation Model (DEM). A global DEM is provided by the Shuttle Radar Topography Mission (SRTM), which provides roughly 20m accurate measurements of global surface elevation (Rodríguez, Morris and Belz, 2006; Mukul *et al.*, 2017).

If we assume the DEM errors are normally distributed, we can quickly estimate the distribution of φ_{topo} using known values from S1 orbital data. The distribution of phase error produced by a normally distributed DEM error is shown in Figure 2-8 using a representative baseline of 50m, range of 600km, incident angle of 40°.

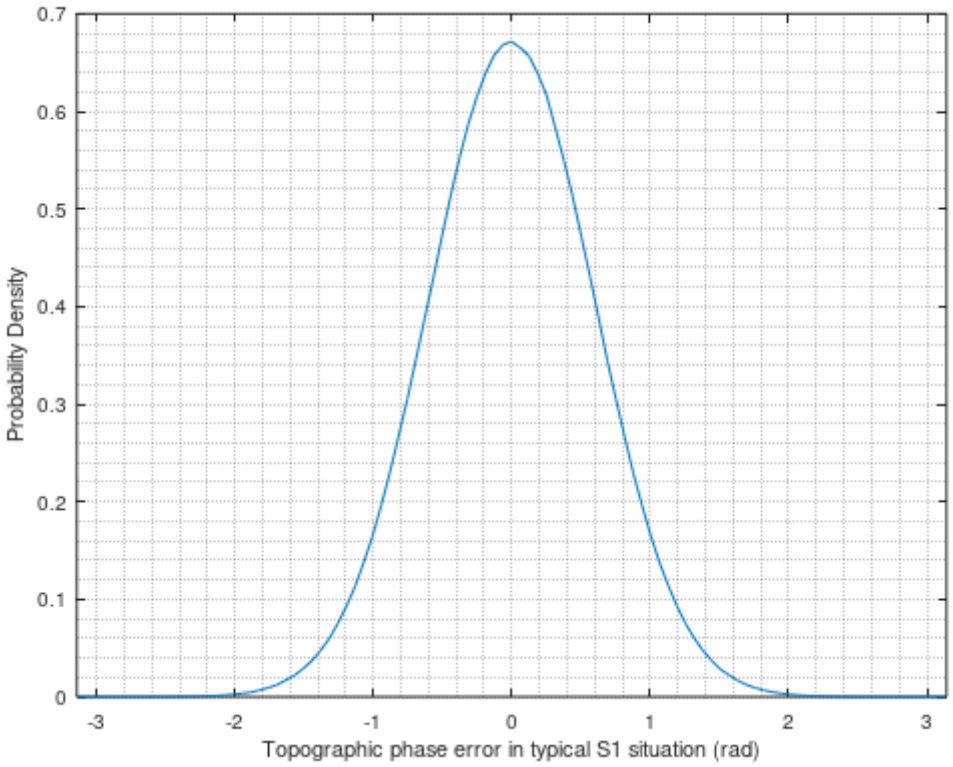


Figure 2-8: Typical phase errors produced by inaccuracy in a DEM.

Here we can see that a height error can produce quite a significant shift in the phase, but this phenomena alone is extremely unlikely to cause a wrapping error. Fortunately, the deviation in baseline for S1 (and most satellites) is not correlated in time. Hence there is little correlation between the topographical error and other error sources, while orbital data for determination of the baseline is highly accurate, and thus regression to estimate Δh is highly effective when the number of images is large.(Ferretti *et al.*, 2007; Rucci *et al.*, 2012)

2.4.4. Atmospheric Phase Screen (APS)

The signal from an earth-orbiting SAR satellite will pass through the atmosphere before scattering from the surface. Sentinel 1 orbits at a height of roughly 700km.

Changes in the distribution of free electrons in the ionosphere and water vapour in the troposphere lead to variable refraction of the radar wave between images. These phenomena in vapour and free electrons are governed by physical processes such as turbulence which are spatially correlated over distance in orders of kilometres.

The resulting phase effects hence appear as long-wavelength spatial trends, correlating over several kilometres as shown Figure 2-9. The combined phase effects from the atmosphere are known as the 'atmospheric phase screen' (APS). The APS is generally estimated through low-pass filtering the interferograms (Ferretti, Prati and Rocca, 2000, p. 200).

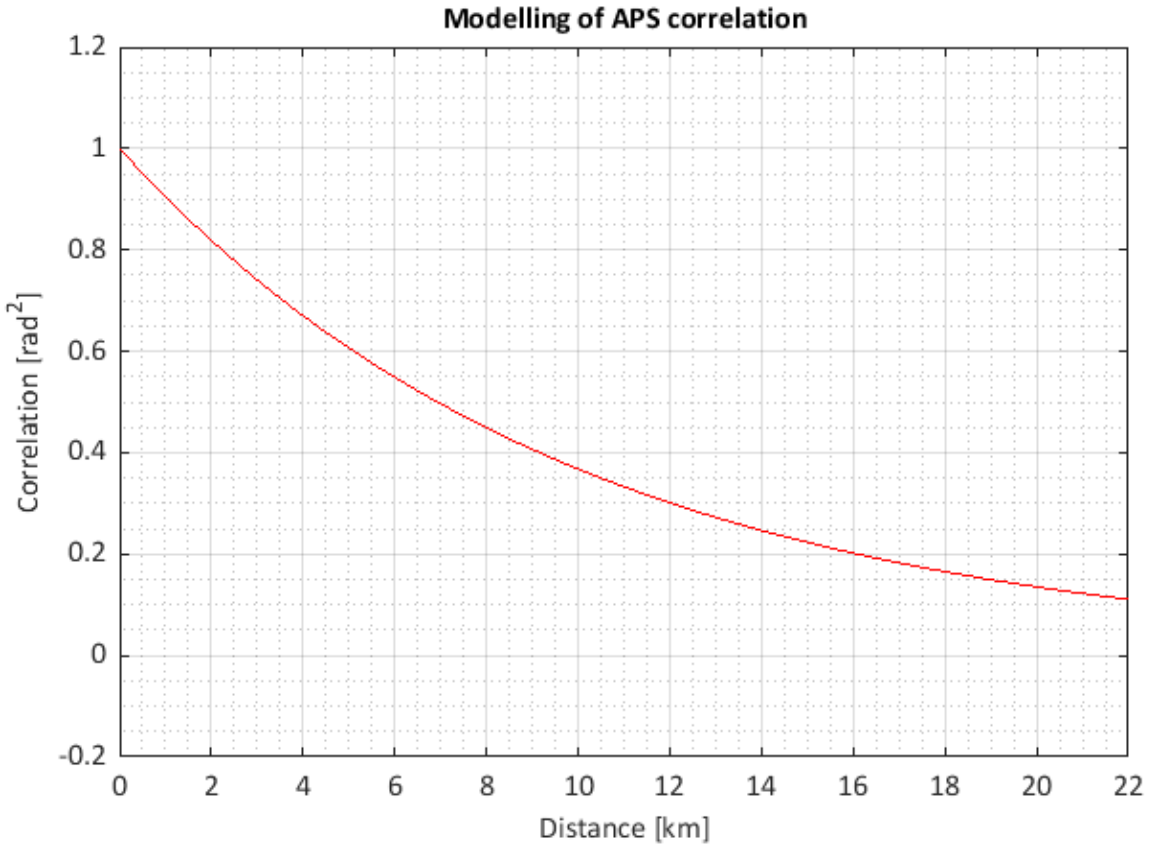


Figure 2-9: Spatial correlation of the atmospheric phase screen (Grebenitcharsky and Hanssen, 2005).

The combination of the APS and orbital error, two significant and unknown a priori low-pass signals in the interferometric data, causes difficulty in measuring any uniform displacement of the entire imaged surface, due to these displacements being generally far smaller in magnitude while having similar spatial frequencies. InSAR studies generally concentrate on resolving relative displacements between scatterers within the scene, often relying on low-pass temporal filtering to resolve gradual movements of extensive areas (Ferretti, Prati and Rocca, 2000, p. 200).

2.4.5. Scatterer behaviour

Scatterers with unstable radiometric properties or geometry will exhibit unstable phase behaviour. There are two broad approaches towards removal of this noisy behaviour, and these can be described as 'Persistent Scatterer' (PS) approaches or 'Distributed Scatterer' (DS) approaches:

PS approaches (Crosetto *et al.*, 2016) seek to identify scatterers which are stable throughout the time series, using stability of amplitude as a proxy and masking out any pixels in the image stack which do not meet a threshold for phase stability.

DS techniques (Berardino *et al.*, 2002) seek to average the interferometric phase signal over an area, such that noisy scattering behaviour in phase (modelled as gaussian, zero-mean) will cancel out under the central limit theorem.

Additionally, PS and DS each counteract more general sources of noise, such as 'thermal noise' in the SAR sensor.

2.4.6. Noise

Noise is typically assumed to be purely random and produced by e.g., thermal excitation, sensitivity of the antenna and electronics to the cosmic microwave background. Typically this signal is treated as a zero-mean gaussian distributed contribution (Rocca, 2007)

which can be minimised by spatial and temporal averaging of the phase (Ferretti *et al.*, 2014; Cigna and Sowter, 2017).

2.4.7. Coherence

The consistency in phase values between SAR measurements can be quantified in terms of coherence. This is effectively a measure of statistical correlation between the two SAR signals, and the absolute value of coherence varies between 0 (denoting purely random, uncorrelated behaviour) and 1 (denoting identical behaviour). The definition for coherence is given in Equation 2-14 (Lee, Miller and Hoppel, 1994):

Equation 2-14: Interferometric coherence

$$\gamma = \frac{E[s_A s_B{}^*]}{\sqrt{E[|s_A|^2]}\sqrt{E[|s_B|^2]}}$$

where for a coherence value, γ:

- s_A and s_B are signals taken from SAR images labelled A and B.
- E is the expectation operator, such that $E[x]$ produces the expected value of x.
- The asterisk * operator denotes complex conjugation such that x^* produces the complex conjugate of x.

Some degree of coherence is essential when decomposing the interferometric phase contributions of phenomena discussed in preceding sections, as otherwise the data would represent pure noise completely unrelated to any physical effects. InSAR analysis techniques therefore utilise coherence in order to appropriately discriminate and weight data from reliable points or areas against that of noisy, unreliable ones (Bamler and Just, 1993; Touzi *et al.*, 1996; Ferretti, Prati and Rocca, 2001; Hooper, 2008).

Calculating the coherence as defined in Equation 2-14 would requires prior knowledge the statistical signal properties at each pixel, however in practice only sampled, noisy, data is available. To estimate coherence, a standard approach is to assume pixels neighbouring the target pixel exhibit the same statistical behaviour and treat their values as realisations of the same process (Hanssen, 2001, chap. 4; Ferretti et al., 2014). The resulting sample estimator is given in Equation 2 15:

Equation 2-15: The sample estimator for interferometric coherence

$$\hat{\gamma} = \frac{\sum_{i=1}^{N} \left(s_{A,i}\, {s_{B,i}}^{*} \right)}{\sqrt{\sum_{i=1}^{N} \left(\left| s_{A,i} \right|^2 \right)} \sqrt{\sum_{i=1}^{N} \left(\left| s_{B,i} \right|^2 \right)}}$$

where the sample estimate of coherence, $\hat{\gamma}$, is indicated by the hat, and relies on summing over a set of N points with the index, i, identifying an individual sample within that set.

A commonly used technique for choosing the set of pixels is to use a boxcar filter, a rectangular selection of pixels centred around the pixel for which $\hat{\gamma}$ is being estimated (Jong-Sen Lee *et al.*, 2003). This however becomes problematic when the scatterers are heterogeneous over the rectangular selection, leading to erroneous estimates for scatterers located at a boundary between different land covers (Jong-Sen Lee *et al.*, 2003; Ferretti *et al.*, 2014).

For example, forests exhibit very noisy interferometric phase while buildings generally exhibit stable phase behaviour; a 'blind' filtering of points at the boundary between these types of landcover will lead to a coherence measurement unrepresentative of either of them. It can further be appreciated that summing over a local area leads to a loss of resolution.

Often, a similar calculation is used to estimate the *temporal coherence* (also termed *phase coherence* (Ferretti, Prati and Rocca, 2000)) as shown in Equation 2-16:

Equation 2-16: Temporal coherence

$$\hat{\gamma}_{temporal} = \frac{\left|\sum_{i=1}^{N} e^{j\varphi_i}\right|}{N}$$

$$where\ \varphi_i = \angle\left(s_{A,i}\, s_{B,i}{}^{*}\right)$$

where a summation over the set of phase values for a single pixel across a time series of interferograms yields a measure of phase stability that is commonly used to fit models of deformation and topographical error to phase time series.

A final, significant, issue with sample estimation of coherence is bias and high estimation variance when the number of pixels in the set is low (Touzi *et al.*, 1996, 1999; Ferretti *et al.*, 2014). As such, sizing the set of values used to estimate coherence is a delicate balance: A large set may lead to undesirable loss of resolution, and loss of accuracy due to inclusion of heterogeneous scatterers. Smaller sets will lose accuracy due to sampling errors and bias.

2.5. InSAR stacks

Many interferograms, generated for SAR images taken at different times, are required to determine the presence of time-series trends in the phase such as deformation. If we treat each interferogram as a measurement of deformation, combining multiple images is equivalent to combining multiple measurements and reducing the power of noise in our estimation.

When multiple SAR images or interferograms are collected they are known as a 'stack'. The stack can be equivalently described as a three-dimensional array with dimensions of azimuth, range, and the image index in a time series. As the third dimension is temporal, and the two-dimensional arrays are SAR images, the stack can be intuitively understood as a SAR video.

To convert a stack of SAR images into a stack of interferograms requires a reference (previously described as a 'master') image from which to calculate phase shifts. Phase time series can be produced by comparing each 'secondary' image against the reference. The most convenient approach is to choose a single reference image, whereby the phase time series for individual pixels in the stack will then be chronological and trends in phase will intuitively correspond to trends in ground deformation, after correction for other phase terms (Ferretti, Prati and Rocca, 2000).

The use of a single reference can reveal ambiguity in the data, however. When interferograms are multi-looked or otherwise filtered, the phase history will vary depending on the choice of reference (Ferretti *et al.*, 2014). This inconsistency in the phase shift is often termed the closure phase (De Zan, Zonno and Lopez Dekker, 2015). As such, approaches using multiple references and all combinations of interferograms offer advantages in reducing phase ambiguity (Rocca, 2007; Guarnieri and Tebaldini, 2008; Ferretti *et al.*, 2014).

2.5.1. Coregistration

To properly combine the SAR images requires that they are aligned (coregistered) such that each pixel corresponds to the same resolution cell throughout the stack. This is important for estimating contributions to the phase, as the scattering phase term from one resolution cell to another is near uniformly random in space.

Data on the satellites orbital position and velocity at points in time known as orbital state vectors (OSV, also termed ephemerides) are a key source of information in determining the location of scatterers in the SAR image, along with timing-related sensor parameters such as the time between pulse radiation and sampling and the sampling rate (Small and Schubert, 2019). OSV for S1 are provided free of charge, consisting of a rough first estimate from the sensor itself, a more accurate 'restituted' update provided a few days after sensing, and finally a 'precise' product provide a couple of weeks later which is accurate to around 3 cm (Peter *et al.*, 2017).

2.5.1.1. Range-Doppler

The process of assigning geographic coordinates to SAR pixels is known as geocoding (Small and Schubert, 2019), as discussed in Section 3.3.2. Precise geolocations for each pixel can be identified if the topography of the imaged surface is known. By comparing the geographic location (northing, easting, height) of pixels in the SAR image, the relative offset of each pixel can be determined and corrected (Sansosti *et al.*, 2006).

2.5.1.2. Incoherence Cross Correlation (ICC)

Another approach for coregistration involves maximising the correlation between images. This approaches can either maximise amplitude cross correlation or coherence (Bamler and Eineder, 2005; De Zan, 2014; Qin, Perissin and Bai, 2018), with the amplitude approach often termed 'speckle tracking' (Guarnieri and Prati, 1997).

2.5.1.3. Enhanced Spectral Diversity (ESD)

As the Doppler centroid varies in a TOPS image, this causes a ramp in phase between consecutive bursts. Enhanced spectral diversity analyses overlapping areas of bursts in order to measure this phase shift and hence correct for any azimuth misregistration (Yague-Martinez, Zan and Prats-Iraola, 2017).

2.5.1.4. Significance of coregistration errors

While the problem of coregistration has been studied in significant detail in literature, it should be noted that small coregistration errors do little to affect the accuracy of ground deformation estimates from InSAR stacks. Coregistration errors cause a rigid offset of the interferometric phase in conventional strip-map SAR and an additional linear ramp in phase for TOPS images (Prats-Iraola *et al.*, 2012). Both phenomena are already estimated and removed as part of APS filtering, while the APS is generally a far more spatially complex and thus unpredictable problem (Crosetto *et al.*, 2016).

2.5.2. Time series decorrelation

The earliest InSAR papers noted the effects of decorrelation in the interferograms, and that these effects were amplified by increasing the spatial baseline (Graham, 1974; Gabriel, Goldstein and Zebker, 1989). Further decorrelation was recognised when increasing temporal baseline, and causal links were drawn to various physical changes in scatterer properties (Graham, 1974; Gabriel, Goldstein and Zebker, 1989; Gray and Farris-Manning, 1993). This led to the development of models for many of these decorrelation phenomena, and recognition of the decorrelation itself being a valuable source of information on the behaviour of the imaged surface (Zebker and Villasenor, 1992).

This initial model for decorrelation (Zebker and Villasenor, 1992) identified the following factors as multiplying to produce the total decorrelation, shown in Equation 2-17:

Equation 2-17: Decorrelation factors for an InSAR time series

$$\rho_{total} = \rho_{temporal} \cdot \rho_{noise} \cdot \rho_{rotational} \cdot \rho_{spatial}$$

where the total decorrelation is the product of decorrelation due to: temporally varying scatterer properties, $\rho_{temporal}$; thermal noise in the instrument, ρ_{noise}; rotation of the imaging geometry causing differential phase observations of distributed scatterers within the resolution cell, $\rho_{rotational}$; and an effect which was originally termed the spatial baseline decorrelation, $\rho_{spatial}$.

2.5.3. Processing InSAR stacks

There are numerous techniques which analyse time-series of InSAR data in an effort to measure ground deformation. Collectively these are often referred to as Multi-temporal InSAR techniques (MTI) (Hooper, 2008), owing to their use of multiple acquisitions with distinct timings. These begin with coregistered stacks of SAR images or interferograms, and subsequently filter or otherwise analyse the data in order to isolate and model-fit the phase change produced by surface deformation.

Widely used techniques include Persistent Scatterers (Ferretti, Prati and Rocca, 2001; Hooper *et al.*, 2004), Small Baseline Subsets (SBAS), (Berardino *et al.*, 2002), and subsequent methods which analyse the entire matrix of available interferometric measurements (Rocca, 2007; Guarnieri and Tebaldini, 2008; Ferretti *et al.*, 2014) (known as the Coherence Matrix). Across these broad themes there is often overlap or combination (Hooper, 2008), and slight variations in the criteria used to select and weight measurements temporally or spatially (Crosetto *et al.*, 2016; Osmanoğlu *et al.*, 2016). Given the extensive range of similar approaches in literature, it has been remarked that it is difficult to distinguish and review many methods individually (Crosetto *et al.*, 2016; Osmanoğlu *et al.*, 2016).

2.6. Summary of gaps in literature

Scattering is a complex phenomenon in non-simple geometries, but even simple geometries are the subject of active research (Khankhoje, Zyl and Cwik, 2013; Abe *et al.*, 2014; De Zan *et al.*, 2014). Predictive modelling of the SAR measurements from complex, vegetative scenes is thus difficult and therefore considerable work is still required to better understand how local scattering behaviour can affect long term time series measurements of interferometric phase.

Factors such as changes in land cover and surface moisture have been shown to affect phase, but practical methods of accounting for these are limited.

Despite this, there is a practically inexhaustible list of slight variations to the MTI processing chain presented in literature (Crosetto *et al.*, 2016; Osmanoğlu *et al.*, 2016). From these it is difficult to determine the optimal approach for rural MTI.

Models for signal decorrelation also vary. Thus, there are challenges to produce a generalised model for localised scattering behaviour, and this has implications for the statistical accuracy of MTI methods whereby the true statistical accuracy of a measurement may be difficult to infer.

2.7. Conclusion

This chapter has reviewed the fundamentals of radar, Synthetic Aperture Radar, and InSAR, in the context. The importance of understanding scattering, wave propagation, and wave interference is emphasised, as these are the only measurable aspects of radar data. While antenna properties are generally known when imaging from a satellite, the propagation towards and return from a scatterer occurs through an atmosphere which varies in space and time. The surface scattering which occurs at any one point in time may be similarly transient.

These phenomena control the quantities which a SAR measures (such as amplitude, phase, and polarisation) and derived quantities (such as speckle correlation, interferometric phase, and coherence). Interpretation of these measurements should be contextualised with an understanding of these low level effects, especially in cases where the scattering is impermanent and signal decorrelation is observed. In this case the scattering phase is time varying through an InSAR stack and can affect measurements. More comprehensive exploration of how scattering changes affect available measurements is conducted in Chapter 4 with practical techniques developed in Chapter 5 to quantify these effects.

Further sources of phase errors in InSAR measurements were reviewed, and the upcoming Chapter 3 will explore practical methodologies to accurately estimate and isolate the effects of these errors in the data.

3. Methodology

3.1. Introduction

Sequences of data processing operations are applied to multiple SAR images acquired over the same area and with the same view geometry, to produce MTI results. A particular sequence of operations may be referred to as a 'processing chain', and a variety of highly effective processing chains have been described and applied in literature and industry (Adam *et al.*, 2009; Crosetto *et al.*, 2016; Osmanoğlu *et al.*, 2016). These different processing chains adopt different methods to compensate for the various error sources inherent in MTI, with very slightly different results (Crosetto *et al.*, 2016; Scoular *et al.*, 2022). As discussed in Chapter 2: Literature Review, ambiguity and variable accuracy are undesirable for research reproducibility or industrial validation, and such issues can be compounded by processing chains being proprietary (Adam *et al.*, 2009) (not in the public domain) or insufficiently defined in literature.

The development of a reliable and validated open source reference methodology for MTI processing is one of the objectives for this research. Hence, this chapter describes in detail the motivation and design process behind '*OpenInSAR*', an MTI processing implementation designed to fulfil this need. *OpenInSAR* has already provided a springboard for analytical developments detailed in Chapters 5 and 6, while the PSI Reference Processor described in Section 3.3 offers a consistent comparator in terms of performance.

3.1.1. Motivation

At the onset of this project (*ca* 2017) there were limitations in available open source software (Bischoff, 2019a). StaMPS (Hooper, 2008), a popular package, was available but had numerous dependencies on other software packages in uncertain states of

maintenance. StaMPS was not adopted for this project as it could not yet process data from Sentinel 1 (Foumelis *et al.*, 2018); a dataset expected to provide a wealth of freely available, regular up-to-date observations for several years (Yague-Martinez *et al.*, 2016). Sarscape (proprietary software owned by L3Harris) was employed but significant errors were common due to its particular implementation (Bischoff, 2019a) which were compounded by poor computational efficiency at the time of testing (*ca* 2017).

A previous MTI project has applied Sarscape software to an area of Wiltshire, South-West England (Agar *et al.*, 2018). Results of this study exhibited statistically significant differences between the behaviour of areas of Chalk and clay geology (British Geological Survey, 2000) as shown in Figure 3-1. Here, areas on Chalk were measured to uplift by an average of 6 mm relative to the clay over an 8-month data set. This phenomenon was not replicated in a biannual data set, suggesting that the supposed deformation was seasonal. The suggested hypothesis was that areas of clay geology were exhibiting shrink-swell in response to increasing surface moisture.

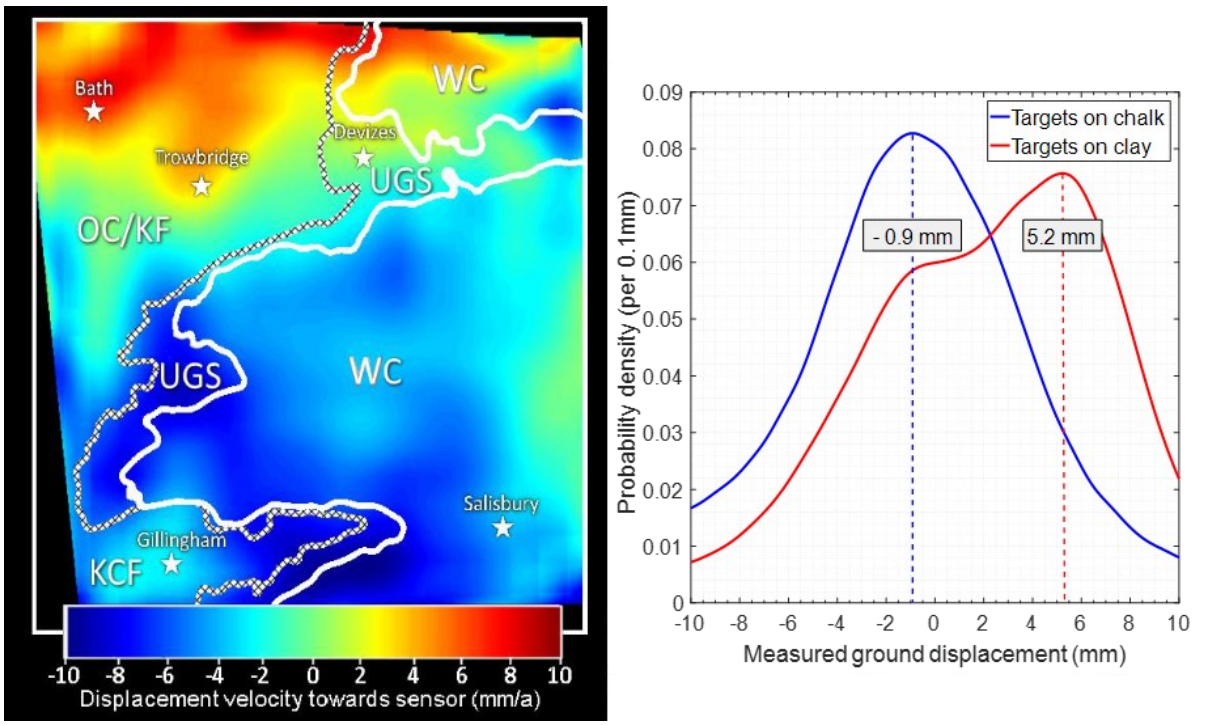


Figure 3-1: Statistically dissimilar behaviour of targets on Chalk and clay in the Salisbury Plain area. A modified PSI processing chain was required to further investigate this observed phenomenon. Key: OC/KF Oxford Clay and Kellaways; KCF: Kimmeridge Clay; UGS; Upper Greensand; WC: White Chalk. (Agar *et al.*, 2018)

Similar results in literature (North *et al.*, 2017) supported a shrink-swell interpretation but, to further investigate this hypothesis, a change to the standard PSI methodology was desired. Namely to model the seasonal deformation directly in the SAR data as a periodic signal (Colesanti *et al.*, 2003) or as a function of surface moisture data (or proxies such as groundwater levels, precipitation history, or simply the time of year). Unfortunately, the closed-source Sarscape software did not allow any such change to its PSI methodology, and implementing one required writing key code for PSI model inversion that grew to become *OpenInSAR* as initial coding efforts for various stages were found to provide significant improvements in computational performance.

It should be noted that since the onset of this project there have been several updates to the software mentioned, many addressing the listed issues. Software is also available from other authors. A fair critique of available software as extant today is beyond the scope of this work, as project effort has been focused on the development of *OpenInSAR* and its application to several wider research goals since its initial prototype.

3.1.2. OpenInSAR

Initial prototypes intended to provide a reference PSI implementation with practically feasible computational requirements for testing and developing data processing approaches in rural areas. These initial prototypes found value within a research community centred around the Geotechnics section of the Department of Civil & Environmental Engineering at Imperial College London. This lead to the application of earlier versions of the *OpenInSAR* code to fields such as coastal erosion (O'Connor *et al.*, 2021), dam stability (Shire *et al.*, 2023), structural geology (Wang *et al.*, 2022).

The wider applicability of this research software has highlighted the value in ensuring *OpenInSAR* becomes a high-quality product for users beyond this project. *OpenInSAR* has hence been developed as an expansible, easy-to-use and easily reproducible system for processing Sentinel 1 data into MTI result sets. The following section details its design and delivery processes.

3.2. High-level Design

This and following sections describe the design and delivery of *OpenInSAR*. The design process followed the general structure of Section 6.4 of ISO/IEC/IEEE 12207 Systems and software engineering – Software life cycle ('ISO/IEC/IEEE International Standard - Systems and software engineering – Software life cycle processes', 2008).

3.2.1. Stakeholders

The key stakeholder for *OpenInSAR* is this thesis research program itself but, given that a much wider userbase exists, it is useful to consider several use cases to determine potential value *OpenInSAR* can provide to the wider research community.

Many current users of *OpenInSAR* and its prototypes are researchers and academics based at Imperial College London and Royal Holloway University of London. Initially, the driving force for these users was the provision of insight into ground deformation phenomena, rather than a technical interest in developing MTI techniques and algorithms. Many of these users have had limited coding experience, and in some cases limited exposure to InSAR theory in general but it is expected that the code can and will be used and developed but future PhD researchers.

3.2.2. Requirements

This section details the needs and requirements of the software, which are summarised here:

R1: Is open source software

Open source software allows for easier review, collaboration and the wider adoption and utilisation by the research community. Open source software facilitates verification and validation.

R2: Has reference MTI processing chain

A reliable baseline processing methodology is required by this project as a springboard for further analysis and developments. A control on the various phase error sources is a particular requirement, in order to better distinguish these from scattering changes as they are explored in further research such as the subsequent chapters of this document. The reference processing chain should implement a widely used and straightforward approach, as more advanced and niche processing chains may be less generally applicable.

R3: Has modular architecture

Chapter 2 detailed various distinct steps inherent in MTI processing chains, and further demonstrates that a range of different approaches exist in literature (such as for PS selection, coregistration, spatial filtering). A modular architecture, with each data processing step implemented as a distinct module, should facilitate adaptation of the software to different use cases. The use cases might include: testing a specific method against another in otherwise controlled conditions; applying a modified processing chain to better analyse a specific problem area; appending additional processing steps for uses beyond deformation measurement.

R4: Facilitates seamless reproduction of results

This project will benefit in terms of credibility if results can be easily reproduced by peers in the research community. This should be facilitated by metadata being generated in tandem with results in order to detail the data lineage. The modular software chain should allow users to reiterate and reproduce results quickly and easily, with each module imprinting details regarding its version and parameterisation at runtime.

R5: Minimise external dependencies

Software dependencies can lower the chances of successful installation and reuse of a system (Trisovic *et al.*, 2022). Over time, libraries or APIs required by the software may no longer be maintained, might become incompatible with modern computing environments, or in a worst case may no longer be available. These issues could break

the dependent system, and potential end its useful life if no developer is available to repair it. Loss of the software runs counter to requirement R4. See also R6.

R6: Is easy to install and set up

Limiting the software to a particular computing environment or placing a large burden of work on potential users before they have used the software, will harm utilisation of the software and reproduction of results by peers.

Code produced in an academic context is renowned for being generally unclear and badly maintained (Martin, 2009b). A recent review of research code sampled 3830 files from the 'Harvard Dataverse' repository and found that only 26% of files ran successfully without editing the code (rising to 44% after editing to fix common errors) (Trisovic *et al.*, 2022).

R7: Is easy to operate

Potential users may not have a strong background in software development or remote sensing, but this should not be a barrier to them getting valuable results.

R8: Is easy to develop

Allowing developers intuitive access to the system is beneficial, as these developers may go on to aid in maintenance or improvement of the system.

Research software needs to adhere to good coding practices for it to be reproducible (National Academies of Sciences, 2019; Trisovic *et al.*, 2022). Incorrect practice in coding may be correlated with software errors (Butler *et al.*, 2009), and where software is difficult to use it limits the time and patience researchers can commit to leveraging its value. Software should be concise and easy to understand in order to be reliable, easy to maintain, and easy to improve (Beck, 2000; Martin, 2009a).

R9: Is feasible to develop within the project

Ultimately, no software is perfect, and some allowances and compromises must be made for this project's practical constraints in terms of timescales and wider research goals.

3.2.3. Specification

This specification outlines the functionality of *OpenInSAR* and the scope and constraints of the environments it is designed to operate in. The specification items listed in this section correspond to the requirement in Section 3.2.2, with the first number indicating the requirement (e.g. S2_2 would be the second specification item designed to meet requirement R2).

S1.1: MIT License

The MIT license is a common, permissive license for widespread use and development of the source code.

S1.2: Source code published on GitHub.

GitHub is a popular platform for sharing and collaborating on code. An accessible location where users can find code is useful to its adoption. At time of this documents publication, the software source code can be found online at https://github.com/insar-uk/OpenInSAR

S2: Has a PSI reference processing chain

This PSI reference processing chain is specified in Section 3.3.

S3: Plugin system

The software uses a plugin system, whereby each plugin performs a distinct operation on the data.

S4.1: All plugins and core classes are versioned.

Users can reproduce past results by using specific versions of each procedure, along with version control via Git.

S4.2: Metadata

Results files will contain metadata regarding the files and processing steps used.

S5.1: Minimal software dependencies

The only software dependency for *OpenInSAR* is Octave 7.2.0 (or later versions), with Matlab 2020b (or later versions) being nearly identical in syntax and therefore equally useable. The libraries used by Octave/Matlab are packaged together.

S6: Single script setup

All operation required for setup should be contained within a single script or executable.

S7: Documentation

Provided plugins and core files should be sufficiently documented,

S8: Common and open data formats

Use of commonly used open data formats allows for easy interoperability with other software and therefore greater opportunity to leverage existing tools.

3.2.4. Architecture

A software systems architecture consists of its component modules and the relationship between these. The architecture is useful to define in order to conceptualise how different parts of the system will cooperate (Martin and Martin, 2018).

It is useful to produce a use case diagram to aid design of the software architecture. A use-case diagram elucidates the flow of information between various interfaces, and the software required to provide the inputs desired by each stakeholder shown. Figure 3-2 shows a use case diagram for MTI analysts, MTI developers, and engineers utilising MTI results.

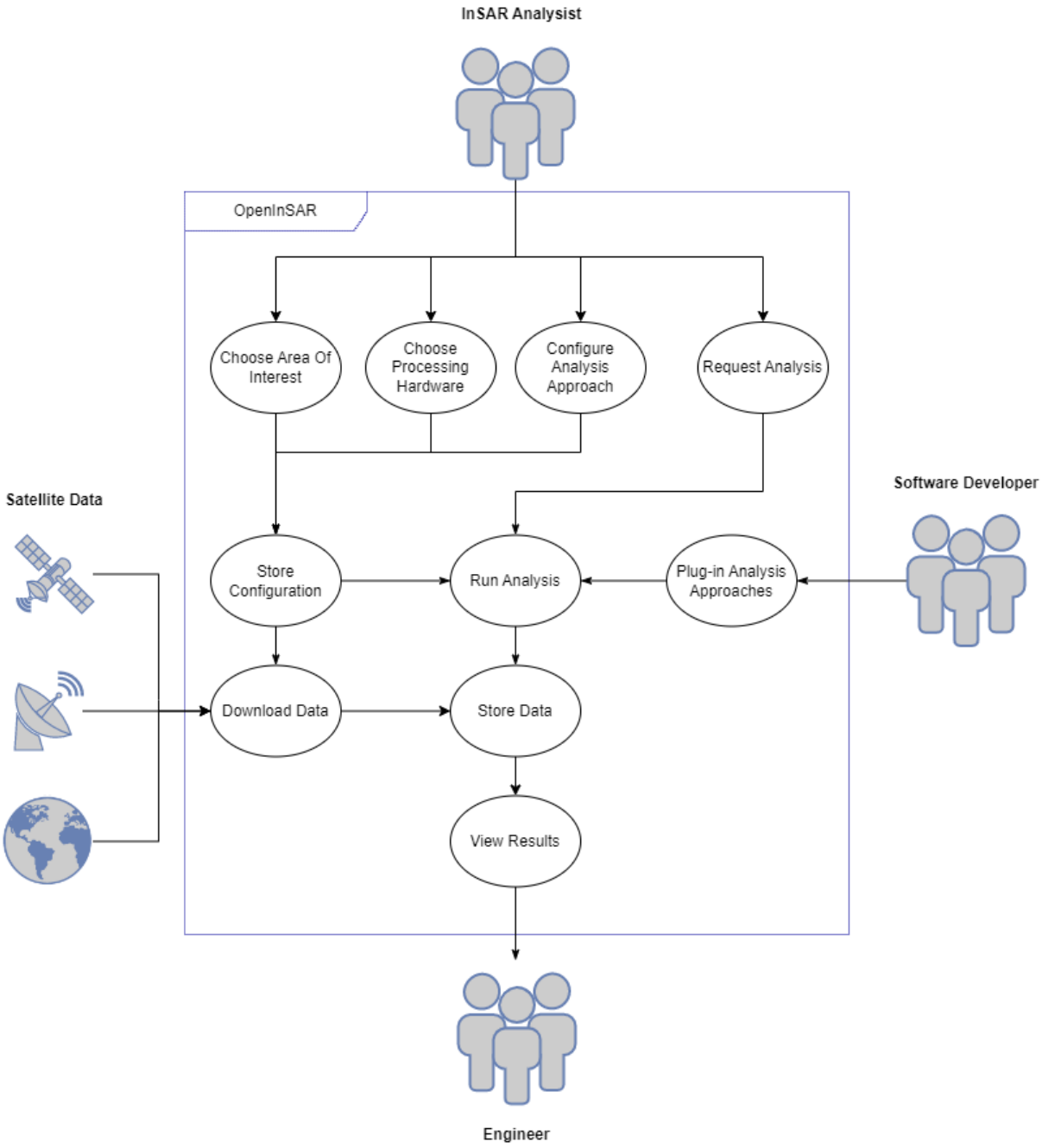


Figure 3-2: Typical use cases for *OpenInSAR* for various stakeholders.

The use case diagram highlights several core functions. Of note is the ability for developers to add their own processing steps, which promotes the use of a 'plug-in' architecture.

A conceptual diagram was developed in order to organise and take responsibility for functions found to be necessary from the use-case diagram, as shown in Figure 3-3. The

concept appears to be relatively simple, with the user (via an interface) configuring and controlling a processor which retrieves files and plugins.

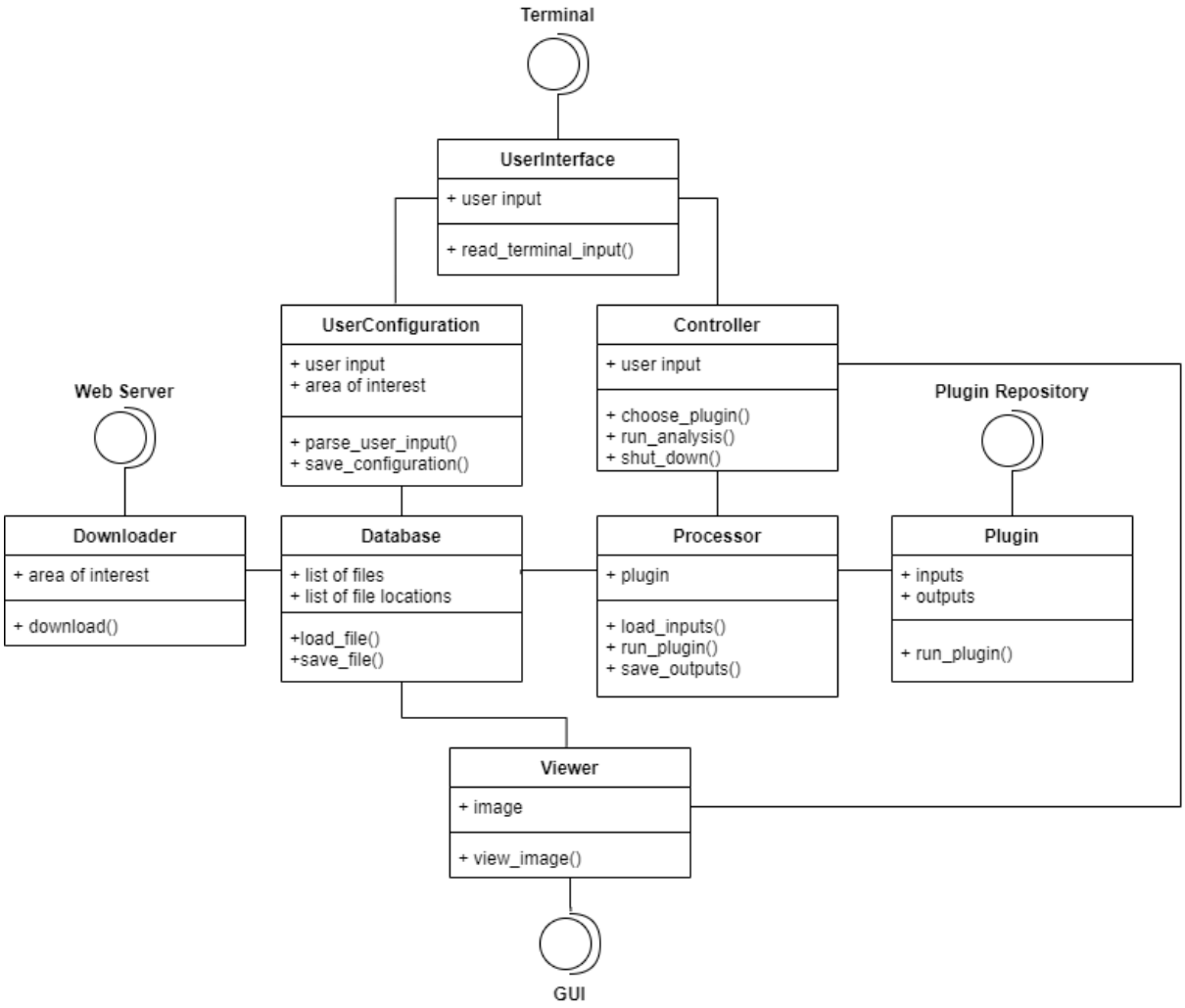


Figure 3-3: High-level conceptual diagram of the *OpenInSAR* Architecture

In implementing the plugin architecture for the prototype, the plugins themselves became a central component, interacting with nearly all elements of the system. While it is important to facilitate new features by ensuring that plugins are powerful and flexible, this high degree of coupling between the main program components and the plugins could be problematic. A change to one of the main program components might then necessitate changes across existing plugins, causing a large degree of unnecessary work effort. The concept can therefore be refined by detaching the UI and GUI from the plugins,

implementing the Downloader as a plugin rather than a core component in order to simplify the high-level architecture.

Coupling refers to the degree of interdependence between components in a system (ISO, 2017). When a group of components are interdependent, an error or change in one could propagate unintended behaviour into other components. Coupling therefore limits the resilience of the system against future change.

Decoupling components of the system was therefore prioritised, given the requirement for *OpenInSAR* to be easy to develop, and the likelihood of ongoing change in remote sensing datasets and approaches.

3.2.5. Delivery

The software was delivered as a package for the Matlab/Octave numerical computing environment. Matlab is widely used in academic contexts, particularly in teaching. This makes it likely that a typical student of InSAR data processing will have encountered the language at some stage in their education and will therefore be able to understand the basic principles of operations. Matlab/Octave offers access to a wide variety of common libraries for numerical analysis, including matrix inversion, factorisation decomposition, statistical analysis and image interpolation. All of these processes are heavily used in InSAR data processing, and thus having readily available and well-tested implementations allows for greater focus on issues specific to the processing of InSAR data.

Recently, the Python programming language has grown significantly in popularity and offers efficient implementations of these matrix manipulation processes through libraries such as NumPy. At the time of this projects onset, the ubiquity of NumPy was less apparent and thus Matlab was favoured. NumPy and Matlab both offer a rich toolset for matrix manipulation, respectable performance, and efficient syntax for development and testing. A number of powerful GUI and visualisation options are available for Python, but these features are built into Matlab/Octave which reduces the need to consider additional libraries.

Criticisms of Matlab include its expensive licensing and poor computational efficiency. Regarding licensing, GNU Octave (Eaton, 2002) offers an open-source alternative with near-identical language syntax and comparable features. Regarding performance, the most computationally intensive operations in InSAR processing involve inversion of matrices and solving of linear systems for which Matlab/Octave is optimised through use of the highly performant LAPACK and BLAS libraries (Lawson *et al.*, 1979; Blackford *et al.*, 1987). Processor developers such as AMD and Intel produce specialised hardware-optimised implementations of these routines. Most performance issues in Matlab/Octave can be remedied through refactoring to avoid inherent overheads in creating variables and passing them between functions.

The software development process aimed to incorporate best practices from recent decades. Test-first approaches (Beck, 2000) and continuous integration (Paul M. Duvall, 2007) allow for immediate feedback on errors and a focus on providing clean and intuitive interfaces between modular components. This synergises well with an agile approach (Martin, 2009a) whereby a programs features and functionality are broken down into small units that are delivered frequently (as opposed to delivery of a monolithic system). Small units of code are ideally broken down into components with limited responsibilities and limited interfaces (Martin, 2009a).

The initial features to deliver were a test system, tools for mocking and tracking user input and logging program output, a system for tracking which files have been loaded and created (for data lineage), tools to load and save common data formats, an interface for running plugins and a queuing system for running processing chains.

Features related to MTI processing steps were then added one-by-one to *OpenInSAR* as plugins, with confidence that the 'core' system was relatively simple, fully tested, and isolated from the data processing operations of relevance to MTI results.

Each plugin specifies its required input data and defines the data it will produce. This allows for an automatic chaining of operations as depicted in Figure 3-4. A single project file specifies the desired data and any specific operations, parameters, or approaches desired to produce it.

Continuous integration was facilitated via a Python script periodically running all tests in Octave 7.2.0 on Windows 10 and Ubuntu 20.04. New versions of the core software and individual plugins were further tested using the latest version of Matlab (currently 2023a) on Windows 10, a common setup in academic environments according to the authors experience.

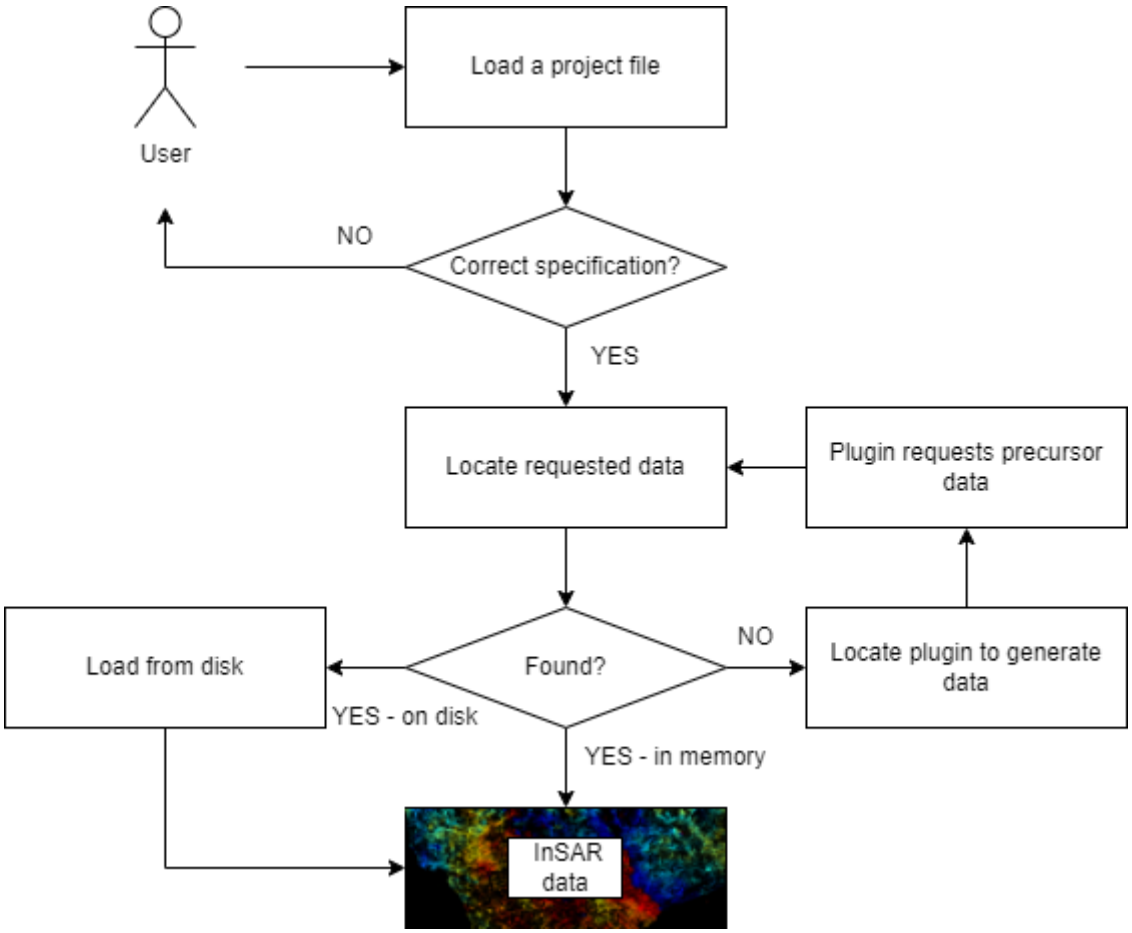


Figure 3-4: Flow diagram depicting how *OpenInSAR* produces results. Plugins specify their requirements and the data they produce, as such processing chains are constructed upon specific data being requested.

3.3. PSI Reference Processor

The PSI Reference Processor detailed in Requirement 2 was developed as a series of plugins, and integrated with the core system. A diagrammatic overview of the data processing chain is shown in Figure 3-5. Individual processing steps form individual plugins, allowing for easy reuse in other applications. Sections 3.3.1 through 3.3.6 provide a description of specific data handling operations performed at each step.

PSI processing steps ultimately aim to deliver accurate measurements of ground deformation from InSAR dataset. This requires that the interferometric phase effects detailed in Section 2.4 are estimated and separated out from the InSAR data. For convenient reference, the typical model for InSAR phase contributions detailed in Equation 2-11 is reiterated here as Equation 3-1 (Ferretti, Prati and Rocca, 2001):

Equation 3-1: The InSAR phase model.

$$\Delta\varphi = \phi_{orbit} + \phi_{topo} + \phi_{defo} + \phi_{atm} + \phi_{scat} + \phi_{noise}$$

This section describes the approach taken to minimise each of these error terms when isolating the deformation signal.

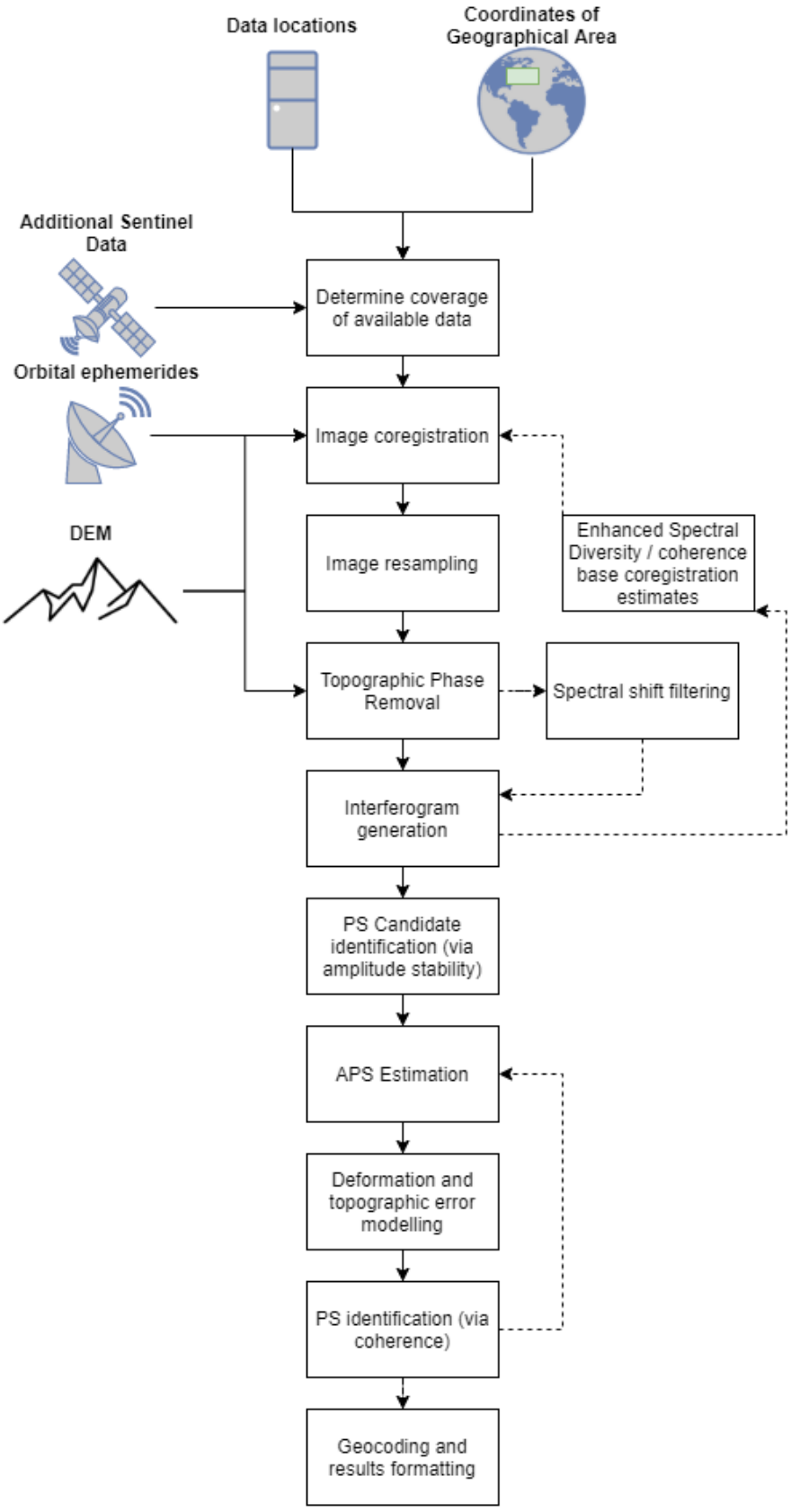


Figure 3-5: Block diagram for the reference PSI processing chain, showing the main InSAR signal processing operations implemented within the software.

3.3.1. Orbital positioning

Satellite orbital positioning data is retrieved from the ESA's 'Precise Orbital Ephemerides' (POE) product. The POE data is provided in 10 second increments.

The accuracy of the POE positioning is around 1 cm (Peter *et al.*, 2017), which is completely acceptable: Orbital positioning errors in this order of magnitude produce a low-frequency phase pattern in the subsequent interferograms, due to the smooth orbital motion of the satellite. This smooth, extensive error can be identified or removed through a variety of means. For this project, the errors are removed during estimation of the more spatially-variable atmospheric phase errors (see Section 3.3.5 Atmospheric Phase Screen, page 88).

In order to estimate the satellite position at the time of each radar pulse, rather than every 10 seconds, the POE data is interpolated using a polynomial fit. The interpolation accuracy is verified using 'leave-one-out' cross validation. Here, a POE sample is removed from the polynomial fitting processes and the spatial distance between the re-fitted value and the original is then calculated. The average discrepancy is approximately 1 μm , which constitutes a negligible error compared to the typical centimetric accuracies of the orbital product (Peter *et al.*, 2017).

3.3.2. Geocoding

The ESA provides Sentinel 1 data in focused 'Single-Look Complex' (SLC) format, with the focusing procedure described in detail (European Space Agency, 2019). The main principle is that a scattering object's spatial position affects the Doppler frequency and timing of the signals it returns to the radar, and this information can be interpreted to determine the objects position (Small and Schubert, 2019).

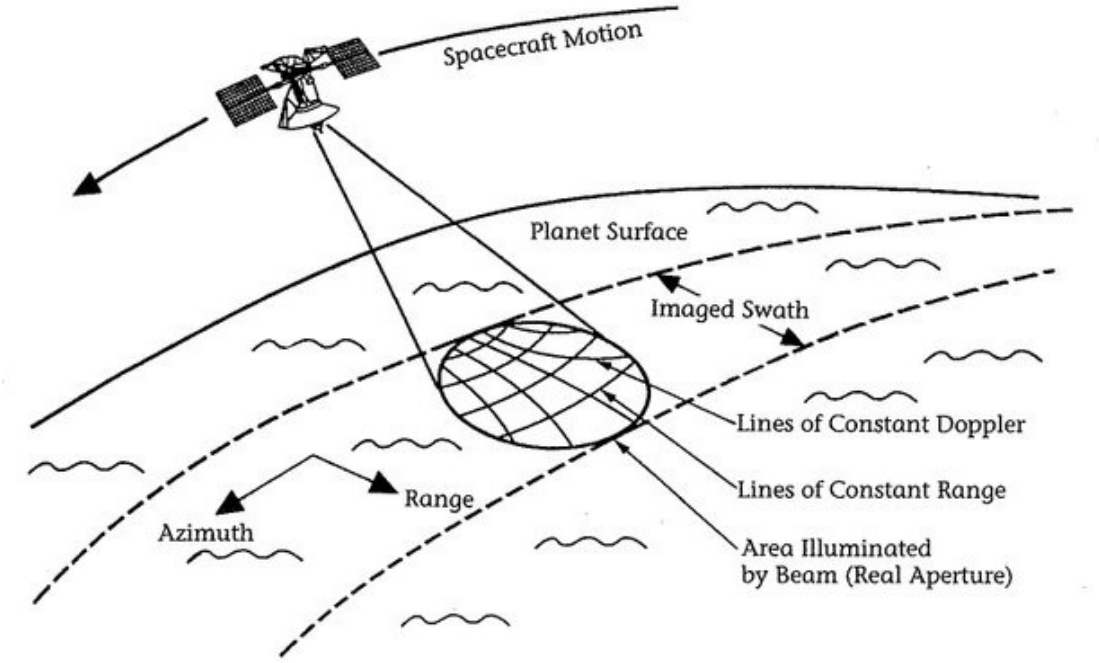


Figure 3-6: SAR imaging geometry. The motion of the satellite along its track produces a Doppler effect that can be used to geolocate samples. This is combined with the timing of the echo which varies with the range between the satellite and scatterers on the ground. (Ford, 1993)

The two dimensions of a SLC image correspond to the timing of a signal being emitted along the satellite 'azimuth', its track of motion, and the travel time in 'range' which the radar signal takes to backscatter from the surface and return to the satellite. This projection is shown diagrammatically in Figure 3-6 (Ford, 1993). The Range-Doppler equations, shown in Equation 3-2, are used to determine ('geocode') an image sample's geographical coordinates (Sansosti *et al.*, 2006):

Equation 3-2: Range-Doppler equations for geocoding and image coregistration.

$$\Delta f = \left(\frac{v(a) \cdot \big(P(lat, lon) - S(r, a)\big)}{c}\right) f_0$$

$$\Delta\tau = \frac{2}{c}|P(lat, lon) - S(a, r)| - \tau(r)$$

$$for\ each\ a, r: \underset{lat,lon}{argmin}|\Delta f(lat, lon)| + |\Delta\tau(lat, lon)|$$

where a and r are the SLC image coordinates in azimuth and range, c is the speed of light. $S(r, a)$ is the corresponding satellite position in the three cartesian dimensions. $P(lat, lon)$ is the cartesian position corresponding to a geographic position given in latitude and longitude (which needs to consider the topographic height of the surface from a Digital Elevation Model (DEM)). In this case the Satellite Radar Topography Mission (SRTM) DEM (Mukul *et al.*, 2017) was used to provide surface elevation data.

For each azimuth and range image coordinate, numerical techniques are used to find the corresponding latitude and longitudinal position on the Earth's surface which minimises Doppler shift, Δf, and difference in range delay, $\Delta \tau$. These depend on the sensor velocity v, signal frequency f_0, and the range delay used to focus the image $\tau(r)$ which are provided by the ESA.

3.3.3. Coregistration

Accurate alignment of the SAR images is required in order to minimise decorrelation loss of useful signal (Zebker and Villasenor, 1992; Yague-Martinez *et al.*, 2016), in a process known as coregistration. The centimetric accuracy of Sentinel 1 orbital data, and the availability of global scale DEM data such as from SRTM, allow for a near-optimal level of alignment simply through solution of the Range-Doppler equations (Equation 3-2).

To validate this, the Coherent Cross-Correlation technique was applied to each image in the series (De Zan, Prats-Iraola and Rodriguez-Cassola, 2018). The algorithm is shown in Equation 3-3:

Equation 3-3: Coherent Cross Correlation optimisation.

$$(t_{az}, t_{rg}) = argmax \left| \sum s_{reference}(a, r) \cdot s_{secondary}(a + t_{az}, r + t_{rg})^* \right|$$

where the optimal shifts in time for the azimuth, t_{az}, and time in range, t_{rg}, for geolocation of input signals $s_{secondary}$ are those which maximise the complex correlation with a reference image s_{ref}. The sum is performed over a local window in azimuth and range.

Having coregistered the 2D images, these can be arranged chronologically and treated as a 3D volume of data termed a *stack*. The InSAR phase contributions are subsequently estimated from this stack.

3.3.4. Persistent Scatterer Identification

Isolating individual phase contributions from the InSAR data is complicated by noise and the fact scatterers change over time. Scattering changes are captured in the ϕ_{scat} term and can cause unpredictable noisy shifts in the interferometric phase. Loss of signal due to these surficial changes is often termed temporal decorrelation (Zebker and Villasenor, 1992; Rocca, 2007).

Identifying pixels in the image stack with low noise and temporally consistent scattering is therefore useful for accurate estimation of phase contributions (Ferretti, Prati and Rocca, 2001; Hooper *et al.*, 2004). These stable pixels will exhibit phase values representative terms being estimated such as φ_{aps}; φ_{defo}; φ_{topo}, rather than ϕ_{scat} and ϕ_{noise} which are generally treated as incoherent noise and only estimated as a residual error.

Reliable points with limited temporal decorrelation in the InSAR stack are termed Persistent Scatterers *(PS)* (Ferretti, Prati and Rocca, 2001; Hooper *et al.*, 2004). The criteria for identifying PS often varies slightly between authors (Hooper, 2008; Crosetto *et al.*, 2016), but a common approach is to first identify pixels as PS via the noise characteristics of amplitude values measured at that pixel, taking the population across each image in the stack, before then refining the selection based on temporal coherence.

To explore this approach, it is useful to model a SAR signal measurement, s, as explored in Equation 3-4:

Equation 3-4: Modelling the relationship between SAR amplitude noise and interferometric phase noise.

$$v \in \mathbb{R}$$

$$s = v + N(\sigma_n)_R + jN(\sigma_n)_I$$

$$\varphi_s = \angle s = \angle \frac{N(\sigma_n)_I}{v + N(\sigma_n)_R}$$

$$A_s \equiv |s| \therefore A_s \in \mathbb{R}, \qquad A_s > 0$$

$$f_{A_s}(x) = \frac{x}{{\sigma_n}^2} I_0\left(\frac{xv}{{\sigma_n}^2}\right) e^{-\frac{x^2+v^2}{2{\sigma_n}^2}}$$

where the signal, s, is composed of a deterministic component v and a gaussian noise process $N(\sigma)$ having a shared standard deviation, σ_n, in the real and imaginary components but independently realised values (i.e. $N(\sigma)_R \not\equiv N(\sigma)_I$). The amplitude, A_s, is resultingly distributed according to the Rician distribution (Ferretti, Prati and Rocca, 2001). It is approximated that the uncorrelated noise processes which produce ϕ_{scat} and ϕ_{noise} are themselves gaussian and thus can be represented by the $N(\sigma)$ process.

Given an increase in signal-to-noise ratio v/σ , both the variance of the phase and the variance of the amplitude will be found to decrease. Where $\sigma_{noise} \ll v$ the approximation in Equation 3-5 holds:

Equation 3-5: The Amplitude Dispersion (D_A) metric for PS identification.

$$D_A := \frac{\sigma_{A_s}}{\mu_{A_s}} \simeq \frac{\sigma_n}{v + \sigma_n} \simeq \sigma_\varphi$$

It should be noted that D_A is a sampled estimate, derived from the realised samples available in the SAR image stack at each pixel. D_A itself is therefore noisy and therefore it is recommended that a high multiple of images (e.g. > 30) are available to increase the sample population (Ferretti, Prati and Rocca, 2001).

The relationship between D_A, σ_φ, and σ_n can be simulated as shown in (Figure 3-7) (Bamler and Just, 1993; Ferretti, Prati and Rocca, 2001; Hooper, 2006). Here, 5000 time series of 37 SAR measurements are simulated to estimate expected values for D_A and σ_φ for a given σ_n. Note that, like D_A, σ_φ is estimated numerically and simulations using less iterations will result in more variance in the realised value of σ_φ.

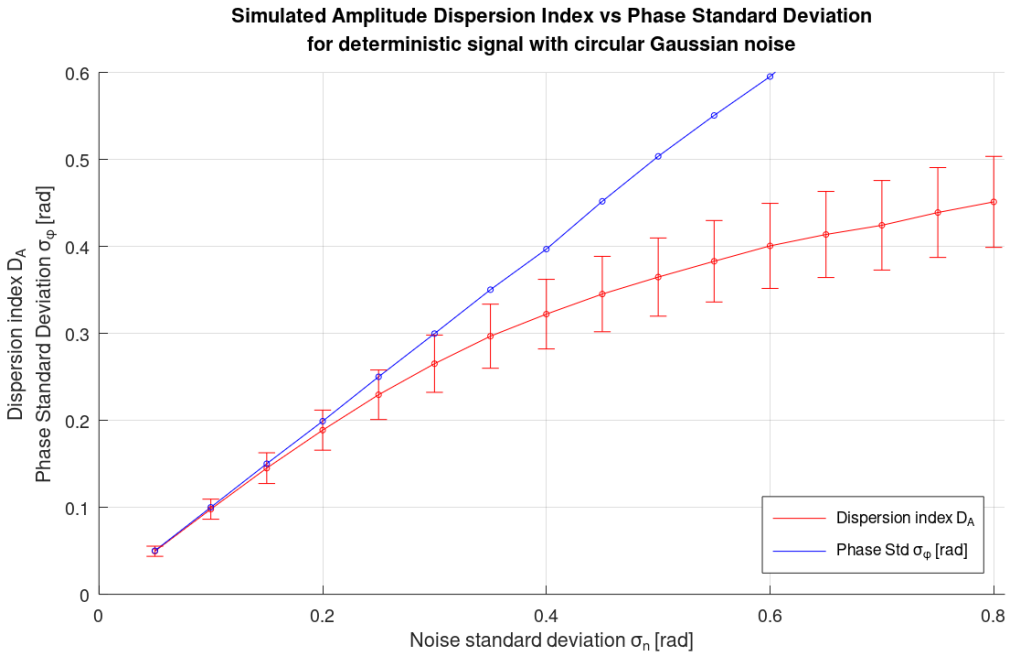


Figure 3-7: Demonstration of the relationship between SAR amplitude dispersion and InSAR phase noise, recreated from (Ferretti, Prati and Rocca, 2001). Both dispersion index (unitless) and phase standard deviation (rad) are plotted on the y-axis.

A threshold D_A of 0.25 is subsequently used to identify PS. As D_A approaches 0 the relationship with phase noise is approximately linear (Ferretti, Prati and Rocca, 2001), as can be seen in Figure 3 . For increasing values of D_A there is a wider distribution for a given σ_n and therefore there is less certainty and accuracy when inferring σ_φ for a given pixel.

Once PS candidates have been selected, their data can be extracted for use in estimating the spatially varying atmospheric error and further interferometric phase contributions.

3.3.5. Atmospheric Phase Screen (APS)

Phase shifts attributable to the APS, ϕ_{atm}, are typically estimated via spatial filtering operations (Liu, 2012). Here, the technique known as Kriging is used (Cressie, 1990; Wackernagel, 2003).

Kriging has been employed for many years in APS estimation (Ferretti, Prati and Rocca, 2001; Meyer *et al.*, 2005; Knospe and Jonsson, 2010). It is sometimes referred to as the 'Best Linear Unbiased Estimation' as it minimises the error variance between input data and interpolation, and thus achieves the best possible statistical fit of the data.

Ordinary Kriging has been employed in this research. In addition to minimising the estimation variance, Ordinary Kriging further assumes that there is an unknown non-zero mean value which varies spatially (as is the case for the APS (Meyer *et al.*, 2005)).

The minimum estimation variance is achieved through solving the system of linear equations:

Equation 3-6: The Ordinary Kriging system.

$$\begin{bmatrix} C(x_1 - x_1) & \dots & C(x_1 - x_n) & 1 \\ \vdots & \ddots & \vdots & \vdots \\ C(x_n - x_1) & \dots & C(x_n - x_n) & 1 \\ 1 & \dots & 1 & 0 \end{bmatrix} \begin{bmatrix} w_1 \\ \vdots \\ w_n \\ \alpha \end{bmatrix} = \begin{bmatrix} C(x_1 - y) \\ \vdots \\ C(x_n - y) \\ 1 \end{bmatrix}$$

$$\hat{Z}(y) = \sum_{i=1}^{n} w_i(y) \cdot Z(x_i)$$

where the APS value $\hat{Z}(y)$ for location y is determined from a linear combination of phase data $Z(x_i)$ from the PS at locations $\{x_1 \dots x_n\}$. The optimal weights $\{w_i \dots w_n\}$ of the linear combination are found by first estimating the correlation function C, measuring the relationship between phase correlation and the distance between PS, and then inverting the matrix (Wackernagel, 2003).

This inversion subsequently accounts for the correlation in errors between nearby PS. For example, if a large number of reliable PS are clustered at some large distance West of y,

while a smaller number of these are located in a cluster at the same distance East, the individual weights will be lower for the larger number of Western PS than the Eastern. This can be intuitively understood as each cluster provides similar information, but the extra individual PS add very little extra information regarding y.

While the APS varies slowly in space, it varies quickly in time (changing rapidly over the course of a few hours) and thus temporal filtering of the APS estimates (Ferretti, Prati and Rocca, 2000) allows for separation of spatially extensive deformation phenomena.

3.3.6. Modelling Height and Linear Deformation

The remaining components in the phase time series are due to surface deformation and inaccuracies in the DEM, which lead to incorrect compensation of parallax errors as the orbital position of the satellite varies slightly between images. This component, often termed the 'height error' can be estimated effectively through regression of the observed phase shifts with the known position of the satellite.

This approach is robust: The satellite position is known to centimetric position, while the differences in satellite position which generates the parallax (known as the 'perpendicular baseline') generally varies by around 50 m for Sentinel 1. Error in modelling height error therefore depends almost entirely on error in the phase, while exploitation of long time series of interferograms aids the regression.

A periodogram approach was used to simultaneously model the height error and linear deformation rate for each pixel (Ferretti, Prati and Rocca, 2001). The algorithm is described in Equation 3-7:

Equation 3-7: The coherence optimisation approach for measurement of height error and linear deformation rate.

$$(v, q) = argmax \left| \frac{1}{N} \sum_{n=1}^{N} \frac{s_n(\Delta t, \Delta k)}{|s_n(\Delta t, \Delta k)|} \cdot e^{-jv\Delta t} e^{-jq\Delta k} \right|$$

where j is the imaginary unit. Individual samples s_n of complex SAR amplitude, in a series of N images will have distinct temporal baselines (distances in time), Δt, with respect to a reference image, and similarly a difference in perpendicular spatial baseline, Δk, due to slight deviations in the satellite orbit. Modelled parameters v and q are the deformation rate and height error. The argmax operator represents the values for v and q that maximise the function with its brackets. The approach seeks to match the modelled phase, $e^{-jv\Delta t}e^{-jq\Delta k}$ to the phase of the measurements $s_n(\Delta t, \Delta k)$. The optimal parameters hence maximise the absolute value of coherence.

3.4. Qualification of the software system

Qualification of the system was performed through a variety of case studies throughout the course of this project, generally produced during MSc projects. During development, the software was tested for areas of London where a number of known deformation phenomena have been previously identified using PSI (Bischoff, 2019b; Scoular *et al.*, 2020). In general, *OpenInSAR* was compared against existing commercial processing software and found good agreement in results.

An MSc project investigated the Ventnor Landslide complex, Isle of Wight, United Kingdom using an early version of *OpenInSAR* (O'Connor *et al.*, 2021). Figure 3-8 shows results for one area of that study.

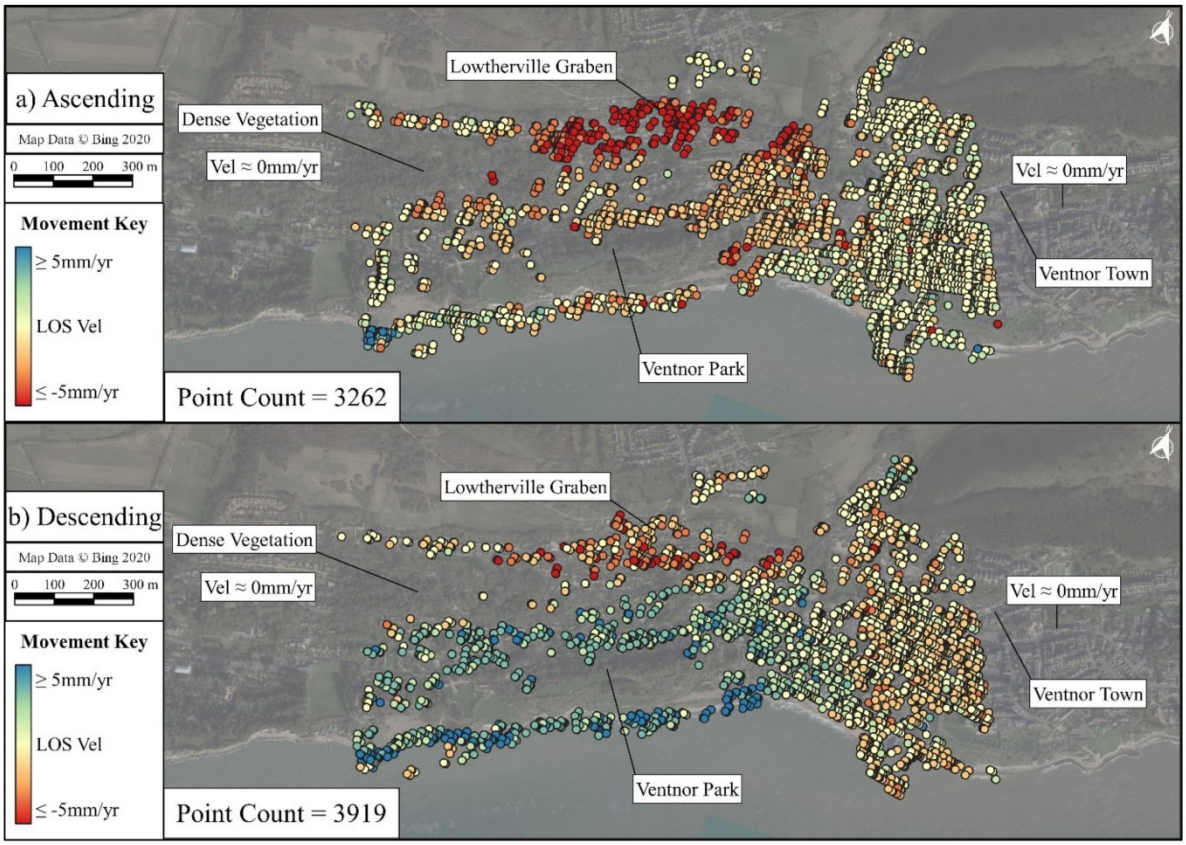


Figure 3-8: Distribution of PS points generated from ascending (a) and descending (b) Sentinel 1 orbits for the Ventnor Scheme 2020.

PSI results highlighted significant ground movements consistent with a rotational landslide. These results were cross-referenced with borehole records and found to be in spatial agreement with the failure surface identified in independent ground models (Halcrow, 2006), specifically the interface between a section of Gault Clay sliding over more competent Monk's Bay Sandstone (O'Connor *et al.*, 2021)..

The clear deformation patterns associated with the landslide demonstrate the value of the *OpenInSAR* prototype as a tool for monitoring ground deformation. The strong spatial correlation in velocity measurements (despite no spatial low-pass filtering of the PS aside from to estimate the APS which is removed) is also indicative the results accuracy.

3.5. Current limitations and ongoing development

The highly modular architecture of *OpenInSAR* allows for straightforward adaptation of the reference PSI algorithms. Various alterations of the approach can be tested in isolation by simply modifying individual plugins. This allows for potential improvements to be investigated, such as weighted kriging of the APS.

Additional features such as the Short BAseline Subset (SBAS) processing chain or coherence matrix approaches are not currently implemented but should in future be delivered as additional plugins.

Currently, documentation and general useability is not at a level that meets the objectives described in Section 3.2.2. An project to develop *OpenInSAR* beyond this investigation has been commission which should allow opportunity to address these issues.

3.6. Hardware and operating systems

The use of Matlab facilitates the use of *OpenInSAR* across a range of computing environments. In general, work present here used either a local Intel Windows 10 PC with AMD processor, or Red Hat Enterprise Linux machines with Intel processors running via Imperial College HPC.

Due to the simple interfaces and built-in process queuing system, adapting the software to a distributed computing environment is straightforward. Distributed operation of *OpenInSAR* has been tested successfully via Amazon Web Services cloud computing platform and Imperial College's HPC system.

At various stages of development, *OpenInSAR* has been tested on Mac OS, Linux Mint, Ubuntu, and AWS cloud computing platforms. Bugs in compatibility are generally rare, aside from issues involving different file-path formats, which are extremely common.

3.7. Conclusion

A comprehensive software solution has been designed and delivered in order to facilitate this projects research into rural MTI phenomena and analytical methods. This software has wider value to the research community as evidenced by recent publications that have used *OpenInSAR* or its earlier prototypes (O'Connor *et al.*, 2021; Wang *et al.*, 2022; Shire *et al.*, 2023).

The plugin architecture allows for MTI developers to focus on developing algorithms, while helpful tools and interfaces allow for easy retrieval of data necessary to run these. Long processing chains are automated through an system whereby the core program determines and generates required data where missing.

In order to validate the software, results were compared with existing commercial software; it was used to measure known deformation phenomena in London; and found to highlight previously unknown deformation phenomena which correlated well with independent evidence provided by a ground model for a landslide complex (O'Connor *et al.*, 2021).

The PSI reference provides a basic, reliable springboard for ongoing developments. This began with investigation into how transient scattering behaviour in rural areas can affect MTI results.

4. Transient Scattering

4.1. Introduction

The majority of rural land cover in the UK is vegetated, and the majority of vegetation experiences substantial seasonal changes (*UK Natural Capital Land Cover in the UK*, 2015; 'A Land Cover Atlas of the United Kingdom (Maps)', 2017). The scattering observed in vegetation can however vary over a matter of hours, due to fluctuating moisture contents in the canopy. Similar moisture changes are observed from soils. An interferometric signal can completely decorrelate as a result of these scattering changes (Zebker and Villasenor, 1992; Bamler and Just, 1993; Rocca, 2007; Jung *et al.*, 2016; Ma *et al.*, 2018)

Transient behaviour of rural scatterers can therefore affect InSAR results (Bamler and Just, 1993; Rocca, 2007; Ferretti *et al.*, 2014), but the exact effects on InSAR observables and the implications for deformation studies remain understudied (De Zan, Zonno and Lopez Dekker, 2015; Zwieback and Hajnsek, 2016). Previous deformation studies have identified significant correlation between time-series InSAR results and land cover with transient properties (Agar *et al.*, 2018), yet a causative role of scattering changes has been difficult to ascertain. Figure 4-1 shows a clear correlation between geographic areas of clay-rich soils and apparent uplift in unfiltered PSI velocity measurements (usually non-PS pixels would be filtered out from analysis). Areas without clay show an apparent relative subsidence.

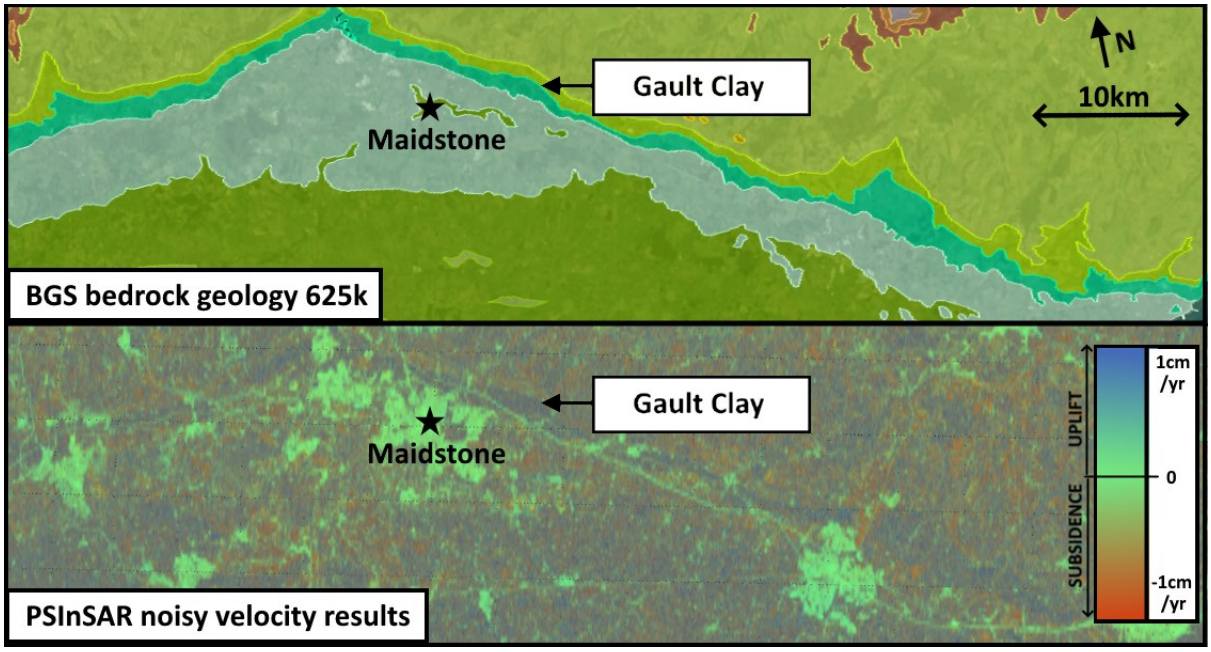


Figure 4-1: Unfiltered deformation rate measurements from Sentinel 1 Orbit 81 between Jan 2015 and August 2019 (Grant, 2020). A clear correlation between apparent uplift (Blue) and Gault Clay areas can be seen, whilst other rural areas show more locally clustered patterns of apparent subsidence behaviour (red) especially south of Maidstone. Urban areas can be seen as areas of relative stability (green). Despite the limitations of the data a land cover correlation can be appreciated.

An argument could be made that results such as in Figure 4-1 are an accurate measurement of geometric swelling of the clay, but this would fail to explain the apparent subsidence of the non-clay areas and persistence of the apparent motion in long-term (i.e. multi-annual) studies. The reported rates of movement are large enough that if they were an accurate representation of ground motion a marked vertical offset between soils would be conspicuous visible after several years.

Another possibility is that the signals being studied are coherent for only a short period of time, which coincides with the periods of high movement compared to the remainder of the year. This would sufficiently explain the overall low temporal coherence in affected time series, and the lack of correlation between result and long-term behaviour, but still fails to explain the apparent subsidence of non-clays. Regardless of the validity of this argument, the effects of seasonal decorrelation upon the results should be considered.

The main argument studied by this work is that transient changes in the scattering behaviour of volumetric natural scatterers cause shifts in the InSAR phase, and

subsequently bias the InSAR deformation measurements. There are a number of studies modelling or observing mechanisms for predictable phase shifts occurring due to typical changes in land cover, but relatively few (Ansari, De Zan and Parizzi, 2021) which confirm their presence in global satellite datasets or detail methods to isolate them.

This work aims to determine the presence of predictable phase shifts occurring from predictable changes in scattering behaviour: 'Transient Scatterers' are henceforth defined as scatterers with transient physical properties causing intermittent periods of coherence and shifts in phase that are not uniform noise or gaussian zero-mean random noise as in prior models (Zebker and Villasenor, 1992; Rocca, 2007; Guarnieri and Tebaldini, 2008). From a radar perspective these scatterers will only be transiently extant in a SAR pixel time series, before another scattering mechanism is dominant in the resolution cell.

4.2. Background

PS are generally modelled as features which effectively backscatter from a deterministic point (Ferretti, Prati and Rocca, 2001). An MTI derived displacement measurement is generally interpreted as a displacement of this point. For DS, the scattering occurs throughout a volume rather than a point. Displacement measurements are therefore modelled as an average displacement of scatterers within the volume.

This model is complicated by non-uniform displacement of the scatterers (temporal decorrelation) and greater measurement sensitivity to changes in incidence angle (geometric decorrelation), but these effects can be modelled as zero-mean noise (Rocca, 2007; Agram and Simons, 2015) and effectively reduced via spatial or temporal filtering. As these effects are zero-mean, there is no mechanism through which they could cause mean phase shifts to be correlated across large regions and multiple imaging dates.

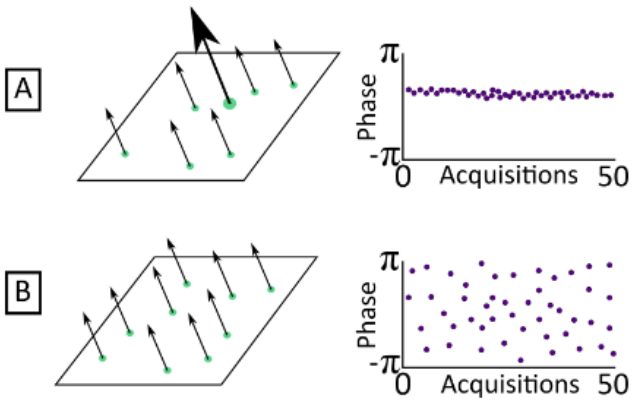


Figure 4-2: Diagram representation of backscatter from a persistent scatterer (a), and a distributed scatterer (b), including phase simulated with small movements of the elementary scatterers between samples. From (Hooper, 2006) via (Grant, 2020).

For DS in rural areas however, trends in interferometric phase may be produced by additional phenomena such as change in vegetative cover or soil moisture changes. These phase shifts are possible due to the penetration of the radar waves into the scattering media. As the microwave signal propagates through semi-transparent media such as vegetation or soil it is delayed, with this delay being dependent on material

properties such as the relative permittivity of the media. A delay in signal propagation during scattering will cause a corresponding delay to the signal being observed at the receiving antenna.

Water is ubiquitous in rural areas of the UK and has a high dielectric permittivity. The water content of soils and vegetation causes significant variations in their relative permittivity. Changes in moisture content due to precipitation and evapotranspiration therefore vary the signal delays encountered in these media, producing a variable shift in the phase of backscattered signals which have penetrated the media. To determine the influence of these dielectric changes, a key question is how much of the measured signal power is due to scattering from the penetrating, delayed portion of the signal as compared to the signal portion which simply reflects from the interface between the media and air.

4.2.1. Reflection and transmission at dielectric interfaces

The three most important factors in the engineering field of Soil Mechanics are idiomatically known to be water, water, and water. This extends to radar/microwave measurements of soil: Relative permittivity ε_r is introduced here as the key material parameter controlling microwave transmission and scattering for dielectric volumes such as soil. This section also describes water content as the key variable controlling ε_r for a volume of soil.

A technical definition of ε_r, the relative permittivity is provided here: As discussed in Section 2.1.1, transmission of an electromagnetic wave such as a microwave occurs via an electromagnetic field progressively exciting the space in is direction of travel. The amount of energy stored in a material (via polarisation of charged particles with in it) in response to the electric field is ε_r, a ratio relative to the amount of energy stored in a vacuum. Historically this value was termed the dielectric constant.

In the context of this work, ε_r affects how a wave propagates and scatters at interfaces. Variations in this single material parameter can affect the magnitude, direction,

polarisation, and phase of a microwave signal, as shown in Equation 4-1 through Equation 4-3. The sketch in Figure 4 3 gives an example geometry to help define terminology. For approximate values, dry matter in soils and vegetation generally have ε_r ~=3 at microwave frequencies, while water has ε_r ~= 80 (Hallikainen et al., 1985).

Another useful value to consider for a material is the refractive index, which is ratio between the speed of propagation in a vacuum and the speed of propagation in the material. The refractive index for a non-magnetic material is calculated as shown in Equation 4-1:

Equation 4-1: Refractive index in non-magnetic media

$$n = \sqrt{\varepsilon_r} = c/v$$

where the refractive index n can be given equivalently in terms of material properties or in terms of speed of propagation in the media, v, as compared to in free space, c.

The amplitude of an electromagnetic wave's electric field can be described by the Fresnel coefficients given in Equation 4-2, which depend on the polarization of a wave. The reflected or transmitted amplitude will be a factor of r and t compared to the amplitude of the incident wave. In electromagnetics, waves are traditionally described as having a 'P' polarized component that is parallel to the interface plane and an 'S' component that is perpendicular to the interface plane (from the German term "senkrecht" meaning vertical or perpendicular).

In satellite radar, a 'Horizontally' (‘H’) polarized wave has its electric field parallel to the Earth's surface but perpendicular to the sensing direction. On the other hand, a 'Vertically' (‘V’) polarized wave is perpendicular to both the horizontal polarization and the sensing direction, and it is oriented vertically to some degree relative to the Earth's surface. This geometry is sketched in Figure 4-4. The main imaging mode for Sentinel 1 emits 'Vertically' polarized waves and measures the return in both vertical and horizontal polarizations. The V polarisation will generally interact as an S wave.

Equation 4-2: Fresnel Coefficients (Born and Wolf, 1999)

$$r_S = \frac{n_1 \cos\theta_i - n_2 \cos\theta_t}{n_1 \cos\theta_i + n_2 \cos\theta_t}$$

$$t_S = \frac{2n_1 \cos\theta_i}{n_1 \cos\theta_i + n_2 \cos\theta_t}$$

$$r_P = \frac{n_2 \cos\theta_i - n_1 \cos\theta_t}{n_2 \cos\theta_i + n_1 \cos\theta_t}$$

$$t_P = \frac{2n_1 \cos\theta_i}{n_2 \cos\theta_i + n_1 \cos\theta_t}$$

where the subscripts of the refractive indices n refer to the medium and the subscripts of the reflected and transmitted amplitudes r and t refer to the polarisation with respect to the interface. These terms can be seen in Figure 4-3. The angle of transmission (direction of the transmission) θ_t is itself a function of the refractive indices as given by Snell's Law in Equation 4-3.

The t_S amplitude coefficients minus the r_S amplitude coefficient will equal 1, as an effect of conservation of energy. The sign of the r_S is negative when $n_2 > n_1$, which indicates a π shift in phase.

Equation 4-3: Snell's Law

$$\theta_t = sin^{-1}\left(\frac{n_1}{n_2} sin\,\theta_i\right)$$

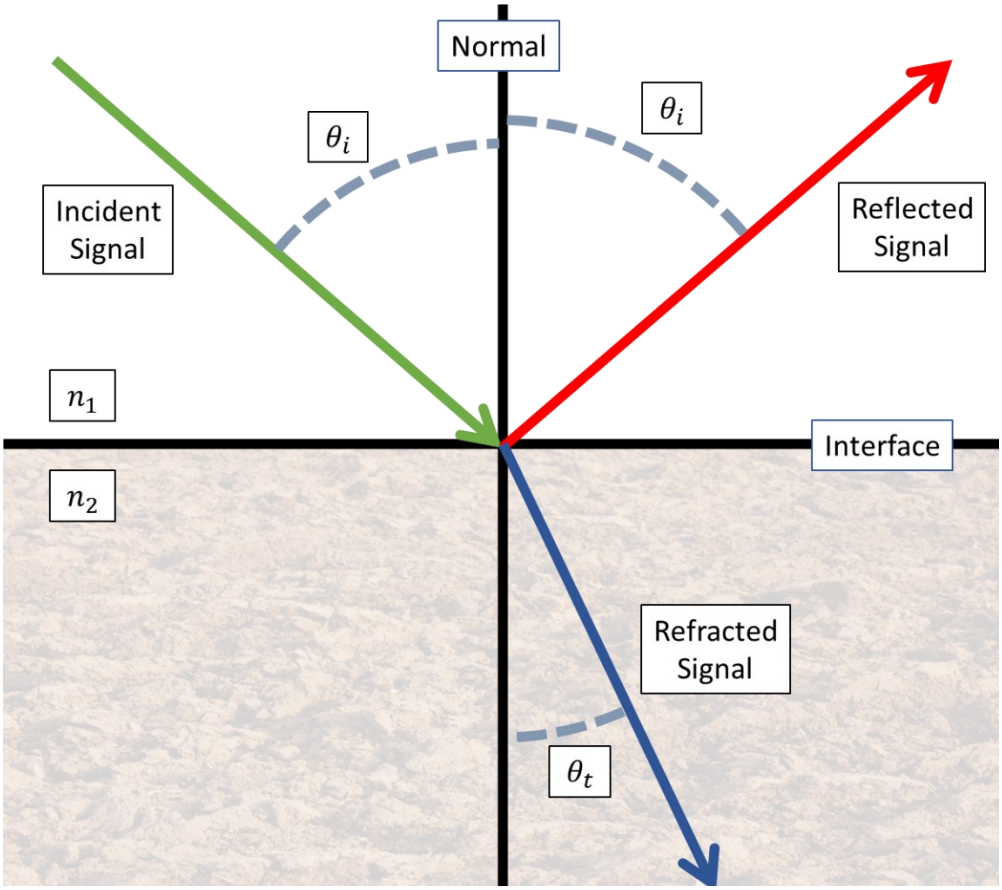


Figure 4-3: Sketch showing reflection and refraction at a dielectric boundary.

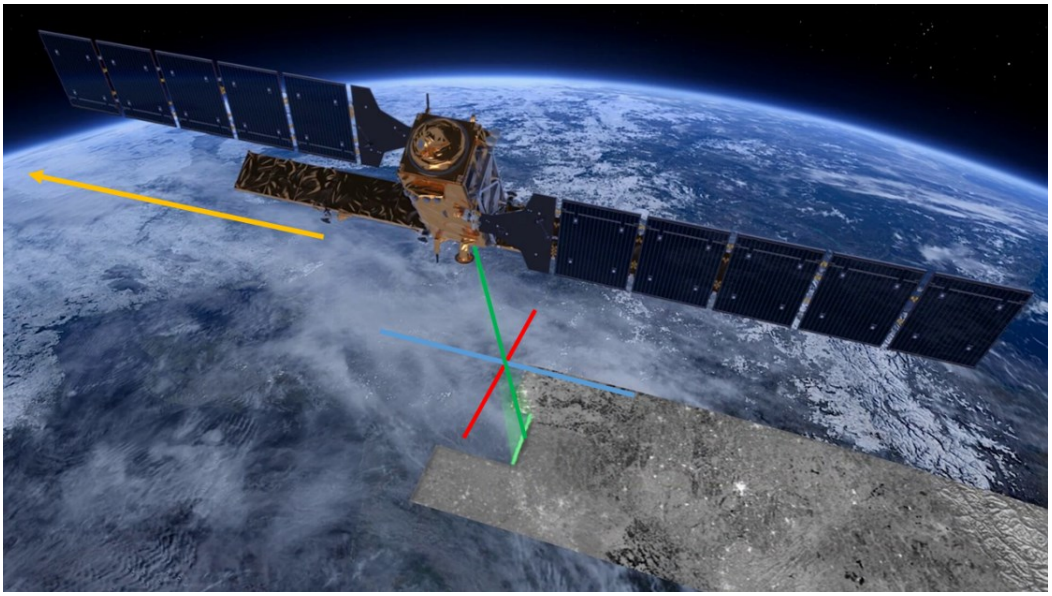


Figure 4-4: Orientation of polarised waves. The satellite's instantaneous velocity is in the axis given in yellow, while signals are emitted in the green line's axis, the Vertical polarisation (V) is measured along the red axis, while Horizontal (H) is measured in the blue axis. Sentinel image credit ESA.

For simple indicative numbers, a signal transmitting through a very wet soil of $\varepsilon_r = 25$ will be 1/4 of its amplitude after incidence from free space at an angle of 45°, as compared to around 3/5 for a thoroughly dry soil of $\varepsilon_r = 3$. It can be appreciated that for a dry soils or vegetative volumes the signals penetrating the media must be considered while for a high moisture content the surficial reflections are stronger.

The reality of radar scattering from volumetric media is much more complex than simple reflections and transmissions from a single interface described above. For a start, the examples above cannot describe how the signal is ultimately backscattered to the sensor without introducing new interfaces (barring the case where $\theta_t = 0$).

In a rural volume scatterer, every blade of grass or clod of soil acts as a dielectric interface that can interact with the radar signal. An individual photon returned may have undergone multiple scattering interactions by the time it has returned to the radar. The 3D orientation of the scatterers relative to the sensing direction will cause depolarization of the backscatter as compared to the 2D example above.

Finally, but perhaps not exhaustively, there are losses due to absorption in dielectric media. Overall, these factors make it challenging to fully explain radar scattering from volumetric media using simple concepts of reflection and transmission at flat interfaces. Going forward, it is useful to simplify scattering in terms of more general and macroscopic models and mechanisms that occur over a large population of cells, rather than try to model every blade of grass in an individual cell.

4.2.2. Scattering models

To examine how transient scattering behaviour can ultimately affect phase, we examine existing scattering models in literature. In SAR polarimetric analysis, Target Decomposition approaches are designed to identify independent scattering processes within sets of measurements. These decompositions are a key tool in understanding and interpreting the physical parameters of a scattering volume (Lopez-Martinez, Pottier and Cloude, 2005).

To some extent each of these models is an abstraction of complex geometric and material factors into a representation which has less mathematical terms than the number of observable variables. In SAR polarimetry, the available data channels are termed VV, HH and VH where the first letter is the emitted signals polarization and the second letter is the polarization of the receiving antenna. The cross-polarized measurement VH is equal to HV in practical situations. Additional observations can be produced by analysing the second-order statistics between channels over a spatial window.

While there are many scattering models (Lopez-Sanchez *et al.*, 2021) a straightforward and well cited example is the Freeman Durden "Three Component" (3C) model (Freeman and Durden, 1998). The 3C model separates polarimetric SAR observation into surface scattering, double-bounce scattering, and volume scattering. The mechanisms are sketched in Figure 4-5 and described as follows:

- Surface scattering, also known as single-bounce scattering, occurs when the radar signal is reflected directly from an interface orientated perpendicular to the direction of sensing. For DS, this occurs more commonly where a number of interfaces are spaced periodically such that the phase of their individual backscatter contribution is similar. The resulting sum of their returns forms the coherent SAR measurement. This is known as Bragg scattering.
- Double-bounce or dihedral scattering, whereby two planar features are orientated orthogonally to one another with the corner facing the sensor. An incident wave will reflect off one plane onto another before returning to the sensor, which creates a geometrically very similar path length and therefore very similar phase and a strong coherent return. Trihedral and further integer scattering arrangements are possible but not explicitly modelled in 3C.
- Volumetric scattering. A volume of randomly orientated scatterers are present at different optical depths. This produces depolarisation and is the only contribution of the 3C model which can explain cross-polar amplitudes and coherences.

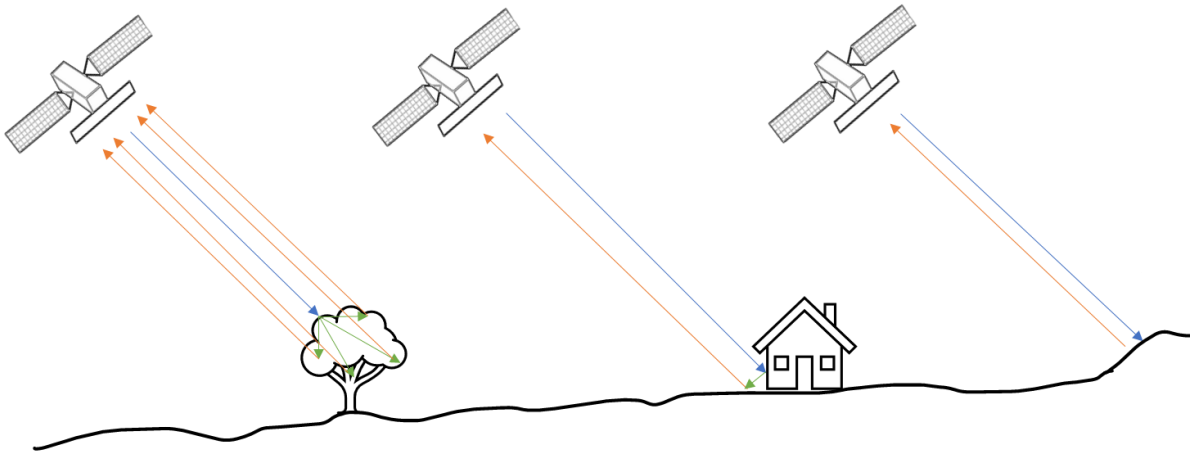


Figure 4-5: Volumetric, double-bounce, and single-bounce scattering

Figure 4-6 shows how these mechanisms can correlate significantly with land cover. Notably if the land cover changes over time, so too will the relative contribution of the scattering mechanisms. Each mechanism is assumed to have uncorrelated phase with the other mechanisms in the 3C model, which suggests a loss of InSAR coherence will accompany a change in the relative contribution from mechanism.

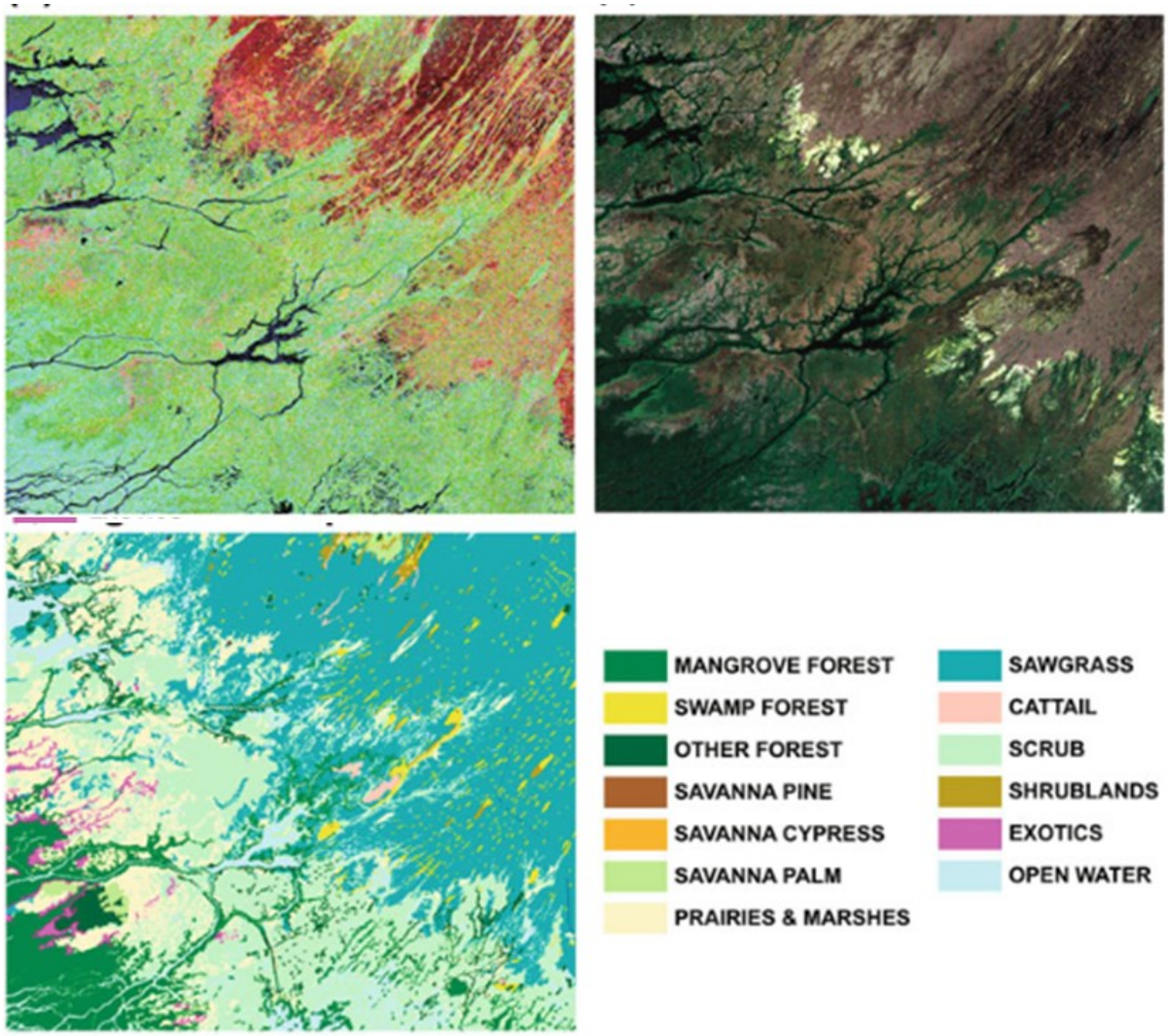


Figure 4-6: The Freeman Durden Three Component Model (3C) (Lopez-Sanchez *et al.*, 2021).

Each class of vegetation in the example of Figure 4-6 has a characteristic signature in the 3C model. Over time, the contribution can change, and thus the measured phase will shift from that of one mechanism to another.

4.3. Soil moisture

Figure 4-7 shows example measurements of a particular soil over a range of volumetric water content. The imaginary part of the relative permittivity dictates thermal losses as the wave travels through the media. A near linear relationship can be seen between water content and both the real and imaginary parts of the permittivity. An increase in moisture content therefore increases the reflection and absorption of the microwaves at the soil interface, while reducing transmitted energy and angle of transmission. The depth profile of the scattering and the signal phase propagation will vary as a result according to the Fresnel equations.

In the UK, soils generally reach saturation in winter months, and retain moisture throughout the year. The effects of soil moisture on SAR time series can hence be expected to have a similarly seasonal pattern.

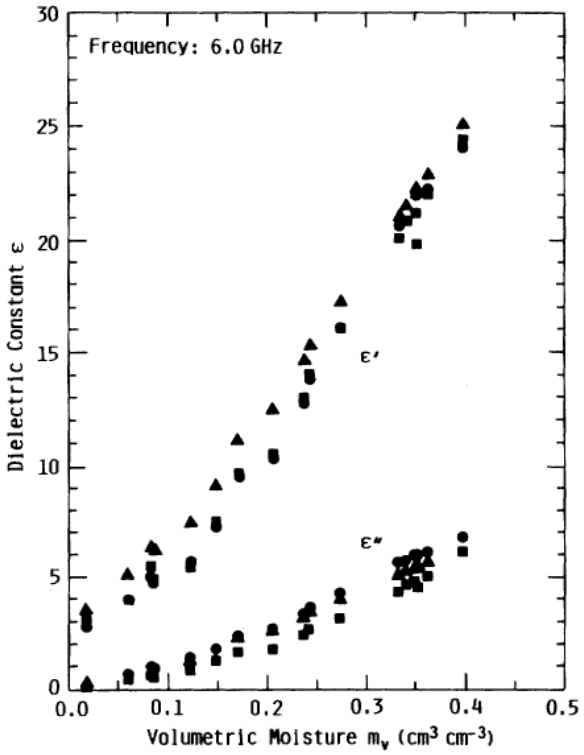


Figure 4-7: The empirically measured relationship between a loamy soil's volumetric moisture content, m_v. and its relative permittivity, ε (Hallikainen *et al.*, 1985). Physical parameters of a soil control both its in-situ moisture retention characteristics and its dielectric relationship.

Modelling this dielectric moisture-sensitivity on remote sensing scales raises additional challenges. Soil properties such as parent material and texture affect the permittivity, with the proportion of sands and clays being noted as particularly important. The in-situ spatial variability of these properties makes it difficult to development a universal model for SAR-based soil moisture measurements.

Further, extant studies have for practical purposes employed sample preparation activities such as oven drying and grinding. These activities can be expected to affect soil volume, chemistry, and particle size distribution and therefore its bulk dielectric properties compared to original undisturbed in situ values.

4.3.1. SAR measurement of soil moisture

Radar time series have been suggested and applied in soil moisture measurement since the 1970's (Ulaby and Batlivala, 1976; Ulaby, Batlivala and Dobson, 1978). More recently the advantages of SAR platforms in providing regional scale mapping and regular updates via satellite has caused considerable interest (Ulaby, Dubois and van Zyl, 1996; Shi *et al.*, 1997; Oh, Sarabandi and Ulaby, 2002; Kornelsen and Coulibaly, 2013). Until recently, the co-polarised SAR amplitude (e.g. VV, HH) has been used almost exclusively.

The relatively low information content of co-polarised SAR amplitude (See 4.2.2) has led to a wide variety of approaches attempting to resolve the approximately linear relationship between volumetric water content and soil relative permittivity, with the far more complex and non linear realities of natural scattering. Despite there being a great many studies fitting empirical models to observations these have been observed to be only valid to the particular surface conditions and radar parameters at time of experiment (Kornelsen and Coulibaly, 2013; Petropoulos, Ireland and Barrett, 2015). Given that many of these empirical studies only use a single region to fit their empirical models, the transferable accuracy and hence value of the empirical fits should be subject to scrutiny.

Analytical models perhaps show more promise as a general approach for regional studies, yet are challenged by the number of parameters required to model the complex

scattering behaviour (Kornelsen and Coulibaly, 2013; Petropoulos, Ireland and Barrett, 2015). The low information content of a single SAR amplitude channel should hence be considered. Recent studies have separately sought to include additional data: optical data (Prakash, Singh and Pathak, 2012), multiple polarisations (Hajnsek *et al.*, 2009), and interferometric coherence (Moeremans and Dautrebande, 2000; Barrett, Whelan and Dwyer, 2012) There have been few if any studies attempting to combine all of this potential information holistically, perhaps limited by a lack of available data of sufficient quality.

4.3.2. Soil moisture in interferometry

Despite difficulties in direct measurement of soil moisture there evidently remains a relationship between moisture content and scattering, and therefore we should examine potential effects on InSAR phase. A number of potential mechanisms exist whereby the interferometric signal can be affected, as will be explored.

Fewer studies have been performed into InSAR sensitivity to soil moisture as compared to SAR amplitude. However, interferometric effects corresponding to moisture changes have been noted in literature (De Zan *et al.*, 2014) as extant across a range of satellites, airborne platforms, and laboratory experiments (Barrett, Whelan and Dwyer, 2012; Nesti *et al.*, 1998; Nolan, Fatland and Hinzman, 2003; Zhang *et al.*, 2008; Hajnsek and Prats, 2008). A range of hypotheses for this moisture-sensitive phase have been proposed (Zwieback, Hensley and Hajnsek, 2015), including soil swelling, penetration depth, and dielectric mechanisms.

4.3.2.1. Swelling

Initial observations of moisture-sensitive phase hypothesised a clay shrink-swell mechanism, whereby the signal path length would be shortened by vertical upward swelling of the ground. Whilst clay shrink swell is a significant and widespread phenomena, and undoubtedly causes a measurable phase (Harrison *et al.*, 2012; North

et al., 2017), there are a number of aspects to the moisture-sensitive phase that cannot be explained by this mechanism. Particularly the decorrelation of the signal (Nesti *et al.*, 1998), polarimetric phase differences (Hensley *et al.*, 2011; Zwieback and Hajnsek, 2016), closure phases (De Zan, Zonno and Lopez Dekker, 2015). Often the sign of the observed phase is opposite to that of a vertical upward motion from swelling of clay (De Zan *et al.*, 2014).

Critically a moisture-sensitive phase can be observed in areas of limited or no clay, and can equate to several centimetres of deformation in many situations where this is implausible (Zwieback, Hensley and Hajnsek, 2015; Hensley *et al.*, 2011). This is especially apparent at longer wavelengths such as L band and P band. Morrison (Morrison *et al.*, 2011) measured shifts of >π at C-band in sand (equivalent to roughly 3cm) while verifying that the movement was only around 1mm using high resolution digital image correlation.

4.3.2.2. Penetration depth

Morrison proposed that increasing moisture content limits the penetration of the wave into the soil, and thus shortens the apparent path length. There are a number of problems with this hypothesis. Firstly, while an increase in moisture will cause the radar wave to be absorbed over a shorter distance (as related to the imaginary part of the permittivity (Hallikainen *et al.*, 1985), see Figure 4-7) there will be a corresponding increase in the real part of the wavenumber and therefore the phase will advance at a much greater rate per unit distance. The total effect is thus opposite to this idea.

Further, a change in the absorption rate in isolation would have limited effect on the phase of the backscattered signal. For the distributed (volumetric) scatterers under study here the SAR measurement is the coherent sum of backscattered fields from over the entire volume. For elemental scatterers to contribute to the measurement they must be correlated with one another. Changing the absorption rate changes the weights of existing scatterers, but without affecting the phase the correlation between these will not change. Changing penetration depth therefore only causes illumination of a different set

of scatterers, a mechanism by which the sets of scatterers are correlated is required for a measurable phase shift.

4.3.2.3. Dielectric

In a situation where the measured scattering is produced by buried scatterers, the wave travels some distance through the soil. As the refractive index of the soil is higher, so too is the wavenumber. The phase of the signal advances at a greater rate per unit distance as compared to travelling in the atmosphere, as illustrated in Figure 4-8. For brevity this has been termed a 'dielectric mechanism' for soil moisture changes to effect interferometric phase, as first termed in literature (Zwieback, Hensley and Hajnsek, 2017).

A uniform soil media would simply absorb the penetrating portion of the wave, so it is assumed that for scattering to be observable there are inhomogeneities in the soil, be they clods (Zwieback, Hensley and Hajnsek, 2017), air gaps, rocks, or inhomogeneous water (Rabus, Wehn and Nolan, 2010), and the backscattering is generated from these.

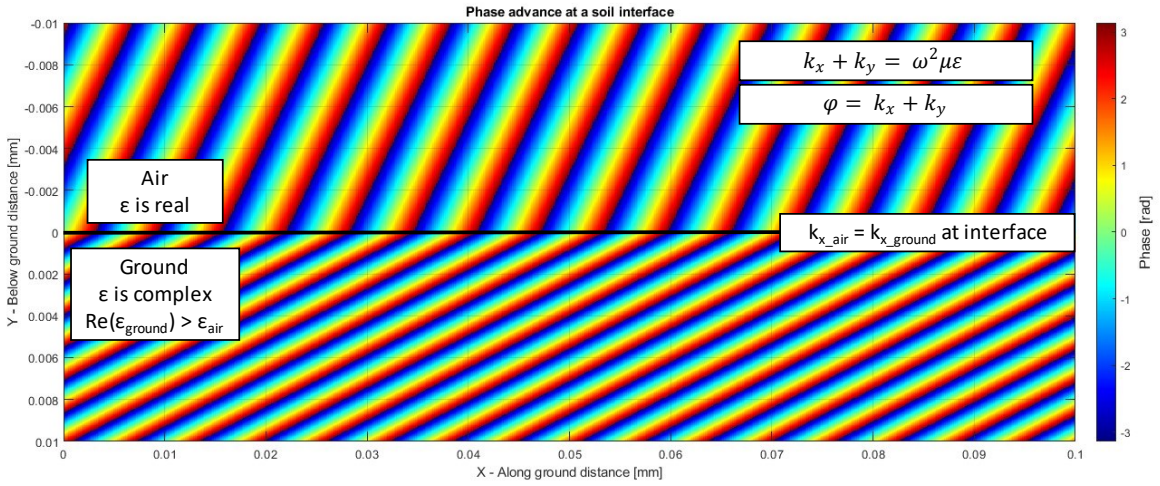


Figure 4-8: The propagation of a microwave in a soil media, in terms of the wavenumber and wave equation, from (De Zan *et al.*, 2014). The phase advances more quickly per unit distance in the soil, owing to its greater permittivity.

Figure 4-9 shows example values for phase and coherence magnitude calculated using the De Zan soil moisture model comparing the interferometric response between sandy soil and a uniform scattering profile (which defines the how the scattering cross-section

varies with depth). The scattering profile is separate to the attenuation of the wave itself as it travels through the lossy soil media. The wave attenuation occurs in the wavenumber calculation, resulting from the imaginary part of the complex permittivity values seen in Figure 4-7.

As a result of the waves attenuation with depth, and it's initial lack of a propagation phase shift at the soil interface where the wave is strongest, the interferometric phase shift does not exceed $\pi/2$ regardless of the soil properties.

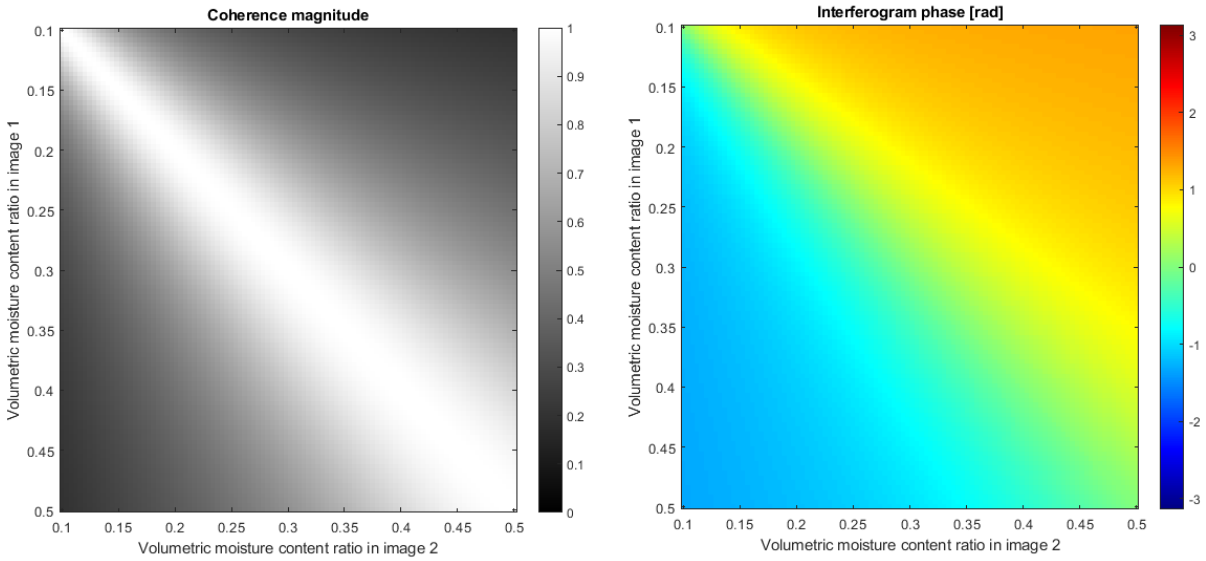


Figure 4-9: Example interferometric phase shift predicted as a result of a difference in soil moisture content, assuming C-band radar and a sandy soil with a uniform distribution of inhomogeneities with depth, following (De Zan *et al.*, 2014).

4.4. Transient scattering in vegetation

The exploitation of amplitude (Craig Dobson, Ulaby and Pierce, 1995) and coherence (Blaes and Defourny, 2003) trends for distinction of vegetation has long been practiced, while systematic phase effects caused by vegetative evolution are commonly observed, an example of which may be seen in Figure 4-10. A regression study of AGRISAR campaign data found that VV interferometric phase was positively correlated with an increase in vegetative biomass over 29 of 32 field areas (Zwieback, Hensley and Hajnsek, 2015). Systematic phase effects appear to vary considerably between different land covers while being much more constrained within areas of similar crops – as can be seen in the very tight distribution of biomass-driven phase offsets for cereals in that study (Zwieback, Hensley and Hajnsek, 2015).

The effect can be well observed in regions with extensive agricultural fields. Figure 4-10 shows significant phase shifts and loss of correlation in a Sentinel 1 Orbit number 63 interferogram from Winnipeg, Canada taken between 23 Jan 2020 and a scene 12 days later.

Microwaves penetrate vegetation to some degree and are thus sensitive to their dielectric as well as geometric properties (Ulaby, Batlivala and Dobson, 1978; Mandal *et al.*, 2020). This is depicted diagrammatically in Figure 4-11. Water content is a key parameter, as for soils: one treatment suggests that the vegetation can be modelled as an equivalent volume of water vapour (Attema and Ulaby, 1978). Experiments have shown clear correspondence between the interferometric phase and the phenological and morphological state of vegetation (Zwieback and Hajnsek, 2016).

The existence of vegetative transient scattering can subsequently bias MTI deformation results. Results in literature demonstrate a relationship between vegetative height or biomass and phase, with increasing vegetative height or biomass producing the same phase trends as produced by scatterers moving away from the sensor (Zwieback, Hensley and Hajnsek, 2015; Zwieback and Hajnsek, 2016).

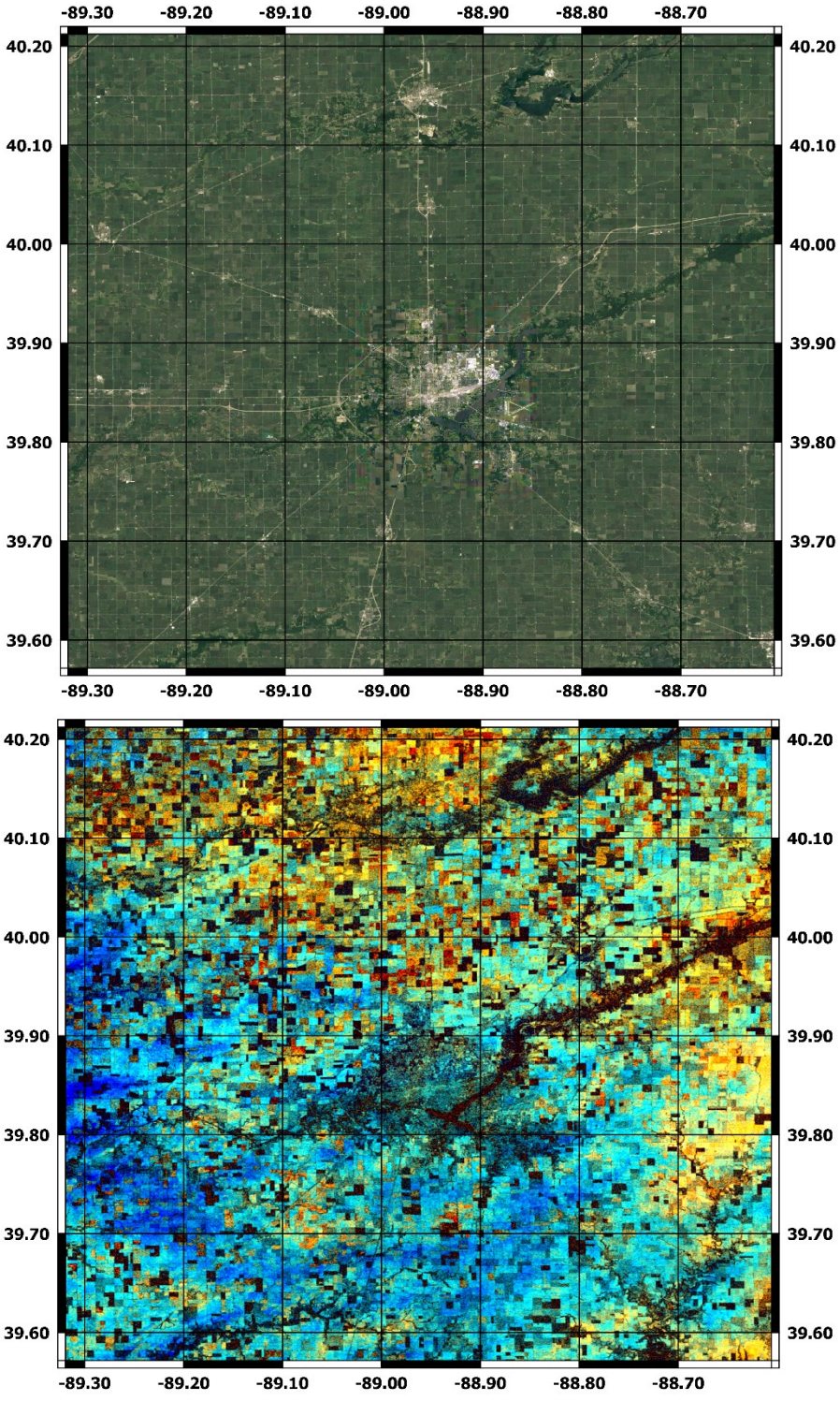


Figure 4-10: [Top] Sentinel 2 optical satellite image showing the extensive agricultural area around Winnipeg, Canada [Bottom] Sentinel 1 C-band interferogram the area. The scene dates are 23 January 2020 and 4 February 2020. A rectangular multi-look of 4 in azimuth and 20 in Investigation has been applied. The colour axis shows phase in the range $[-\pi, \pi]$, while the brightness corresponds to the spatial coherence.

A possible explanation is that scattering from the vegetative canopy is rarely coherent between satellite images. Owing to movement and evapotranspiration (De Zan, Zonno and Lopez Dekker, 2015). This can be evidence of greater rates of InSAR coherence loss in rural areas when using higher-frequency (less penetrating) microwave systems. The scattering phase from vegetative canopies can change in timespans of just a few hours (De Zan, Zonno and Lopez Dekker, 2015) as compared to the 6-12 day repeat imaging from Sentinel 1. If scattering from the canopy rapidly loses coherence it is unlikely to contribute to long-term temporal trends in MTI stacks.

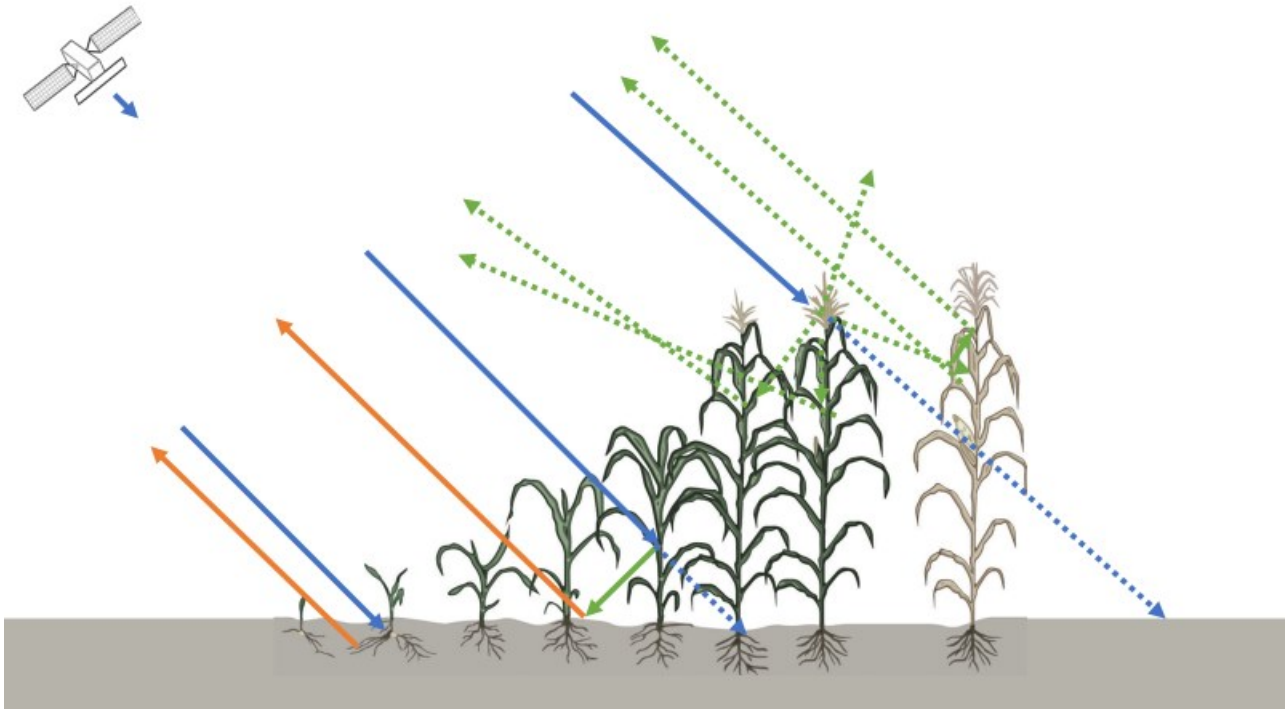


Figure 4-11: Potential mechanism for stratified scattering from the canopy and ground in vegetated areas, developed from (Zwieback and Hajnsek, 2016) to suggest how scattering mechanisms may shift as vegetation grows. The diffuse volumetric scattering from the fully developed crops can be appreciated as highly sensitive to geometry and moisture content of the canopy.

4.5. Isolating transient scattering phase

Persistent Scatterers are quantifiable as stable in terms of their scattering behaviour. The high coherence and amplitude stability values that identify them grant statistical evidence that there have been limited changes in the scattering throughout the image series (Ferretti, Prati and Rocca, 2001; Crosetto *et al.*, 2016). Subsequently, interferometric phase shifts measured over these scatterers cannot be attributed to significant scattering changes. Although some noise is still present in their measurements, PS exhibit higher stability in terms of both spatial and temporal interferometric coherence as compared to non-PS.

A subset of non-PS suspected to have undergone scattering changes can therefore be investigated in terms of interferometric phase shifts with reference to proximal PS. If the subset of non-PS is selected based on some criteria that concerns their scattering, significant shared phase offsets between this subset and the PS indicate the selection criteria is correlated with the phase offsets. Firstly, it is useful to define how the subset of non-PS can be calibrated against the reference phase of the PS, while secondly it will be useful to quantify what a significant difference might be.

Traditionally the phase contribution from inconsistent scattering has been assumed to be a zero mean gaussian noise. More recent evidence shows that scatterers phase may vary progressively due to gradual processes, such as growth of vegetation or accumulation of moisture content. The scattering is therefore 'transient' in that the scattering response and its phase may change over time. A 'transient scattering' phase term can be introduced into the traditional model for InSAR phase (Ferretti, Prati and Rocca, 2001), to account for non-zero mean scattering contributions. The resulting model is shown in Equation 4-4:

Equation 4-4: Model for estimating the transient scattering phase

$$\varphi_{TS} = \varphi - \left(\varphi_{defo} + \varphi_{topo} + \varphi_{atm} + \varphi_{noise}\right)$$

where φ_{TS} is a new term accounting for non-zero mean scattering, φ_{defo} is phase change due to uniform displacement of the scatterers, φ_{topo} is due to topographical differences (a.k.a. 'height error') between the observed scene and a reference DEM used to correct for range differences due to sensor baseline, φ_{atm} is due to differential propagation in the atmospheric phase screen (APS), and φ_{noise} is phase decorrelation due to instrument noise and clutter. After removing the various known or estimated phase factors, this quantity is sometimes termed the calibrated phase in literature (De Zan *et al.*, 2014).

If the scattering behaviour does not change, such as in the case of a PS, then the expected value for φ_{TS} will be zero. Individual phase measurements may vary due to noise, but these remaining noise terms after isolating scattering effects are still assumed to be zero mean (Agram and Simons, 2015), while over a larger population the mean will tend towards zero assuming an unbiased estimation of the terms.

Hence by taking a subset of Distributed Scatterers (DS) from within a SAR image stack, calibrating the phase (see Equation 4-4), and then calculating the mean phase offset, we can investigate the presence of non-zero φ_{TS} and therefore evidence that scattering changes are predictably biasing the MTI time series. The subset might be chosen on some *a priori* knowledge about the presence of particular crops as explored in Section 4.6, or by some shared patterns in other scattering metrics such as amplitude, as explored in Chapter 5. The resulting coherence is termed the 'Subset of Scatterers Coherence', γ_S, as defined in Equation 4 5:

Equation 4-5: The coherence of interferometric phases in a subset of scatterers

$$\gamma_S(k) = \frac{1}{N_k} \sum_{i \in S_k}^{N_k} e^{-j\phi_{TS}}$$

where S_k is the set of DS in cluster k, N_k is the number of DS in that set, and $\phi_{TS}$is the calibrated phase of the DS at index i in the set, S_k. Phase signals of low spatial frequency such as due to orbital errors are here assumed to have been interpreted as components of the APS and removed during phase calibration. Similarly, changes due to decorrelation

and dissimilar height error or deformations should generally cancel to zero after calibration where N_k is high. Remaining phase offsets which are correlated over the subset of DS, S_k, suggest an additional factor in the phase model that is hard to account for without acknowledging the scattering criteria used to separate this subset.

The estimator in Equation 4-5 does not use amplitude values, unlike the standard coherence estimator shown in Equation 2-15. Rather, the estimator for γ_S is similar in form to the estimator used for temporal coherence shown in Equation 2-16. While weighting samples by their power could theoretically increase accuracy in estimating the SAR signal, in practice the pixels in SAR images often measure objects that are temporarily present in the resolution cell with much higher amplitude such as vehicles or clutter due to aircraft or nearby buildings. These intrusive amplitude values can be extremely high and skew the phase estimation. Therefore it was decided, for simplicity, to focus on the average phase rather than the average signal.

The absolute value of the Subset of Scatterers Coherence, $|\gamma_S|$, is a useful metric for the correlation of the phase across the cluster. A high value implies a good explanation of the phase anomalies by some quality of the chosen scattering subset. A low consistency implies that there may be no deterministic relationship between the subset criteria and the phase offsets.

The value for $|\gamma_S|$,can be processed into an estimate of how the mean phase over the subset may vary, given the number of samples, under the assumption that the errors are zero-mean phase offsets due to scattering changes. The actual measured mean phase can then be compared to the range of likely values which would occur if the phase shifts attributable to scattering are zero-mean.

Assuming the errors remain gaussian, albeit offset by a particular value, the significance of a given phase offset as compared to a zero-mean error can be calculated as given in Equation 4-6. The measured error should first be standardised into a '*Z*-score' before conversion into a corresponding probability of arising in the normal distribution using the error function:

Equation 4-6: Estimate of the probability for a give phase offset under a zero-mean phase model hypothesis.

$$\hat{Z} = \frac{\hat{\varphi}_{TS}}{\sqrt{\hat{\sigma}_{TS}{}^2}}$$

$$P(Z > \hat{Z}) = \frac{1}{2}\left[1 + \mathrm{erf}\left(\frac{\hat{Z}}{\sqrt{2}}\right)\right]$$

where 'erf' is the error function, Z is known as the Z-score or standard score, while the hat accent denotes a measurement. $P(Z > \hat{Z})$ gives the probability of this value occurring in a zero-mean gaussian distribution.

The significance measured in this way will vary from interferogram to interferogram. If a $\hat{\varphi}_{TS}$ measurement is particularly noisy (such as due to high uncertainties in calibration or complete decorrelation) then $\hat{\sigma}_{TS}{}^2$ will be great while $\hat{\varphi}_{TS}$ will be difficult or impossible to unwrap ($\hat{\varphi}_{TS} > \pi$), leading to low error scores. The phase for DS may also be similar to that of PS in certain interferograms, perhaps as a result of minimal changes or effects in vegetative cover or moisture contents between the image dates. It is therefore appropriate to assess the significance over many or all available interferograms to better characterize how transient scattering affects the measurements over the entire period of study. A high mean significance of phase offsets should be useful in identifying where cluster-specific phase offsets can be identified as distinct from other sources of phase error.

Equation 4-7: Significance of a set of interferograms

$$\zeta = \frac{1}{N_{ifg}}\frac{1}{N_S}\sum_{i1=1}^{N_{IFG}}\sum_{i2=1}^{N_{DS}} Z$$

Through the combination of numerous individual error sources over numerous individual fields the combined error distribution can be approximated as gaussian under the central limit theorem. The statistical significance of a distribution of systematic offsets can

therefore be quantified by comparing the Z values from a sample of interferograms with the chi squared distribution, which is the distribution for a sum of squared, standardized (scaled in magnitude such that their standard deviation is 1) normally distributed variables such as the Z scores here. . A simple approach is shown in Equation 4-8:

Equation 4-8: Total significance of offsets over a set of interferograms, for a subset of DS selected based on their distinct scattering behaviour

$$X^2 = \sum_{i_{ifg}}^{N_{ifg}} Z^2$$

$$\alpha_Z = f\left(X^2, N_{ifg}\right)$$

where α_Z is the significance, found for X^2 using the inverse chi-squared distribution with N_{ifg} degrees of freedom, equal to the number of interferograms.

It is worth exploring other potential phenomena which could introduce non-zero phase errors into the phase after calibration.

Firstly, if the scatterers under analysis are situated local to one another in the area of interest, there is a possibility that a non-zero mean phase can be introduced by localized errors in e.g. APS estimation. The potential for correlated errors in APS estimation producing a common error can be estimated as follows:

- The APS is interpolated from PS. Error in the APS estimation is a combination of error in the underlying data and error due to interpolation from sparse points.
- An APS estimate using kriging (Meyer *et al.*, 2005; Kirui *et al.*, 2021) is simply a weighted combination of the phases from the PS, with the weights at each point varying based on distance and reliability of the individual 'training' PS phases.
- Where DS are localized, they will rely on the same PS for their interpolated APS estimate. Hence an error in one PS can affect multiple DS. The contribution of this error depends on the weight of other PS.

In practical terms, a large population of DS with APS estimates determined by a number of distinct PS will minimize the contribution to the mean from errors in individual noisy

PS. Where the DS are distributed over distances beyond the correlation length of the APS, the contribution to the mean value from correlated interpolation errors will also be minimized.

Other potential localized errors can be treated much the same as the APS. Orbital errors are generally correlated over much larger distances and observed as a ramp in the APS which is removed. DEM errors are usually small (Rodríguez, Morris and Belz, 2006) and correlated over much smaller distances as compared to the APS. Any long wavelength errors in the DEM will manifest as long wavelength errors in the phase which will be misinterpreted as APS but nevertheless removed effectively from the other terms by standard InSAR processors.

A further potential source of non-zero mean phase may occur if all scatterers within a set share the same deformation behaviour. Seasonal soil related deformations such as clay-shrink swell may therefore be misinterpreted as scattering-related phenomena. This is a significant limitation of the approach presented here, to be aware of. Deformation behaviour that is not shared by the subset of DS will however be preserved.

Some phenomena, such as regional tectonic activity, may affect large proportions of the scatterer set. In many cases these long-wavelength deformation phenomena will affect PS as well as DS and therefore will be extracted during the course of calibrating the data using the local PS population. In situations where the calibration is poor, due to a lack of nearby PS or deformation phenomena esoteric to the set of DS as described previously, then the subsequent estimation of transient scattering phase may unintentionally include long-wavelength deformation phase contributions. The ultimate effect upon the analysis is hard to predict without knowledge the geospatial arrangement of PS/DS set and the rates and extent of the specific deformation process.

Further analysis focusing on regression of the scattering phase with other indicators such as changes in coherence or closure phases may yield further separation of the true deformation effects from the transient scattering phase, as explored in Chapter 5.

In cases of relatively few DS where the errors may potentially result from correlated error in, e.g. localised fluctuations in the APS or correlated deformation, the deviation from zero-mean behaviour can still be examined.

As the estimators here are investigating the presence of mean phase offsets beyond the traditional model, it makes sense to model the various inherent error sources in estimating the terms of the model. The error budget for each DS used in a cluster analysis is given in Equation 4-9:

Equation 4-9: Combined error variance of the calibrated phase

$$\sigma_{TS}{}^2 = \sigma_{defo}{}^2 + \sigma_{topo}{}^2 + \sigma_{atm}{}^2 + \sigma_{noise}{}^2$$

where $\sigma_{factor}{}^2$ indicates the variance of a particular factor in the phase mode. The error budget can be calculated to estimate the expected phase error for each DS for each interferometric pair. The error analysis of individual DS then provides an *a posterior* estimate of error in the overall population. This error budget has two key implications. Firstly, the estimate of transient scattering phase for a class can be improved by weighting the input data according to their expected errors as given in Equation 4-10:

Equation 4-10: Weighted estimation of the coherence in phase over a subset of scatterers

$$\gamma_{mv}(k) = \frac{\sum_{i \in S_k}^{|S_k|} \left(\frac{e^{-j\phi_{TS}}}{\sigma_{TS}{}^2} \right)}{\sum_{i \in S_k}^{|S_k|} \left(\frac{1}{\sigma_{TS}{}^2} \right)}$$

Secondly, the inverse of the expected variance due to calibration error can be used to appropriately calculate the significance of $\gamma_{mv}(k)$ as compared to the assumption that $arg(\gamma_{mv}(k)) = 0$ as in the case where scattering changes have no effect on the mean interferometric phase.

It is worth exploring potential approaches toward calculation of the error variance terms. The error in APS estimation can be calculated as a result of the Kriging interpolation process discussed in Section 3.3.5. Errors due to topography might be estimated from *a priori* knowledge of the specific DEM used to calibrate the data, adjusting the standard deviation of height error in the DEM (Rodríguez, Morris and Belz, 2006; Mukul *et al.*, 2017) into equivalent phase error using the factor described in Section 3.3.6. More general phase noise variance may be estimated from measurements of interferometric coherence or amplitude dispersion as discussed in Section 2.4.7 and 3.3.4. This is however difficult due to bias in coherence estimation and variance of amplitude dispersion metrics where signal-to-noise ratios are low (Touzi *et al.*, 1996; Hooper, 2008). Estimating the deformation phase variance is further challenging, without reliable *a priori* knowledge of the deformation phenomena in an area on a DS-by-DS basis. Results shown in Sections 4.7, 5.5.5, and 6.3 however show that the magnitude of transient scattering phase offsets are far larger than the deformation phenomena of interest to this work. While *a priori* estimation of $\sigma_{TS}{}^2$ is therefore plausible, there are a number of extant difficulties and uncertainties.

4.6. Investigation

An MTI analysis was performed to demonstrate the presence of transient scattering phases and investigate the potential mechanisms that produce them. To this end we investigated the relative contribution of soils and vegetations through use of a priori maps of soil type and crop cover.

The Vale of Glamorgan South Wales, United Kingdom was chosen as an agriculturally fertile area with a broad variety of crops. The vale's limestone bedrock contributes to its nutrient-rich soils. Repeated glaciation has flattened the topography of the area, through erosion and deposition. The vale is a low-lying region with gently rolling hills and shallow valleys, known as cwms. The influence of topography and topographic phase errors in the InSAR processing is subsequently limited.

The area of interest is shown in Figure 4-12, with the optical imagery showing this is a highly vegetated area with numerous urban centres interspersed, allowing for PS to be found (Plank, Singer and Thuro, 2013) and facilitate accurate calibration of the APS. The relatively low-wavelength changes in topography over the lowland agricultural area can be seen in the DEM in Figure 4-13, minimising the contribution of topographic errors in the calibration while implying that slope movements will be minimal such as compared to the steep, looser materials found in the Brecon Beacons mountain range to the north of this area.

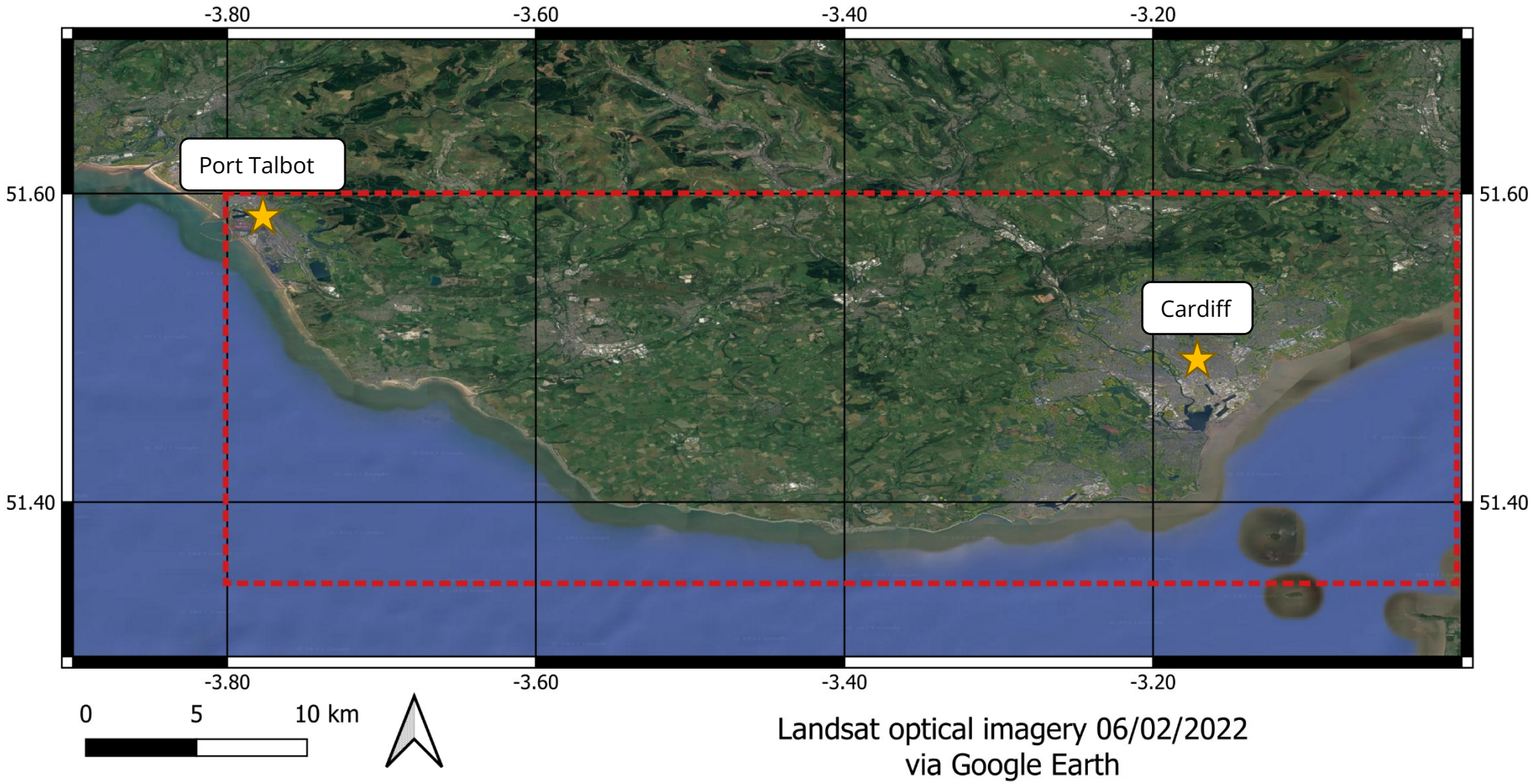


Figure 4-12: Optical imagery for the area of interest in the Vale of Glamorgan, shown encapsulated by the red polygon. The area can be seen here and in

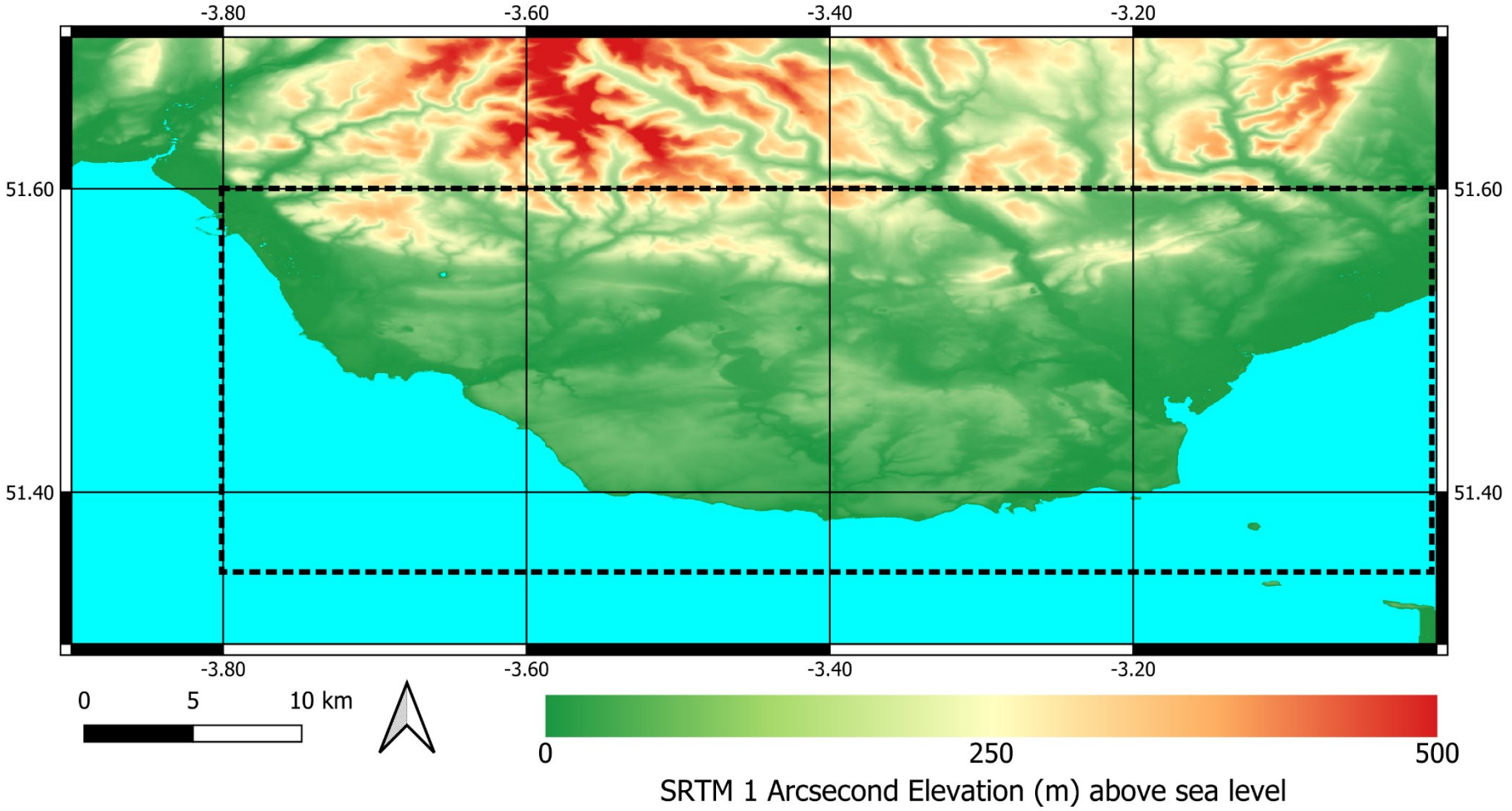


Figure 4-13: Topographic elevation for the area of interest in the Vale of Glamorgan, given by the black dotted polygon.

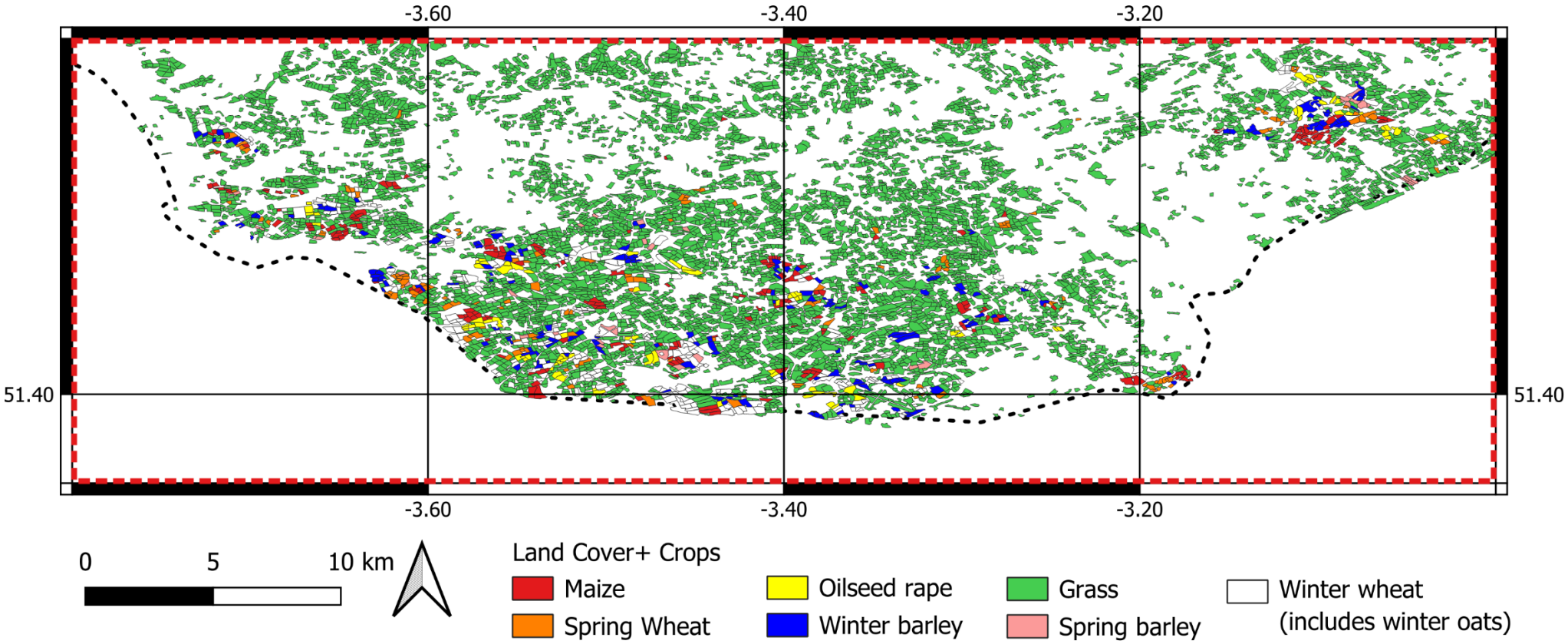


Figure 4-14: Crop polygons used, via the UKCEH Land Cover® plus: Crops dataset (UK Centre for Ecology and Hydrology, 2018)

4.6.1. Land cover data

The phase behaviour of different crops was investigated to analyse relationships between scattering behaviour and interferometric phase in agricultural fields. This was performed in order to test the hypothesis that the crops present in an area and their change in biomass had a significant influence on the measured interferometric phase, as indicated in literature (Zwieback and Hajnsek, 2016).

Independent *a priori* maps of cropping patterns from the UK Centre for Environment and Hydrology (CEH) (UK Centre for Ecology and Hydrology, 2018) were used to separate out samples from the SAR image stack corresponding to individual agricultural fields. The field boundaries and UKCEH Land Cover® plus: Crops classifications relied upon can be found in Figure 4-14. For brevity we will henceforth refer to this as 'the land cover data'.

4.6.2. Methodology

Geocoded polygons for each field in the UKCEH data were extracted and back-geocoded into SAR coordinates of azimuth and range. Corresponding samples in azimuth and range were used as a window in order to calculate a sample coherence matrix for each agricultural field. These measurements of interferometric phase were subsequently calibrated by subtracting the atmospheric phase screen estimated via a persistent scatterer interferometry analysis. The use of PSI ensured that the APS was calculated from scatterers which are unlikely to undergo significant transient behaviour, being subject to an amplitude stability filter and coherence filter. The calibrated interferometric phase is hence a measure of the difference in phase between persistent scatterers and the distributed scatterers of each agricultural field.

Section 4.5 discussed difficulties in weighting each DS sample measurement according to the calibration error, and therefore a simpler approach was taken for this initial analysis. Transient scattering phase was estimated by simple averaging of the normalised phase of the coherence matrix as shown in Equation 4 5.

4.7. Results

The results of the investigation are shown in Figure 4-15 through Figure 4-20, and focus on various aspects of the interferometric coherence matrix which is used extensively by MTI processing techniques for measurement of ground deformation. Coherence matrices were formed for each crop, after calibrating the data. Quantities were then analysed over subsets of the crops selected based on crop classification in the land cover data. Analysis of the results is provided in Section 4.8.

Data was analysed for the 6 major types of vegetation for which a representative (>20) number of fields were present in the land cover data. The data classification of the crops in the land cover data is grass, maize, spring wheat, spring barley, winter wheat (including winter oats), and winter barley.

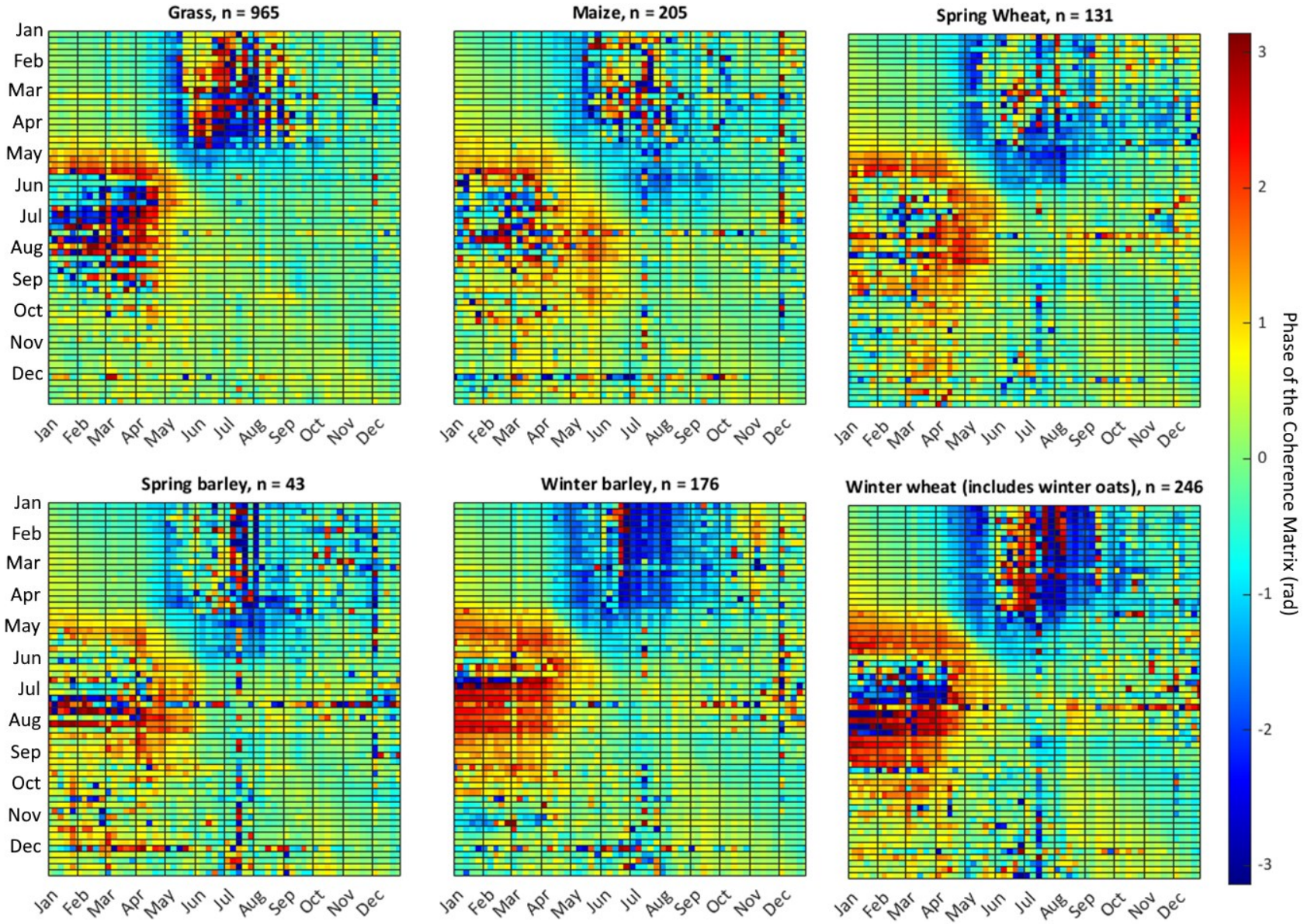


Figure 4-15: Phase of the mean coherence matrix measured from crop subsets after calibration for non-scattering errors, the argument of $\gamma_S(k)$.

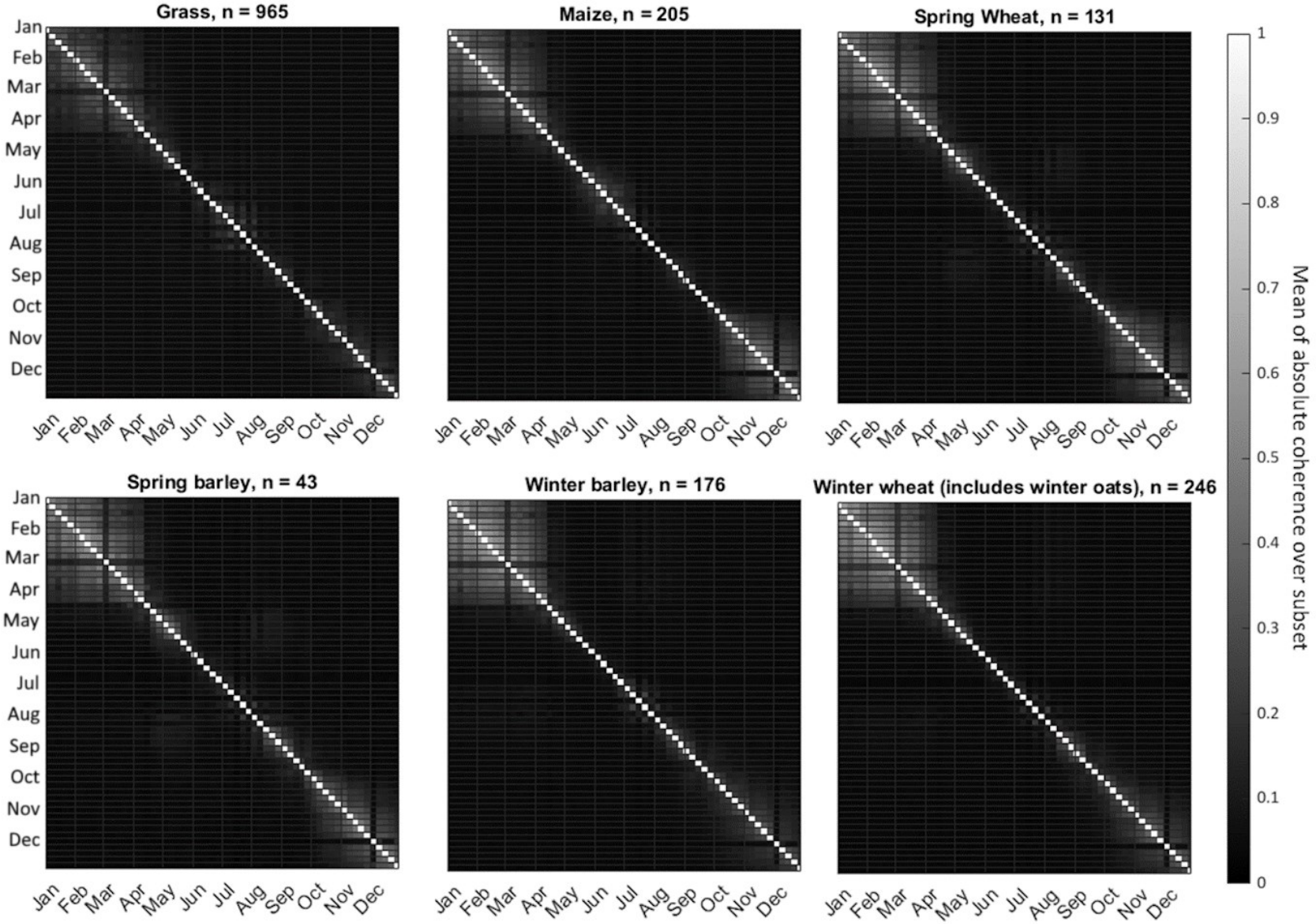


Figure 4-16: Mean absolute coherence of the coherence matrices for DS corresponding to each field in the Land Cover+ Crops data.

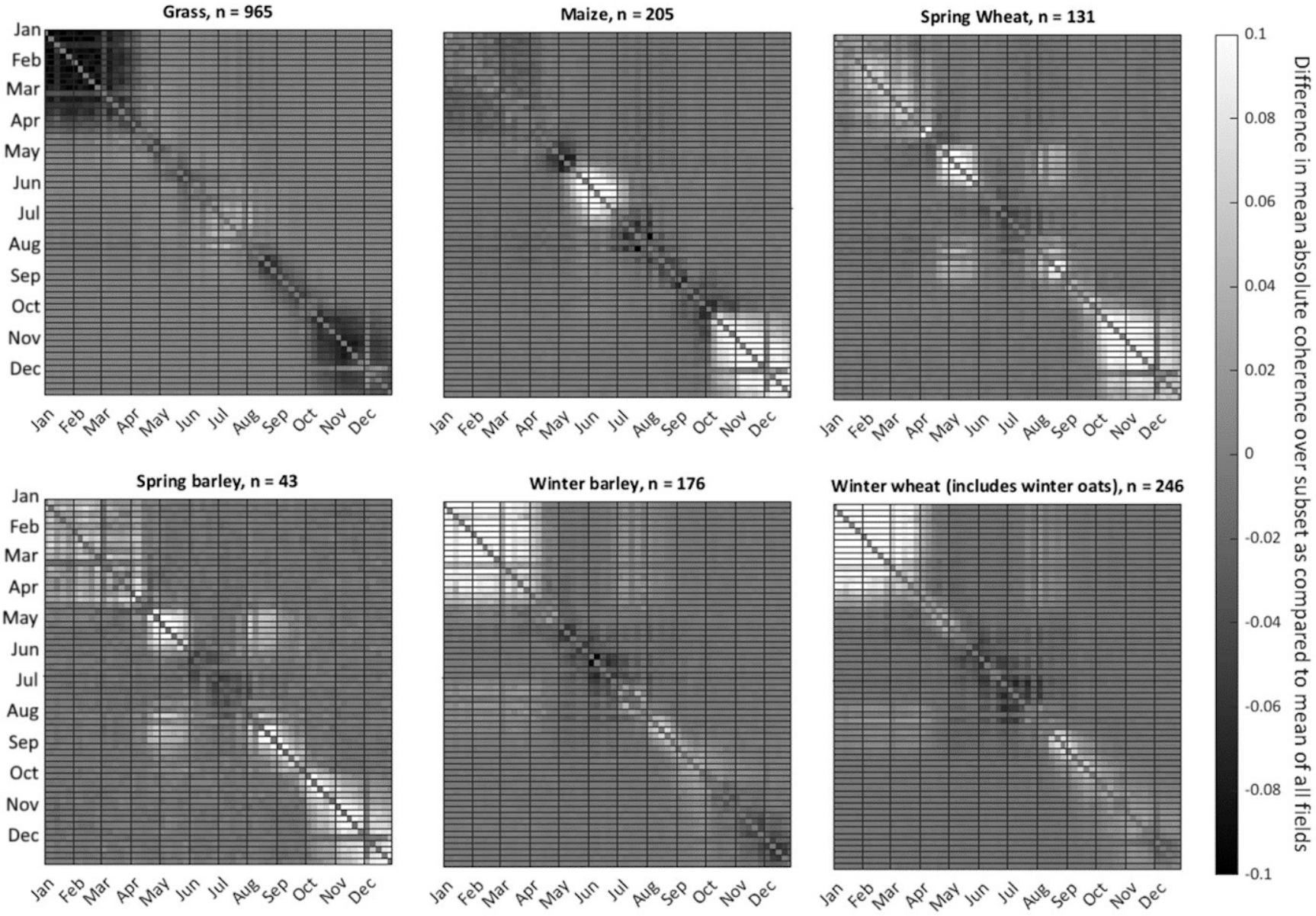


Figure 4-17: Difference in absolute coherence as compare to the whole population of fields, for each subset of crops.

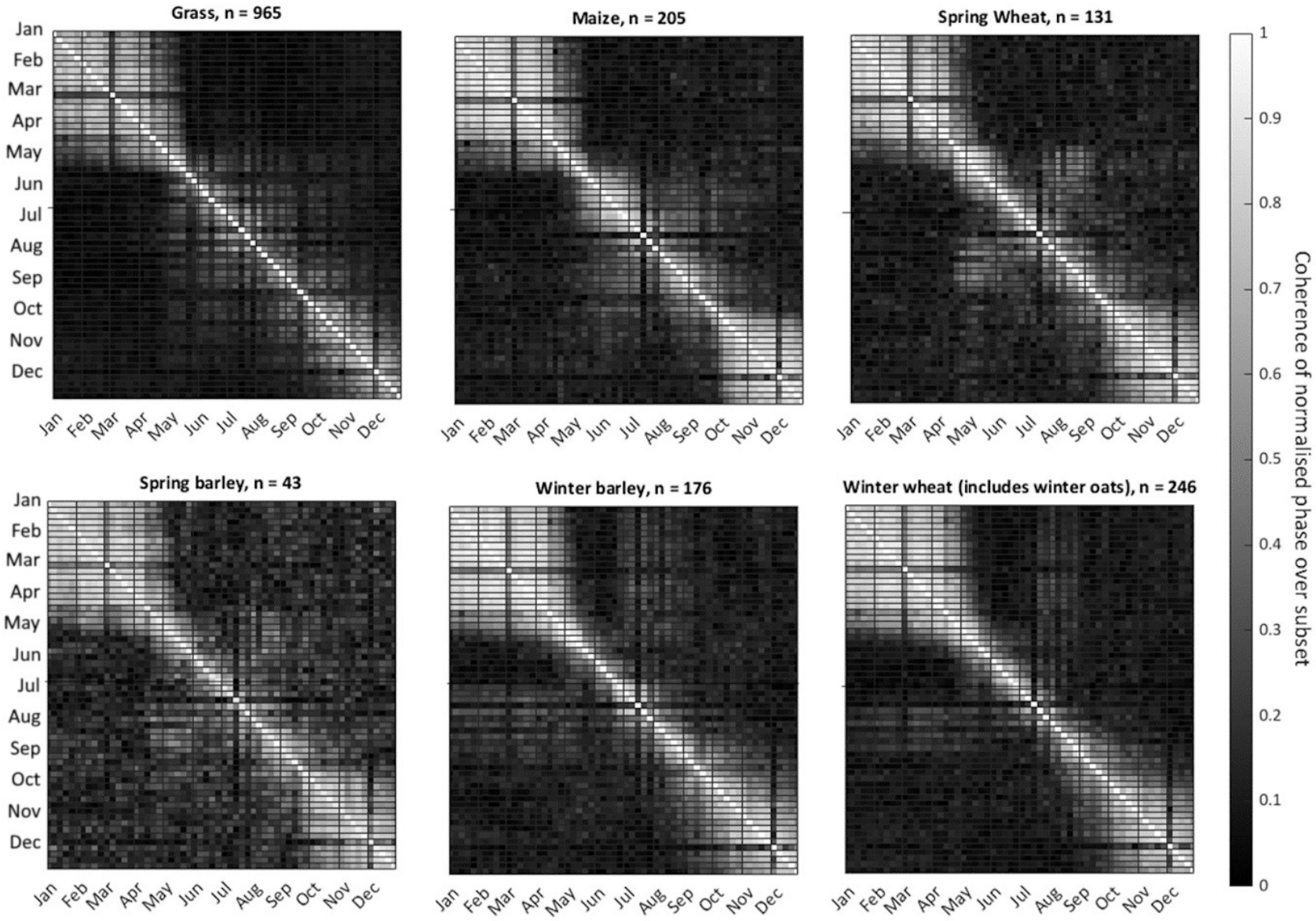


Figure 4-18: Coherence of normalised phase values for the coherence matrices under analysis, the magnitude of γ_S.

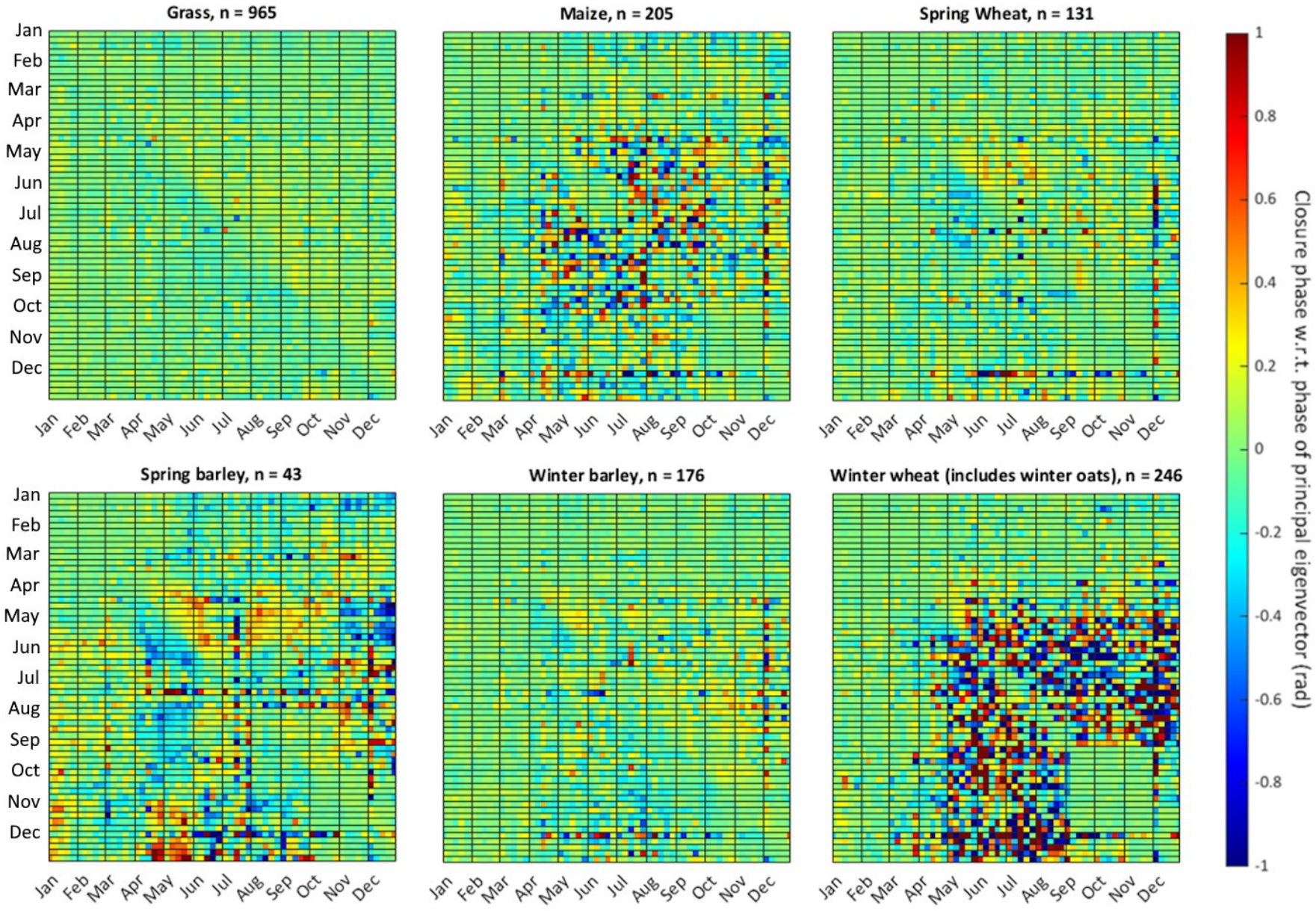


Figure 4-19: Average phase residual after removing the phase of the principal eigenvector for the types of crop under study.

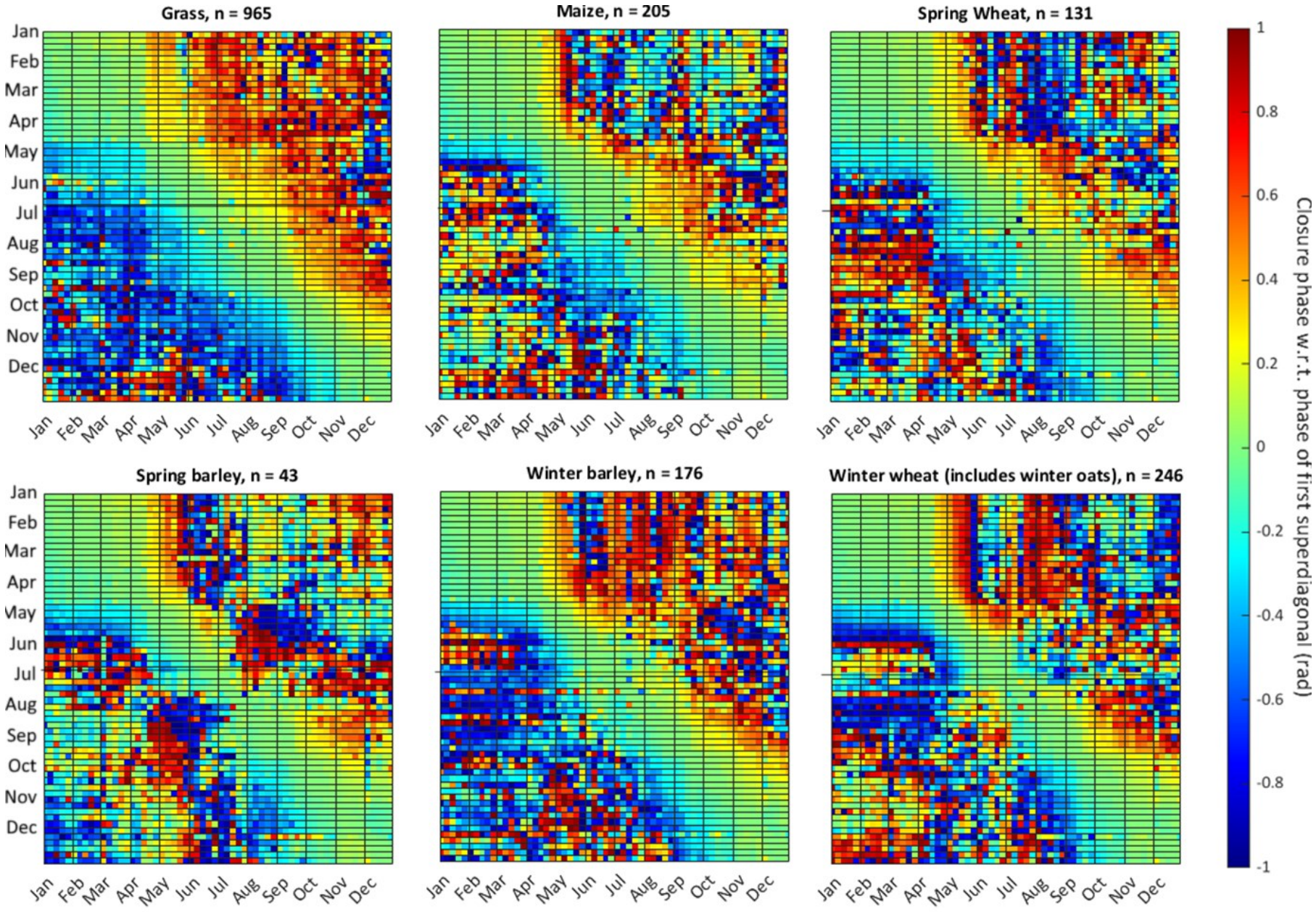


Figure 4-20: Average residual phase after removing the phase from the first super-diagonal of each field DS, for each crop under study.

4.8. Analysis

The scatterers under analysis show behaviour that is unexpected when assuming that errors from decorrelation are zero-mean or alternatively applying the models found from literature presented in prior sections. Further analysis of this behaviour is warranted.

Figure 4-15 shows the average phase of the coherence matrices for each class of crop, produced by the estimator in Equation 4-5. The results show significant common phase offsets apparent for each and all of the crop types under analysis. A trend in which the phase shifts by approximately π radians between April and June is common to all types of crop. This result is unexpected, as no mechanism for the deformation is apparent to explain this sudden shift which is limited to spring months. MTI processing algorithms currently take no account of shifts such as this, which could therefore significantly bias estimates of ground deformation.

The consistent and pervasive π radian phase shifts seen between reference scenes in Jan-April and May-July are too large to be explained using the soil moisture model presented in literature, which suggest a maximum value of $\pi/2$ (De Zan *et al.*, 2014). Alterations to the dielectric models are necessary, perhaps accounting for π radian shifts in reflection from media with a higher relative permittivity.

While later figures explore closure phase (De Zan, Zonno and Lopez Dekker, 2015) explicitly, the triangular inconsistency of the phase histories can be appreciated at face value. Shifts along the first super-diagonals (i.e. the sequence of elements $\{C_{i,i+1}, C_{i+1,i+2}, \ldots, C_{i+n-1,i+n}\}$ of the coherence matrix C) are relatively small at the time of the aforementioned π shifts. Histories with reference scenes around November similarly appear to avoid this dramatic shift to an extent.

Figure 4-16 shows the average magnitude of elements in the coherence matrices taken over each class of crop. There is limited expected coherence between any images separated by more than a few months, and thus to produce a complete, long-term time-series history of the area it is essential that biases in the phase as shown in Figure 4-15 are minimised. The low coherence magnitude for interferograms with significant phase

shifts implies thresholding based on spatial coherence is an effective mitigating step (Hooper *et al.*, 2004).

Figure 4-17 shows how the coherence magnitude differs for each class of crop as compared to the mean of the combined 6 sets. The timing of the coherence suggests a significant role of either the vegetative cover or the agricultural land practices in affecting the measured phase. Coherence is high in winter for Winter Wheat and Winter Barley, reflecting their dormancy over this period after being planted. More complex patterns of coherence can be seen for Spring Wheat and Spring Barley.

In general, coherence is low for interferograms which exhibit large consistent phase shifts over the subset. As such MTI techniques which rely on spatial coherence to mask out noisy areas or interferograms should generally filter out the particularly problematic pairs (Berardino *et al.*, 2002; Hooper, 2008; Hetland *et al.*, 2012). Similarly, techniques which filter out points based on amplitude stability and temporal coherence (Ferretti, Prati and Rocca, 2001; Crosetto *et al.*, 2016)will generally reject these areas. Ideally, though, useful data should be recover where possible rather than rejected. Further, coherence matrix MTI techniques (Rocca, 2007; Guarnieri and Tebaldini, 2008; Ferretti *et al.*, 2014) will generally make use of these low-coherence pairs and can thus easily misinterpret these shifts.

Figure 4-18 shows the coherence of the normalised phase values, $|\gamma_{mv}|$ as described in Section 4.5. This can be seen to significantly exceed the coherence measured in Figure 4-17. The consistency in phase offsets despite the extremely limited coherence for e.g. Winter Wheat is promising in its implication that these shifts can be predicted as correlated with land cover and timing.

Figure 4-19 shows the closure phase (De Zan, Zonno and Lopez Dekker, 2015) calculated by removing the phase from the principle eigenvector of the matrix (Ansari, De Zan and Bamler, 2018). This is a straightforward method of 'squeezing' the 2D coherence matrix into a 1D phase history. This subsequent closure phase represents the residual error after squeezing the matrix as is performed in MTI processing in one manner or another (Ferretti *et al.*, 2014).

Figure 4-20 shows the closure phase but instead after removing the phase history produced by 'chaining' the interferograms which are adjacent in time. Explicitly, the interferogram formed from image 1 and image 2 is calculated, and then image 2 and image 3, and henceforth image index $(i, i+1)\ where\ i = 1 \ldots N$. These phases are found as the first super-diagonal of the coherence matrix.

It is worth noting the closure phase patterns revealed in Figure 4-19 and Figure 4-20 present a double problem for MTI techniques which seek to invert the coherence matrix in order to find a representative 1D time series. Firstly, none of the $\hat{\varphi}_{TS}$ offset will be filtered out by the inversion. While some MTI techniques mask noisy pairs or areas, coherence matrix approaches generally do not. The principle eigenvalue, as used to for triangular reference in Figure 4-19, is often used as an initial or ultimate solution to the inversion (Ansari, De Zan and Bamler, 2018). The lack of any residual phase offsets after estimating and removing this eigenvector suggests it contains all of the error, which will then propagate through the inversion.

Secondly, Figure 4-20 demonstrates closure phases of mean +/- π after referencing against the first super-diagonal. As the temporally closest interferometric samples generally have the highest coherence and therefore weighting, while the π shifted extreme diagonals are often crucial in resolving ambiguity given their position in providing information to link the two extremes of the time-series. Given the complete ambiguity between the proximal and distant diagonals, successful inversion of the complete time series is likely impossible.

4.8.1. Soil moisture

The applicability of the existing De Zan soil moisture model was investigated towards an explanation of the measured phase shifts. Notably however, the De Zan model predicts a maximum shift of $\pi/2$.

It is useful to compare this model with the observed phase. Data regarding typical moisture content variations in soil are necessary for this. These were derived from nearby 'COSMOS-UK' soil moisture monitoring stations (Cooper *et al.*, 2021; Stanley, 2021), which

estimate volumetric moisture content in soil be measuring neutron radiation in soil – as wetter soil attenuates both the neutrons and cosmic rays.

There were no COSMOS-UK stations within the area of interest, however some insight into the behaviour of soil moisture models is still worth exploring. The seasonal trend in soil moisture content (high moisture content in wet winters, low moisture content in dry summers) can be assumed to have similar behaviour across the UK, and was modelled by a simple sinusoid as shown by the orange curve in Figure 4-21. The sinusoid model is simplistic but is given in Equation 4-11 for reference:

Equation 4-11: Sinusoidal model for a seasonal soil moisture trend typical of the UK

$$m(d) = p_1 \sin(t + p_2) + p_3$$

$$t \in [0, 2\pi]$$

$$d = \frac{365t}{2\pi}$$

$$p_1 = 10, \qquad p_2 = 1.62\,, \qquad p_3 = 25$$

where d is the day of the year starting from 1st of January, parameters p_i were found numerically to minimise the square difference between the model and data from the nearest COSMOS-UK site 'Holme Lacy', shown by the blue curve in Figure 4 21. The site is approximately 50km to the North East of the AOI shown in Figure 4-12 . (Cooper *et al.*, 2021)

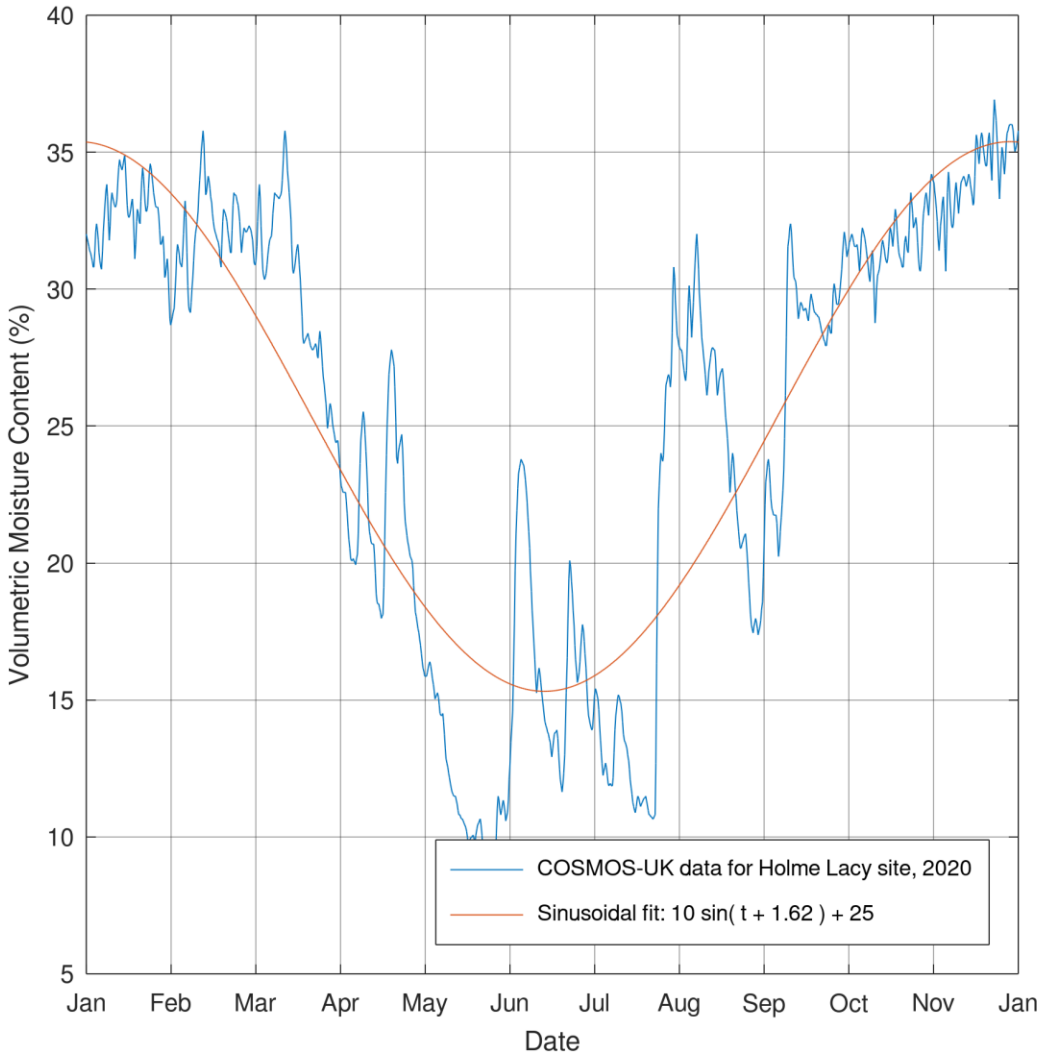


Figure 4-21: COSMOS-UK soil moisture data and a simple sinusoidal model.

This simple estimate of annual moisture variations was then used as input to the De Zan model for interferometric phase due to soil moisture changes, with the results shown in Figure 4-22.

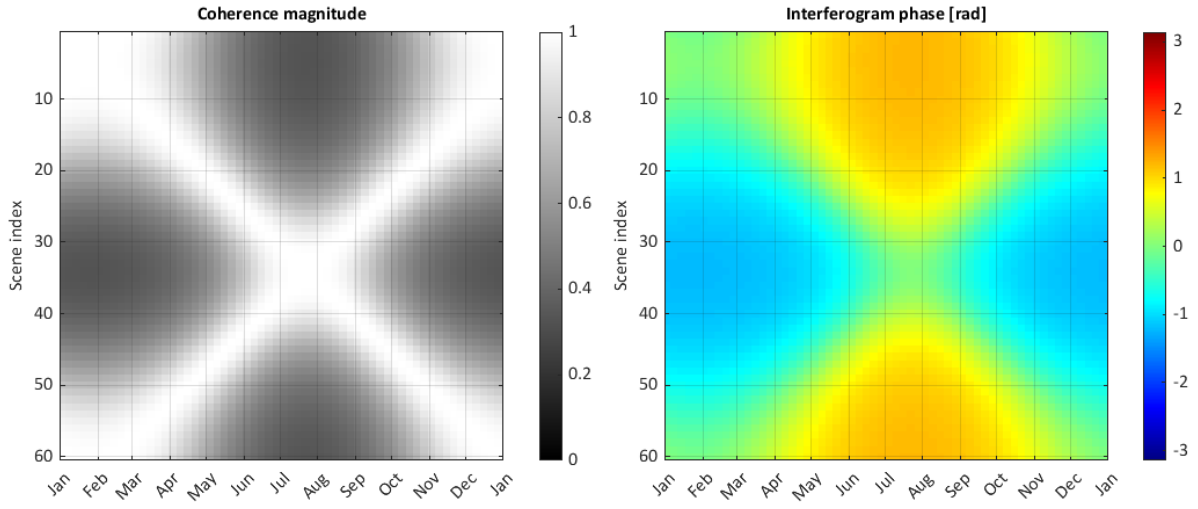


Figure 4-22: Simulated moisture driven phase shift using the model of (De Zan *et al.*, 2014) and approximate figure and timings for soil moisture contents using UK cosmic ray sensors (Stanley, 2021).

The general pattern of phase is promising, with the sign correct and the rate of shift occurring in Spring matching data. However, the coherence is far higher in the simulation than borne out in experimental data, and inevitably the phase shift is far lower.

To account for these discrepancies, one speculative modification to this model was explored involving reflection phase shifts. Upon reflection from an interface with higher refractive index a wave will undergo a shift of π in phase. If then, in winter months when moisture contents were high, the top of the soil surface or its cover had high permittivity and generated a significant backscatter, then this would backscatter a signal with phase shifted by π. If in later months when moisture and permittivity was lower, this surface was less visible to the radar then the volumetric or double-bounce mechanisms (see Section 4.2.2) would dominate instead, and the π phase shift might no longer occur. This is simulated in Figure 4-23, whereby the reflection phase shift is incorporated as an additive term.

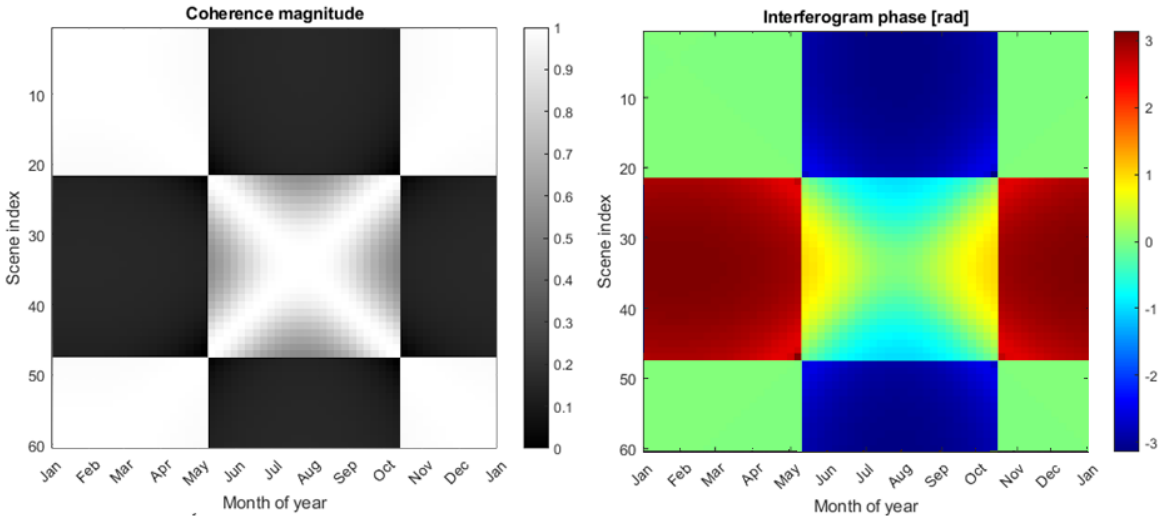


Figure 4-23: Results for a speculative reflection phase shift occurring in only winter months.

Contrary to this model, it is a widely accepted assumption that the scattering is uncorrelated between different mechanisms (Freeman and Durden, 1998). This model requires that backscatter from the soil or vegetation surface (in wet conditions) and backscatter from the volume (in drier conditions) will be somewhat correlated spatially. Further work to determine this possibility is therefore required before this model can be relied upon or should be discounted. These further investigations might use small-scale radar systems in controlled environments (Morrison *et al.*, 2011). A suggested mechanism for correlation is that as backscatter is preferentially generated close to the surface (the signal is attenuated the deeper it travels), multi-bounce scatterers or inhomogeneities with lower permittivity located close to the surface may be more likely to contribute to the backscatter and therefore capable of producing a π-shifted signal with non-zero coherence if the overall geometry and arrangement of material remains consistent.

Some variation of this model may be useful in explaining the significant π shifts. Notably the coherence is also lower for this model, as in the coherence of the measured data seen in Figure 4-16 and the coherence of the average transient scattering phase estimated in Figure 4-18.

4.9. Conclusions

A range of transient scattering mechanisms can be found in literature which suggest scattering changes can yield spatially and temporally correlated phase offsets. This is counter to prior assumptions about decorrelation being a zero-mean phase process, on which many MTI processing techniques rely.

Consistent phase shifts have been demonstrated in Sentinel 1 data for a range of agricultural crops, as shown in Figure 4-15. This 'Spring shift' of π radians is sufficient to cause a phase unwrapping errors during MTI inversion. In general these shifts are accompanied by low spatial coherence, leading to affected areas and interferograms being screened out of many MTI analysis, but low spatial coherence is not guaranteed and shifts remain present even above typical threshold values. Techniques which seek to exploit the entire coherence matrix for its data content are inevitably affected by this unexpected shift in data.

Transient scattering patterns in closure phase and coherence accompany the shifts for these subsets. While dielectric mechanisms for phase shifts predict a relationship between these values, further work is required to demonstrate such a relationship explicitly and subsequently model the particular mechanism. It is possible that these patterns in coherence and closure phase are coincidental, but the mutual occurrence of the 'Spring shift' in all three measurement channels, across all types of crop, suggests these observable changes are linked.

It should be noted that, to the authors knowledge, the use of *a priori* data on land cover has not been used to directly estimate phase offsets in an MTI time series study, and thus these findings present a novel contribution which raises interesting questions regarding the value and mitigation of these complex behaviours.

5. Quantitative analysis of transient scatterers

5.1. Introduction

Several time-varying 'transient' scattering mechanisms that can cause InSAR phase shifts are explored in the previous chapter. There are a number of indications that these 'transient scattering' phase shifts (φ_{TS}) are unrelated to ground deformation. These indications include the high magnitudes (Hensley *et al.*, 2011), temporal inconsistency (De Zan, Zonno and Lopez Dekker, 2015), and direction (De Zan *et al.*, 2014) of the apparent shifts. These ambiguities and inconsistencies merit further analysis.

Chapter 4 highlighted a range of potential mechanisms for scattering changes to affect InSAR phase and coherence in processes that are spatially correlated with land cover. 'Dielectric' mechanisms in literature suggest that, as both the wavenumber and attenuation of a signal are controlled by material and geometric properties of semi-transparent media such as soil and vegetation, changes in soil and vegetation will subsequently vary the backscattered signal. Small changes in moisture or biomass may produce spatially consistent phase shifts, as opposed to the random decorrelation or zero-mean noise traditionally used to model with unstable scatterers.

These dielectric mechanisms are promising in that they can explain the coincident phase, coherence, amplitude, and closure phase effects observed in data. However, the relationship between these variables depends on the positioning and properties of the dielectric scattering material present in a resolution cell. In general, the structure and properties of scatterers are not known *a priori* in MTI studies, and thus it is difficult to envisage a general approach which directly models and corrects the observed φ_{TS} according to the particular arrangement found in any one SAR resolution cell.

Analysing scattering changes quantitatively, rather than focusing on particular models or proposed mechanisms for the observation, should be useful in building a more general understanding of transient scattering. If clear relationships can be found between SAR or InSAR measurements such as amplitude, coherence and mean phase, then these relationships could be used to predict the transient scattering mechanisms which took place and correct for them before further MTI analysis of the phase. One useful and relatively simple approach would be to simply identify the geographic areas which exhibit transient scattering phase shifts (φ_{TS}) so that they can be given due consideration. For instance, in MTI deformation analysis phase shifts and errors correlated with land cover have the potential to be misinterpreted as spatially-correlated phenomena such as atmospheric phase delay. Excluding areas with likely φ_{TS} may yield improved accuracy in APS estimation which will carry forward in estimating the deformation history of more stable targets that are nearby.

Identifying areas of likely φ_{TS}further allows for more informed interpretation when analysing ground deformation results. Beyond the need to measure ground deformation, φ_{TS}can reveal important information about land cover, vegetation and soil moisture. While this study is principally motivated to improve MTI deformation analysis, studies in literature have sought to isolate $\varphi_{TS}$from deformation in order to measure crop biomass or soil moisture.

Here, it is hoped that metrics and analysis will allow prediction of $\varphi_{TS}$to remove it and yield more accurate estimates of ground deformation. Approaches in literature generally focus on a particular land cover or soil present in a SAR cell, and these have differing behaviours. Where information is available, physical parameters such as crop type, biomass, and phenology, soil type and soil moisture, as well as observable metrics such as interferometric coherence can be used as predictors of φ_{TS}.

Chapter 4 showed there is potential for land cover information to exhibit characteristic phase signatures. This implies potential value in land cover ground truth data being used as an input to MTI processing in order to better estimate remaining phase errors. Unfortunately there are limitations in pursuing this forward model approach. Firstly, land cover ground truth information may not be available or accurate for a given area.

Secondly, the active mechanisms operating within a particular resolution cell will depend on additional factors such as the internal geometry and localised variability in the cover. Instead, deriving estimated transient scattering effects from the SAR data itself may be useful in terms of spatial and temporal coincidence with deformation estimates.

It is worth noting that any derived method of identifying land cover from the observed transient scattering behaviour, i.e. a backwards model, would in itself be valuable. As alluded to previously, land cover data is often unavailable or limited compared to the spatial and temporal resolutions achievable with SAR.

For any particular acquisition date, a SAR measures the amplitude and phase for each active polarimetric channel, yielding potentially 4 independent predictor variables for Sentinel 1's main VV/VH imaging mode to tackle the modelling of complicated scattering phenomena. The field of polarimetry examines spatial correlations in the local area to derive additional insight on scattering, while MTI analysis examines temporal correlations (and spatial patterns, in the case of Distributed Scatterers, as under analysis here) to separate deformation, elevation, and atmosphere measurements. From the various observables it is hoped that valuable predictors of φ_{TS}can be identified.

The following candidate metrics for identifying and quantifying transient scattering as a phenomenon were identified and explored:

- Stability in amplitude and time series coherence of VV and VH to identify unaffected areas (such as PS)
- Amplitude distributions and change detection to identify transient scattering and changes in scattering mechanism.
- Coherence, entropy of the coherence matrix, closure phases to detect multiple scattering mechanisms being present.
- Relationships between φ_{TS}, decorrelation, and changes in scattering mechanism to isolate $\varphi_{TS}$from deformation.

5.2. Useful observables

This section explores data observables for potential value in quantifying transient scattering.

5.2.1. Stability and stationarity

Chapter 4 discussed the stability of PS and how they may be used as a reference source for calibrating and investigation of other nearby scatterers. By definition, scattering processes characteristic of PS are not transient, and PS should be omitted and treated as usual when performing MTI analysis (Ferretti, Prati and Rocca, 2001; Ferretti *et al.*, 2014). PS can be identified in a stack through a variety of techniques (Crosetto *et al.*, 2016) such as amplitude stability and temporal coherence.

PS amplitude distribution is worth exploring. Where the scattering is stable, this results in a Rice distribution (Ferretti, Prati and Rocca, 2001) which occurs due to additive noise in the radar in-phase and quadrature channels overlaid on a non-zero signal. At high signal-to-noise (SNR) ratios the Rice distribution asymptoptically becomes a gaussian distribution, while for low SNR (noise) it asymptoptically becomes the Rayleigh distribution. An example of the Rice distribution can be seen in Figure 5-1.

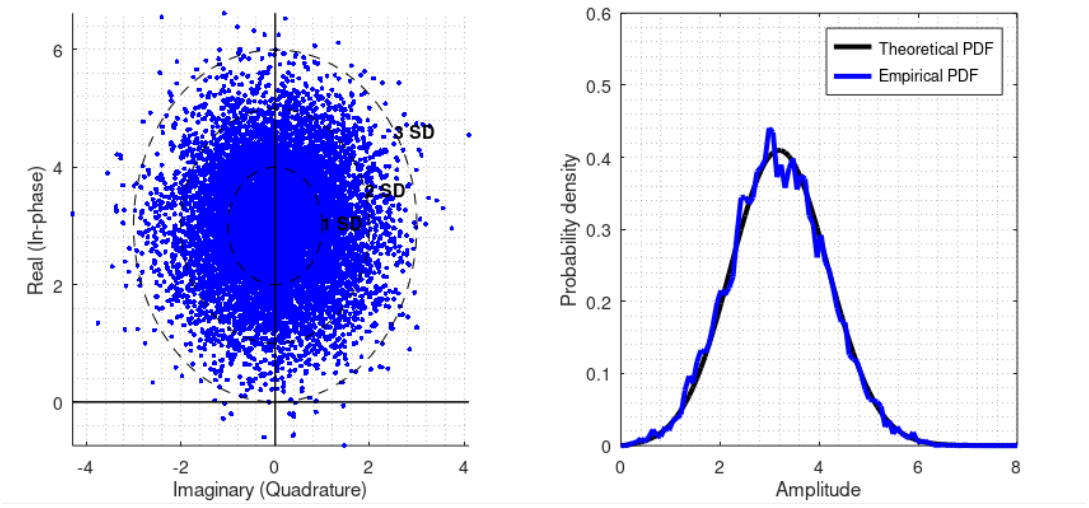


Figure 5-1; Real and imaginary components of a stable but noisy scatterer. The distribution of amplitude values is described by the Rice distribution.

A Brownian motion mechanism has been discussed in the literature (Zebker and Villasenor, 1992; Rocca, 2007; Guarnieri and Tebaldini, 2008) as a model for decorrelation. Some processes, such as vegetation growth or soil changes, cause the elementary scatterers within a resolution cell to change their apparent position over time. This leads to a drift in their position and the in-phase and quadrature measurements will be shifted from the stable pattern, as the elementary backscatter contributions correlate and decorrelate to from the signal. This is shown in Figure 5-4, and has been simulated as cumulated additive noise applied to the same Rician distribution shown in Figure 5-1.

It can be noted, perhaps unsurprisingly, that the observed amplitude distribution no longer matches the initial Rician distribution. In statistical terms, the process generating the amplitude samples is non-stationary. A stationary stochastic process is one where the mean, variance, and higher order moments of the distribution are constant in time (or some other specified dimension). Some parameter of the Rician probability density function (PDF) here in Figure 5-2 has been modified (specifically the mean) according to the drift from the Brownian noise.

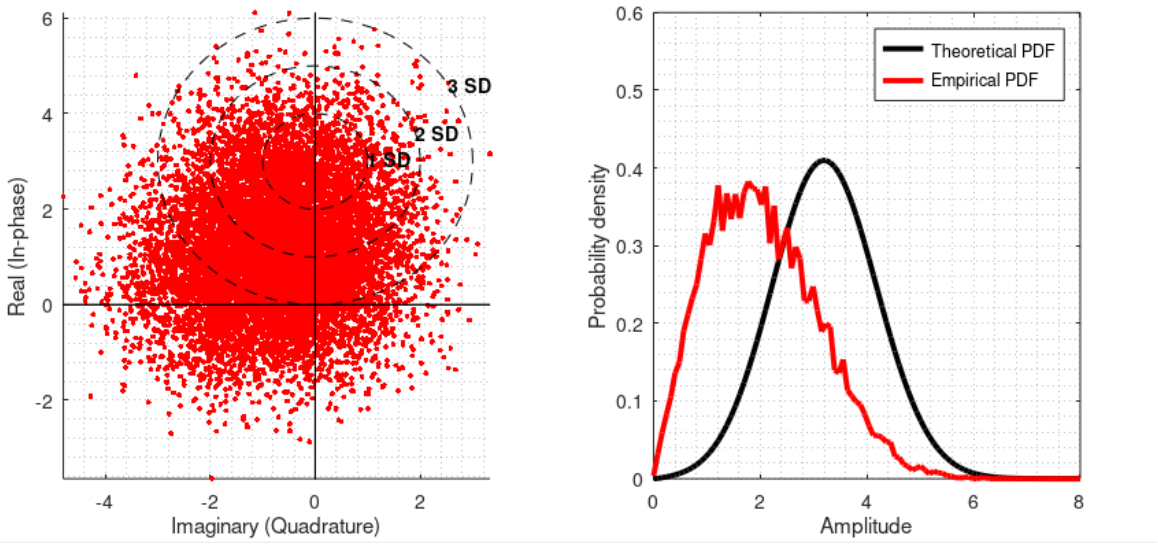


Figure 5-2: A stable scatterer with additive noise, identical to that of Figure 1, albeit with an additional contribution from a Brownian noise component and hence a drift in in-phase and quadrature amplitudes.

Amplitude dispersion is commonly used in MTI processing to assert there has been limited changes in mean amplitude and hence identify PS candidates. Low threshold values of amplitude dispersion below e.g. 0.25 are used to select the candidates (Ferretti, Prati and Rocca, 2001). Comparatively, the mean value recovered from pure zero-mean noise (i.e. zero signal to noise) is 0.523, as can be determined from the variance of the Rayleigh distribution. If an amplitude series is measured to have dispersion significantly higher than this value, it evidences that some additional phenomenon has shifted the amplitude to a greater extent than can be attributed to noise alone. This can be seen in Figure 5-3 whereby agricultural fields are highlighted. It is expected that due to growth of vegetation the amplitude of these fields has drifted as detected by this statistical metric.

The mean of multiple Brownian noise signals will also exhibit a drift in mean, albeit the shift will be somewhat 'smoother' due to the averaging process. Amplitude values for DS with Brownian elementary scatterers will hence exhibit similar non-stationary drift behaviour to that shown in Figure 5-2 for a single scatterer.

In general, any scattering changes will affect the mean amplitude measurements of a DS. When a scatterer changes, so does its characteristic signal behaviour and the likelihood distributions of its measurements. Figure 5 3 shows low amplitude stabilities are observed across agricultural fields, where phenology of vegetation leads to a significant shift in the mean amplitude over time.

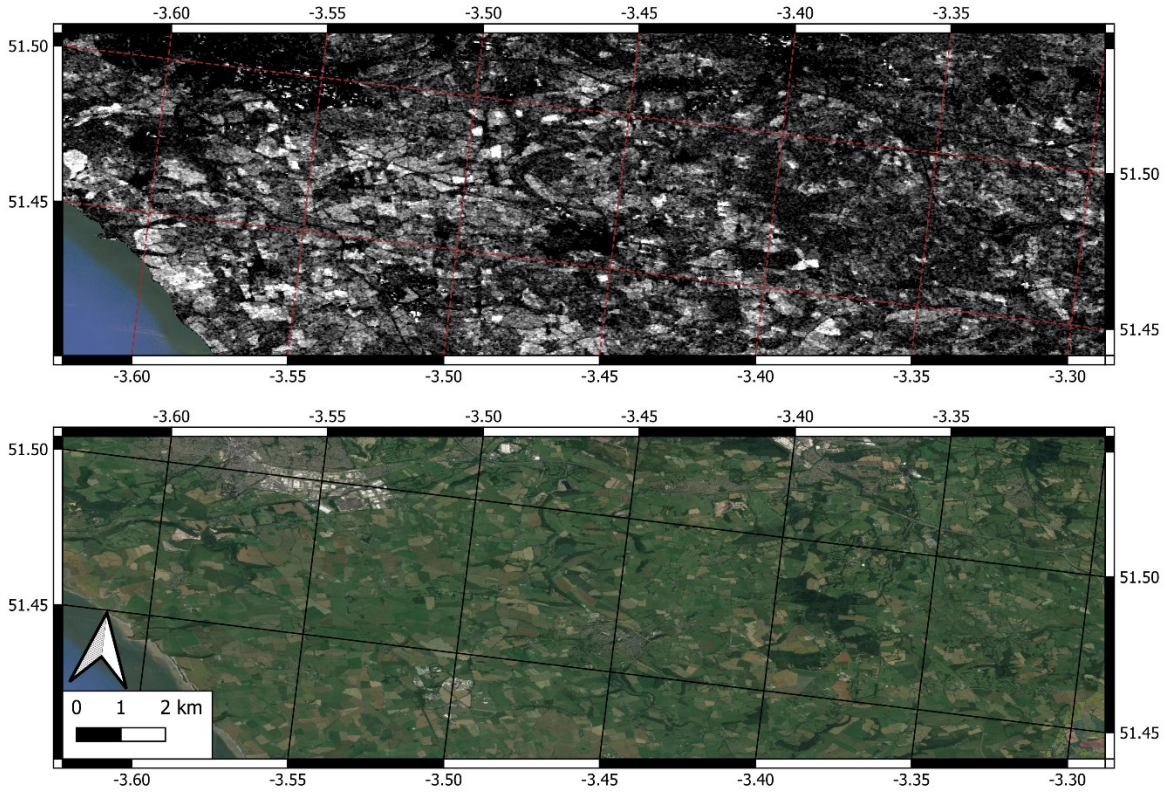


Figure 5-3: [Top] Amplitude stability measurements for the Vale of Glamorgan, 2018. The colour axis has been scaled such that black pixels are represent the 1st percentile of expected measurements from a Rayleigh distributed time series of equivalent size (1.8644), as produced by pure noise in the in-phase and quadrature channels. White values are an arbitrary value below this (1.5) chosen for display purposes.

5.2.2. Amplitude analysis

Techniques for analysing stationarity are therefore useful to spatially map areas of transient scattering in an MTI stack. Two useful approaches would be to apply the Kolmogorov-Smirnov (KS) (Ferretti *et al.*, 2014), or the similar Anderson-Darling test (Parizzi and Brcic, 2011; Ansari, De Zan and Bamler, 2018). These tests seek to determine the statistical likelihood that two sets of samples were drawn from the same stochastic process. They are non-parametric tests, which avert the need to determine the particular distribution under study or introduce errors when fitting model parameters. test applied in existing studies or the similar Anderson-Darling test (Parizzi and Brcic, 2011; Ansari, De Zan and Bamler, 2018). These tests seek to determine the statistical likelihood that two sets of samples were drawn from the same stochastic process. These tests are non-

parametric, which averts the need to determine the particular distribution under study or introduce errors when fitting model parameters.

In MTI analysis these tests are traditionally used to filter a local area to determine if neighbouring time series exhibit the same scattering processes, and therefore may be treated as representing the same distributed scatterer (i.e. by then filtering to reduce noise).

Here, we can compare windows in time for a given area and determine if two temporal windows exhibit consistent scattering behaviour. Following the logic of the spatial tests, if the null hypothesis of the KS test is not met – implying the distributions are different – then the two datasets cannot be treated as the same (temporally) distributed scatterer: The scattering process is transient and has changed, and the two time periods contain separate scatterers that should be treated separately.

Practical application of the KS test becomes difficult due to the number of combinations of windows that can be compared over a SAR time series spanning hundreds of scenes. The KS test is not trivial, computationally (Parizzi and Brcic, 2011; Ferretti *et al.*, 2014). Practical application of the KS test becomes difficult due to the number of combinations of windows that can be compared over a SAR time series spanning hundreds of scenes. The KS test is not trivial computationally (Parizzi and Brcic, 2011; Ferretti *et al.*, 2014).

Stationarity can instead by tested by techniques such as the Augmented Dicky Fuller (ADF) test (Shumway and Stoffer, 2017). The ADF test fits an Autoregressive model to a sample time series and examines the parameters to indicate whether the sample mean depends wholly on existing, earlier, values, in which case the mean behaviour has drifted over time.

5.2.3. Coherence analysis

The majority of transient scattering mechanisms explored in Chapter 4 involve decorrelation as well as phase shifts. This link between coherence magnitude |γ| and φ_{TS} is of particular interest as it establishes a direct relationship from which to separate

deformation phase from scattering phase, assuming suitable decorrelation mechanisms are accurately identified. Approaches to distinguish these separate shifts will be explored later, as in the first instance simply identifying transient scattering behaviour should be valuable and comparatively straightforward.

A difficulty is that measurements of interferometric coherence are noisy and significantly biased (Touzi *et al.*, 1996), particularly when the (true value of) coherence is low or the number of independent samples is low.

5.2.3.1. Temporal decorrelation

There exist two conditions which are required for a decorrelation mechanism to bias deformation estimates: Firstly, the mechanism must produce a phase shift which is non-zero in the mean. Secondly, the phase shifts must be progressive and temporally correlated to alias as the deformation phase signal, which is identified via its temporal correlation (Ferretti, Prati and Rocca, 2000). Thus while a range of decorrelation mechanism exist (Zebker and Villasenor, 1992), temporal decorrelation as shown in Equation 5-1 is of particular relevance in transient scattering.

Equation 5-1: Temporal Decorrelation.

$$\gamma_{temporal} = e^{-\frac{|\Delta t|}{\tau}}$$

It is useful to first define how scatterers are expected to decorrelate over time and assess whether this will match the aforementioned criteria for phase bias. Existing models for decorrelation have often focused on Brownian random motion of the elementary scatterers in a resolution cell (Zebker and Villasenor, 1992; Rocca, 2007). No predictable phase shift will occur, movement is uncorrelated so the expected value of the phase shift is zero (Samiei-Esfahany *et al.*, 2016). Where the process causing the motion is statistically stationary then the coherence will decay exponentially in time.

The coherence can decay to zero, implying no correlation between scatterers in the two scenes. Given this progressive decay, the point in time in which a distributed scatterer loses its identity is semantically unclear, much like the Ship of Theseus discussed in philosophy. It is perhaps easier to classify a scattering process as transient through the temporal rate of decay, τ, which should remain stable if the decorrelation process is stationary. Estimates of τ can be fitted for a DS in a stack of MTI data, with a value for each reference scene in an interferogram time series. The resulting series of τ estimates can then be tested for stationarity (e.g. using the ADF test described in Section 5.2.2) to determine if the scattering process is itself stationary or transient.

Where decorrelation occurs due to a sudden shift in scattering from one physical state to another, this can be described by a Markovian model (Rocca, 2007). In this case the scatterers in a resolution cell have a given state at any one point in time, and have a chance of shifting to another state over any discrete period of time. Much like the case of Brownian noise the description of the models in literature generally assume the phase is uncorrelated between states (Rocca, 2007; Samiei-Esfahany *et al.*, 2016) and thus do not explore temporally correlated phase shifts. If the rate of change from a given state is constant then the resulting coherence time series from a given reference date can be modelled as an exponential decay much like in the Brownian motion case.

Where the timing and properties of each scattering state are unknown, the model is often referred to as a Hidden Markov Model. Further analysis will often focus on identifying a number of distinct states, *k*, within the data and their associated distributions. This can be approached through clustering algorithms, such as the K-means algorithm (Smyth, 1997; Bishop, 2006) as will be explored in Section 5.4

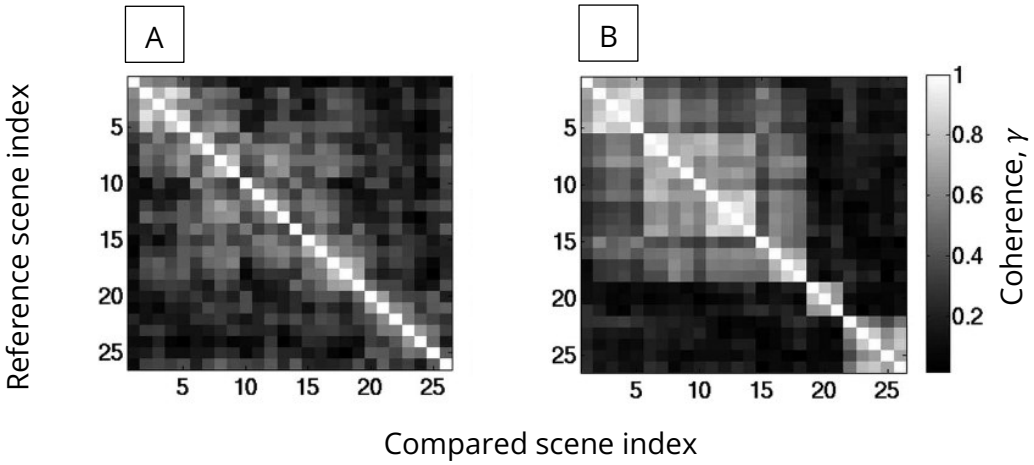


Figure 5-4: Coherence matrices resulting from two similar models of temporal coherence. Exponential decay (a) occurs where there are Brownian noise processes while sudden jumps in coherence between dates can be described with a Markov model (b), from (Rocca, 2007).

5.2.3.2. Decomposition of the coherence matrix

In SAR polarimetry, Eigen decomposition of the coherence matrix formed between polarimetric channels is a common approach towards analysing scatterers (Cloude and Pottier, 1996, 1997; Cloude, Papathanassiou and Hajnsek, 2000; Lopez-Martinez, Pottier and Cloude, 2005; Alvarez-Perez, 2011). Eigen decomposition projects a matrix into a set of vectors which are orthogonal to one another and a set of accompanying values that scale their associated vector. In this context, each vector describes a dimension in which incident waves are transformed in the process of backscattering.

It has been argued (Cloude and Pottier, 1997) albeit debatably (Alvarez-Perez, 2011), that each eigenpair describes an individual mechanism through which incident waves will be transformed in the process of backscattering. While there may not be a one-to-one correspondence between eigenvectors and independent scattering phenomenon, the technique does help separate phenomena with orthogonal polarimetric responses (Alvarez-Perez, 2011).

Analogously in MTI analysis of deformation, eigenvectors of the temporal coherence matrix are useful to describe how the decorrelation and phase shifts, with reference to

one point in time, may be transformed in a different manner as compared to another point in time. In other words, the apparent deformation may vary depending on the selection of reference image used in the interferograms.

The use of Eigen decomposition is widespread in MTI analysis for the purposes of phase triangulation (recovering a single descriptive time series of phase values from a coherence matrix). For PS or ensembles of highly correlated targets, a single eigenvector and value pair (eigenpair) can explain most of the detail in how the measured phase and coherence will vary over time. In other words, the phase history of an ideal PS can be wholly recovered by using any image in a stack as a reference (equivalently any row or column of the coherence matrix). The additional rows in $\boldsymbol{C}$ are therefore redundant, and the dimension of the transform it describes is equal to 1 (Ferretti *et al.*, 2014).

For DS, the phase and decorrelation are by contrast triangularly inconsistent (De Zan, Zonno and Lopez Dekker, 2015). The dimensionality or rank of the coherence matrix is greater than 1 and numerical techniques are required to 'squeeze' the information from the 2D matrix into a 1D time signal for deformation analysis, which is a sensitive procedure subject to focus in literature (Rocca, 2007; Zan, Rocca and Rucci, 2007; Guarnieri and Tebaldini, 2008; Ferretti *et al.*, 2014; Cao, Lee and Jung, 2015; Ansari, De Zan and Bamler, 2018).

While Eigen decomposition is widely used in phase triangulation techniques, there has been limited focus on physical interpretation of the eigenpairs beyond that the principal eigenpair is representative of the most stable, correlated, scatterers within a DS (Zan, Rocca and Rucci, 2007; Ansari, De Zan and Bamler, 2018) and that subsequent eigenpairs may represent additional scattering processes (De Zan, Zonno and Lopez Dekker, 2015).

On one extreme, an ideal PS has a single eigenvalue and N-1 zero eigenvalues as alluded to previously. On the other extreme, $\boldsymbol{C}$ for complete uniform noise will be an identify matrix and the resulting spectrum of eigenvalues will be N identical values. It is a complex topic, beyond the scope of this work, to fully describe the distribution of spectra in between these two extremes of stability. Instead, it is far simpler to focus on a few key metrics.

Entropy is widely used in polarimetry to quantify the amount of independent information within a coherency matrix. The widely used Shannon Entropy definition is given in Equation 5-2:

Equation 5-2: Shannon Entropy, H, as a function of eigenvalues λ_i.

$$H = -\sum_{i}^{N} \lambda_{\mathrm{i}} \log \lambda_{\mathrm{i}}$$

Conventionally, eigenvalues are normalised such that $\sum \lambda_{\mathrm{i}} = 1$.The entropy, H, for the ideal PS case is 0. For incoherent noise the normalised eigenvalues equal, $1/N$ and thus $H = \log N$. A similar measure, used in Principal Component Analysis is the number of significant eigenpairs as assessed by e.g. the Kaiser criterion (*Principal Component Analysis*, 2002). This identifies significant value as those greater than the expected value of incoherent noise. Calculation of the Kaiser criterion is shown in Equation 5 3:

Equation 5-3: Number of significant eigenpairs, given by the Kaiser criterion.

$$k_\lambda = \sum_{\mathrm{i}=1}^{\mathrm{N}} \mathbb{1}\left(\lambda_{\mathrm{i}} > \frac{1}{N}\right)$$

where $\mathbb{1}$ is the indicator function returning 1 if the inequality is satisfied and 0 otherwise. For consistency with Equation 5-2 eigenvalues are assumed to have been similarly normalised.

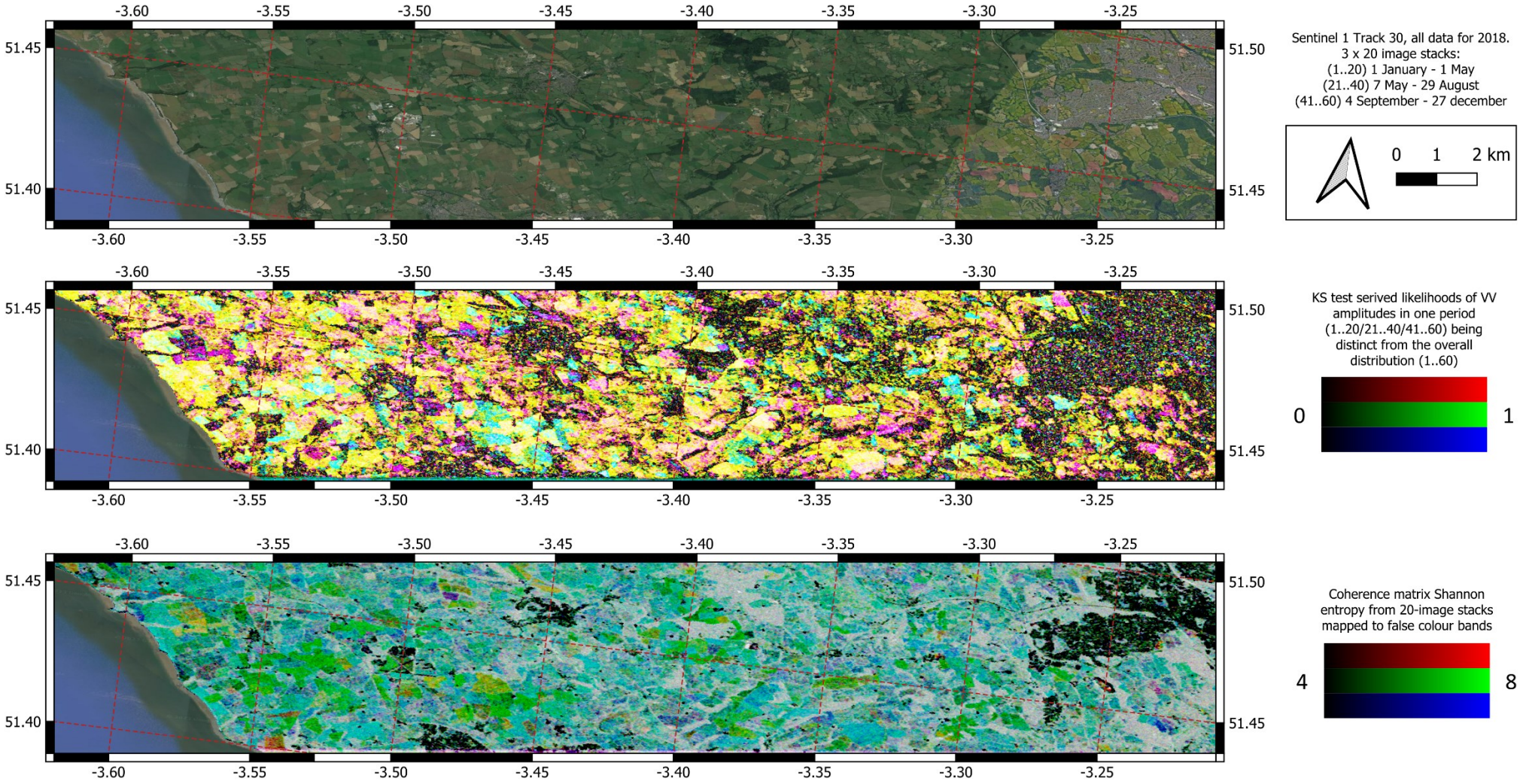


Figure 5-5: 60 scenes were available from Sentinel 1's orbital track 30 for the year 2018. These were split into interferometric stacks of 20 each. [Top] optical image showing the area of interest, the Vale of Glamorgan [Middle] false-colour image showing KS test probability of amplitudes from each stack as being drawn from the same distribution as values for the entire year [Bottom] Shannon entropy false-colour image whereby each smaller stack is used to form a band.

5.2.4. Polarimetry

Common elementary scattering mechanisms such as Bragg surface scattering, and scattering from any number of smooth surfaces are observed to produce no cross-polarised backscatter (Freeman and Durden, 1998; Cloude, Papathanassiou and Hajnsek, 2000; Van Zyl and Kim, 2011). In common cases a non-zero Sentinel 1 VH measurement can instead be explained by either noise, scattering from a volume, or complex artificial scatterers such as antennae (Van Zyl and Kim, 2011; Sato *et al.*, 2012; Zou *et al.*, 2015).

The ratio of VH to VV amplitude (henceforth VH/VV) is therefore useful in rural areas for determining volumetric scatterers, such as crops and forests, as distinct from more sparse vegetation and bare soil (Banque *et al.*, 2015). VH/VV is isomorphic to a metric termed the 'Radar Vegetation Index' in quad-polarisation contexts (Van Zyl and Kim, 2011) if HH amplitude is omitted due to being unavailable in Sentinel 1's main imaging mode. A change in the distribution of VH amplitude or VH/VV ratio is indicative of scattering changes in the same manner described in Section 5.2.1.

The cross-polar VH channel can be utilised for MTI deformation analysis just as co-polar VV or HH channels can, albeit with the data being considerably noisier and in general measuring a different ensemble of scattering mechanisms. In some cases the VV and VH interferometric phases are coherent, however. In the hypothetical case of complete coherence and correlation between the VV and VH channels, each will provide the same information to MTI measurements of APS, topography, and deformation (Shamshiri, Nahavandchi and Motagh, 2018).

Coherence between the VV and VH channels is visualised in Figure 5-6 (Top). For VV and HH channels there exist scattering mechanisms that inherently produce a consistent phase offset between the channels. For example, due to phase shifting on reflection depending on orientation, the phase difference between the VV and HH channels is expected to be π radians for double bounce scattering (Cloude and Pottier, 1996; Ramya and Kumar, 2021). For scattering from a smooth surface, the VV and HH phase difference is expected to be 0 on average (Rignot, Chellappa and Dubois, 1992; Cloude and Pottier,

1997). No such mechanisms exist that are predicted to both producing a significant VH return and a spatially consistent phase offset between VV and VH.

A temporal high coherence between VV and VH phase is thus a useful indicator that transient scattering is not present, as a change in scattering contributions is expected to yield new and uncorrelated VV and VH phase centres.

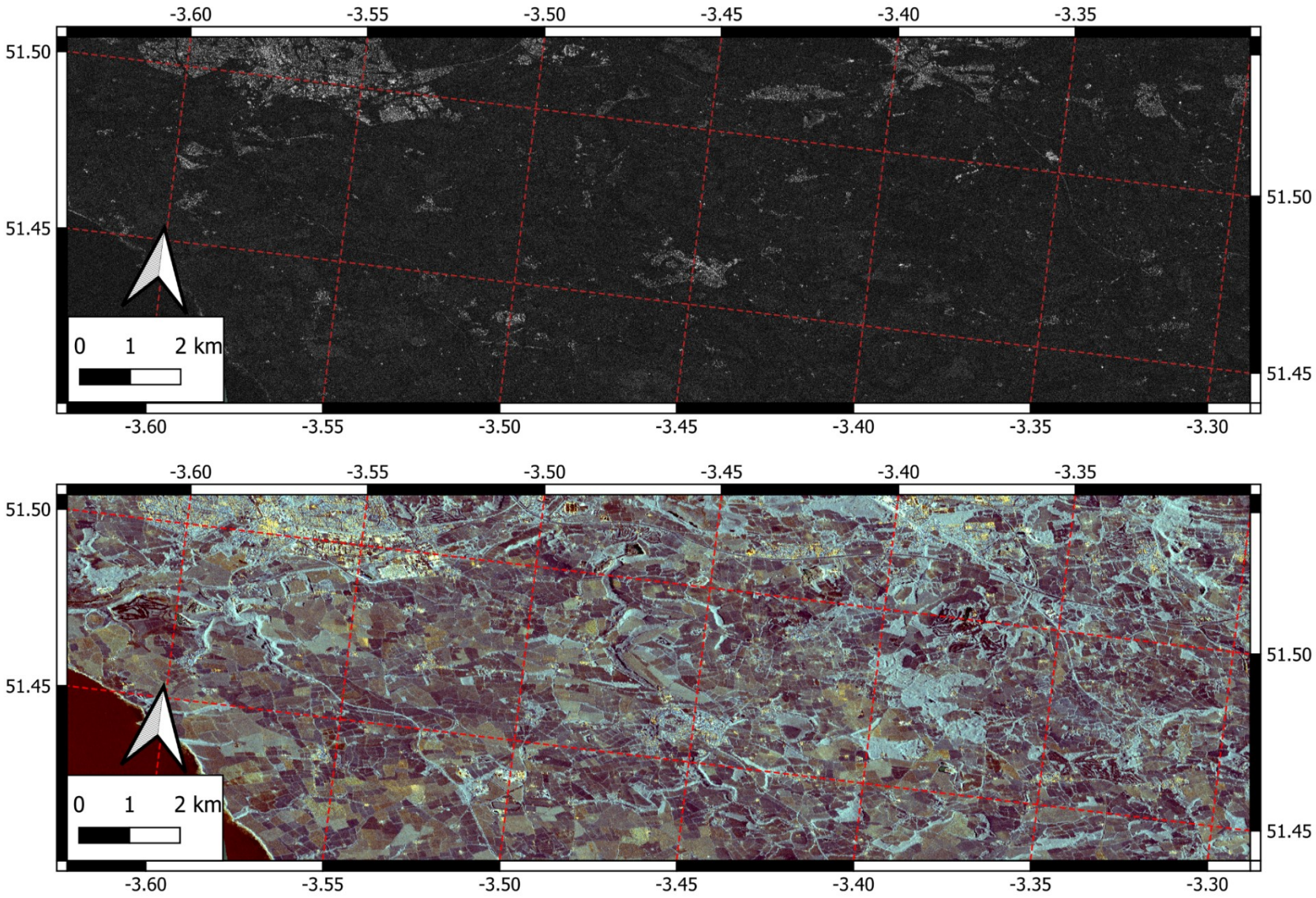


Figure 5-6: [Top] Temporal coherence between VV and VH measurements (0-1), with white indicating maximum coherence and black indicating no coherence. An additional metric for PS. [Bottom] False colour polarisation image, with channels scaled for visualisation purposes (R) log VV amplitude (G) log mean product of VV and VH amplitude (B) log mean VH amplitude.

5.3. Identifying TS

To summarise, TS will generally exhibit:

- Low temporal coherence
- Low amplitude stability
- Non-stationary amplitude processes
- Non-stationary rates of temporal decorrelation
- High entropy of the coherence matrix, a high proportion of significant eigenvalues.
- Decorrelation of VV and VH phase

A variety of data channels which provide information regarding transient scattering have been observed, but the optimal approach for combining these different metrics to discriminate the different scatterers is not immediately obvious. Many of these metrics (amplitude stability, coherence between polarimetric channels, entropy of the coherence matrix) appear more useful for identifying PS rather than determining which DS have behaviour that will produce consistent MTI phase errors. PS are generally defined as having high amplitude stability (Ferretti, Prati and Rocca, 2001), polarimetric stability, and low entropy of the coherence matrix (Ferretti *et al.*, 2014).

An ideal metric would quantify the change in scattering. Approaches presented which measure variations in entropy and amplitude distributions over time as in Figure 5-5 are promising, but the flexible choice of window parameters adds ambiguity, while performing repeated statical tests and Eigen decomposition over a sliding window becomes computationally expensive for long time series.

Our ultimate interest is in identifying spatially and temporally consistent (and therefore predictable) trends in the scattering which may affect the MTI phase time series. Pragmatically, to identify consistent spatiotemporal trends temporal correlation should be investigated, with a view to then assessing common patterns across the spatial data. The subsequent section analyses temporal correlation in polarimetric amplitudes and coherence.

5.4. Time series analysis via Fourier components

It is the temporal patterns of these values that distinguish them from one another. We therefore use the frequency domain to analyse these variables. Any temporally correlated trends will manifest in the frequency components of a discrete Fourier transform, while random errors due to noise in the time-series variables will manifest as zero-mean gaussian noise in the frequency-domain representation, symmetrically clustered around 0 (Shumway and Stoffer, 2017). This property conveniently allows for temporally correlated patterns to be quantified and compared from sample-to-sample.

If we use both the real and imaginary components of the Discrete Fourier Transform (DFT) as input data for a K-means algorithm, minimizing the distance between clusters is equivalent to maximizing the cross correlation between points within a cluster. The normalized cross correlation is a common metric for synchronicity between signal time series. As we look to identify synchronous time-series behaviour between scatterers, we are principally interested in their value at zero-time lag taken between two scatterer time series, which is simply the sum of the Fourier amplitudes with unit weightings, normalized by the energy of each signal:

Equation 5-4: Cross-correlation between pixels measured via discrete Fourier transform.

$$\vec{A} = \{A_{t=1}, A_{t=2}, \dots A_{t=Nscenes}\}$$

$$\eta(i_{pix1}, i_{DFT}) = \frac{F(\vec{A}_{pix1}, i_{DFT})}{\sqrt{\sum_{i=1}^{N_{DFT}} \left|F(\vec{A}_{pix1}, i_{DFT})\right|^2}}$$

$$\rho(i_{pix1}, i_{pix2}) = \sum_{i_{DFT}=1}^{N_{DFT}} \eta(i_{pix1}, i_{DFT})^* \cdot \eta(i_{pix2}, i_{DFT})$$

where $\vec{A}$ is a vector containing the amplitude time series for arbitrary spatial index p or q, $F(a, w)$ is the discrete Fourier transform of a taken over a series of frequency components indexed by w and of length W. The asterisk(η^*) denotes complex conjugation. The cross correlation at zero lag of the normalized Fourier transform vectors is then ρ. This formula for computing cross correlation may be familiar to those who have calculated the coherence of complex interferometric samples, while here it is applied to Fourier transforms of real valued time series.

To interpret the significance of a given ρ value we should first explore the statistical features of the Discrete Fourier Series (DFS). Of notable use is the fact that Fourier component amplitudes of gaussian distributed samples are also gaussian distributed, with individual variances in the frequency domain being the reciprocal of that in the sample domain. Temporally uncorrelated sources of noise such as speckle, thermal, clutter, calibration errors, baseline effects will increase the variance of the time series but are uncorrelated in time and only contribute stochastically to the DFS. For uncorrelated signal amplitudes, the real and imaginary parts of normalized DFS components have variance $1/2(\ N_{DFT}\ -\ 1\ )$ for all non-zero frequencies. The probability that a magnitude of ρ is simply the product of uncorrelated noise then follows as:

Equation 5-5: Significance of an individual DFT component

$$\alpha_\rho = 1 - \mathrm{erf}\left(2\sqrt{2(N_{DFT} - 1)}|\rho|\right)$$

where 'erf' is the error function and α_ρ is the significance. To determine if a single sample time series is temporally correlated, we can thus test the set of Fourier components for normality such as through one of the many tests available such as KS, Lilliefors, Anderson-Darling, Shapiro Wilks (Walpole, Myers and Myers, 2012).

Figure 5-7 shows that high correlations can be found between areas of crops beyond samples local to the particular field. Areas of grassland typically yield lower correlations. Forests, roads, hedges, and urban areas are typically uncorrelated.

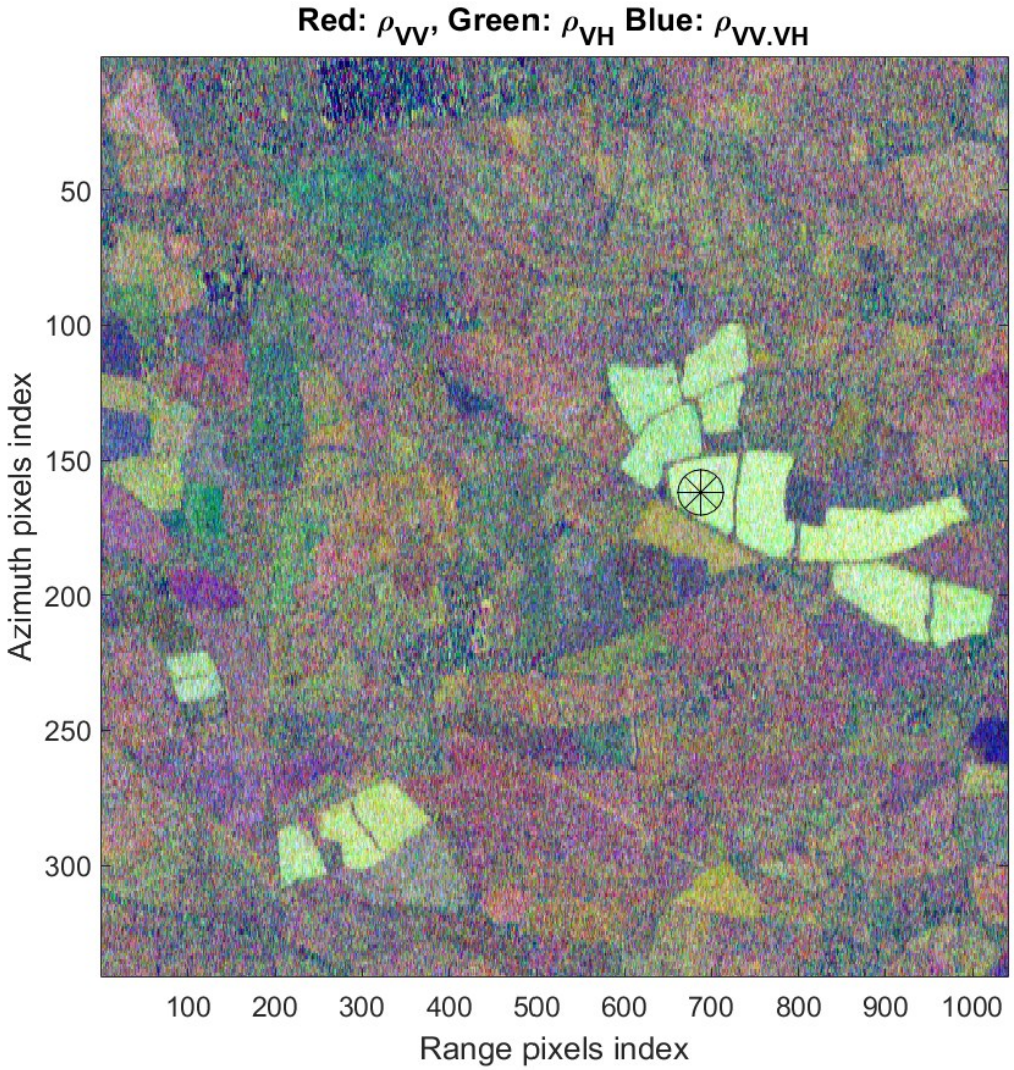


Figure 5-7: False colour image showing the correlation coefficient between time-series DFTs of the pixel indicated by the black wheel and the rest of the image. Correlations take values between 0 and 1 corresponding directly to the brightness of the channels: (R) VV amplitude, (G) VH amplitude, (B) the product of VV and VH.

It should be noted that the DFT assumes a periodic signal, where the SAR amplitude and other observables may not appear as periodic. The DFT will in these cases assume any discontinuity between the values at the start and end of the sample time series is a high-frequency 'jump' in the signal before it repeats.

As such, it may be advantageous to apply the DFT in annual windows, such that some common annual value appears at both ends of the sample time series. Other remedies such as low-pass filtering the affected high-frequency components may also be effective.

5.5. Time series clustering

Much as PS can be identified via high amplitude stability and coherence, a transient scatterer may be identified via time series variation in these quantities. Given the widespread use of SAR data in LULC analysis and crop biomass tracking, an opportunity exists to use the SAR data itself to segment the scatterers under analysis. Given the clear correlation between crop types and the observed time-series scattering in terms of amplitude and coherence measurements (as exampled in Figure 5-5) clustering areas in the SAR image series according to these observables may yield more specific and accurate estimates of the transient scattering phase.

5.5.1. K-means clustering

K-means (Lloyd, 1982) is a popular algorithm for clustering noisy data sets. The algorithm finds k characteristic signal 'centroids' in a set of training data provided, with k specified. A typical implementation of the algorithm proceeds as follows:

1) Define a matrix Ω of size $[N\ x\ M]$ to contain data for clustering. The N rows each correspond to the location of a sample in the SAR image stack (i.e., a coordinate in azimuth and range). The M columns each contain an arbitrary measurement of the samples.
2) Given a number of clusters k, find k initial estimates of the centroids (Arthur and Vassilvitskii, 2007). Each centroid is a $[1\ x\ M]$ row of values in the measurement space designed to represent a characteristic value for a subset (cluster) of the samples.
3) Treating the M measurements as a Euclidean space, we then find the Euclidean distance between the N sample rows and the k cluster centroids.
4) The closest centroid for each of the N samples is found, the N samples are then labelled as members of that centroids cluster.
5) Update the k cluster centroids by finding the M mean measurement values over the cluster's member samples.

6) Iterate the steps between 3) and 5) until the N cluster labels are unchanged between iterations.

Rather than develop a bespoke K-means implementation we can simply make use of existing offerings such as in Matlab as in these examples (MATLAB, 2023), or popular open software such as R, scikit, QGIS. The only parameter required is the number of clusters k. However, attention is required in the selection of input measurements for clustering over, and the scaling and relative weighting of these.

5.5.2. Training Data

This approach can be extended to include further polarimetric amplitude and coherence channels by simply appending the normalized DFT spectra to the matrix of training data. By scaling the input to the DFT by the inverse of its standard deviation, and the resulting DFT components by a factor of $2/\sqrt{2\,N}$, the resulting real and imaginary components will be standard normally distributed for temporally uncorrelated data. In this manner, distances between clusters will only be related to the temporally correlated signal variance as compared to its noise, and not to any particular scaling of each channel.

This allows arbitrary time series to be combined and exploited in a straightforward manner. For Sentinel 1 data used in this paper we exploited the VV and VH amplitude time series, along with time series of coherence magnitude from temporally consecutive VV and VH interferograms.

The relative value of each time series in isolating distinct clusters is derived from their ability to identify distinct patterns of temporally correlated, shared, behaviour in sample populations. It therefore follows that the VV amplitude is of most immediate value to clustering: The VH amplitude is generally noisier, being secondary scatter from the vertical signal; the VH coherence magnitude is generally correlated with the VV coherence magnitude for similar reasons (Freeman and Durden, 1998) and thus the additional discriminatory power of each channel is far lower than if they were independent variables. The coherence magnitude is also distorted due to being an absolute-value

projection of the true complex coherence, and includes further errors due to the bias in its sample estimator at lower magnitudes (Touzi *et al.*, 1999) (see Section 2.4.7).

It is advisable to avoid clustering based on the phase time series itself: The objective is to identify changes in scattering behaviour that explain observed phase trends rather than to distinguish the phase trends themselves. Spatially extensive phase behaviour may be a product of atmospheric effects or ground deformation, which are generally independent from changes in amplitude and absolute coherence. As ground deformation is often the most valuable output of MTI analyses for end-users, it is important not to misinterpret these as due to processes in the scattering media and therefore remove these phase signals from results.

5.5.3. Automation

After selecting appropriate training data, the only remaining parameterization is the number of clusters, k. Choosing k Is generally a difficult problem which requires *ad hoc* solutions or prior experience (Hamerly and Elkan, 2003). It is hence worth reflecting that the goal is to isolate specific, coherent patterns in MTI datasets. It is therefore valuable to examine the coherence matrices at the sample locations and the 'Subset of Scatterers' coherence $|\gamma_S|$, defined in Chapter 4, Equation 4-5, which measures the spatially consistent component of coherence matrix phase for members of the subset.

It should be noted that this clustering approach may find value in other applications, such as land cover classification (see Section 5.5.4). In this case some other *ad-hoc* approach may be more appropriate.

The ideal value solution would isolate φ_{TS} for each individual interferometric measurement in the coherence matrix of a given sample. This is important, given the substantial lack of phase triangularity highlighted in Chapter 4.

For a clustering approach it is appropriate to define a correction matrix for each subset. By calculating the mean coherence matrix over the set of samples, any phase offsets which are common to the set will be removed, thus removing the influence of any

common transient scattering behaviour and allowing more accurate recovery of the traditional MTI measurements as specific to each individual samples. The Subset of Scatterers coherence is defined in Equation 5-6 for a sampled estimate over a cluster:

Equation 5-6: Subset of Scatterers coherence as sampled for a cluster

$$\Phi_{n_i,j} = e^{i \angle \gamma_{n_i,j}}$$

$$\hat{\gamma}_{S_k} \equiv \frac{1}{N_k} \sum_{n \in k} \Phi_n$$

where $\{\gamma_1, \gamma_2, \ldots, \gamma_N\}$ is the coherence matrix for a member of the subset, $\Phi_{n_i,j}$ is the normalised phase value for each element i,j in a sample coherence matrix. $\sum \gamma_n$ is the elementwise sum of these normalised phase matrices.

$\hat{\gamma}_{S_k}$ is then the coherence for Subset of Scatterers k. The magnitude of the elements $|\gamma_{S_i,j}|$ measure the level of agreement in phase over $\{\gamma_1, \gamma_2, \ldots, \gamma_N\}$. Maximising the total agreement over all elements of all sample coherence matrices will maximise the subset phase that is isolated.

Equation 5-7: Score for a given clustering solution.

$$\beta_K \equiv \sum_k \sum_i \sum_j |\hat{\gamma}_{S_i,j}|$$

A clustering solution, where K subsets have been fitted, will yield a score defined as β_K, the total level of agreement of subset phase. This simple approach can be seen as similar to an existing measure of 'goodness of fit' in phase triangulation (Ferretti *et al.*, 2014).

As K becomes large issues of bias become problematic. In an extreme solution where K is equal to the total number of coherence matrices being analysed, each $\hat{\gamma}_{S_k}$ will be equal to 1 and all useful phase information will be removed. The increase in score between β_K and β_{K+1} should therefore be monitored and can be compared against the increase in β_K

for a random solution to ensure improvements in agreement are not simply selection bias.

To investigate automation, the clustering approach with DFT training data was applied to the crop maps dataset described in Chapter 4. The same stack of 60 Sentinel 1 Track 30 images was used from the calendar year 2018. Figure 5-8 shows how the agreement in $\hat{\gamma}_{S_k}$ improves through application of the K-means approach. The figure plots β_K (as a ratio of the initial $\beta_{K=0}$ where no correction was applied) against K for various approaches.

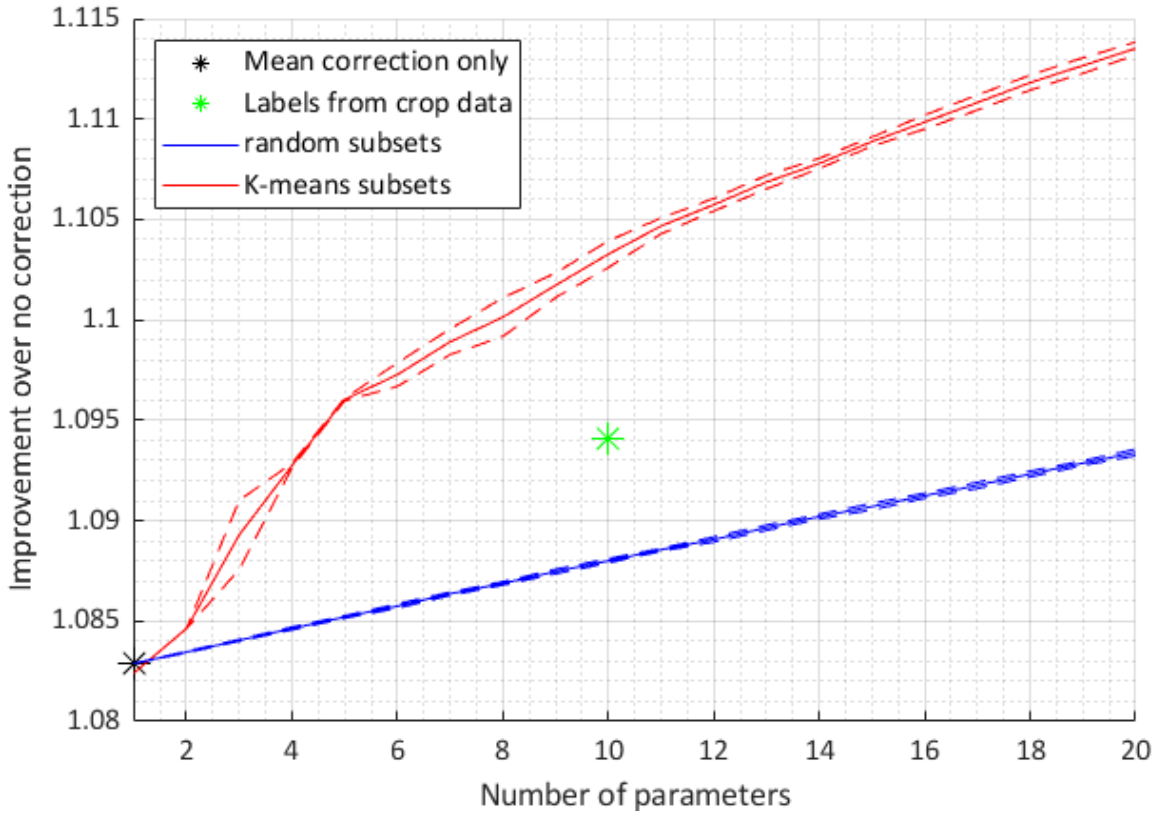


Figure 5-8: Improvement in score under a variety of subset correction approaches (Y axis) as a ratio of the score calculated when no correction is applied. The X axis shows the number of clusters (in the case of K-means, red curve, or randomly selected subsets, blue curve). For the crop data, green wheel, the X axis represents the number of labels. Multiple iterations of the sub-setting were performed, with the dotted lines representing +/-1 standard deviation.

The improvement in β_K score from the K-means approach is significant when moving from $K = 1$ to around $K = 4$. From $K = 5$ onwards the K-means approach exceeds the improvement granted through use of the *a priori* labels of crop map for the fields, despite there being 10 labels in the a priori data. Beyond approximately $K = 13$ the improvement

per K is lower and becomes comparable to the random subsets, indicating any further reduction in scattering error will be counteracted by an increase in selection bias due to overfitting. An appropriate number of clusters can then be found where the improvement from sub-setting exceeds the spurious improvement (bias) being introduced by over-parameterisation.

Figure 5-9 shows how a maxima in improvement can be found, following this approach.

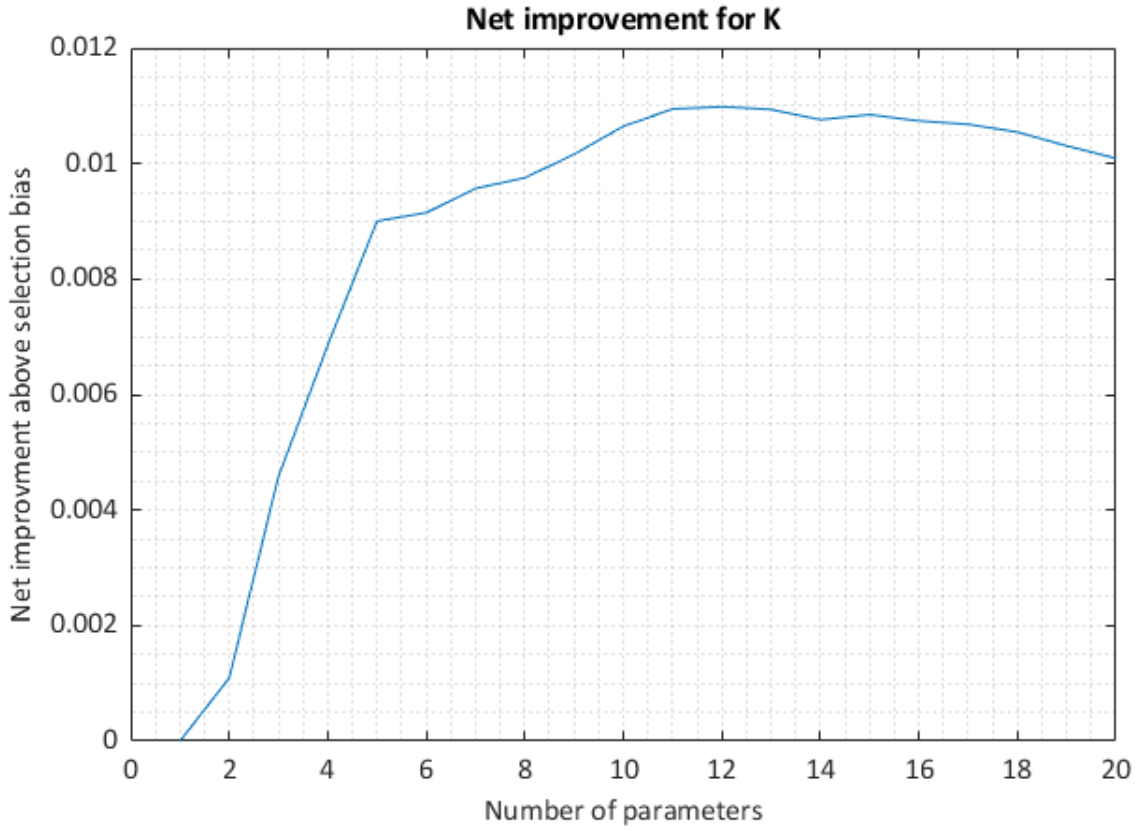


Figure 5-9: By finding the maximum of $\beta_{K_K-means} - 2 * \beta_{K_Random}$ the improvement of β_K should be maximised while ensuring each increment outweighs the error introduced due to selection bias.

5.5.4. Basic classification

Another, non-automated, method may be to exploit available a priori data, such as the UKCEH data described in Section 4.6.1. Given that vegetation type has an apparently

significant effect upon the phase, an effective clustering solution should therefore be adept in distinguishing different types of vegetation known to be in the data set.

The K-means clusters do not provide any information, in isolation. about the underlying physical labels for their member samples. It is therefore challenging to directly compare crop labels and cluster indices, especially when the number of clusters differs from the number of labels.

One approximate solution is to use the *a priori* data as a reference and choose the labels found most frequently at the locations of cluster samples. This is shown in Figure 5-10, where a classification is hence produced by this modal approach.

Following this, an appropriate number of clusters can be estimated by finding the point where agreement no longer improves upon adding more clusters, as shown in Figure 5-13. Here the agreement improves significantly up to roughly 15 clusters and then fails to improve.

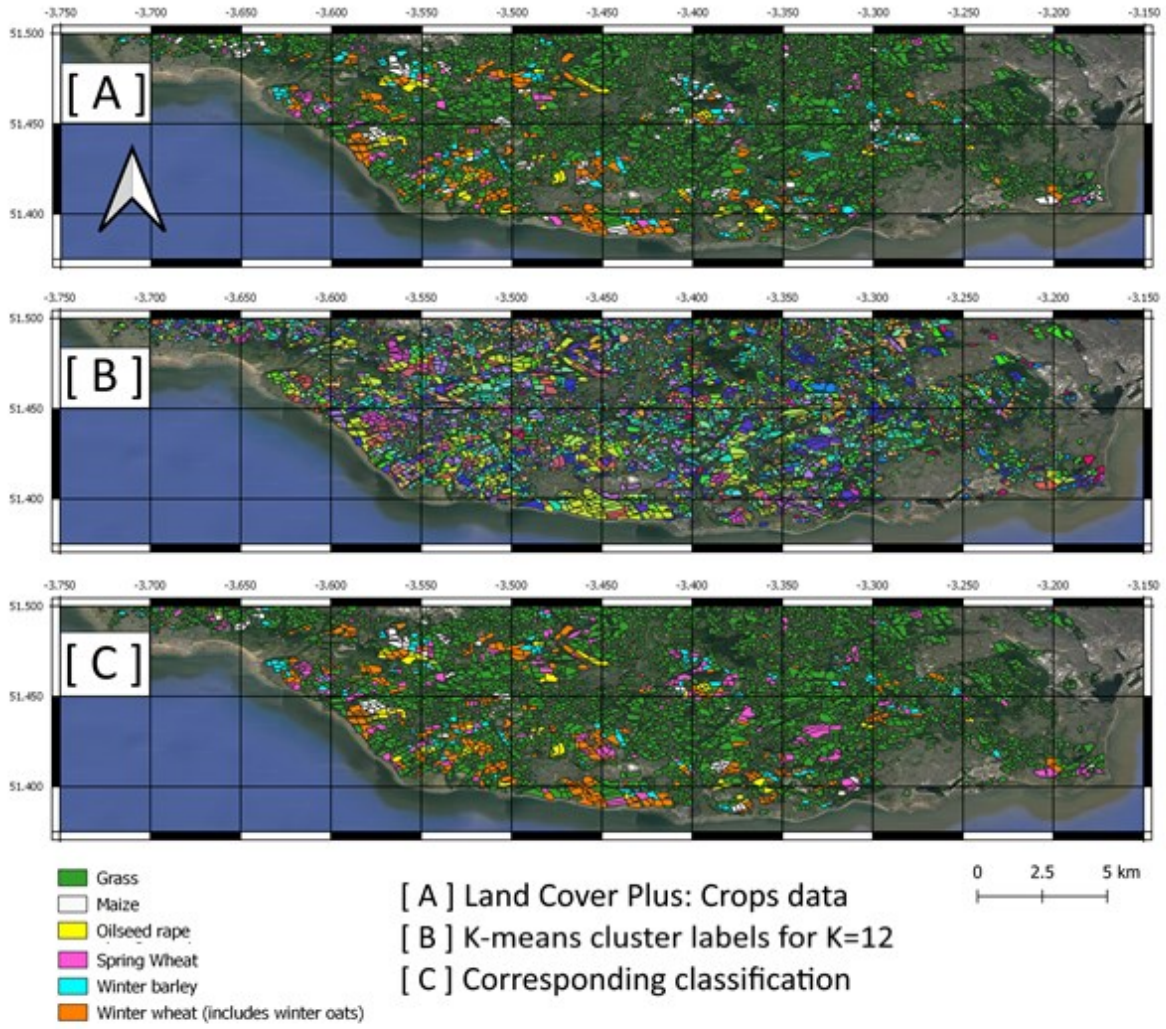


Figure 5-10: Agreement between land cover data and the K-means clustering solution.

The K-means clustering solution, on a regional scale in in Figure 5-10, appears to group large areas of grass in correspondence with the *a priori* land cover labels. The correlation between this grouping and the grass areas suggests vegetation type is a key control on the radar time series used in clustering. It is notable that the two datasets agree, despite the 'Grass' label in the *a priori* crop data covering a range of grass uses such as pasture, hay, and fallow (UK Centre for Ecology and Hydrology, 2018).

Discerning agricultural crops beyond grass is, however, is perhaps more interesting for applications of land cover classification. As such, Figure 5-11 and Figure 5-12 demonstrate the levels of agreement between the K-means solution and the *a priori* land cover data

for areas of cereal crop land use, showing areas with relatively high and low agreement respectively. Figure 5-13 shows the relationship between agreement and the number of clusters fitted.

In Figure 5-11, K-means clusters for Winter Wheat (orange), Maize (white), and Oilseed Rape (yellow) are in high agreement with the labels in the Land Cover+ Crops data. In the detection of these crops, there are only 2 disagreements over 42 field parcels.

In Figure 5-12 it can be visually interpreted that while the K-means solution is relatively reliable in identifying cereal crops as distinct from 'grass', the ability to determine the type of crop can be limited (under the assumption that the *a priori* data is accurate here). Here many Maize fields were not identified, while many Spring Wheat (pink) fields were falsely identified. Agreement can still be seen as high in identification of Winter Wheat, Oilseed Rape, and Winter Barley (cyan) fields.

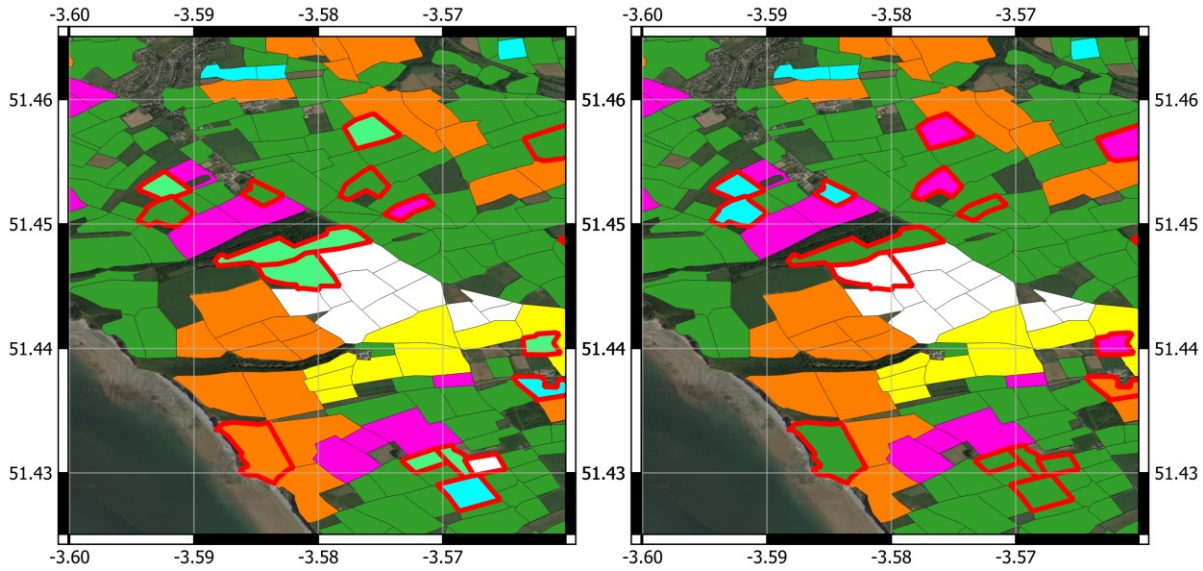


Figure 5-11: Extract from the a priori Land Cover map and the K-means clustering solution, showing an area of relatively good agreement in groupings. For crop label colour legend see Figure 5-10.

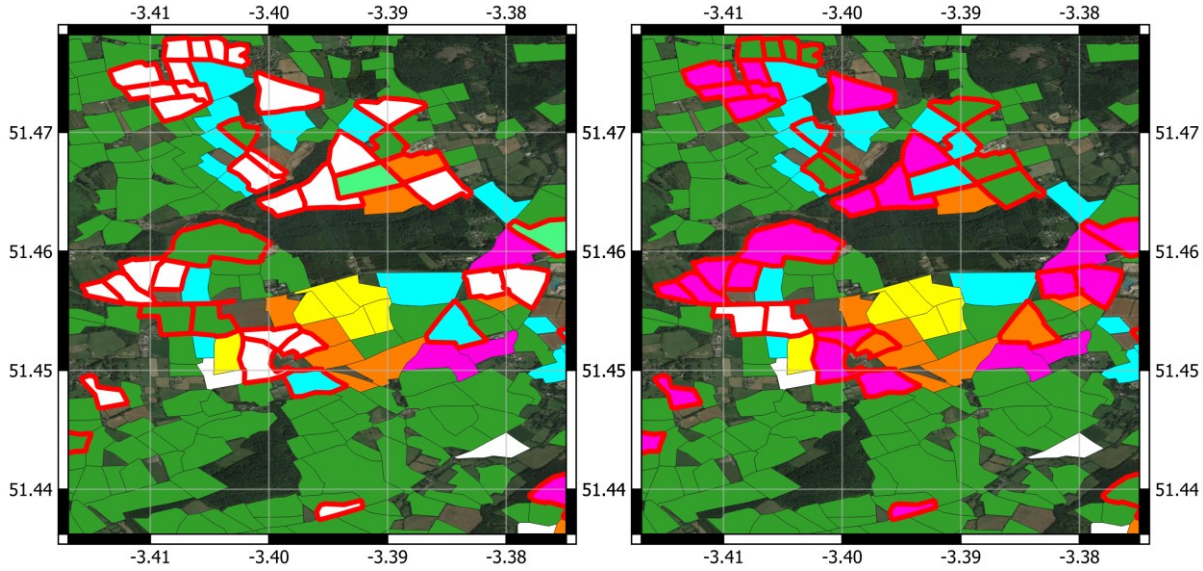
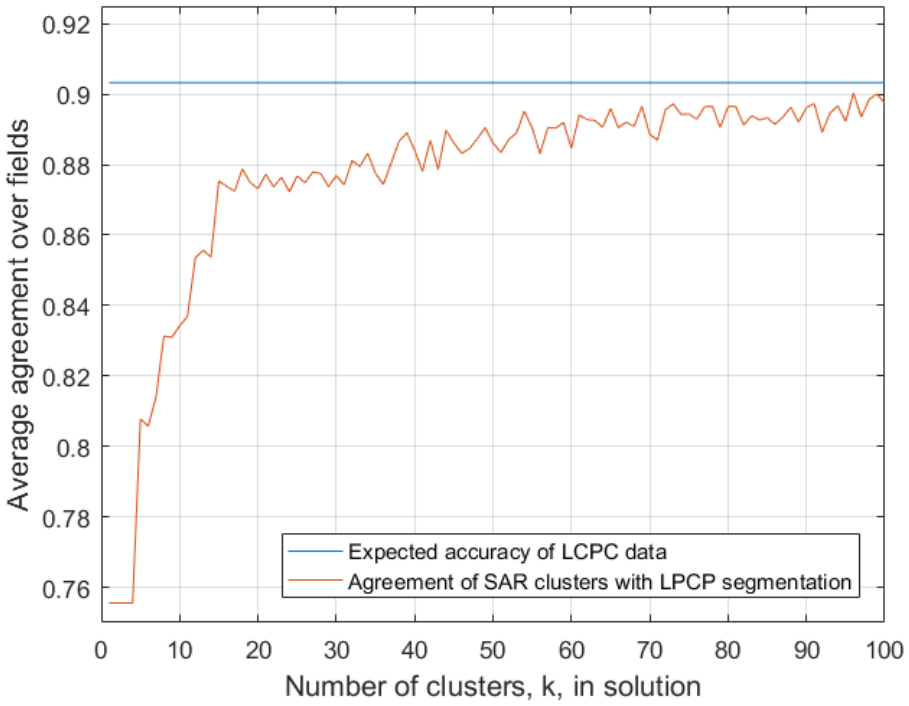


Figure 5-12: Area of relatively poor agreement between the a priori Land Cover map and the K-means clustering solution. For crop label colour legend see Figure 5-10.



	Grass	Maize	Canola	Spring Barley	Spring Wheat	Winter barley	Winter wheat
Number of fields present in LCPC data	3484	168	69	24	106	168	275
Stated accuracy of LCPC data	0.94	0.8	0.91	0.76	0.25	0.68	0.9

		Agreement between K-means clustering and LCPC data						
Number of clusters in solution	5	0.89	0.00	0.00	0.00	0.00	0.00	0.42
	10	0.89	0.00	0.90	0.00	0.00	0.00	0.49
	15	0.93	0.54	0.91	0.00	0.00	0.63	0.72
	20	0.94	0.50	0.91	0.00	0.00	0.74	0.83
	25	0.94	0.60	0.91	0.00	0.28	0.76	0.84
	50	0.95	0.64	0.87	0.00	0.50	0.88	0.74
	100	0.95	0.70	0.94	0.00	0.51	0.89	0.78

Figure 5-13: Agreement between clustering solution and *a priori* crop map. As the number of clusters *k* increases, as does the agreement with the available ground truth regarding land cover. Due to limitations of either the clustering or the ground truth this will converge at reach a point where further improvements are minimal. This point can be seen around 15 clusters for the data above.

5.5.5. Analysis

Figure 5-14 shows the phase and magnitude of the Subset of Scatterers coherences, $\hat{\gamma}_{S_k}$, fitted to MTI data for the crop dataset. As in Chapter 4, significant phase ramps of roughly π are seen between periods of winter coherence and more variable summer behaviour. The level of agreement within the clusters is again very high, as quantified by Figure 5-8.

The general trend of the clusters appears to be remarkably similar, with a period of relatively low phase offsets following the aforementioned, paticularly, large shift in Spring. The timing of the 'Spring shift' and the magnitude of its phase offsets appears to differ slightly from cluster to cluster but in general the mechanisms appear very similar. It is possible that this Spring shift is a common mechanism in the paticularly population of fields under study, which is mainly agricultural fields.

It is possible that many of the field polygons used to generate the coherence matrices contain some signal contribution from nearby signal targets, in which case the patterns in φ_{TS} could be 'masked' by coherence from these PS or PS-like targets in interferograms where the transient scatterers have low spatial coherence. Cluster 11 in paticular appears to have stable phase and persistent coherence. Additional work may investigate how to best filter within the DS themselves to isolate the multiple scatterer populations.

The agreement in phase offset within the clusters is paticularly noteworthy, considering the large sample sizes involved and the magnitudes recorded for many of the offsets. The patterns in agreement appear more distinct than the patterns in phase, suggesting the value of coherence changes in determining the timing of φ_{TS} shifts.

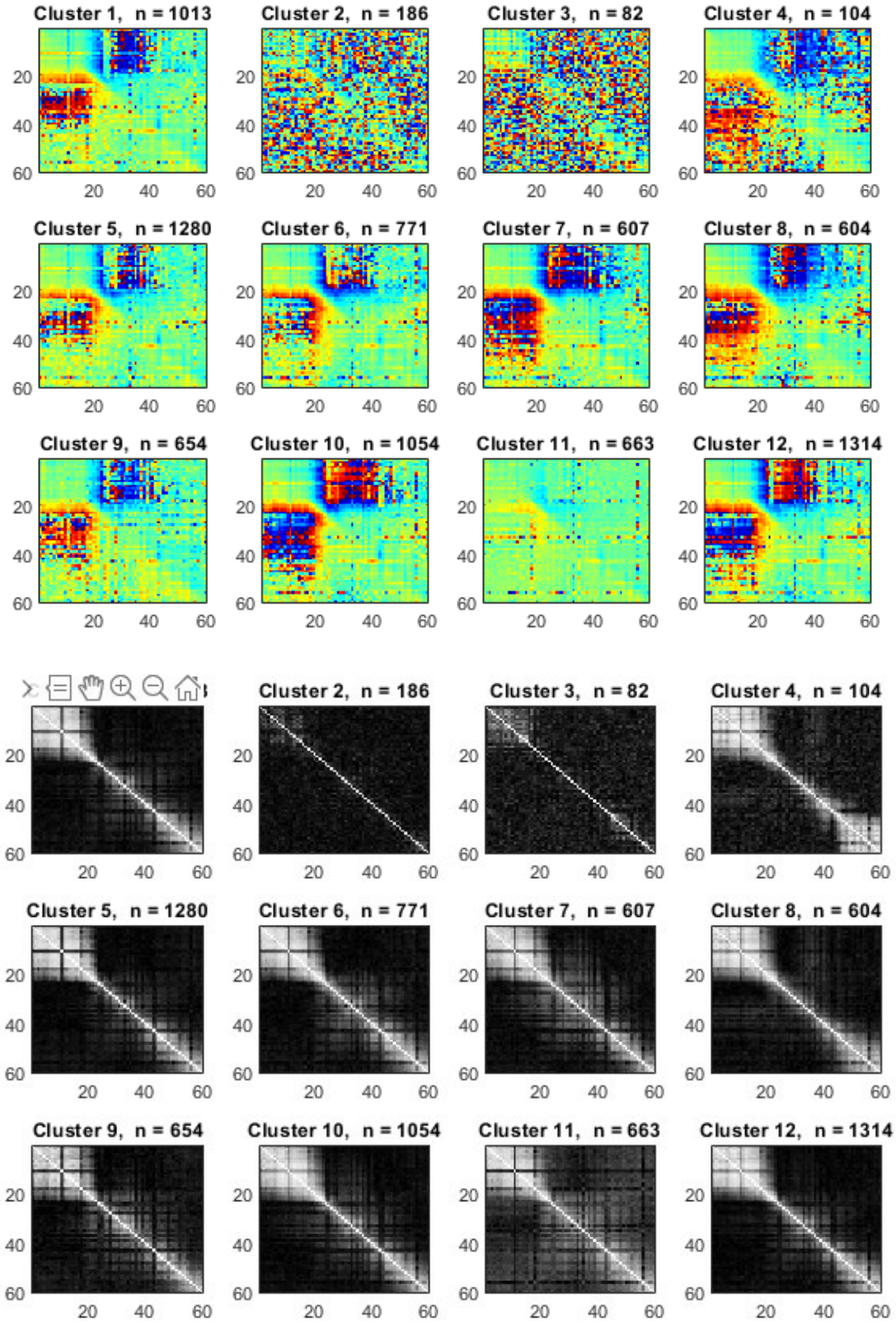


Figure 5-14: [Top] Argument of the Subset of Scatterers coherence $\angle\hat{\gamma}_{S_k}$, corresponding to average phase for clusters automatically fitted to the *a priori* crop data. [Bottom] Magnitude of this coherence $|\hat{\gamma}_{S_k}|$, reflecting the degree of agreement between normalised phase values over the subset.

5.6. Conclusions

A range of metrics for transient scattering have been discussed, including amplitude stability, amplitude distribution testing, coherence matrix entropy, and polarimetric coherence and ratios in the context of dual-polarisation Sentinel 1 data. These metrics are perhaps more useful for identifying PS and screening them as opposed to discrimination which non-PS exhibit predictable φ_{TS} shifts. In order to achieve this, temporal correlation in scattering metrics were explored instead.

Analysing the data in the Frequency domain appears effective. Uncorrelated data is transformed into zero-mean gaussian random variables in the real and imaginary components of the DFT, allowing for easier discrimination and testing for correlated trends. The cross correlation may be used to identify scatterers with similar time-series trends in a computationally efficient manner, as shown in Figure 5-7. Finally, the measurement of correlation rather than particular distributions allows for dissimilar data sources such as amplitude and coherence from difference polarimetric channels to be combined effectively without necessitating complicated and likely *ad-hoc* weightings to be devised in order to facilitate the data fusion.

These combined measurements of temporal correlation can be used to train algorithms to search spatially for scatterers with similar behaviour. The K-means clustering algorithm is an efficient implementation which minimises the distance between automatically-identified clusters. Training the K-means centroids with DFT components is convenient in normalising the distances, otherwise outlier values for e.g. amplitude, such as from a very bright PS, can produce large distances in the training data and produce clusters with little analytical value.

The K-means + DFT approach suggested here provides significant power in identifying areas of similar scattering phase offsets. Outperforming the use of *a priori* crop map data with half the number of parameters (5 clusters vs 10 crop labels).

It should be noted that this approach was designed for mapping of crops and land cover, but rather as a tool to isolate scattering phase offsets. The value of K-means + DFT as a

land cover classifier is, however, promising. Correlation with existing land cover data is good (see Figure 5-13) but additional testing is required especially given the limitations in accuracy of the data compared against. This could imply disagreements between the K-means + DFT classifier and UKCEH data may not always reflect inaccuracies for the developed technique.

To adapt K-means + DFT for land cover mapping it may be appropriate to examine the best choice of training data, ideally including additional information regarding amplitudes and mean coherences rather than just the temporal correlation of these measurements. Careful thought will be necessary to best assign physical labels rather than arbitrary numbers for cluster indices, as the same class of land cover may have different scattering behaviour depending on (e.g.) its orientation, ground topography, incidence angle (Engdahl, 2013).

The additional level of data offered by combining polarimetric amplitudes and coherences is novel and particularly promising for data fusion purposes in classification. Additionally, $\hat{\gamma}_s$ may offer its phase and magnitude as two new data channels for use toward land cover classification.

The agreement in subset phase, $|\hat{\gamma}_s|$ can be used as a metric to automate the last user-specified parameter of the K-means approach which is the number of clusters. The improvement is assessed against the selection bias introduced as the number of clusters increases, via comparison to a bootstrapped random solution.

This automated system can be straightforwardly applied to the correction of φ_{TS} in MTI data stacks, albeit some care must be taken not to mask regionally extensive deformation as discussed in Section 4.5. In terms of coherence matrix MTI approaches, φ_{TS} calibration can occur immediately after adaptive spatial filtering of the DS: Nearby PS are first used to provide a calibration of the APS and long-wavelength deformation to allow for automatic selection of K and clustering. Once the $\hat{\gamma}_s$ set has been calculated the TS coherence matrices can be corrected, allowing for improved phase triangulation (removal of closure phase) as well as the correction of the main eigenvectors. The MTI analysis can then proceed as normal with 'squeezing' of the improved coherence matrices.

6. Transient scatterer deformation analysis in South Wales

6.1. Introduction

Chapter 5 highlighted the significant phase shifts associated with vegetated terrain. It subsequently demonstrated a method toward isolating these phase shifts by identifying distinct subsets of scatterer based on their behaviour in non-phase SAR and InSAR observables, and further demonstrated that this approach was effective.

The approaches described in Chapter 5 was applied to an MTI deformation study, to better investigate how correcting for φ_{TS} affected the deformation results. To continue the case study, a wider area of South Wales was analysed, including areas of known deformation corresponding to historical coal mining.

The valleys of South Wales were host to intense mining activity from the mid 19th century until the end of the 20th century. Significant ground instabilities associated with slopes and subsidence have long been recognised (Department of the Environment Welsh Office, 1990; Bromhead *et al.*, 2000). While activity has dwindled in recent years, the legacy of more than a century of extraction remains as evidenced by ongoing slope instabilities (Lee and Giles, 2020).

A previous InSAR study (Bateson *et al.*, 2015) suggested significant rebound deformation was occurring due to cessation of groundwater extraction.

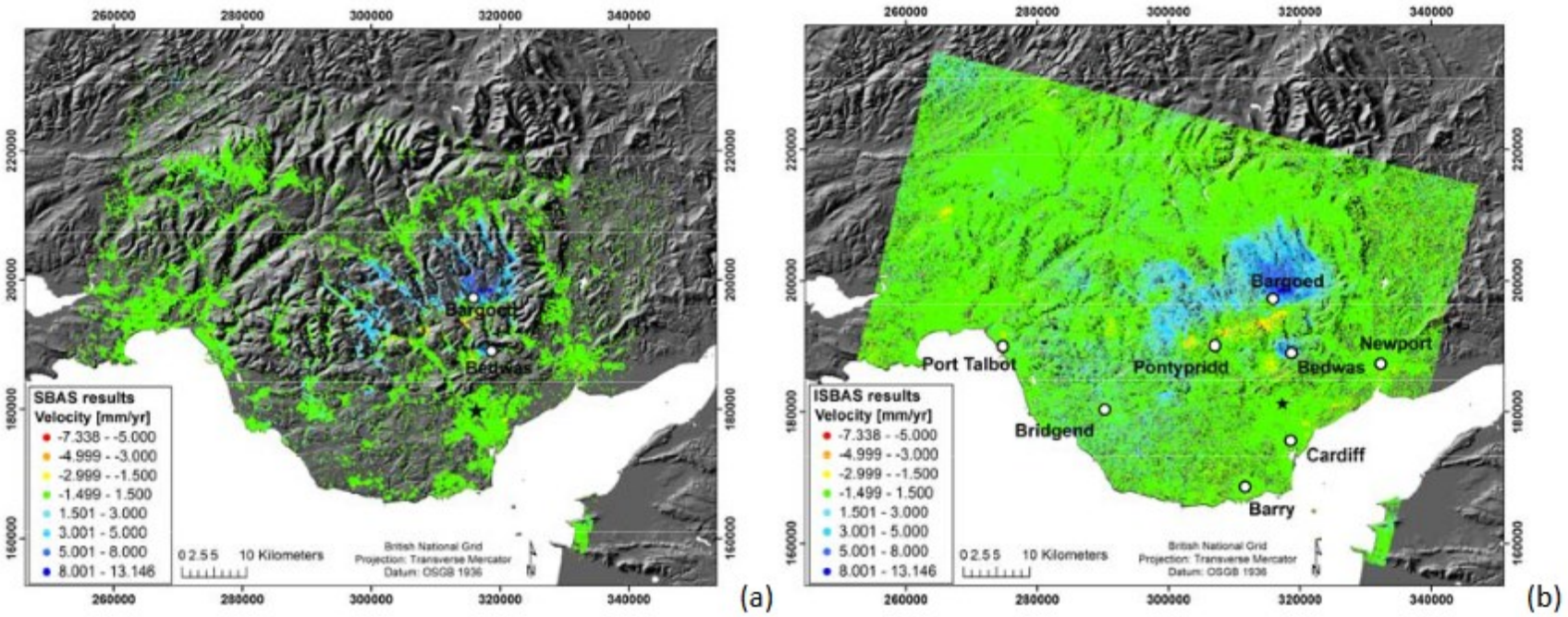


Figure 6-1: Results from a prior study of the area of interest (Bateson *et al.*, 2015). Bateson et al. used European Remote-Sensing Satellite 1 and 2. (a) SBAS methodology (Berardino *et al.*, 2002) and Intermittent SBAS (Sowter *et al.*, 2013) which uses any interferogram for which sufficient spatial coherence exists, rather than the traditional approach which requires sufficient spatial coherence for all small-baseline interferograms.

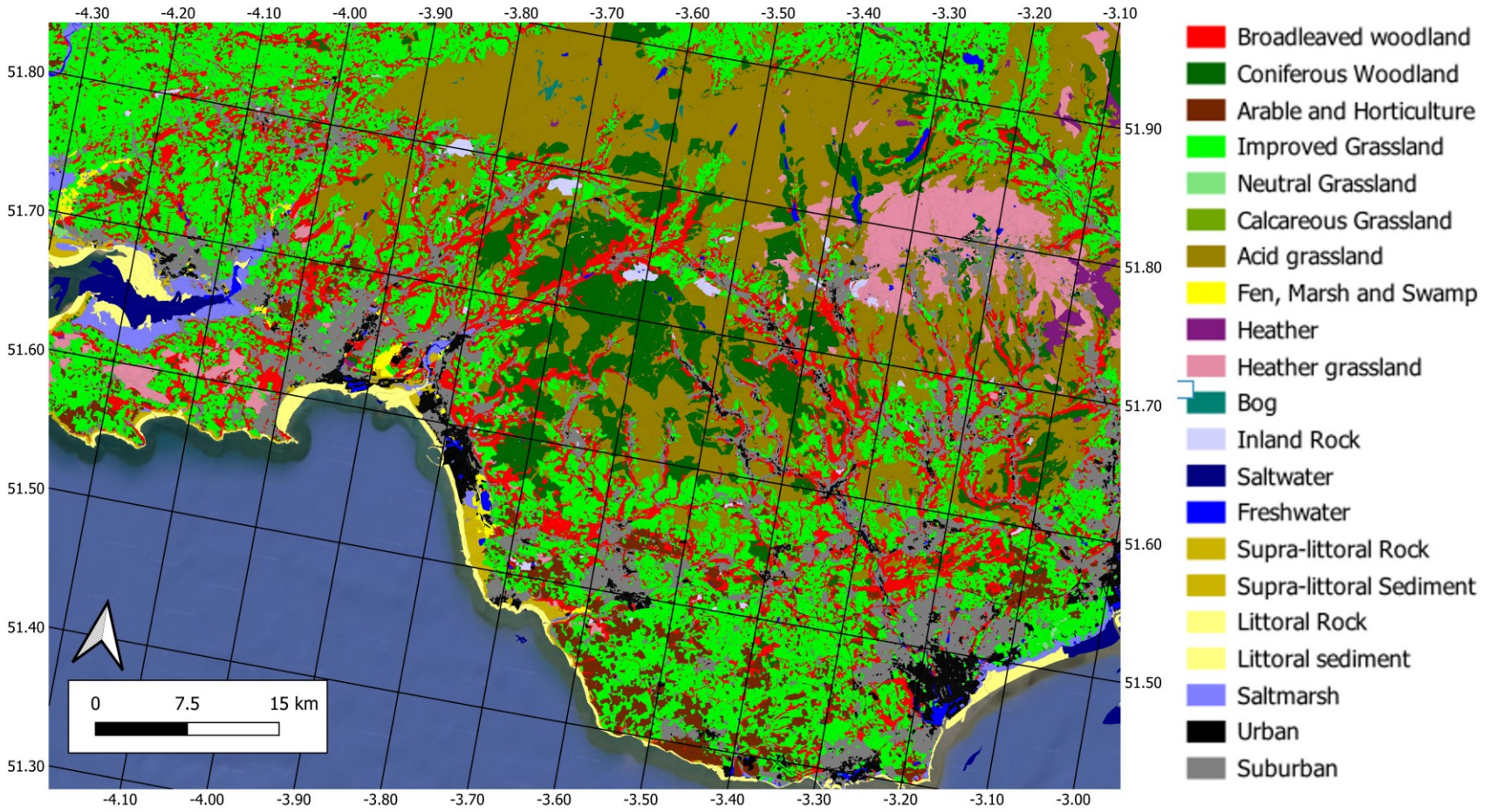


Figure 6-2: UKCEH Land Cover Map 2018 for comparison with Figure 6-4.

6.2. Methodology

230 scenes were processed, consisting of Sentinel 1A and 1B data from March 2015 to December 2019. After coregistration according to the procedure described in Chapter 3, single-look samples were adaptively filtered to find 'statistically homogenous pixels' (SHP) according to the KS test (Ferretti *et al.*, 2014) with a maximum window of 11 azimuth lines and 21 range samples. The significance threshold for the KS test was 0.1.

The data was then clustered via trends in the VV and VH amplitude and interferometric coherence using the K-means approach described in Chapter 5, as applied to DFT components of average time series amplitude and the magnitude for the first-super diagonal of the SHP coherence matrix. The number of clusters which optimised the significance of phase offsets was $K = 20$.

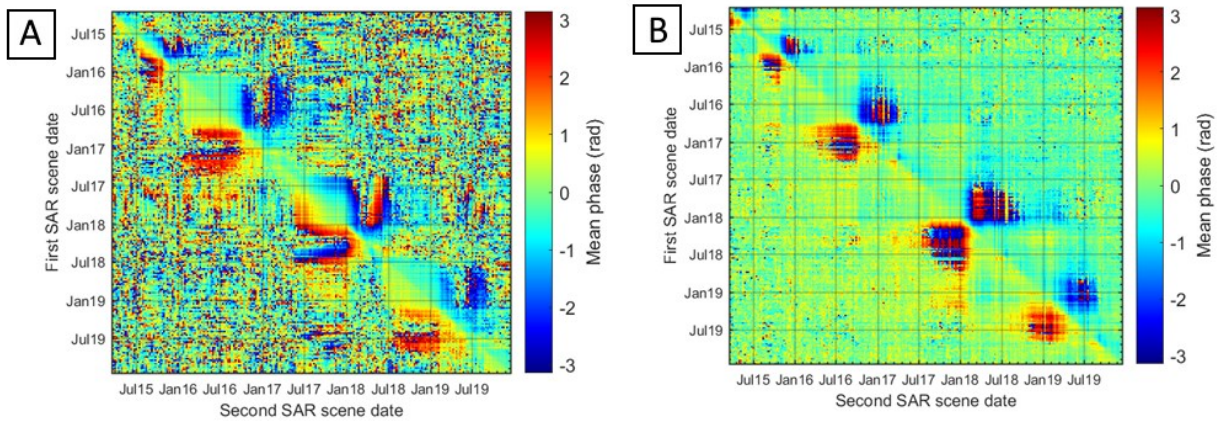


Figure 6-3: Phase of the scattering subset coherence, γ_S, for two cluster labels corresponding to areas classified as [A] arable and horticulture (presumed by author to be mainly winter wheat) and [B] improved grassland (presumed by author to be livestock-grazed).

The scattering subset coherence matrices, $\{\gamma_{S_K(1)}, \gamma_{S_K(2)}, \ldots, \gamma_{S_K(20)}\}$, were then formed and the average phase offsets used to correct the coherence matrices of the SHP according to

their corresponding scatterer label. Two examples of the γ_S phase can be seen in Figure 6-3, which shows the large ($\sim\pi$ radians) 'Spring shift' offsets first mentioned in Chapter 4 are a regular occurrence.

The remaining inversion of APS, height error, and deformation rates was performed as described in Chapter 3.

6.3. Results

The deformation rates measured as a result of the aforementioned process are shown from Figure 6-5, Figure 6-6 and throughout.

Figure 6-5 shows the PSI measurements obtained over the area of interest by way of comparison. Results are seen to be isolated to urban areas such as in Cardiff, Swansea, and the towns in the Valleys. Data is sparse and yet some deformation features are found corresponding to quarries and slopes associated with historical mining.

Figure 6-4 shows the K-means cluster labels assigned during the analysis through the methodology described in Chapter 5.

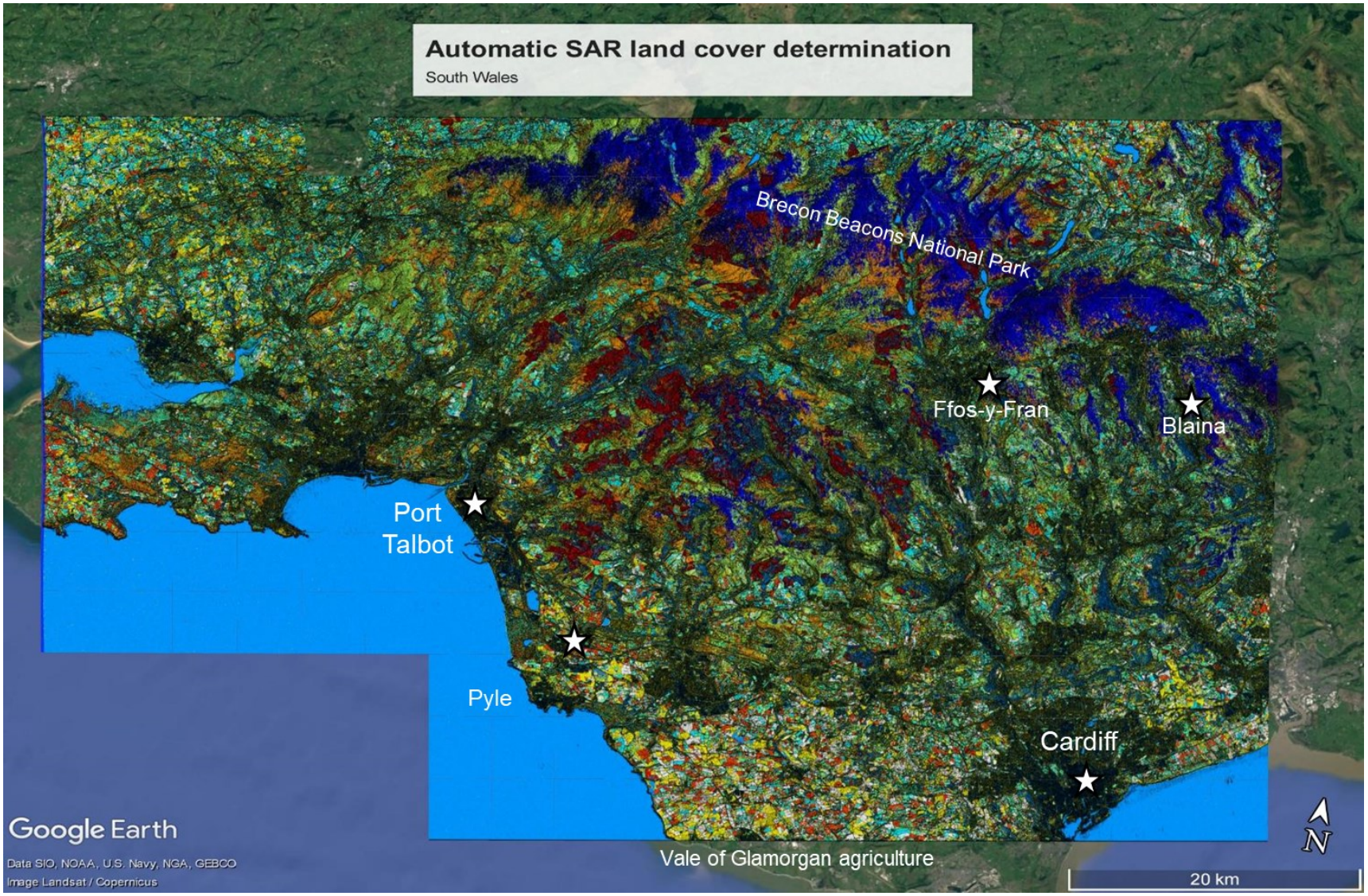


Figure 6-4: Geocoded K-means cluster labels automatically assigned to SAR pixels. A random colour has been assigned to each. Black pixels indicate those marked as PS or DS which exhibit limited transient scattering behaviour, including woodlands.

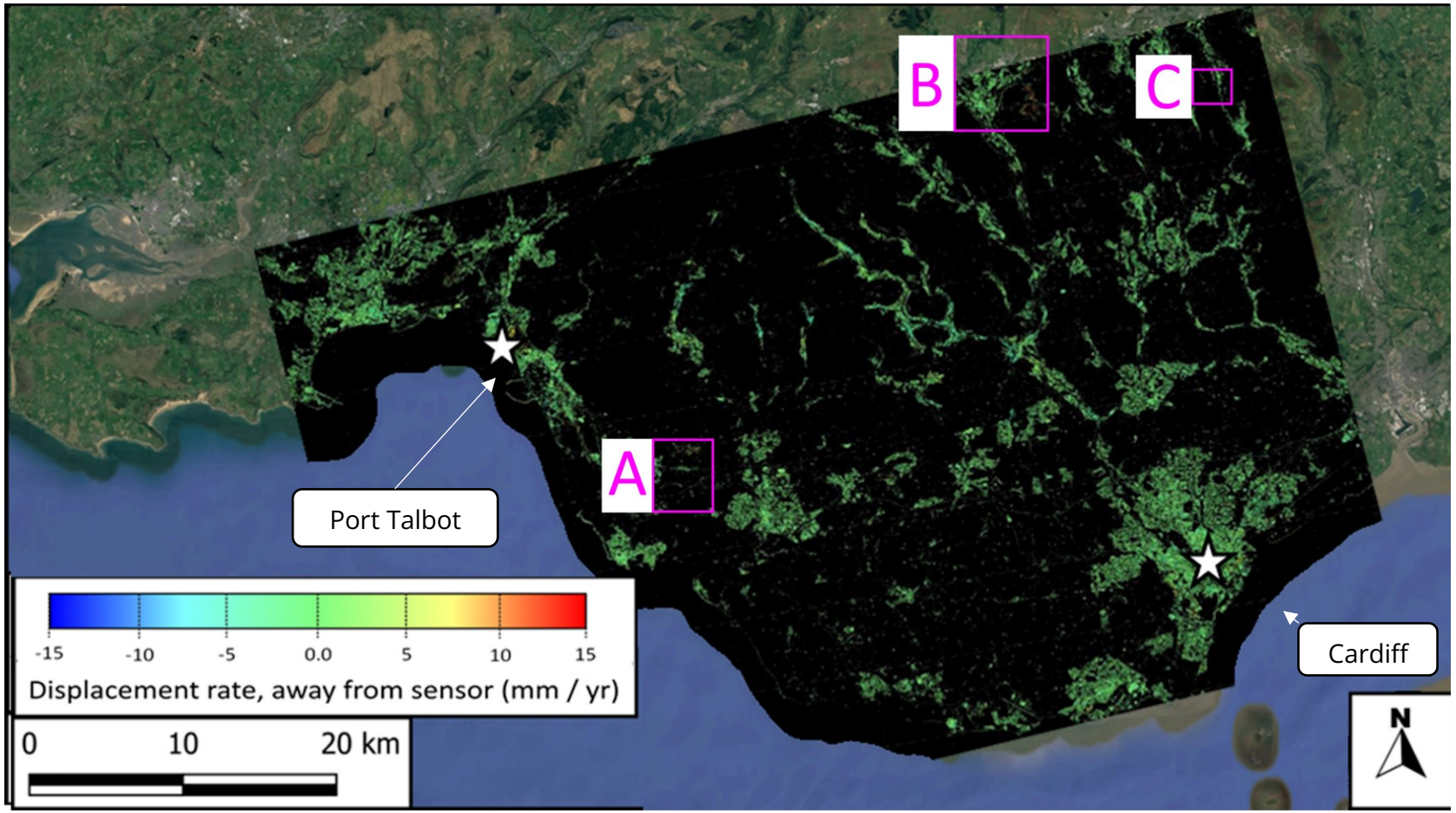


Figure 6-5: Results from PSI study of South Wales. The pink rectangles demarcate areas discussed in further detail in Section 6.4, the corresponding labels are as follows - A: Margam Open Pit (Figure 6 10); B: Ffos-y-Fran project (Figure 6 11); C: Blaina landslides (Figure 6 7).

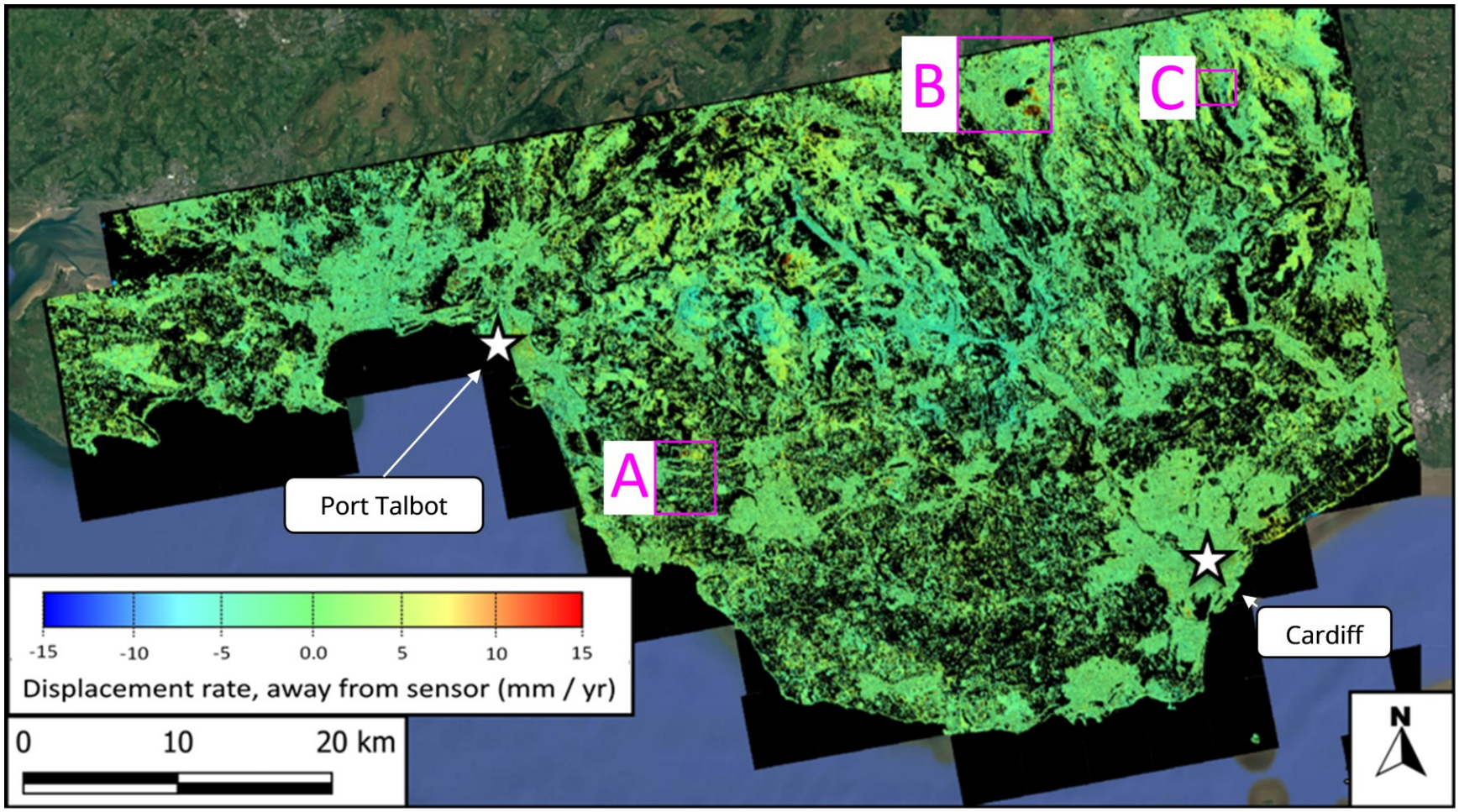


Figure 6-6: Results from MTI study of South Wales including compensation of apparent Transient Scattering behaviour. The pink rectangles demarcate areas discussed in further detail in Section 6.4, the corresponding labels are as follows - A: Margam Open Pit (Figure 6-17); B: Ffos-y-Fran project (Figure 6-18); C: Blaina landslides (Figure 6-12).

6.4. Analysis

The K-means labels assigned, seen in Figure 6-4, show an extensive and varied population of TS being identified. These labels correspond well with existing land cover classes.

The Brecon Beacons can be seen as exhibiting extensive areas of relatively homogenous cluster labels (blue and orange colouring), matching areas marked as 'acid grassland' and 'heather grassland' in existing land cover data shown in Figure 6-2 (Morton, 2018). The shape and approximately 50km extent of Brecon corresponds well between the existing and novel map, demonstrating that the K-means + DFT approach works well on wide regions of particular land cover as well as on a scale of agricultural fields analysed in prior chapters.

In the agriculturally fertile Vale of Glamorgan, a range of distinct cluster labels can be seen coinciding with the boundaries of fields. This implies the range of different crops exhibit distinct scattering behaviour, as discussed in Chapter 4. These clusters correspond well with the 'arable and horticulture' classes in the existing land cover map.

Black areas in Figure 6-4 depict PS, which can be seen in Cardiff and the industrial area around Port Talbot, and woodlands across the area. A less diverse range of scatterer labels (yellow and cyan colouring) can be found in remaining vegetated areas, which are less fertile and thus predominantly grass for livestock. The labelling still follows the distinct boundaries of the fields, and matches the 'improved grassland' class in the land cover map.

PSI deformation results reveal some deformation phenomena present in urban and industrial areas. Figure 6-7 shows PSI results from the Port Talbot, an area that has been heavily industrialised towards iron and steel production since 1831. Here, an area of housing to the north of the works can be seen as subsiding with rates between 3 and 15 mm a-1. the highest rates of movement detected from a school constructed in the year c. 2015 and a housing estate constructed in the year c. 2012. Deformation of the southern harbour sea wall of around 5 mm a^{-1} is also apparent.

In Cardiff, PSI results show settlement or subsidence of recent constructions at a marina site, and apparent slope movement of spoil heaps. Deformation activity at the marina site is corroborated by records showing its historical use as a landfill (Natural Resources Wales, 2017).

The TS corrected data, as seen in Figure 6-6, exhibits far more extensive data coverage in rural areas. This should be analysed in order to assess the validity of results. A large pattern of apparent uplift consistent with the results of previous studies (Bateson *et al.*, 2015) is observed. The suggested mechanism for this movement is groundwater recovery across the region after cessation of pumping for extensive coal mining which formed the major industry in the region until the late 1980's. A process, observed via various means including MTI, to occur across the UK (Forster *et al.*, 1994; Culshaw *et al.*, 2009; Mason *et al.*, 2015; Bischoff, 2019b). The rates of movement are somewhat lower than those measured by Bateson et al., perhaps reflecting the slowing of this phenomena over time as groundwater levels return to their original equilibrium.

New areas of active deformation can be identified in Figure 6-6 as compared to existing work of Bateson et al. shown in Figure 6-1. These new patterns of movement correlate with geographic features where deformation behaviour is expected, as will be analysed in the proceeding subsections. For example, Figure 6-10 and Figure 6-12 shows that K-means + DFT corrected MTI results show deformation occurring for the 'East Pentwyn' and 'Bourneville' landslides close to settlements of Blaina and Abertillery in Wales.

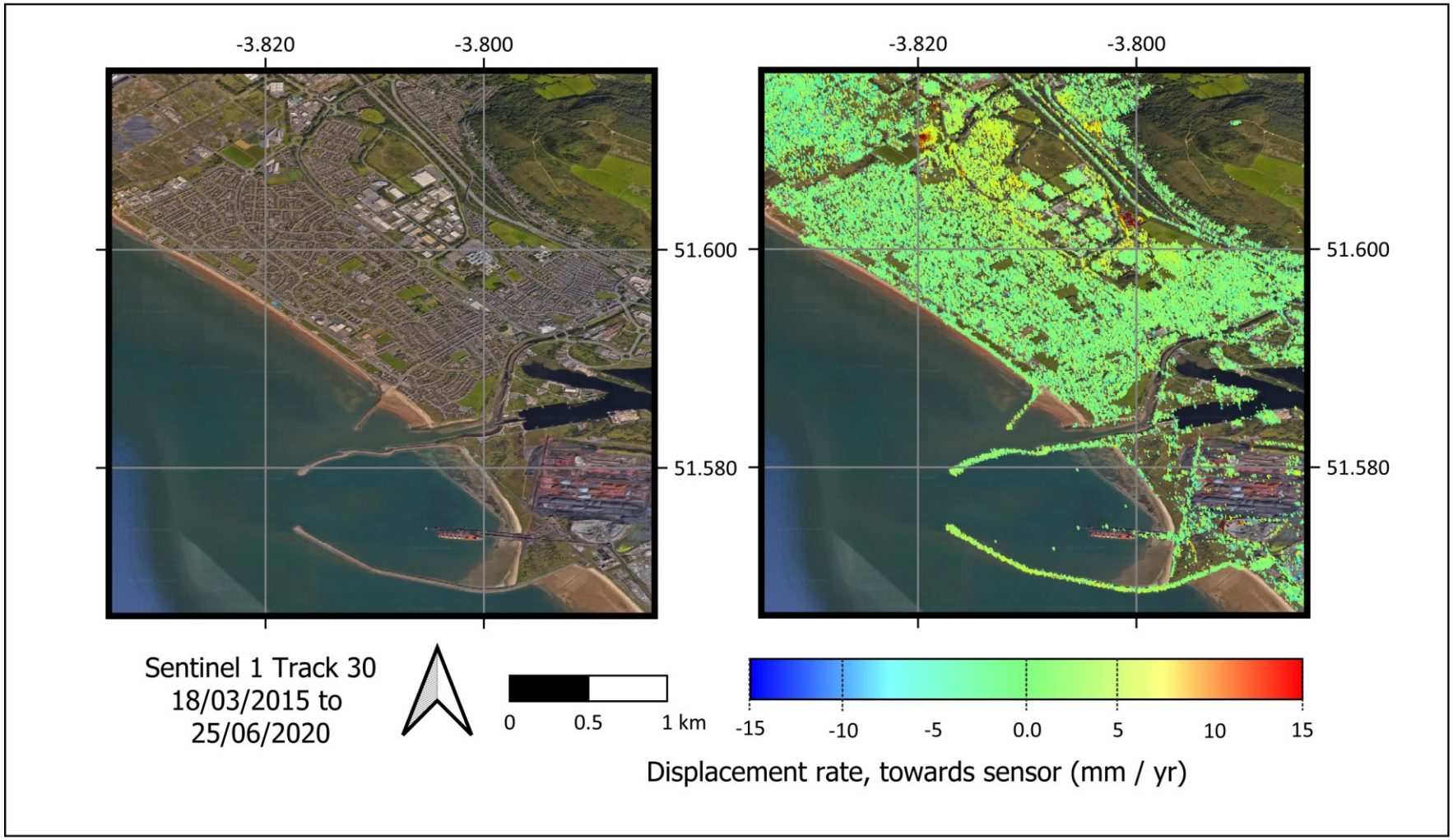


Figure 6-7: PSI results for Port Talbot showing subsidence of residential areas built upon sites of historical landfill and deformation of a harbour wall.

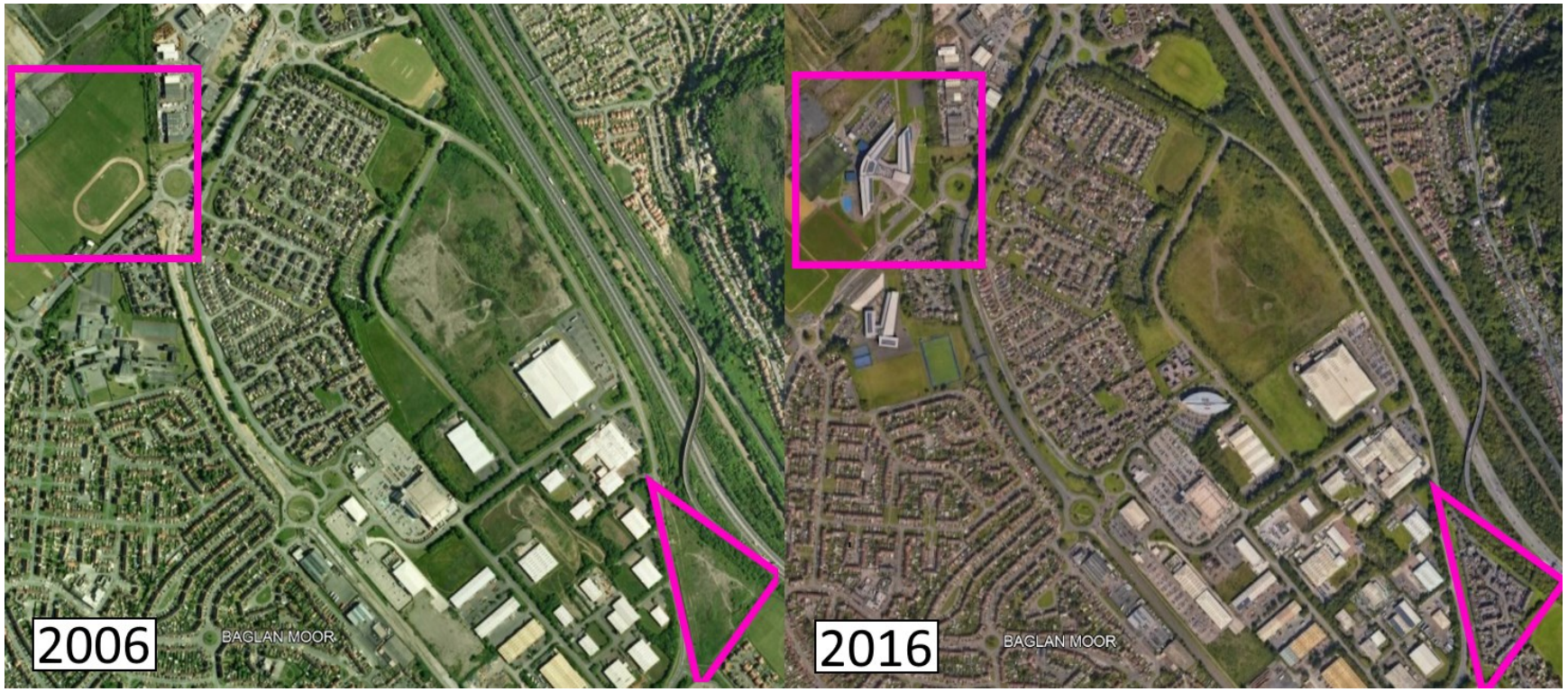


Figure 6-8: Historical imagery for the areas of settlement and subsidence shown in Figure 6-7. The pink square shows the construction of a large school, where the pink triangle shows construction of a number of houses on an existing landfill site. Other landfill sites are visible in the area, in line with the areas extensive industrial usage.

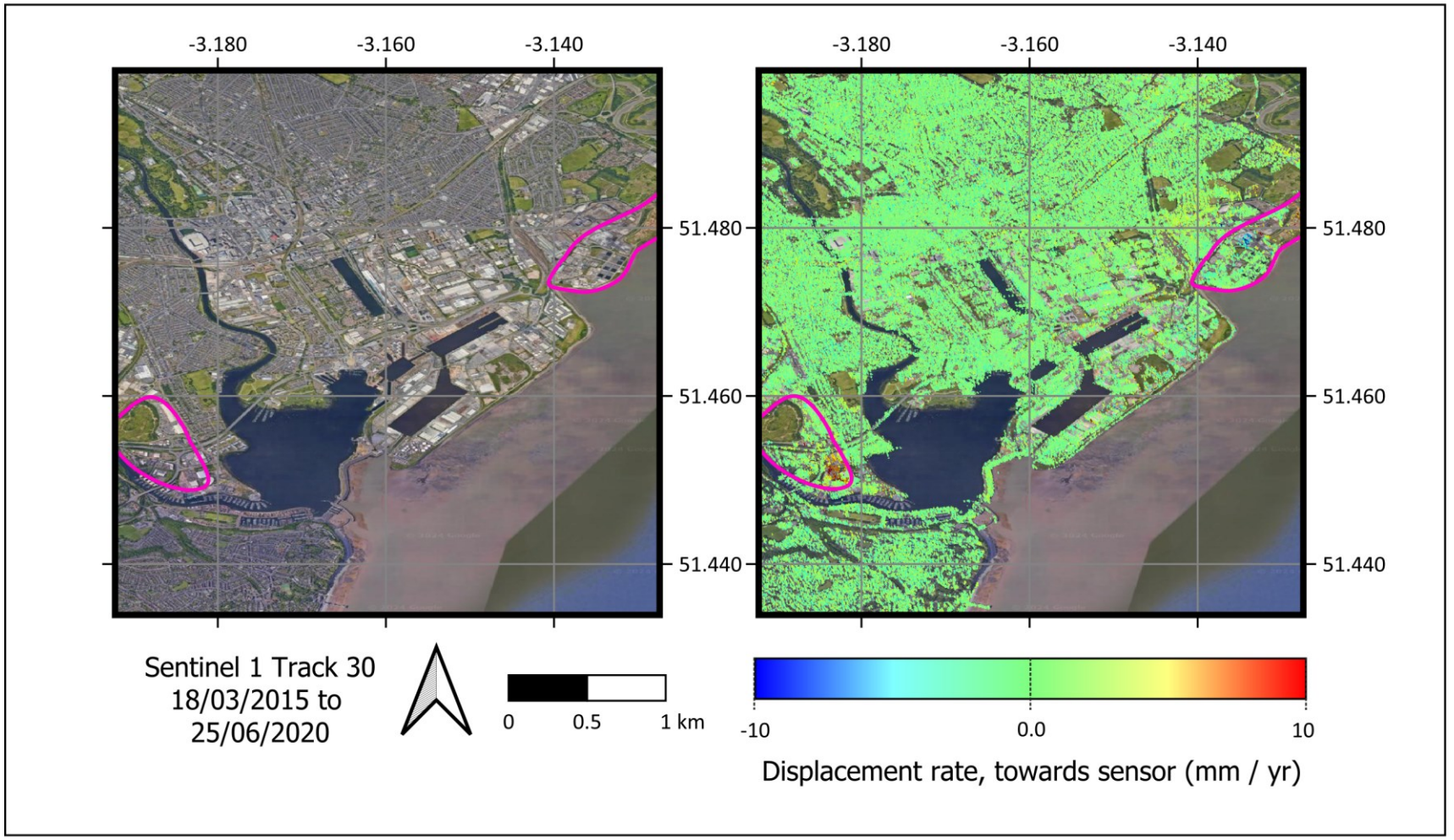


Figure 6-9: PSI Deformation Rate results showing settlement of a marina and spoil heap slope movements associated with areas of historically recorded and ongoing landfill activity (Natural Resources Wales, 2017) shown via pink polygons.

6.4.1. East Pentwyn and Bourneville Landslides

The town of Abertillery and nearby village of Blaina lie within a steep valley. Here, mining activity is widely attributed as a initiating multiple landslide events recorded over the last century (Siddle, Bromhead and Bassett, 2000). One key mechanism in this area may have involved reactivation of faults due to differential subsidence (Gostelow, 1977).

In Transient Scatterer compensated data (Figure 6-6, Figure 6-10, Figure 6-12), significant movement of two west facing scree slopes is clear. The data shows around 15 mm a^{-1} of movement in the direction of the satellite, which is equivalent to roughly 30 mm a^{-1} of movement downslope (due to the angle of the slope with respect to the satellite incident angle). While the ground movements associated with landslides can be complex, with e.g. rotational mechanisms leading to near-vertical slumping of upper blocks and heave of the toe, literature suggests the movement measured here is translational sliding of the debris downslope (Siddle, Bromhead and Bassett, 2000, chap. 8).

The rate of movement appears spatially consistent with the scree slope, and temporally consistent as seen by the time series in Figure 6-11. There is some minor evidence of additional instability during winter months as can be seen by noisy time series behaviour in January 2016 and January 2019 and an apparent acceleration of around 1cm beginning in January 2018 , This seasonal variability would support previously suggested deformation mechanisms which implicate groundwater mobilisation of material along faults (Lee and Giles, 2020).

The rates of movement involve imply the landslide process is currently active. After contact with the local council, Blaenau Gwent, it was confirmed that the landslide is under active monitoring. Existing diagrams and photography were kindly provided, as shown in Figure 6-14 and Figure 6-15 which validates the TS analysis by confirming the geographical boundaries of the deformation feature.

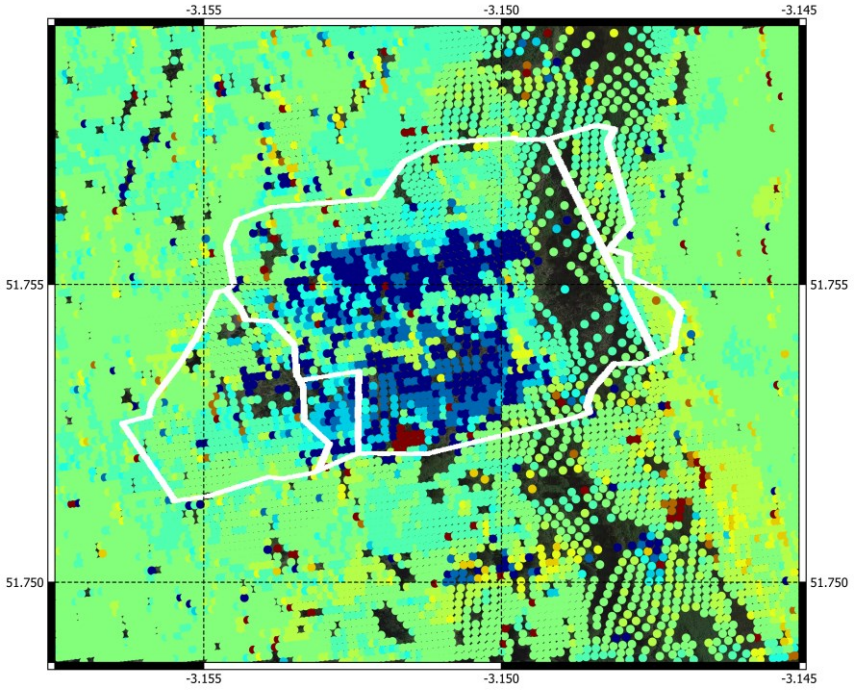


Figure 6-10: Deformation results for Bourneville Landslide, Abertillery, South Wales. The white overlay demarcates the extent of landslide zones identified by Blaenau Gwent council as shown in Figure 6-14.

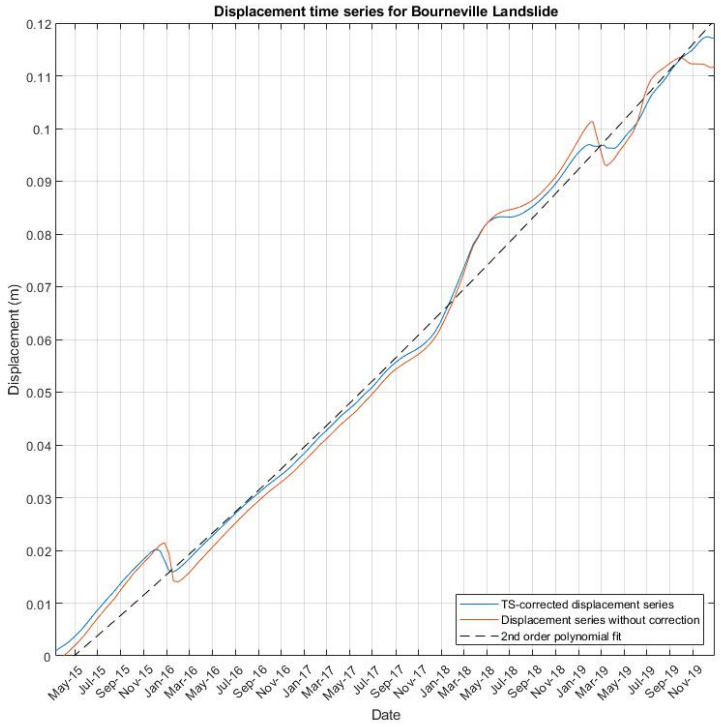


Figure 6-11: Displacement time series for Bourneville landslide. The blue curve corresponds to TS-corrected data, the red to DS data without correction, and the black dashed line follows a 2nd order polynomial fit of the TS-corrected data.

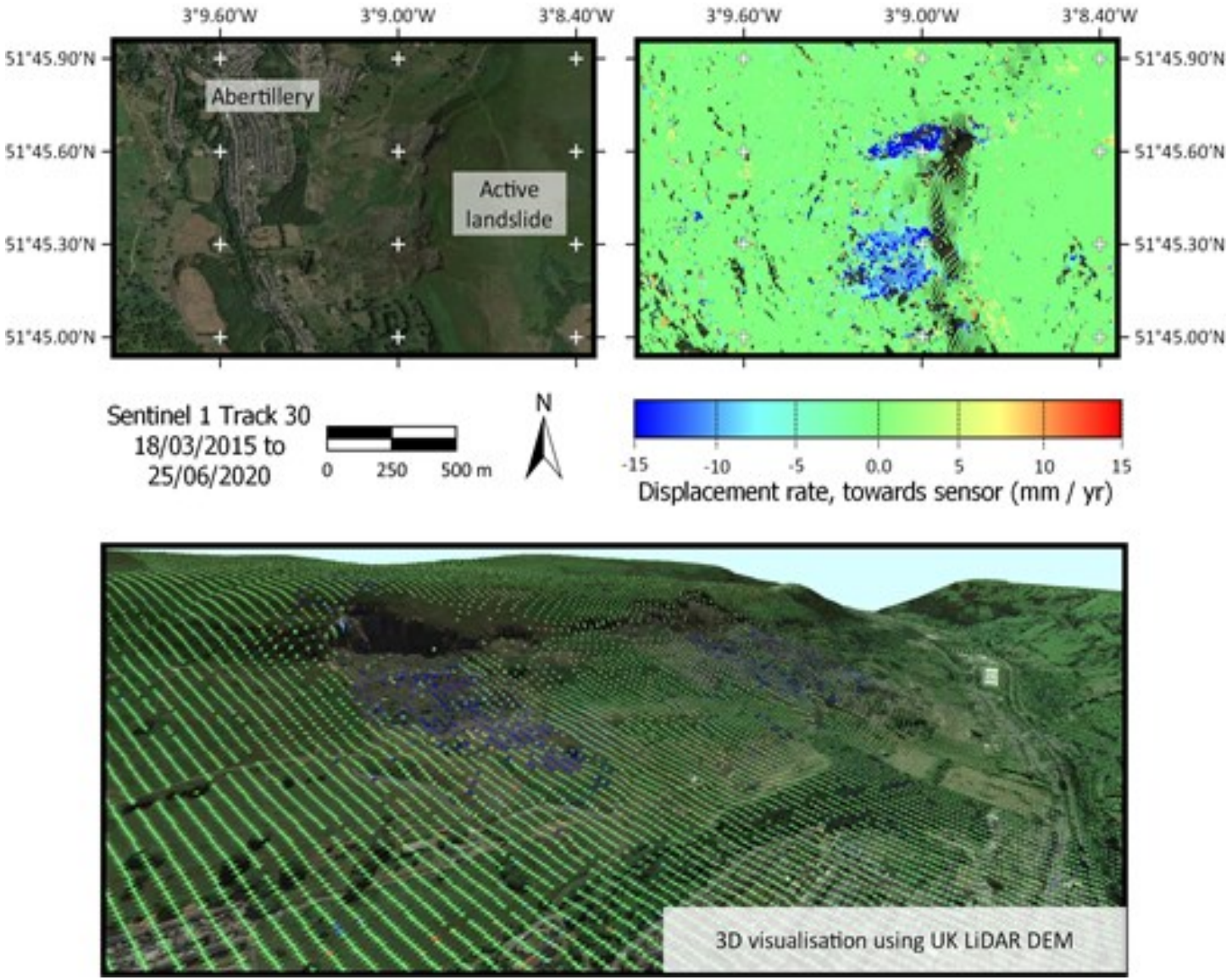


Figure 6-12: Overview and 3D projection of the East Pentwyn and Bourneville landslides, near Abertillery.

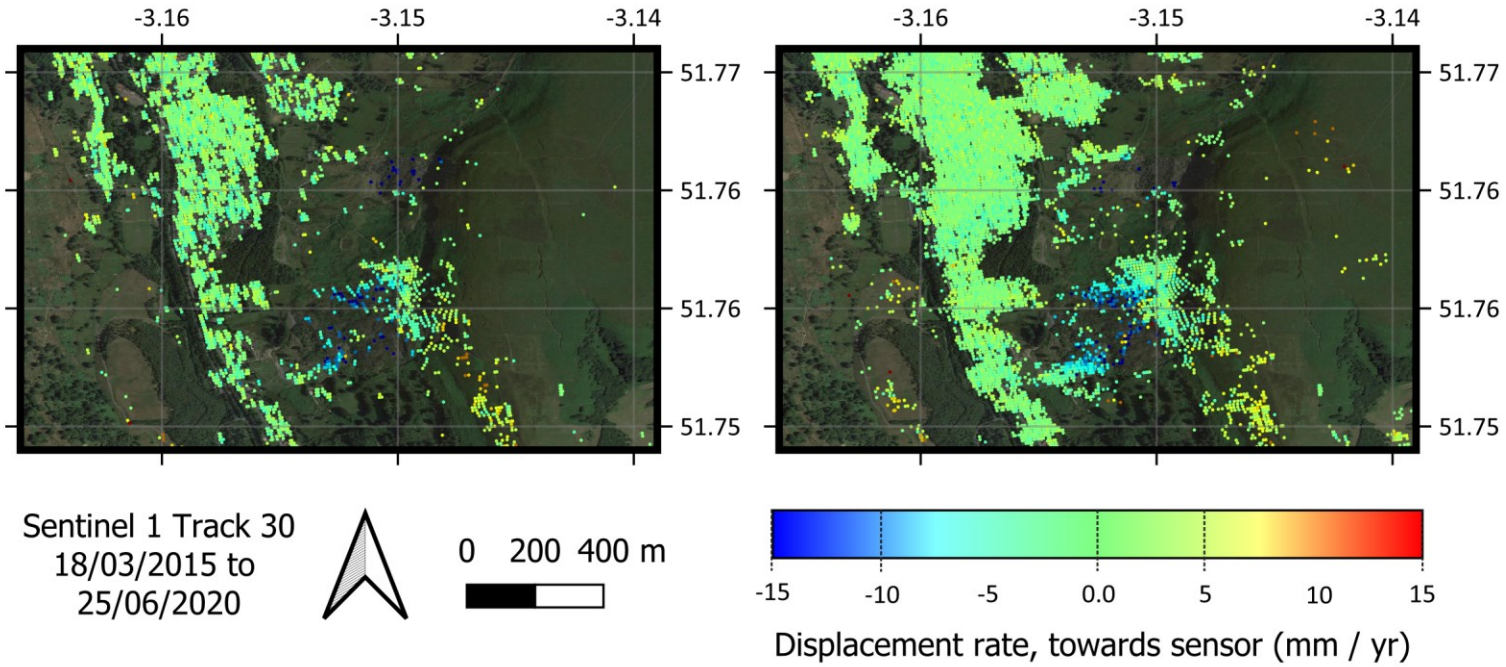


Figure 6-13: Deformation rates for East Pentwyn and Bourneville landslides, as measured by PSI (left) and DS data without correction for TS behaviour (right).

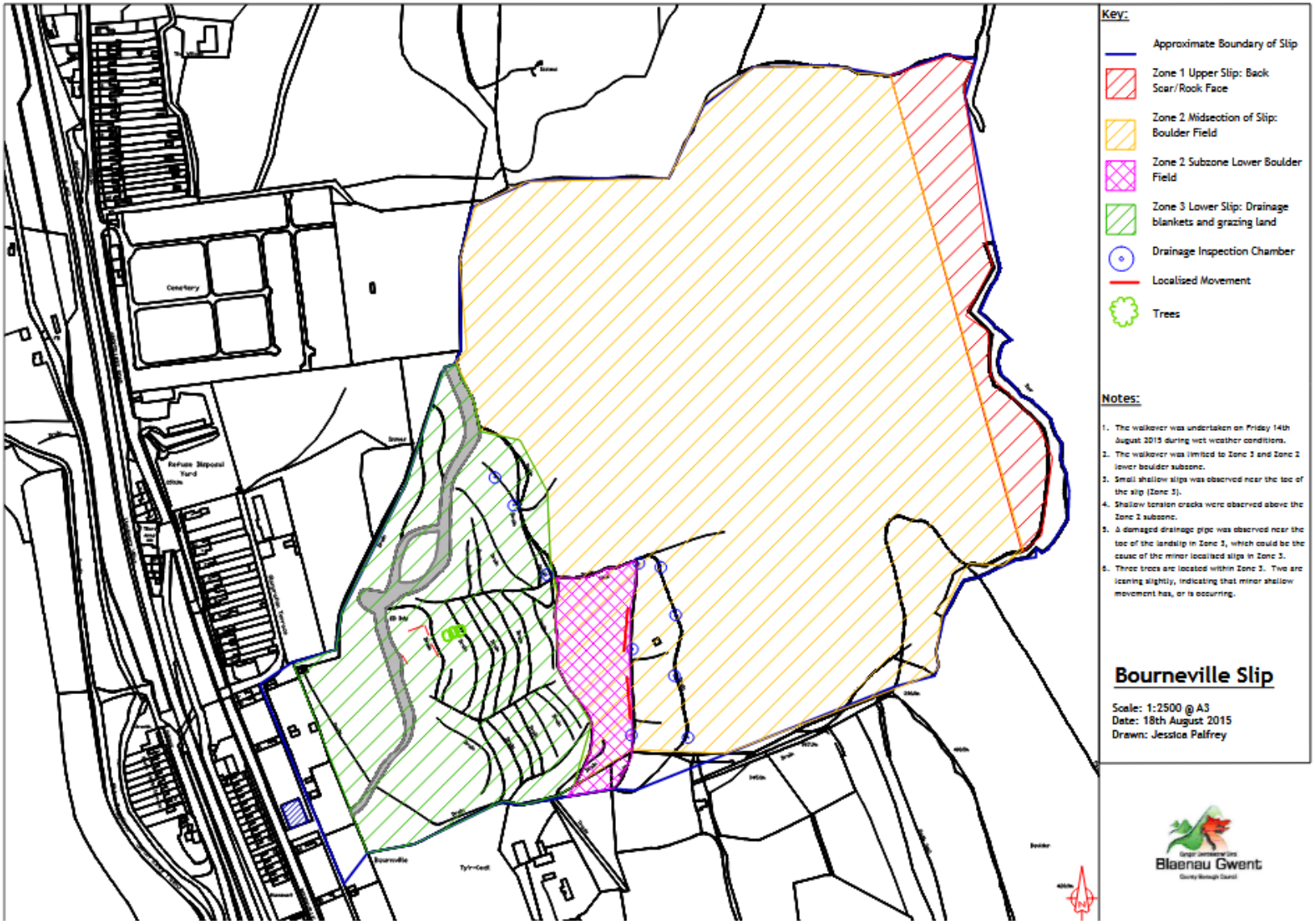


Figure 6-14: Map of the Bourneville Slip landslide near Blaina, kindly provided by Blaenau Gwent council.



Figure 6-15: Photographs of the Bourneville Slip kindly provided by Blaenau Gwent council.

6.4.2. Margam mine

The Margam open cast mine seen in Figure 6-16 was mothballed in 2008 and is yet to undergo permanent restoration. Results suggest a range of deformation phenomena, with the material surrounding the void being observed as moving towards the satellite implying a progressive slip of material downslope. The extensive spoil heap to the east appears to be undergoing settlement.

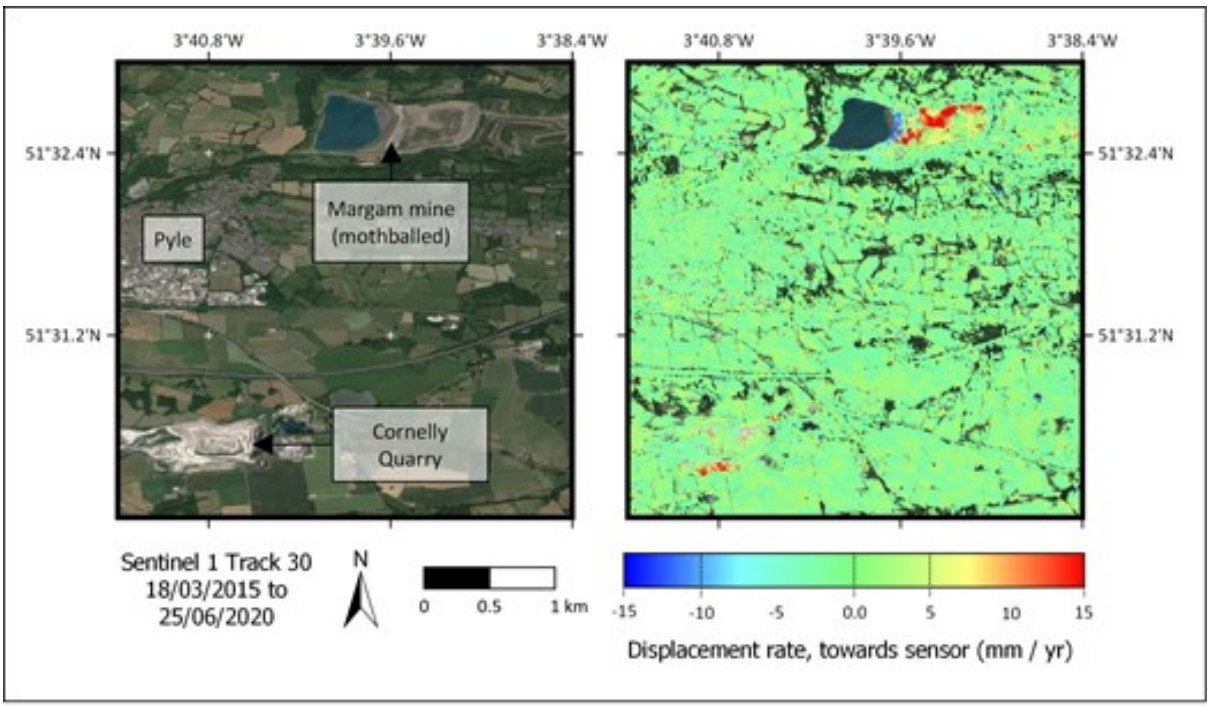


Figure 6-16: Slope movement and settlement at the Margam open cast mine.

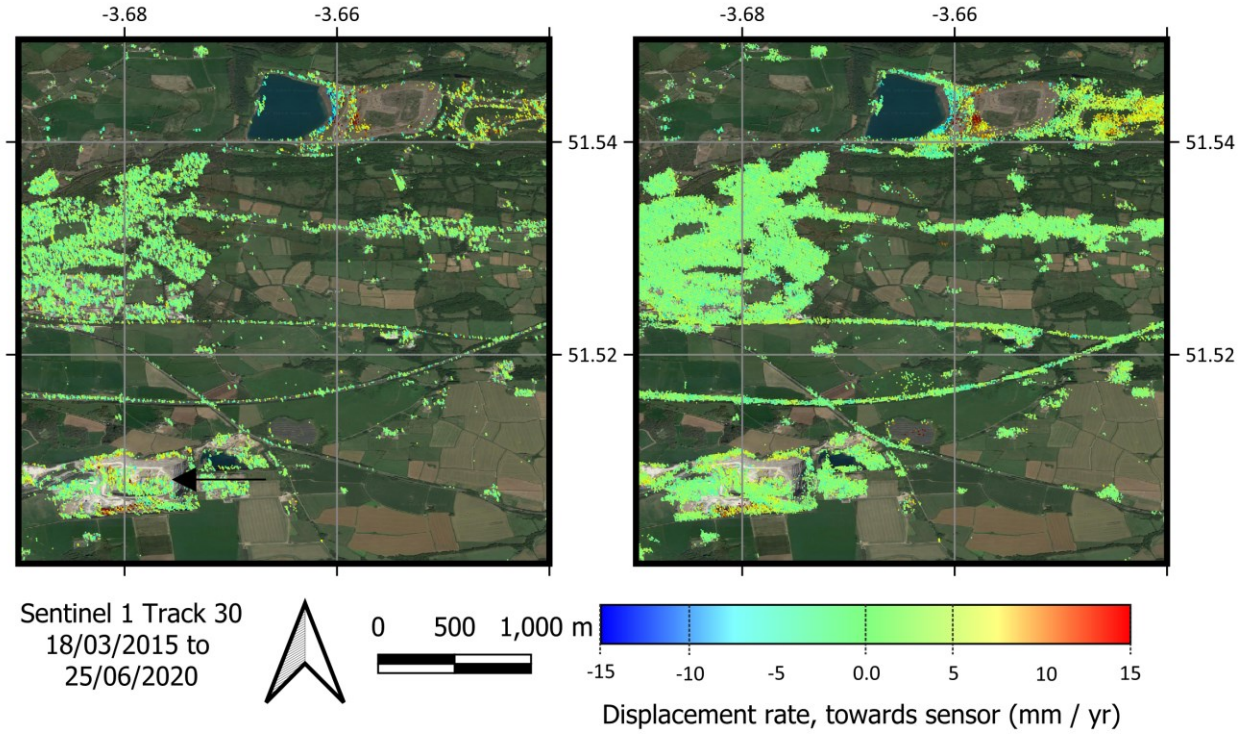


Figure 6-17: Deformation rates for Margan open cast mine, as measured by PSI (left) and DS data without correction for TS behaviour (right).

6.4.3. Ffos-y-fran project

The spoil heap for the active Ffos-Y-Fran excavation and land reclamation scheme is similarly observed to be undergoing settlement. The western side of the pit had recently undergone significant reclamation works prior to the measurement period, and thus widespread settlement of backfill material can be observed. Similar magnitudes of movement can be seen from the large spoil heaps to the east of the mine. The northernmost heap has a steep west-facing slope, which appears to be moving towards the satellite (blue), indicating material is moving downslope.

The geographic locations of the measured deformation phenomena can be seen as aligning with the works shown in the associated plans for the scheme. Figure 6-20 shows plans for the emplacement of spoil immediately prior to the MTI data, while Figure 6-21 shows the planned state of the mine and groundworks over the window of time where the MTI data was being captured, as can be seen reflected in the loss of coherence over the pit seen in Figure 6-18 and Figure 6-19.

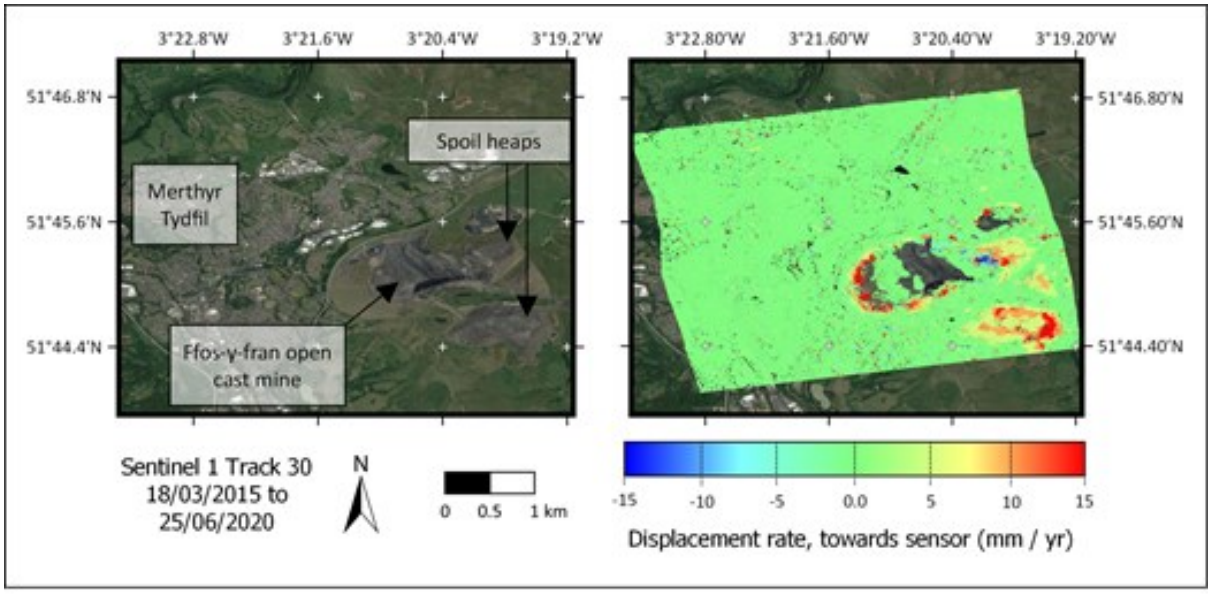


Figure 6-18: Downslope ground movement at Ffos-y-fran open cast coal mine (Scoular *et al.*, 2021).

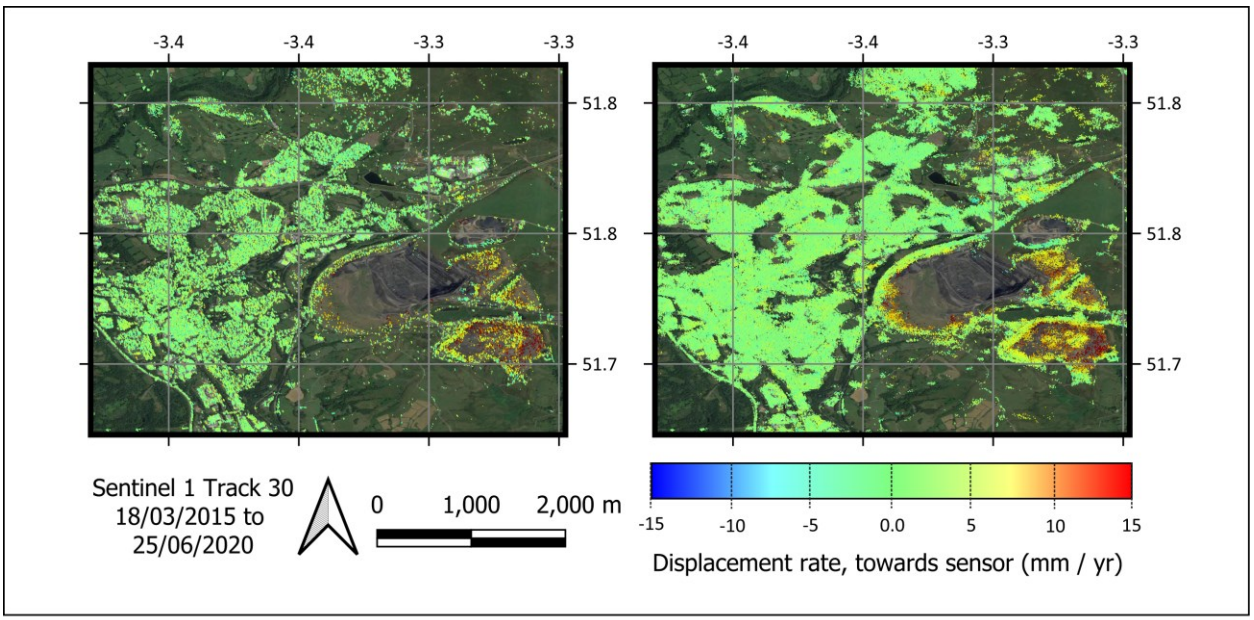


Figure 6-19: Deformation rates for Ffos-y-Fran, as measured by PSI (left) and DS data without correction for TS behaviour (right).

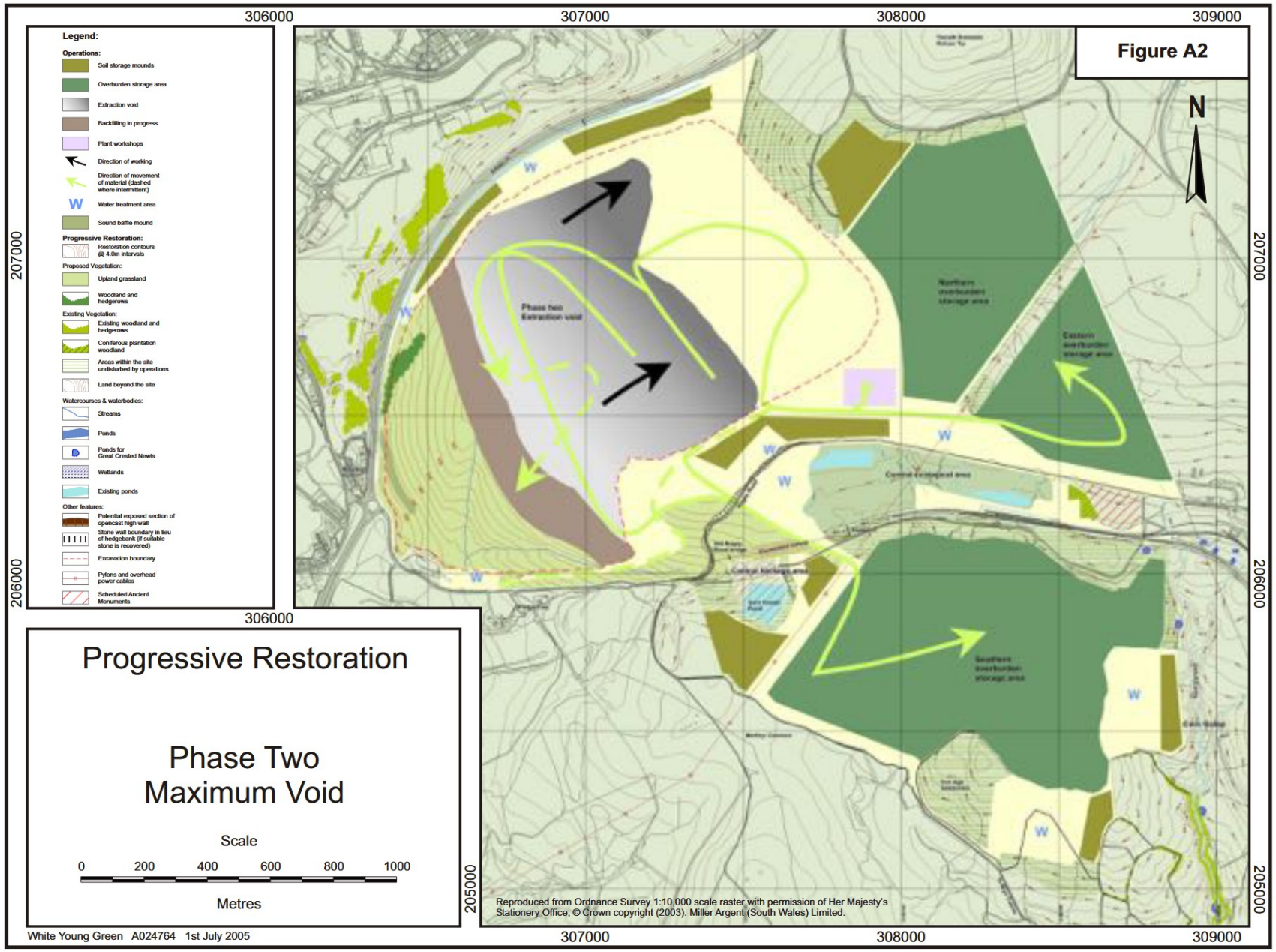


Figure 6-20: Plans for the Ffos-y-Fran land reclamation and coal excavation scheme, showing the stage immediately prior to this investigation (Miller Argent & RPS, 2015).

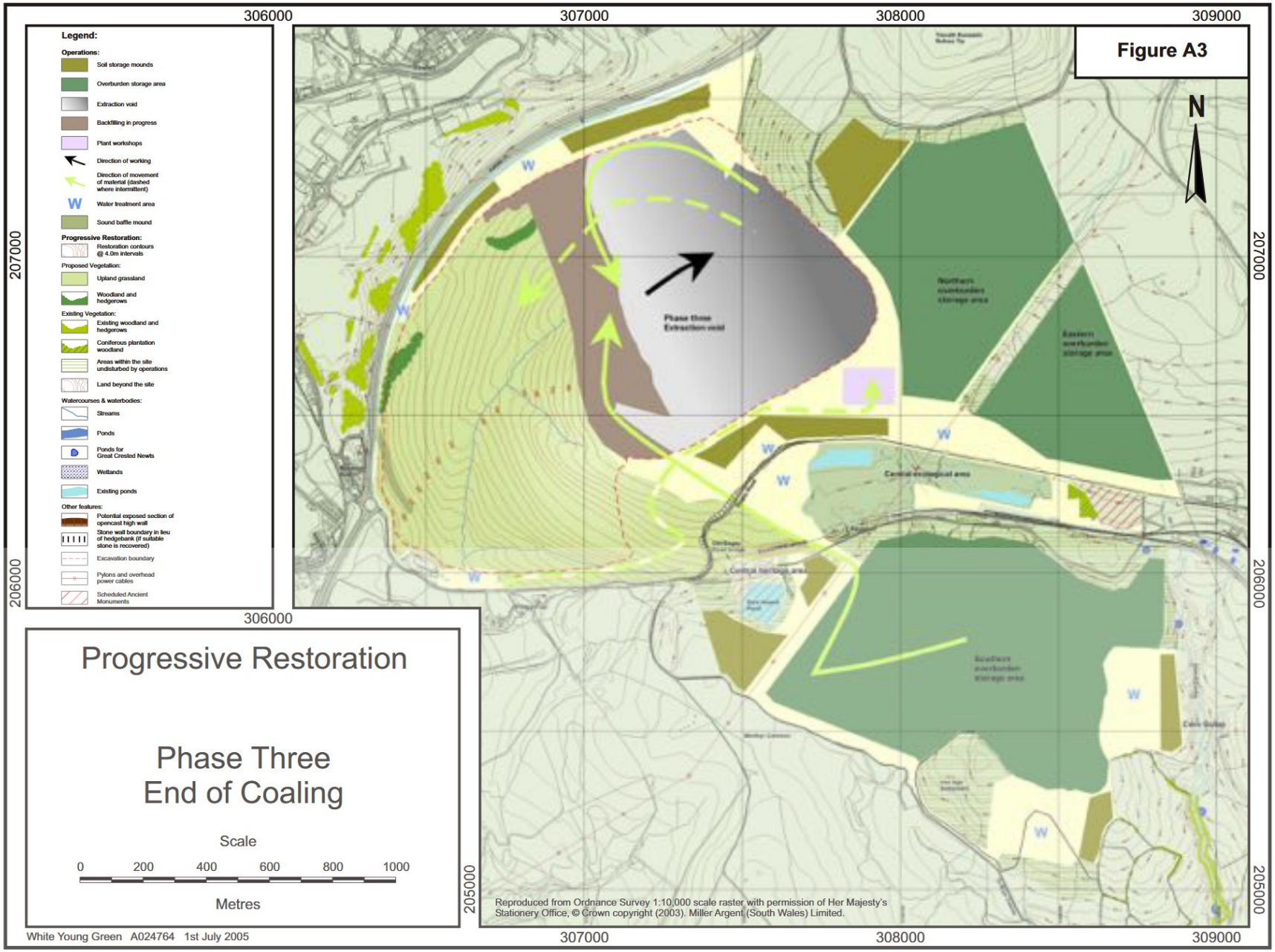


Figure 6-21: Plans for the Ffos-y-Fran land reclamation and coal excavation scheme, showing the planned status of the groundworks at the time of this investigation (Miller Argent & RPS, 2015).

6.4.4. K-means and land cover

The K-means clustering approach described in Section 5.5, and subsequently employed in this chapter, extracts scatterers with similar time-series behaviour. Section 5.5.4 further explored how this approach performed in identifying crop types, when using *a priori* field boundaries. This showed good agreement with independent crop type mapping. The performance of the K-means approach in sample-by-sample land cover estimation is therefore worth exploring.

Figure 6-22 compares the K-means cluster labels with *a priori* land cover mapping from the UKCEH (Morton, 2018), across the main sites explored in this chapter. The UKCEH dataset classifies land cover to a resolution of 20m, using random-forest classification of optical data. The labels incorporate some land use factors (urbanisation, agriculture) but mainly focus on vegetative habitats.

By comparison, the K-means labels here have no inherent human meaning, aside from reflecting radar behaviour. A legend was intentionally not provided in Figure 6-22, therefore, as any manually assigned labels for vegetation would be dependent on orientation, topography, and timing of the vegetation phenology for each specific scatterer.

Some areas of e.g. water, improved grassland, heather grassland can be seen as jointly demarcated between the optical and radar data. However, in general the K-means labels in column C of Figure 6-22 can be seen as heterogeneous or noisy as compared than the optical classification. This is especially apparent in urban areas due to the mixture of strong artificial scatterers interspersed with vegetation. The K-means data has not been grouped into habitats, and radar data generally offers a higher resolution product.

It is apparent that fusion of optical and radar time-series data could offer benefit to future studies of both land cover and deformation. For applications in land cover classification, radar data can offer generally higher resolutions; relative immunity to cloud cover and weather; penetration into material. For MTI, optical data may provide a valuable data set to independently identify common Transient Scattering behaviours and therefore allow for unbiased compensation of phase shifts.

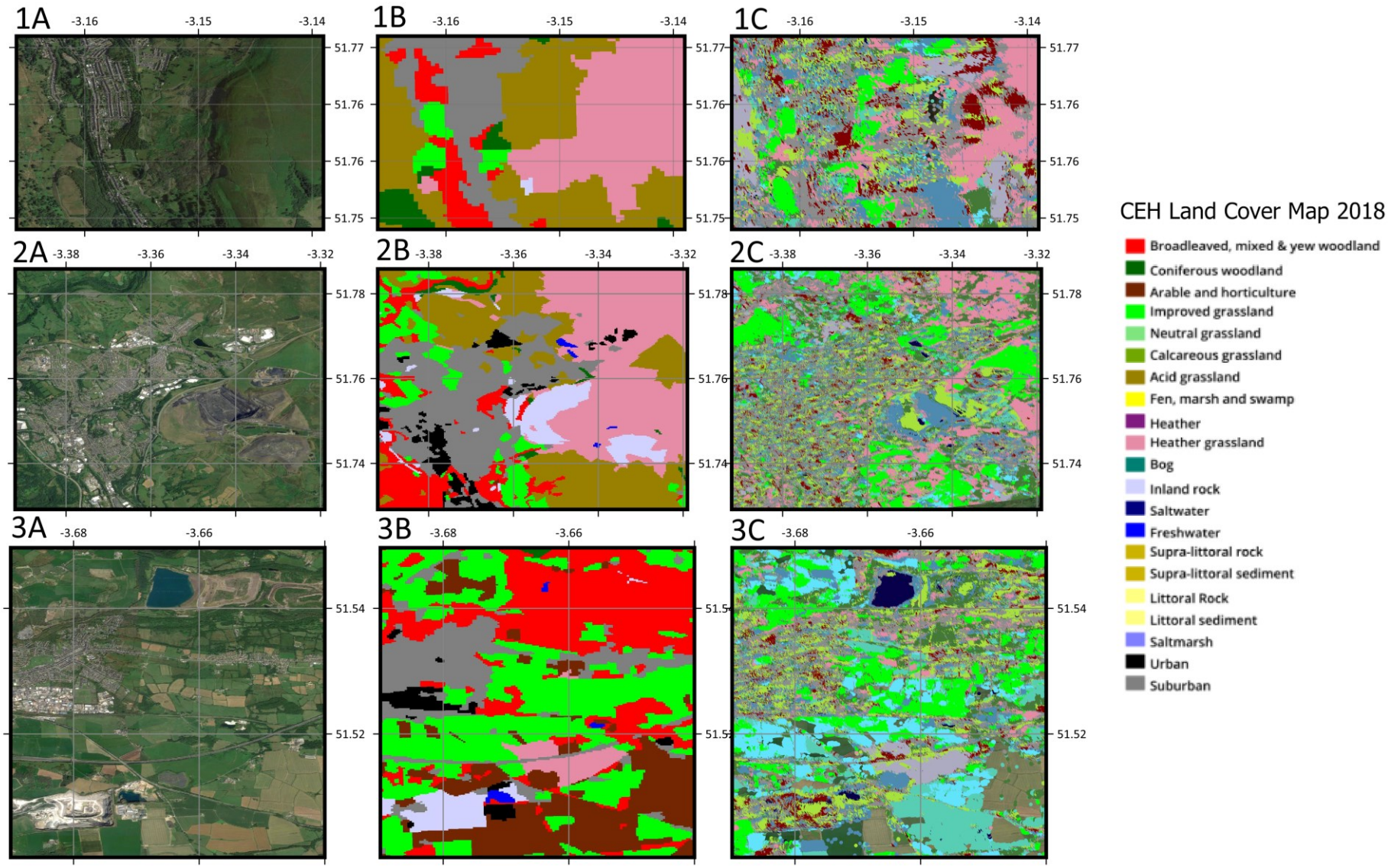


Figure 6-22: Comparison of land cover labels for the main sites analysed: 1) Blaina; 2) Ffos-y-fran; 3) Margam.
A) Google Earth optical imagery; B) CEH Land Cover Crop Classification (legend); C) K-mean radar cluster labels (see text regarding omission of legend).

6.5. Conclusion

The deformation phenomena revealed by the increased coverage all appear credible. We hence believe that analysis of φ_{TS} is a useful additional step in the MTI chain, which successfully isolates the effects of vegetative biomass and moisture changes in MTI time series as distinct from true ground deformation as can be observed in this case study.

The K-means + DFT approach appears effective in isolating a wide range of vegetated land covers, distinguishing transient scattering areas of natural grasslands, improved grasslands, and arable land as distinct from areas of PS and noisy scatterers from wooded areas.

The approach has been used to isolate and remove the predictable phase offsets from these classes of land cover in order to perform an MTI deformation analysis, which yielded increased data coverage as compared to PSI and highlighted deformation behaviour for a variety of areas which were unresolved in existing works using SBAS and ISBAS (Bateson *et al.*, 2015). Deformation phenomena related to landslides, mining spoil, and reclaimed land have been highlighted as examples.

The wide range in the spatial scales of deformation phenomena analysed highlights the value of MTI as a tool that may be applied to localised movements or regional and national scale phenomena. The results in this chapter cover nearly 20% of the area of Wales and were processed with a total wall time of 18 hours using around 100 virtual machines on the Imperial College HPC system 4 virtual CPUs; 16GB memory each.

The majority of processing time was spent on data input/output operations, loading and saving data to the networked storage system. Using systems with larger memory or more efficient caching of data could reduce the need to utilise disk storage, and hence dramatically increase the time required. The additional overhead in sampling the transient scattering behaviour and clustering the samples is limited and can be performed on a single machine, as compared to existing operations in DS processing such as phase triangulation which requires each of the DS pixels undergo computationally expensive Eigen decomposition and a numerical matrix inversion (Ansari, De Zan and

Bamler, 2018). This impressive range of spatial scales is equally demonstrated in the mapping of scatterer classes. This work highlights that there is significant value in developing K-means + DFT or similar approaches to properly exploit the information content of MTI for purposes of land cover mapping and biomass estimation. The global scale of available data suggests extremely valuable contributions to food security and carbon sequestration may be possible, given the merits of SAR over optical data in terms of all-weather, day-night coverage and greater penetration into the scattering volumes under study.

The analysis of transient scatterers therefore shows tangible benefits to the study of ground deformation using MTI. At the very least, transient scattering analysis provides a new perspective from which MTI results from affected areas should be interpreted with additional scrutiny as to the origin of their phase signals.

7. Conclusions

This research has investigated MTI as a tool to measure ground deformation in rural areas of the UK. The driving motivation was to ultimately improve the accuracy and spatial coverage of results. To do so, the scattering being measured required further analysis.

Rural areas of temperate regions such as the UK are characterised by seasonal changes in vegetation, with the underlying soil also undergoing significant changes in moisture content over a range of time scales. Literature has shown experimentally and theoretically that these phenomena can affect the SAR scattering behaviour. Equally well known in literature is that these phenomena can decorrelate interferometric phase signals, which prevents accurate MTI measurement in many areas.

Often the resulting decorrelation is modelled as a zero-mean noise. This is convenient as thus spatiotemporal low-pass filtering should theoretically act to minimise this noises effect, while regression with deterministic models of deformation or atmospheric processes should be unbiased by it. However, more recent literature has evidenced that certain shifts in soil moisture and vegetative biomass may cause coherent shifts in phase rather than pure noise. If this is the case, coherent shifts in phase will be correlated in time (with seasonal changes in biomass or moisture) or space (with specific land cover types), leading to inaccurate models of the deformation and atmospheric processes.

This research hence examined whether these potential shifts were apparent in MTI data stacks of Sentinel 1 data. This chapter summarises this work, highlights the subsequent novel findings, and then recommends avenues for further research.

7.1. Summary of research

A bespoke MTI processor, *OpenInSAR,* was designed and developed to facilitate this research and wider efforts. Reusability was achieved through a modular architecture, with generic data processing confined to the core program and implemented SAR processing being deferred to isolated plugins such that researchers could focus on their particular area of study.

Earlier prototypes have been applied to research of landslide complexes (O'Connor *et al.*, 2021), dam stability (Shire *et al.*, 2023), and structural geology (Wang *et al.*, 2022). The approach to develop this software is described in Chapter 3. Source code is available via the following link at time of this documents publication: https://github.com/insar-uk/OpenInSAR

A reference processing chain was implemented to provide a baseline, enabling reproducible results and a known environment in which to investigate the novel TS phenomena that are the focus of this research.

Chapter 4 explored potential TS mechanisms presented in literature. A method for calibrating MTI data and isolate potential TS phase effects ($TS\varphi$) was detailed. A procedure for estimating the statistical significance of the resulting $TS\varphi$ measurements was also derived.

The significance of phase shifts is a useful indicator that phase effects observed over a subset of scatterers cannot be adequately explained by noise. This analysis was applied to an agricultural area of South Wales, UK, where *a priori* data regarding crop type was available. Significant phase offsets as compared to PS were found for every type of crop. The distinction in phase offsets between different crop types was still significant, but less pronounced and limited to certain periods of time.

A limitation of the subset-significance approach is that it does not provide definitive evidence in isolation that the phase effects are not due to some unmodelled deformation effect. However, the rates of deformation and the inconsistency of the phase time series

between different interferometric references (closure phases) suggest intuitively that deformation is not an adequate explanation for these phase shifts.

Chapter 5 then explored further methods for quantifying the TS processes. Regardless of whether the observed phase shifts are representative of deformation or scattering changes, the fact remains that these shifts are not representative of deformation. Given the near complete correlation of these shifts with natural land cover, it remains that these areas should be isolated and the average deviation and inconsistencies in each interferogram compensated for before estimating the atmospheric phase screen (APS). Isolating these areas may also allow for further analysis in areas such as land cover mapping, crop biomass tracking, or soil moisture measurement.

A wide range of metrics for identifying the areas of potential Transient Scattering were explored for these purposes. These included: the statistical stationarity of amplitude and coherence; entropy of the coherence matrix; polarimetric stability; temporal correlation of amplitude and coherence.

It was further explored how these metrics correlated with φ_{TS} significance, suggesting the value of the metrics in separating deformation and scattering phenomena. For example, the significant relationship between decorrelation and φ_{TS} cannot be adequately explained by deformation phenomena but can be explained by dielectric mechanisms presented in Chapter 4.

A method for clustering the data according to the observed transient scattering behaviour using the K-means approach was provided. This allows for targeted compensation of the phase from affected areas.

Chapter 6 applied this compensation to a wider area of South Wales and demonstrated a wide range of credible deformation phenomena better measured as a result of removing the estimated φ_{TS}.

7.2. Novel contributions

This research has made several novel contributions to the field of MTI analysis and investigations into interferometric scattering behaviour. These contributions can be summarised as follows:

6) MTI processing software

An open, modular, and flexible MTI processor has been designed, developed, and tested. Prototypes of this software have been employed in and MSc dissertations and published research papers, demonstrating its value as a tool for education and research.

The software is made publicly available along with a number of implemented plugins, and is hoped to provide streamlined access to MTI processing for users with a wide range in level of expertise. The software is hoped to be easy to configure and operate for new users, while offering novel processing ideas for experts.

7) Review of MTI phase offsets in rural land cover

A review of mechanisms producing predictable shifts in MTI phase associated with scattering changes has been conducted. This review has shed light on the influence of dielectric scattering mechanisms on MTI results. A novel approach for characterising transient scattering effects using a priori land cover data and calibrated phase has been developed and detailed. The Subset of Scatterers Coherence has been shown as a simple method of calculating these shifts, and then correcting for them using its conjugate.

Experimental data regarding the influence of agricultural crops on InSAR phase shows particularly high phase offsets are a regular occurrence in long-term MTI datasets. The 'Spring shift' in particular shows high closure phase as shown in Chapter 4, and occurs regularly over many years as shown in Chapter 6.

8) A novel method for isolating scatter phase offsets

A method has been developed to use the frequency domain, particularly the Discrete Fourier Transform (DFT), to analyse temporal correlation within samples. This provides a novel and effective way to appropriately weight otherwise dissimilar values of various

polarimetric amplitudes and coherences. The statistical validity of this approach is shown through the fact that temporally uncorrelated fluctuations are transformed into uncorrelated zero-mean noise in the DFT, and therefore will not bias the estimated correlations in time-series behaviour of scatterers.

The value of this data has been demonstrated via the popular K-means clustering algorithm to isolate common components of phase for subsequently identified clusters. The 'Subset of Scatterers' coherence estimate, $\hat{\gamma}_S$, is calculated and defined as the characteristic transient scattering phase behaviour found over the cluster. The conjugate of $\hat{\gamma}_S$ can be used to remove transient scattering phase.

9) Improvement of MTI data processing through removal of transient scattering phase

Isolating phase behaviours that are distinct to patterns of scattering changes allows for improved phase triangulation and model inversion of MTI phase histories. This allows for a wide range of ground deformation phenomena to be better isolated from the complex phase behaviour of rural DS, and measured to produce improved resolution of ground movement. This is demonstrated over South Wales for phenomena such as landslides, settlement of made ground, mining subsidence, and rebound from groundwater recharge.

7.3. Recommendations for further work

This investigation has highlighted a range of potentially valuable avenues for which to direct additional effort. There is overlap to many of these areas, which can be summarised as developing improved understanding transient scattering processes and the methods used to measure and exploit the information these provide.

1) Improve our physical understanding of transient scatterers.

Modelling the complex geometry and optical properties of volumetric scatterers as they vary in time and space is a difficult task. However:

- Would better understanding of the polarimetric phase and coherence processes in common soils and vegetations allow us to better measure important physical properties such as moisture content and vegetative biomass using MTI?
- Would better understanding of key mechanism affecting polarimetric phase and coherence response for a range of common land covers allow for quantifiably accurate distinction between deformation and scatterer effects on a pixel-by-pixel basis?
- Would this understanding of transient scatterers be aided by laboratory scale experiments and repeated UAV surveys?

2) Assess the effects of transient scattering in wider datasets.

A limitation of this study has been, for purposes of scope and resource, its singular focus on the use of Sentinel 1 data. However, a wealth of remote sensing data is available or could be generated:

- Could SAR satellite constellation (such as ALOS, TerraSAR-X) capable of produce regular quad-polarized measurements demonstrate improved definition of TS while retaining the valuable MTI characteristics of the Sentinel-1 constellation?
- Is transient scattering similarly present in commercial satellite data such as COSMO SkyMed, and older freely available ERS and Envisat data? Can the approaches developed for Sentinel 1 be transferred?

- Could optical and multispectral data be fused into the analysis of transient scatterers to provide more effective clustering and more granular isolation of phase phenomena?

3) Apply findings to wider fields of study.

The global coverage of SAR datasets can amplify the value of even modest improvements in accuracy over existing techniques. By expanding the fields of application of transient scattering analysis, extremely valuable products could be produced:

- Can improved physical models of transient scattering and φ_{TS} allow for regular MTI monitoring of regional scale soil moisture, improving upon the accuracy or resolution of existing remote sensing techniques?
- Can soil moisture data allow for greater understanding of crop health and therefore regional food security? Can crop biomass be measured instead or as well to predict yields and produce nearly real-time warning of drought crises?
- Can global SAR assessments of crop biomass, or the geographic extent of vegetative scatterers shown here, be used to monitor desertification, deforestation, or in general quantify and map climate change processes or carbon sequestration?

Many of these recommendations will require substantial work effort. However, it is the authors belief that these further investigations into the complex volumetric behaviour of transient scatterers is merited, given the significant potential rewards.

References

'A Land Cover Atlas of the United Kingdom (Maps)' (2017). The University of Sheffield. Available at: https://doi.org/10.15131/shef.data.5219956.v1.

Abe, H., Yamaguchi, Y., Yamada, H. and Cui, Y. (2014) 'Estimation of soil moisture content and surface roughness using oh model and scattering power decomposition', in *2014 IEEE International Workshop on Electromagnetics (iWEM). 2014 IEEE International Workshop on Electromagnetics; Applications and Student Innovation (iWEM)*, Sapporo, Japan: IEEE, pp. 32–33. Available at: https://doi.org/10.1109/iWEM.2014.6963621.

Adam, N., Parizzi, A., Eineder, M. and Crosetto, M. (2009) 'Practical persistent scatterer processing validation in the course of the Terrafirma project', *Journal of Applied Geophysics*, 69(1), pp. 59–65. Available at: https://doi.org/10.1016/j.jappgeo.2009.07.002.

Agar, S.A., Lawrence, J.A., Ghail, R.C., Mason, P.J. and Thompson, S. (2018) 'PSInSAR remote sensing observations of deformation behaviour at Salisbury Plain, UK.', in *Engineering in Chalk. Chalk 2018 Engineering in Chalk*, Imperial College, London, UK: ICE Publishing, pp. 269–274. Available at: https://doi.org/10.1680/eiccf.64072.269.

Agram, P.S. and Simons, M. (2015) 'A noise model for InSAR time series', *Journal of Geophysical Research: Solid Earth*, 120(4), pp. 2752–2771. Available at: https://doi.org/10.1002/2014JB011271.

Alvarez-Perez, J.L. (2011) 'Coherence, Polarization, and Statistical Independence in Cloude–Pottier's Radar Polarimetry', *IEEE Transactions on Geoscience and Remote Sensing*, 49(1), pp. 426–441. Available at: https://doi.org/10.1109/TGRS.2010.2056375.

Ansari, H., De Zan, F. and Bamler, R. (2018) 'Efficient Phase Estimation for Interferogram Stacks', *IEEE Transactions on Geoscience and Remote Sensing*, 56(7), pp. 4109–4125. Available at: https://doi.org/10.1109/TGRS.2018.2826045.

Ansari, H., De Zan, F. and Parizzi, A. (2021) 'Study of Systematic Bias in Measuring Surface Deformation With SAR Interferometry', *IEEE Transactions on Geoscience and Remote Sensing*, 59(2), pp. 1285–1301. Available at: https://doi.org/10.1109/TGRS.2020.3003421.

Arthur, D. and Vassilvitskii, S. (2007) 'k-means++: the advantages of careful seeding', in *Proceedings of the eighteenth annual ACM-SIAM symposium on Discrete algorithms*. USA: Society for Industrial and Applied Mathematics (SODA '07), pp. 1027–1035.

Attema, E.P.W. and Ulaby, F.T. (1978) 'Vegetation modeled as a water cloud', *Radio Science*, 13(2), pp. 357–364. Available at: https://doi.org/10.1029/RS013i002p00357.

Bamler, R. (2000) 'Principles Of Synthetic Aperture Radar', *Surveys in Geophysics*, 21(2), pp. 147–157. Available at: https://doi.org/10.1023/A:1006790026612.

Bamler, R. and Eineder, M. (2005) 'Accuracy of differential shift estimation by correlation and split-bandwidth interferometry for wideband and delta-k SAR systems', *IEEE Geoscience and Remote Sensing Letters*, 2(2), pp. 151–155. Available at: https://doi.org/10.1109/LGRS.2004.843203.

Bamler, R. and Just, D. (1993) 'Phase statistics and decorrelation in SAR interferograms', in *Proceedings of IGARSS '93 - IEEE International Geoscience and Remote Sensing Symposium*. *IGARSS '93 - IEEE International Geoscience and Remote Sensing Symposium*, Tokyo, Japan: IEEE, pp. 980–984. Available at: https://doi.org/10.1109/IGARSS.1993.322637.

Banque, X., Lopez-Sanchez, J.M., Monells, D., Ballester, D., Duro, J. and Koudogbo, F. (2015) 'Polarimetry-Based Land Cover Classification with Sentinel-1 Data', 729, p. 13.

Barrett, B., Whelan, P. and Dwyer, E. (2012) 'The use of C- and L-band repeat-pass interferometric SAR coherence for soil moisture change detection in vegetated areas', *Open Remote Sensing Journal*, 5, pp. 37–53. Available at: https://doi.org/10.2174/1875413901205010037.

Bateson, L., Cigna, F., Boon, D. and Sowter, A. (2015) 'The application of the intermittent SBAS (ISBAS) InSAR method to the South Wales Coalfield, UK', *International Journal of Applied Earth Observation and Geoinformation*, 34, pp. 249–257. Available at: https://doi.org/10.1016/j.jag.2014.08.018.

Beck, K. (2000) *Extreme Programming Explained: Embrace Change*. Addison-Wesley.

Berardino, P., Fornaro, G., Lanari, R. and Sansosti, E. (2002) 'A new algorithm for surface deformation monitoring based on small baseline differential SAR interferograms', *IEEE Transactions on Geoscience and Remote Sensing*, 40(11), pp. 2375–2383. Available at: https://doi.org/10.1109/TGRS.2002.803792.

Bischoff, C.A. (2019a) 'Chapter 3', in *Monitoring ground movements and infrastructure in London, UK, using Permanent Scatterer Interferometry*. Imperial College London. Available at: https://doi.org/10.25560/73901.

Bischoff, C.A. (2019b) *Monitoring ground movements and infrastructure in London, UK, using Permanent Scatterer Interferometry*. Imperial College London. Available at: https://doi.org/10.25560/73901.

Bishop, C.M. (2006) *Pattern recognition and machine learning*. New York: Springer (Information science and statistics).

Blackford, L.S., Choi, J., Cleary, A., D'Azevedo, E., Demmel, J., Dhillon, I., Dongarra, J., Hammarling, S., Henry, G., Petitet, A., Stanley, K., Walker, D. and Whaley, R.C. (1987) *ScaLAPACK Users' Guide*. Philadelphia: Society for Industrial and Applied Mathematics.

Blaes, X. and Defourny, P. (2003) 'Retrieving crop parameters based on tandem ERS 1/2 interferometric coherence images', *Remote Sensing of Environment*, 88(4), pp. 374–385. Available at: https://doi.org/10.1016/j.rse.2003.08.008.

Born, M. and Wolf, E. (1999) *Principles of optics: electromagnetic theory of propagation, interference and diffraction of light*. 7th expanded ed. Cambridge ; New York: Cambridge University Press.

British Geological Survey (2000) 'Solid and Drift Geology. Frome. England and Wales Sheet 281.' Keyworth, Nottingham.

Bromhead, E., Siddle, H.J., Bassett, M.G., Great Britain Welsh Office, National Museums & Galleries of Wales, Great Britain Department of the Environment, and International Symposium on Landslides (2000) *Landslides and landslide management in South Wales*. Cardiff: Amgueddfeydd ac Orielau Cenedlaethol Cymru (Geological series ; no.18).

Butler, S., Wermelinger, M., Yu, Y. and Sharp, H. (2009) 'Relating Identifier Naming Flaws and Code Quality: An Empirical Study', in *2009 16th Working Conference on Reverse Engineering*. *2009 16th Working Conference on Reverse Engineering*, Lille, France: IEEE, pp. 31–35. Available at: https://doi.org/10.1109/WCRE.2009.50.

Cao, N., Lee, H. and Jung, H.C. (2015) 'Mathematical Framework for Phase-Triangulation Algorithms in Distributed-Scatterer Interferometry', *IEEE Geoscience and Remote Sensing Letters*, 12(9), pp. 1838–1842. Available at: https://doi.org/10.1109/LGRS.2015.2430752.

Cheney, M. and Borden, B. (2009) *Fundamentals of Radar Imaging*. Society for Industrial and Applied Mathematics (CBMS-NSF Regional Conference Series in Applied Mathematics). Available at: https://doi.org/10.1137/1.9780898719291.

Cigna, F. and Sowter, A. (2017) 'The relationship between intermittent coherence and precision of ISBAS InSAR ground motion velocities: ERS-1/2 case studies in the UK', *Remote Sensing of Environment*, 202, pp. 177–198. Available at: https://doi.org/10.1016/j.rse.2017.05.016.

Cloude, S.R., Papathanassiou, K. and Hajnsek, I. (2000) 'An Eigenvector Method for the Extraction of Surface Parameters in Polarmetric SAR', 450, p. 693.

Cloude, S.R. and Pottier, E. (1996) 'A review of target decomposition theorems in radar polarimetry', *IEEE Transactions on Geoscience and Remote Sensing*, 34(2), pp. 498–518. Available at: https://doi.org/10.1109/36.485127.

Cloude, S.R. and Pottier, E. (1997) 'An entropy based classification scheme for land applications of polarimetric SAR', *IEEE Transactions on Geoscience and Remote Sensing*, 35(1), pp. 68–78. Available at: https://doi.org/10.1109/36.551935.

Cohen, L. (1995) *Time-frequency analysis*. Englewood Cliffs, N.J: Prentice Hall PTR (Prentice Hall signal processing series).

Colesanti, C., Ferretti, A., Novali, F., Prati, C. and Rocca, F. (2003) 'Sar monitoring of progressive and seasonal ground deformation using the permanent scatterers technique', *IEEE Transactions on Geoscience and Remote Sensing*, 41(7), pp. 1685–1701. Available at: https://doi.org/10.1109/TGRS.2003.813278.

Cooper, H.M., Bennett, E., Blake, J., Blyth, E., Boorman, D., Cooper, E., Evans, J., Fry, M., Jenkins, A., Morrison, R., Rylett, D., Stanley, S., Szczykulska, M., Trill, E., Antoniou, V., Askquith-Ellis, A., Ball, L., Brooks, M., Clarke, M.A., Cowan, N., Cumming, A., Farrand, P., Hitt, O., Lord, W., Scarlett, P., Swain, O., Thornton, J., Warwick, A. and Winterbourn, B. (2021) 'COSMOS-UK: national soil moisture and hydrometeorology data for environmental science research', *Earth System Science Data*, 13(4), pp. 1737–1757. Available at: https://doi.org/10.5194/essd-13-1737-2021.

Craig Dobson, M., Ulaby, F.T. and Pierce, L.E. (1995) 'Land-cover classification and estimation of terrain attributes using synthetic aperture radar', *Remote Sensing of Environment*, 51(1), pp. 199–214. Available at: https://doi.org/10.1016/0034-4257(94)00075-X.

Cressie, N. (1990) 'The origins of kriging', *Mathematical Geology*, 22(3), pp. 239–252. Available at: https://doi.org/10.1007/BF00889887.

Crosetto, M., Monserrat, O., Cuevas-González, M., Devanthéry, N. and Crippa, B. (2016) 'Persistent Scatterer Interferometry: A review', *ISPRS Journal of Photogrammetry and Remote Sensing*, 115, pp. 78–89. Available at: https://doi.org/10.1016/j.isprsjprs.2015.10.011.

Culshaw, M., Tragheim, D., Bateson, L. and Donnely, L. (2009) 'Measurement of ground movements in Stoke-on-Trent (UK) using radar interferometry', *Geological Society, London, Engineering Geology Special Publications*, 22(1), pp. 317–317. Available at: https://doi.org/10.1144/EGSP22.I.

De Zan, F. (2014) 'Accuracy of Incoherent Speckle Tracking for Circular Gaussian Signals', *IEEE Geoscience and Remote Sensing Letters*, 11(1), pp. 264–267. Available at: https://doi.org/10.1109/LGRS.2013.2255259.

De Zan, F. and Guarnieri, A.M. (2006) 'TOPSAR: Terrain Observation by Progressive Scans', *IEEE Transactions on Geoscience and Remote Sensing*, 44(9), pp. 2352–2360. Available at: https://doi.org/10.1109/TGRS.2006.873853.

De Zan, F., Parizzi, A., Prats-Iraola, P. and López-Dekker, P. (2014) 'A SAR Interferometric Model for Soil Moisture', *IEEE Transactions on Geoscience and Remote Sensing*, 52(1), pp. 418–425. Available at: https://doi.org/10.1109/TGRS.2013.2241069.

De Zan, F., Prats-Iraola, P. and Rodriguez-Cassola, M. (2018) 'The theoretical performance of different algorithms for shift estimation between SAR images', in *EUSAR 2018; 12th European Conference on Synthetic Aperture Radar*. *EUSAR 2018; 12th European Conference on Synthetic Aperture Radar*, pp. 1–4.

De Zan, F., Zonno, M. and Lopez Dekker, P. (2015) 'Phase Inconsistencies and Multiple Scattering in SAR Interferometry', *Geoscience and Remote Sensing, IEEE Transactions on*, 53, pp. 6608–6616. Available at: https://doi.org/10.1109/TGRS.2015.2444431.

Department of the Environment Welsh Office (1990) *Planning Policy Guidance: Development on Unstable Land*. 14. Department of the Environment Welsh Office. Available at: https://webarchive.nationalarchives.gov.uk/ukgwa/20120919122719/http://www.communities.gov.uk/documents/planningandbuilding/pdf/147471.pdf (Accessed: 30 April 2023).

Desnos, Y., Foumelis, M., Engdahl, M., Mathieu, P., Palazzo, F. and Ramoino, F. (2017) 'Sentinel-1 mission scientific exploitation activities', in *2017 IEEE International Geoscience and Remote Sensing Symposium (IGARSS)*. *2017 IEEE International Geoscience and Remote Sensing Symposium (IGARSS)*, pp. 5521–5524. Available at: https://doi.org/10.1109/IGARSS.2017.8128254.

Eaton, J.W. (2002) *GNU Octave: A High-level Interactive Language for Numerical Computations*. Network Theory.

El-Darymli, K., McGuire, P., Gill, E., Power, D. and Moloney, C. (2014) *Understanding the significance of radiometric calibration for Synthetic Aperture Radar Imagery*, *Canadian Conference on Electrical and Computer Engineering*. Available at: https://doi.org/10.1109/CCECE.2014.6901104.

Engdahl, M. (2013) *Multitemporal InSAR in land-cover and vegetation mapping*. Aalto University.

European Space Agency (ed.) (2007) *InSAR principles: guidelines for SAR interferometry processing and interpretation - Part C*. Noordwijk, the Netherlands: ESA Publications, ESTEC (ESA TM, 19).

European Space Agency (2019) *Sentinel-1 Level 1 Detailed Algorithm Definition*. DI-MPC-IPFDPM. European Space Agency, p. 88. Available at: https://sentinel.esa.int/documents/247904/1877131/Sentinel-1-Level-1-Detailed-Algorithm-Definition (Accessed: 28 March 2023).

Ferretti, A., Fumagalli, A., Novali, F., Prati, C., Rocca, F. and Rucci, A. (2014) 'A New Algorithm for Processing Interferometric Data-Stacks: SqueeSAR', *IEEE TRANSACTIONS ON GEOSCIENCE AND REMOTE SENSING*, p. 12.

Ferretti, A., Prati, C. and Rocca, F. (2000) 'Nonlinear subsidence rate estimation using permanent scatterers in differential SAR interferometry', *IEEE Transactions on Geoscience and Remote Sensing*, 38(5). Available at: https://doi.org/10.1109/36.868878.

Ferretti, A., Prati, C. and Rocca, F. (2001) 'Permanent Scatterers in SAR Interferometry', *IEEE TRANSACTIONS ON GEOSCIENCE AND REMOTE SENSING*, 39(1), p. 13.

Ferretti, A., Savio, G., Barzaghi, R., Borghi, A., Musazzi, S., Novali, F., Prati, C. and Rocca, F. (2007) 'Submillimeter Accuracy of InSAR Time Series: Experimental Validation', *IEEE Transactions on Geoscience and Remote Sensing*, 45(5), pp. 1142–1153. Available at: https://doi.org/10.1109/TGRS.2007.894440.

Ford, J.P. (1993) *Guide to Magellan Image Interpretation*. First Edition. Nasa/Jet Propulsion Laboratory.

Forster, A., Arrick, A., Culshaw, M.G. and Johnston, M. (1994) *A geological foundation for planning in Wigan*. British Geographical Survey (WN/95/003).

Foumelis, M., Delgado Blasco, J.M., Desnos, Y.-L., Engdahl, M., Fernandez, D., Veci, L., Lu, J. and Wong, C. (2018) 'Esa Snap - Stamps Integrated Processing for Sentinel-1 Persistent Scatterer Interferometry', in *IGARSS 2018 - 2018 IEEE International Geoscience and Remote Sensing Symposium*. *IGARSS 2018 - 2018 IEEE International Geoscience and Remote Sensing Symposium*, pp. 1364–1367. Available at: https://doi.org/10.1109/IGARSS.2018.8519545.

Freeman, A. and Durden, S.L. (1998) 'A three-component scattering model for polarimetric SAR data', *IEEE Transactions on Geoscience and Remote Sensing*, 36(3), pp. 963–973. Available at: https://doi.org/10.1109/36.673687.

Gabriel, A.K., Goldstein, R.M. and Zebker, H.A. (1989) 'Mapping small elevation changes over large areas: Differential radar interferometry', *Journal of Geophysical Research*, 94(B7), p. 9183. Available at: https://doi.org/10.1029/JB094iB07p09183.

Gatelli, F., Monti Guamieri, A., Parizzi, F., Pasquali, P., Prati, C. and Rocca, F. (1994) 'The wavenumber shift in SAR interferometry', *IEEE Transactions on Geoscience and Remote Sensing*, 32(4), pp. 855–865. Available at: https://doi.org/10.1109/36.298013.

Goodman, J.W. (1976) 'Some fundamental properties of speckle*', *Journal of the Optical Society of America*, 66(11), p. 1145. Available at: https://doi.org/10.1364/JOSA.66.001145.

Gostelow, T.P. (1977) *A report on valley instability at Blaina, South Wales*. British Geological Survey (British Geological Survey Technical Report, EG/77/11).

Graham, L.C. (1974) 'Synthetic interferometer radar for topographic mapping', *Proceedings of the IEEE*, 62(6), pp. 763–768. Available at: https://doi.org/10.1109/PROC.1974.9516.

Grant, B. (2020) *Cliff and Landslide Monitoring with PSInSAR in Folkestone Warren, Kent, UK*. MSci. Imperial College London.

Gray, A.L. and Farris-Manning, P.J. (1993) 'Repeat-pass interferometry with airborne synthetic aperture radar', *IEEE Transactions on Geoscience and Remote Sensing*, 31(1), pp. 180–191. Available at: https://doi.org/10.1109/36.210459.

Grebenitcharsky, R. and Hanssen, R. (2005) 'Spatial modeling of atmospheric delays for InSAR and GPS sensors', in. *7th European Conference on Applications of Meteorology (ECAM)*, p. 1.

Guarnieri, A.M. and Prati, C. (1997) 'SAR interferometry: a "Quick and dirty" coherence estimator for data browsing', *IEEE Transactions on Geoscience and Remote Sensing*, 35(3), pp. 660–669. Available at: https://doi.org/10.1109/36.581984.

Guarnieri, A.M. and Tebaldini, S. (2008) 'On the Exploitation of Target Statistics for SAR Interferometry Applications', *IEEE Transactions on Geoscience and Remote Sensing*, 46(11), pp. 3436–3443. Available at: https://doi.org/10.1109/TGRS.2008.2001756.

Hajnsek, I., Jagdhuber, T., Schon, H. and Papathanassiou, K.P. (2009) 'Potential of Estimating Soil Moisture Under Vegetation Cover by Means of PolSAR', *IEEE Transactions on Geoscience and Remote Sensing*, 47(2), pp. 442–454. Available at: https://doi.org/10.1109/TGRS.2008.2009642.

Hajnsek, I. and Prats, P. (2008) 'Soil Moisture Estimation in time with D-InSAR', in *IGARSS 2008 - 2008 IEEE International Geoscience and Remote Sensing Symposium*. *IGARSS 2008 - 2008 IEEE International Geoscience and Remote Sensing Symposium*, p. III-546-III–549. Available at: https://doi.org/10.1109/IGARSS.2008.4779405.

Halcrow (2006) *Ventnor Undercliff, Isle of Wight Coastal Instability Risk: Interpretative Report and Quantitative Risk Analysis*. Isle of Wight Council.

Hallikainen, M., Ulaby, F., Dobson, M., El-Rayes, M. and Wu, L.-K. (1985) 'Microwave Dielectric Behavior of Wet Soil-Part 1: Empirical Models and Experimental Observations', *Geoscience and Remote Sensing, IEEE Transactions on*, GE-23, pp. 25–34. Available at: https://doi.org/10.1109/TGRS.1985.289497.

Hamerly, G. and Elkan, C. (2003) 'Learning the k in k-means', in *Advances in Neural Information Processing Systems*. MIT Press. Available at: https://papers.nips.cc/paper_files/paper/2003/hash/234833147b97bb6aed53a8f4f1c7a7d8-Abstract.html (Accessed: 28 April 2023).

Harrison, A.M., Plim, J.F.M., Harrison, M., Jones, L.D. and Culshaw, M.G. (2012) 'The relationship between shrink–swell occurrence and climate in south-east England', *Proceedings of the Geologists' Association*, 123(4), pp. 556–575. Available at: https://doi.org/10.1016/j.pgeola.2012.05.002.

Hees, A., Koch, P., Rostan, F., Huchler, M., Croci, R. and Østergaard, A. (2013) 'Sentinel-1 antenna model validation: Pattern prediction vs. PNFS measurements', in *2013 IEEE International Symposium on Phased Array Systems and Technology*. *2013 IEEE International Symposium on Phased Array Systems and Technology*, pp. 604–610. Available at: https://doi.org/10.1109/ARRAY.2013.6731898.

Hensley, S., Michel, T., Van Zyl, J., Muellerschoen, R., Chapman, B., Oveisgharan, S., Haddad, Z.S., Jackson, T. and Mladenova, I. (2011) 'Effect of Soil Moisture on polarimetric-

interferometric repeat pass observations by UAVSAR during 2010 Canadian Soil Moisture campaign', in *2011 IEEE International Geoscience and Remote Sensing Symposium*. *2011 IEEE International Geoscience and Remote Sensing Symposium*, pp. 1063–1066. Available at: https://doi.org/10.1109/IGARSS.2011.6049379.

Herrera, G., Notti, D., García-Davalillo, J.C., Mora, O., Cooksley, G., Sánchez, M., Arnaud, A. and Crosetto, M. (2011) 'Analysis with C- and X-band satellite SAR data of the Portalet landslide area', *Landslides*, 8(2), pp. 195–206. Available at: https://doi.org/10.1007/s10346-010-0239-3.

Hetland, E.A., Musé, P., Simons, M., Lin, Y.N., Agram, P.S. and DiCaprio, C.J. (2012) 'Multiscale InSAR Time Series (MInTS) analysis of surface deformation', *Journal of Geophysical Research: Solid Earth*, 117(B2). Available at: https://doi.org/10.1029/2011JB008731.

Hooper, A. (2008) 'A multi-temporal InSAR method incorporating both persistent scatterer and small baseline approaches', *Geophysical Research Letters*, 35(16). Available at: https://doi.org/10.1029/2008GL034654.

Hooper, A., Zebker, H., Segall, P. and Kampes, B. (2004) 'A new method for measuring deformation on volcanoes and other natural terrains using InSAR persistent scatterers', *Geophysical Research Letters*, 31(23). Available at: https://doi.org/10.1029/2004GL021737.

Hooper, A.J. (2006) *Persistent Scatterer Radar Interferometry for Crustal Deformation Studies and Modeling of Volcanic Deformation*.

IAEA Safety Standards: Geological Disposal Facilities for Radioactive Waste (2011). SSG-14. International Atomic Energy Agency.

'II. A dynamical theory of the electromagnetic field' (1864) *Proceedings of the Royal Society of London*, 13, pp. 531–536. Available at: https://doi.org/10.1098/rspl.1863.0098.

Implementing Geological Disposal (2014). 14D/235. Department of Energy & Climate Change.

ISO (2017) 'International Standard - Systems and software engineering–Vocabulary', *ISO/IEC/IEEE 24765:2017(E)*, pp. 1–541. Available at: https://doi.org/10.1109/IEEESTD.2017.8016712.

'ISO/IEC/IEEE International Standard - Systems and software engineering – Software life cycle processes' (2008) *IEEE STD 12207-2008*, pp. 1–138. Available at: https://doi.org/10.1109/IEEESTD.2008.4475826.

Jong-Sen Lee, Cloude, S.R., Papathanassiou, K.P., Grunes, M.R. and Woodhouse, I.H. (2003) 'Speckle filtering and coherence estimation of polarimetric SAR interferometry data for forest applications', *IEEE Transactions on Geoscience and Remote Sensing*, 41(10), pp. 2254–2263. Available at: https://doi.org/10.1109/TGRS.2003.817196.

Jung, J., Kim, D., Lavalle, M. and Yun, S. (2016) 'Coherent Change Detection Using InSAR Temporal Decorrelation Model: A Case Study for Volcanic Ash Detection', *IEEE Transactions on Geoscience and Remote Sensing*, 54(10), pp. 5765–5775. Available at: https://doi.org/10.1109/TGRS.2016.2572166.

Kemeling, I. (2006) *Persistent scatterer interferometry to monitor mining related ground surface deformation for data-driven modelling*. Durham University. Available at: http://etheses.dur.ac.uk/2592/.

Khankhoje, U.K., Zyl, J.J. van and Cwik, T.A. (2013) 'Computation of Radar Scattering From Heterogeneous Rough Soil Using the Finite-Element Method', *IEEE Transactions on Geoscience and Remote Sensing*, 51(6), pp. 3461–3469. Available at: https://doi.org/10.1109/TGRS.2012.2225431.

Kirui, P.K., Reinosch, E., Isya, N., Riedel, B. and Gerke, M. (2021) 'Mitigation of Atmospheric Artefacts in Multi Temporal InSAR: A Review', *PFG – Journal of Photogrammetry, Remote Sensing and Geoinformation Science* [Preprint]. Available at: https://doi.org/10.1007/s41064-021-00138-z.

Knospe, S. and Jonsson, S. (2010) 'Covariance Estimation for dInSAR Surface Deformation Measurements in the Presence of Anisotropic Atmospheric Noise', *IEEE Transactions on Geoscience and Remote Sensing*, 48(4), pp. 2057–2065. Available at: https://doi.org/10.1109/TGRS.2009.2033937.

Kornelsen, K.C. and Coulibaly, P. (2013) 'Advances in soil moisture retrieval from synthetic aperture radar and hydrological applications', *Journal of Hydrology*, 476, pp. 460–489. Available at: https://doi.org/10.1016/j.jhydrol.2012.10.044.

Lawson, C.L., Hanson, R.J., Kincaid, D.R. and Krogh, F.T. (1979) 'Basic Linear Algebra Subprograms for Fortran Usage', *ACM Transactions on Mathematical Software*, 5(3), pp. 308–323. Available at: https://doi.org/10.1145/355841.355847.

Lee, E.M. and Giles, D.P. (2020) 'Chapter 4 Landslide and slope stability hazard in the UK', *Geological Society, London, Engineering Geology Special Publications*, 29(1), pp. 81–162. Available at: https://doi.org/10.1144/EGSP29.4.

Lee, J.-S., Miller, A.R. and Hoppel, K.W. (1994) 'Statistics of phase difference and product magnitude of multi-look processed Gaussian signals', *Waves in Random Media*, 4(3), pp. 307–319. Available at: https://doi.org/10.1088/0959-7174/4/3/006.

Liu, S. (2012) *Satellite radar interferometry: Estimation of atmospheric delay*. Delft University of Technology. Available at: https://repository.tudelft.nl/islandora/object/uuid%3A21b9ea98-b9f0-4520-9460-3cfdc14601f2 (Accessed: 14 June 2021).

Lloyd, S.P. (1982) 'Least squares quantization in pcm', *IEEE Transactions on Information Theory*, 28, pp. 129–137.

Lopez-Martinez, C., Pottier, E. and Cloude, S.R. (2005) 'Statistical assessment of eigenvector-based target decomposition theorems in radar polarimetry', *IEEE Transactions on Geoscience and Remote Sensing*, 43(9), pp. 2058–2074. Available at: https://doi.org/10.1109/TGRS.2005.853934.

Lopez-Sanchez, J.M., Ballester-Berman, J.D., Vicente-Guijalba, F., Cloude, S.R., McNairn, H., Shang, J., Skriver, H., Jagdhuber, T., Hajnsek, I., Pottier, E., Marechal, C., Hubert-Moy, L., Corgne, S., Wdowinski, S., Touzi, R., Gosselin, G., Brooks, R., Yamaguchi, Y. and Singh, G. (2021) 'Agriculture and Wetland Applications', in Irena Hajnsek and Y.-L. Desnos (eds) *Polarimetric Synthetic Aperture Radar: Principles and Application*. Cham: Springer International Publishing (Remote Sensing and Digital Image Processing), pp. 119–178. Available at: https://doi.org/10.1007/978-3-030-56504-6_3.

Ma, G., Zhao, Q., Wang, Q. and Liu, M. (2018) 'On the Effects of InSAR Temporal Decorrelation and Its Implications for Land Cover Classification: The Case of the Ocean-Reclaimed Lands of the Shanghai Megacity', *Sensors (Basel, Switzerland)*, 18(9). Available at: https://doi.org/10.3390/s18092939.

Mandal, D., Kumar, V., Ratha, D., Dey, S., Bhattacharya, A., Lopez-Sanchez, J.M., McNairn, H. and Rao, Y.S. (2020) 'Dual polarimetric radar vegetation index for crop growth monitoring using sentinel-1 SAR data', *Remote Sensing of Environment*, 247, p. 111954. Available at: https://doi.org/10.1016/j.rse.2020.111954.

Martin, R.C. (ed.) (2009a) *Clean code: a handbook of agile software craftsmanship*. Upper Saddle River, NJ: Prentice Hall.

Martin, R.C. (ed.) (2009b) 'Foreword', in *Clean code: a handbook of agile software craftsmanship*. Upper Saddle River, NJ: Prentice Hall.

Martin, R.C. and Martin, R.C. (2018) *Clean architecture: a craftsman's guide to software structure and design*. London, England: Prentice Hall (Robert C. Martin series).

Mason, P.J., Devanthér, N., Camafort, M., Scoular, J., Payàs, B., Lawrence, J. and Ghail, R.C. (2022) *C805 InSAR and Earth Observation techniques for infrastructure*. CIRIA.

Mason, P.J., Ghail, R.C., Bischoff, C. and Skipper, J.A. (2015) 'Detecting and monitoring small-scale discrete ground movements across London, using Persistent Scatterer InSAR (PSI)', in. *Geotechnical Engineering for Infrastructure and Development: XVI European Conference on Soil Mechanics and Geotechnical Engineering*, ICE Publishing, p. 9.

MATLAB (2023) *9.14.0.2206163 (R2023a)*. Natick, Massachusetts: The MathWorks Inc.

Meyer, F., Kampes, B., Bamler, R. and Fischer, J. (2005) 'Methods for Atmospheric Correction in INSAR Data', in. *ESA Fringe 2005*, p. 7.

Miller Argent & RPS (2015) *Ffos-Y-Fran Land Reclamation Scheme Restoration Plan*. Miller Argent & RPS. Available at: https://www.merthyr.gov.uk/media/5003/ed038-ffos-y-fran-

land-reclamation-scheme-phase-1-restoration-plan-full-document-november-2015.pdf (Accessed: 30 April 2023).

Miranda, N. and Meadows, P.J. (2015) *Radiometric Calibration of S-1 Level-1 Products Generated by the S-1 IPF*. ESA-EOPG-CSCOP-TN-0002.

Moeremans, B. and Dautrebande, S. (2000) 'Soil moisture evaluation by means of multi-temporal ERS SAR PRI images and interferometric coherence', *Journal of Hydrology*, 234(3), pp. 162–169. Available at: https://doi.org/10.1016/S0022-1694(00)00251-1.

Moreira, A., Prats-Iraola, P., Younis, M., Krieger, G., Hajnsek, I. and Papathanassiou, K.P. (2013) 'A tutorial on synthetic aperture radar', *IEEE Geoscience and Remote Sensing Magazine*, 1(1), pp. 6–43. Available at: https://doi.org/10.1109/MGRS.2013.2248301.

Morrison, K., Bennett, J.C., Nolan, M. and Menon, R. (2011) 'Laboratory Measurement of the DInSAR Response to Spatiotemporal Variations in Soil Moisture', *IEEE Transactions on Geoscience and Remote Sensing*, 49(10), pp. 3815–3823. Available at: https://doi.org/10.1109/TGRS.2011.2132137.

Morton, C.S., R.D. ;Marston, C.G. ;O'Neil, A.W. ;Rowland (2018) 'Land Cover Map 2018'. UK Centre for Environment and Hydrology. Available at: https://doi.org/10.5285/9f7f7f70-5137-4bfc-a6a3-f91783d5a6a6.

Mukul, Manas, Srivastava, V., Jade, S. and Mukul, Malay (2017) 'Uncertainties in the Shuttle Radar Topography Mission (SRTM) Heights: Insights from the Indian Himalaya and Peninsula', *Scientific Reports*, 7. Available at: https://doi.org/10.1038/srep41672.

National Academies of Sciences, E. (2019) 'Recommendation 6-6', in *Reproducibility and Replicability in Science*. Available at: https://doi.org/10.17226/25303.

Natural Resources Wales (2017) 'Historical Landfill Sites'.

NDA / RWMD (2011) *Site characterisation for a geological disposal facility. Status Report: March 2010*. NDA/RWMD/017. Nuclear Decomissioning Authority.

Nesti, G., Tarchi, D., Despan, D., Rudant, J.-P., Bedidi, A., Borderies, P. and Bachelier, E. (1998) 'Phase Shift and Decorrelation of Radar Signal Related to Soil Moisture Changes', *Proc. of 2nd International Workshop on Retrieval of Bio-Geo-physical Parameter from SAR Data for Land Applications* [Preprint].

Nolan, M., Fatland, D.R. and Hinzman, L. (2003) 'Dinsar measurement of soil moisture', *IEEE Transactions on Geoscience and Remote Sensing*, 41(12), pp. 2802–2813. Available at: https://doi.org/10.1109/TGRS.2003.817211.

North, M., Farewell, T., Hallett, S. and Bertelle, A. (2017) 'Monitoring the Response of Roads and Railways to Seasonal Soil Movement with Persistent Scatterers Interferometry over Six UK Sites', *Remote Sensing*, 9(9), p. 922. Available at: https://doi.org/10.3390/rs9090922.

O'Connor, W., Mider, G., Lawrence, J.A., Agar, S., Mason, P.J., Ghail, R. and Scoular, J. (2021) 'An Investigation into Ground Movement on the Ventnor Landslide Complex, UK Using Persistent Scatterer Interferometry', *Remote Sensing*, 13(18), p. 3711. Available at: https://doi.org/10.3390/rs13183711.

Oh, Y., Sarabandi, K. and Ulaby, F.T. (2002) 'Semi-empirical model of the ensemble-averaged differential Mueller matrix for microwave backscattering from bare soil surfaces', *IEEE Transactions on Geoscience and Remote Sensing*, 40(6), pp. 1348–1355. Available at: https://doi.org/10.1109/TGRS.2002.800232.

Osmanoğlu, B., Sunar, F., Wdowinski, S. and Cabral-Cano, E. (2016) 'Time series analysis of InSAR data: Methods and trends', *ISPRS Journal of Photogrammetry and Remote Sensing*, 115, pp. 90–102. Available at: https://doi.org/10.1016/j.isprsjprs.2015.10.003.

Ozdemir, C. (2012) 'Inverse Synthetic Aperture Radar Imaging With MATLAB Algorithms', in.

Panetti, A., Rostan, F., L'Abbate, M., Bruno, C., Bauleo, A., Catalano, T., Cotogni, M., Galvagni, L., Pietropaolo, A., Taini, G., Venditti, P., Huchler, M., Torres, R., Lokas, S., Bibby, D. and Geudtner, D. (2014) 'Copernicus Sentinel-1 Satellite and C-SAR instrument', in *2014 IEEE Geoscience and Remote Sensing Symposium*. *2014 IEEE Geoscience and Remote Sensing Symposium*, pp. 1461–1464. Available at: https://doi.org/10.1109/IGARSS.2014.6946712.

Parizzi, A. and Brcic, R. (2011) 'Adaptive InSAR Stack Multilooking Exploiting Amplitude Statistics: A Comparison Between Different Techniques and Practical Results', *IEEE Geoscience and Remote Sensing Letters*, 8(3), pp. 441–445. Available at: https://doi.org/10.1109/LGRS.2010.2083631.

Paul M. Duvall, S.M. (2007) *Continuous Integration: Improving Software Quality and Reducing Risk*. 1st edn. Lebanon, Indiana, U.s.a.: Addison-Wesley Professional. Available at: https://www.biblio.com/book/continuous-integration-improving-software-quality-reducing/d/1328272037 (Accessed: 23 December 2022).

Peter, H., Jäggi, A., Fernández, J., Escobar, D., Ayuga, F., Arnold, D., Wermuth, M., Hackel, S., Otten, M., Simons, W., Visser, P., Hugentobler, U. and Féménias, P. (2017) 'Sentinel-1A – First precise orbit determination results', *Advances in Space Research*, 60(5), pp. 879–892. Available at: https://doi.org/10.1016/j.asr.2017.05.034.

Petropoulos, G.P., Ireland, G. and Barrett, B. (2015) 'Surface soil moisture retrievals from remote sensing: Current status, products & future trends', *Physics and Chemistry of the Earth, Parts A/B/C*, 83–84, pp. 36–56. Available at: https://doi.org/10.1016/j.pce.2015.02.009.

Plank, S., Singer, J. and Thuro, K. (2013) 'Assessment of number and distribution of persistent scatterers prior to radar acquisition using open access land cover and topographical data', *ISPRS Journal of Photogrammetry and Remote Sensing*, 85, pp. 132–147. Available at: https://doi.org/10.1016/j.isprsjprs.2013.09.001.

Pottier, E. and Lee, J.-S. (2017) *Polarimetric Radar Imaging : From Basics to Applications*. CRC Press. Available at: https://doi.org/10.1201/9781420054989.

Prakash, R., Singh, D. and Pathak, N.P. (2012) 'A Fusion Approach to Retrieve Soil Moisture With SAR and Optical Data', *IEEE Journal of Selected Topics in Applied Earth Observations and Remote Sensing*, 5(1), pp. 196–206. Available at: https://doi.org/10.1109/JSTARS.2011.2169236.

Prats-Iraola, P., Scheiber, R., Marotti, L., Wollstadt, S. and Reigber, A. (2012) 'TOPS Interferometry With TerraSAR-X', *IEEE Transactions on Geoscience and Remote Sensing*, 50(8), pp. 3179–3188. Available at: https://doi.org/10.1109/TGRS.2011.2178247.

Principal Component Analysis (2002). New York: Springer-Verlag (Springer Series in Statistics). Available at: https://doi.org/10.1007/b98835.

Project Ankhiale: Estimating the uplift due to high-heat-generating waste in a Geological Disposal Facility (2015). RP51 W1.1d. AMEC Foster Wheeler.

Qin, Y., Perissin, D. and Bai, J. (2018) 'Investigations on the Coregistration of Sentinel-1 TOPS with the Conventional Cross-Correlation Technique', *Remote Sensing*, 10(9), p. 1405. Available at: https://doi.org/10.3390/rs10091405.

Rabus, B., Wehn, H. and Nolan, M. (2010) 'The Importance of Soil Moisture and Soil Structure for InSAR Phase and Backscatter, as Determined by FDTD Modeling', *IEEE Transactions on Geoscience and Remote Sensing*, 48(5), pp. 2421–2429. Available at: https://doi.org/10.1109/TGRS.2009.2039353.

Ramya, M.N.S. and Kumar, S. (2021) 'PolInSAR coherence-based decomposition modeling for scattering characterization: A case study in Uttarakhand, India', *Science of Remote Sensing*, 3, p. 100020. Available at: https://doi.org/10.1016/j.srs.2021.100020.

Rignot, E., Chellappa, R. and Dubois, P. (1992) 'Unsupervised segmentation of polarimetric SAR data using the covariance matrix', *IEEE Transactions on Geoscience and Remote Sensing*, 30(4), pp. 697–705. Available at: https://doi.org/10.1109/36.158863.

Rocca, F. (2007) 'Modeling Interferogram Stacks', *IEEE Transactions on Geoscience and Remote Sensing*, 45(10), pp. 3289–3299. Available at: https://doi.org/10.1109/TGRS.2007.902286.

Rodríguez, E., Morris, C.S. and Belz, J.E. (2006) 'A Global Assessment of the SRTM Performance', *Photogrammetric Engineering & Remote Sensing*, 72(3), pp. 249–260. Available at: https://doi.org/10.14358/PERS.72.3.249.

Rosen, P.A., Hensley, S., Joughin, I.R., Li, F.K., Madsen, S.N., Rodriguez, E. and Goldstein, R.M. (2000) 'Synthetic aperture radar interferometry', *Proceedings of the IEEE*, 88(3), pp. 333–382. Available at: https://doi.org/10.1109/5.838084.

Rucci, A., Ferretti, A., Monti Guarnieri, A. and Rocca, F. (2012) 'Sentinel 1 SAR interferometry applications: The outlook for sub millimeter measurements', *Remote Sensing of Environment*, 120, pp. 156–163. Available at: https://doi.org/10.1016/j.rse.2011.09.030.

Samiei-Esfahany, S., Martins, J.E., van Leijen, F. and Hanssen, R.F. (2016) 'Phase Estimation for Distributed Scatterers in InSAR Stacks Using Integer Least Squares Estimation', *IEEE TRANSACTIONS ON GEOSCIENCE AND REMOTE SENSING*, 54(10), p. 17.

Sansosti, E., Berardino, P., Manunta, M., Serafino, F. and Fornaro, G. (2006) 'Geometrical SAR image registration', *Geoscience and Remote Sensing, IEEE Transactions on*, 44, pp. 2861–2870. Available at: https://doi.org/10.1109/TGRS.2006.875787.

Sato, A., Yamaguchi, Y., Singh, G. and Park, S.-E. (2012) 'Four-Component Scattering Power Decomposition With Extended Volume Scattering Model', *IEEE Geoscience and Remote Sensing Letters*, 9(2), pp. 166–170. Available at: https://doi.org/10.1109/LGRS.2011.2162935.

Scoular, J., Agar, S., Carpenter, A., Morgan, T., Lawrence, J., Ghail, R. and Mason, P. (2021) 'Expanding horizons', *GEOSCIENTIST*, 31 May. Available at: https://geoscientist.online/sections/features/expanding-horizons/ (Accessed: 29 March 2023).

Scoular, J., Ghail, R., Mason, P. and Lawrence, J. (2022) 'Are measured InSAR displacements a function of the chosen processing method?', *Quarterly Journal of Engineering Geology and Hydrogeology*, 55(4), pp. qjegh2022-049. Available at: https://doi.org/10.1144/qjegh2022-049.

Scoular, J., Ghail, R., Mason, P., Lawrence, J., Bellhouse, M., Holley, R. and Morgan, T. (2020) 'Retrospective InSAR Analysis of East London during the Construction of the Lee Tunnel', p. 19.

Sentinel-1 Product Specification (2016). S1-RS-MDA-52–7440. European Space Agency, p. 197.

Sevgi, L. (2014) *Electromagnetic Modeling and Simulation*.

Shamshiri, R., Nahavandchi, H. and Motagh, M. (2018) 'Persistent Scatterer Analysis Using Dual-Polarization Sentinel-1 Data: Contribution From VH Channel', *IEEE Journal of Selected Topics in Applied Earth Observations and Remote Sensing*, 11(9), pp. 3105–3112. Available at: https://doi.org/10.1109/JSTARS.2018.2848111.

Shi, J., Wang, J., Hsu, A.Y., O'Neill, P.E. and Engman, E.T. (1997) 'Estimation of bare surface soil moisture and surface roughness parameter using L-band SAR image data', *IEEE Transactions on Geoscience and Remote Sensing*, 35(5), pp. 1254–1266. Available at: https://doi.org/10.1109/36.628792.

Shire, T., Lawrence, J., Agar, S., Ghail, R. and Judge, T. (2023) 'Satellite remote sensing of UK embankment dams: influence of dam features on monitoring quality', *Dams and Reservoirs*, pp. 1–11.

Shumway, R.H. and Stoffer, D.S. (2017) *Time Series Analysis and Its Applications: With R Examples*. Cham: Springer International Publishing (Springer Texts in Statistics). Available at: https://doi.org/10.1007/978-3-319-52452-8.

Siddle, H.J., Bromhead, E. and Bassett, M.G. (2000) *Landslides and landslide management in South Wales*. Cardiff: Amgueddfeydd ac Orielau Cenedlaethol Cymru (Bulletin (Geological Survey of Canada : 1921)).

Skolnik, M.I. (2001) *Introduction to Radar Systems*. McGraw-Hill.

Small, D. and Schubert, A. (2019) *Guide to Sentinel 1 Geocoding v1.10*. UZH-S1-GC-AD. Telespazio/Vega, p. 42.

Smyth, P. (1997) 'Clustering Sequences with Hidden Markov Models', in *Advances in Neural Information Processing System*. MIT Press, pp. 648–654.

Sowter, A., Bateson, L., Strange, P., Ambrose, K. and Syafiudin, M.F. (2013) 'DInSAR estimation of land motion using intermittent coherence with application to the South Derbyshire and Leicestershire coalfields', *Remote Sensing Letters*, 4(10), pp. 979–987. Available at: https://doi.org/10.1080/2150704X.2013.823673.

Stanley, J.B., S.;Antoniou, V.;Askquith-Ellis, A.;Ball, L.A.;Bennett, E.S.;Blake, J.R.;Boorman, D.B.;Brooks, M.;Clarke, M.;Cooper, H.M.;Cowan, N.;Cumming, A.;Evans, J.G.;Farrand, P.;Fry, M.;Hitt, O.E.;Lord, W.D.;Morrison, R.;Nash, G.V.;Rylett, D.;Scarlett, P.M.;Swain, O.D.;Szczykulska, M.;Thornton, J.L.;Trill, E.J.;Warwick, A.C.;Winterbourn (2021) 'Daily and sub-daily hydrometeorological and soil data (2013-2019) [COSMOS-UK]'. NERC Environmental Information Data Centre. Available at: https://doi.org/10.5285/b5c190e4-e35d-40ea-8fbe-598da03a1185.

Torres, R., Snoeij, P., Geudtner, D., Bibby, D., Davidson, M., Attema, E., Potin, P., Rommen, B., Floury, N., Brown, M., Traver, I.N., Deghaye, P., Duesmann, B., Rosich, B., Miranda, N., Bruno, C., L'Abbate, M., Croci, R., Pietropaolo, A., Huchler, M. and Rostan, F. (2012) 'GMES Sentinel-1 mission', *Remote Sensing of Environment*, 120, pp. 9–24. Available at: https://doi.org/10.1016/j.rse.2011.05.028.

Touzi, R. (2002) 'A review of speckle filtering in the context of estimation theory', *IEEE Transactions on Geoscience and Remote Sensing*, 40(11), pp. 2392–2404. Available at: https://doi.org/10.1109/TGRS.2002.803727.

Touzi, R., Lopes, A., Bruniquel, J. and Vachon, P. (1996) 'Unbiased estimation of the coherence from multi-look SAR data', in *IGARSS '96. 1996 International Geoscience and Remote Sensing Symposium*. *IGARSS '96. 1996 International Geoscience and Remote Sensing Symposium*, pp. 662–664 vol.1. Available at: https://doi.org/10.1109/IGARSS.1996.516435.

Touzi, R., Lopes, A., Bruniquel, J. and Vachon, P.W. (1999) 'Coherence estimation for SAR imagery', *IEEE Transactions on Geoscience and Remote Sensing*, 37(1), pp. 135–149. Available at: https://doi.org/10.1109/36.739146.

Trisovic, A., Lau, M.K., Pasquier, T. and Crosas, M. (2022) 'A large-scale study on research code quality and execution', *Scientific Data*, 9(1), p. 60. Available at: https://doi.org/10.1038/s41597-022-01143-6.

UK Centre for Ecology and Hydrology (2018) 'Land Cover plus: Crops (2018)'. EDINA Environment Digimap Service. Available at: https://digimap.edina.ac.uk.

UK Natural Capital Land Cover in the UK (2015). Office for National Statistics. Available at: https://www.ons.gov.uk/economy/environmentalaccounts/articles/uknaturalcapitallandcoverintheuk/2015-03-17 (Accessed: 10 March 2021).

Ulaby, F.T. and Batlivala, P.P. (1976) 'Optimum Radar Parameters for Mapping Soil Moisture', *IEEE Transactions on Geoscience Electronics*, 14(2), pp. 81–93. Available at: https://doi.org/10.1109/TGE.1976.294414.

Ulaby, F.T., Batlivala, P.P. and Dobson, M.C. (1978) 'Microwave Backscatter Dependence on Surface Roughness, Soil Moisture, and Soil Texture: Part I-Bare Soil', *IEEE Transactions on Geoscience Electronics*, 16(4), pp. 286–295. Available at: https://doi.org/10.1109/TGE.1978.294586.

Ulaby, F.T., Dubois, P.C. and van Zyl, J. (1996) 'Radar mapping of surface soil moisture', *Journal of Hydrology*, 184(1–2), pp. 57–84. Available at: https://doi.org/10.1016/0022-1694(95)02968-0.

Van Zyl, J. and Kim, Y. (2011) *Synthetic aperture radar polarimetry*. Hoboken, NJ: Wiley (JPL space science and technology series).

Wackernagel, H. (2003) *Multivariate Geostatistics: An Introduction with Applications*. 3rd edn. Berlin Heidelberg: Springer-Verlag. Available at: https://doi.org/10.1007/978-3-662-05294-5.

Walpole, R.E., Myers, R.H. and Myers, S.L. (2012) *Probability and Statistics for Engineers and Scientists*. 9th edn. Prentice Hall Internationa.

Wang, Z., Lawrence, J., Ghail, R., Mason, P., Carpenter, A., Agar, S. and Morgan, T. (2022) 'Characterizing Micro-Displacements on Active Faults in the Gobi Desert with Time-Series InSAR', *Applied Sciences*, 12(9), p. 4222. Available at: https://doi.org/10.3390/app12094222.

White, M.J., Bennett, D.G., Crawford, M.B., Emsley, S. and Associates, G. (2004) *Techniques for Post-Closure Monitoring*. Nirex, p. 176.

Yague-Martinez, N., Prats-Iraola, P., Rodriguez Gonzalez, F., Brcic, R., Shau, R., Geudtner, D., Eineder, M. and Bamler, R. (2016) 'Interferometric Processing of Sentinel-1 TOPS Data',

IEEE Transactions on Geoscience and Remote Sensing, 54(4), pp. 2220–2234. Available at: https://doi.org/10.1109/TGRS.2015.2497902.

Yague-Martinez, N., Zan, F.D. and Prats-Iraola, P. (2017) 'Coregistration of Interferometric Stacks of Sentinel-1 TOPS Data', *IEEE Geoscience and Remote Sensing Letters*, 14(7), pp. 1002–1006. Available at: https://doi.org/10.1109/LGRS.2017.2691398.

Zan, F., Rocca, F. and Rucci, A. (2007) 'PS processing with decorrelating targets', in. *Envisat Symposium 2007*, Montreux, Switzerland: European Space Agency. Available at: https://www.semanticscholar.org/paper/PS-PROCESSING-WITH-DECORRELATING-TARGETS-Zan-Rocca/fef44b636c6960e3b3cc856dae3ae6832841ce8e (Accessed: 30 April 2023).

Zebker, H.A. and Villasenor, J. (1992) 'Decorrelation in interferometric radar echoes', *IEEE Transactions on Geoscience and Remote Sensing*, 30(5), pp. 950–959. Available at: https://doi.org/10.1109/36.175330.

Zhang, T., Zeng, Q., Li, Y. and Xiang, Y. (2008) 'Study on relation between INSAR coherence and soil moisture', *The International Archives of the Photogrammetry, Remote Sensing and Spatial Information Sciences*, 37.

Zou, B., Zhang, Y., Cao, N. and Nghia, P. (2015) 'A Four-Component Decomposition Model for PolSAR Data Using Asymmetric Scattering Component', *IEEE Journal of Selected Topics in Applied Earth Observations and Remote Sensing*, 8, pp. 1–11. Available at: https://doi.org/10.1109/JSTARS.2014.2380151.

Zwieback, S. and Hajnsek, I. (2016) 'Influence of Vegetation Growth on the Polarimetric Zero-Baseline DInSAR Phase Diversity—Implications for Deformation Studies', *IEEE Transactions on Geoscience and Remote Sensing*, 54(5), pp. 3070–3082. Available at: https://doi.org/10.1109/TGRS.2015.2511118.

Zwieback, S., Hensley, S. and Hajnsek, I. (2015) 'Assessment of soil moisture effects on L-band radar interferometry', *Remote Sensing of Environment*, 164, pp. 77–89. Available at: https://doi.org/10.1016/j.rse.2015.04.012.

Zwieback, S., Hensley, S. and Hajnsek, I. (2017) 'Soil Moisture Estimation Using Differential Radar Interferometry: Toward Separating Soil Moisture and Displacements', *IEEE Transactions on Geoscience and Remote Sensing*, 55(9), pp. 5069–5083. Available at: https://doi.org/10.1109/TGRS.2017.2702099.